

2008

Predicting loads on ground engaging tillage tools using computational fluid dynamics

Mark Eugene Barker
Iowa State University

Follow this and additional works at: <https://lib.dr.iastate.edu/rtd>

 Part of the [Agriculture Commons](#), [Bioresource and Agricultural Engineering Commons](#), [Geology Commons](#), [Geotechnical Engineering Commons](#), and the [Mechanical Engineering Commons](#)

Recommended Citation

Barker, Mark Eugene, "Predicting loads on ground engaging tillage tools using computational fluid dynamics" (2008). *Retrospective Theses and Dissertations*. 15886.
<https://lib.dr.iastate.edu/rtd/15886>

This Dissertation is brought to you for free and open access by the Iowa State University Capstones, Theses and Dissertations at Iowa State University Digital Repository. It has been accepted for inclusion in Retrospective Theses and Dissertations by an authorized administrator of Iowa State University Digital Repository. For more information, please contact digirep@iastate.edu.

Predicting loads on ground engaging tillage tools using computational fluid dynamics

by

Mark Eugene Barker

A dissertation submitted to the graduate faculty
in partial fulfillment of the requirements for the degree of

DOCTOR OF PHILOSOPHY

Major: Mechanical Engineering

Program of Study Committee:
J. Adin Mann III, Major Professor
James Bernard
Don Flugrad
Thomas Rudolphi
David White

Iowa State University

Ames, Iowa

2008

UMI Number: 3307054

INFORMATION TO USERS

The quality of this reproduction is dependent upon the quality of the copy submitted. Broken or indistinct print, colored or poor quality illustrations and photographs, print bleed-through, substandard margins, and improper alignment can adversely affect reproduction.

In the unlikely event that the author did not send a complete manuscript and there are missing pages, these will be noted. Also, if unauthorized copyright material had to be removed, a note will indicate the deletion.



UMI Microform 3307054
Copyright 2008 by ProQuest LLC
All rights reserved. This microform edition is protected against
unauthorized copying under Title 17, United States Code.

ProQuest LLC
789 East Eisenhower Parkway
P.O. Box 1346
Ann Arbor, MI 48106-1346

DEDICATION

I would like to dedicate this to my wife Renea for all her support while I pursued my educational goals. For enduring all of the evenings and weekends I was busy with school. For our two wonderful children that came along the way. I am finally done.

TABLE OF CONTENTS

ACKNOWLEDGEMENTS.....	v
ABSTRACT.....	vi
1. INTRODUCTION.....	1
1.1 Benefits of Using FEA-CFD.....	4
1.2 Detriments to Using FEA-CFD.....	5
1.3 Literature Review.....	5
1.4 Brief Overview of Finite Element Analysis.....	17
1.5 Brief Overview of Computational Fluid Dynamics.....	18
1.6 Overview of Fluid-Structure Interaction.....	20
1.7 Research Outline.....	21
2. SOIL PROPERTY TEST.....	22
2.1 Soil Viscometer.....	22
2.2 Experiment Setup.....	24
2.3 Results.....	26
2.4 Statistical Analysis.....	35
2.5 Conclusions.....	36
3. RIGID FLAT BAR LAB TEST.....	45
3.1 Test Setup.....	45
3.2 Results.....	48
3.3 Statistical Analysis.....	52
3.4 Conclusions.....	53
4. FIELD CULTIVATOR STANDARD LAB TEST.....	54
4.1 Setup.....	54
4.2 Results.....	57
4.3 Statistical Analysis.....	63
4.4 Modal Analysis.....	68
4.5 Frequency Analysis of Measured Draft Force.....	72
4.6 Conclusions.....	80
5. CFD SOIL MODEL.....	82
5.1 Model.....	83
5.2 Results.....	84
5.3 Conclusions.....	87
6. RIGID FLAT BAR SIMULATION.....	88
6.1 Model.....	88
6.2 Results.....	96
6.3 Conclusions.....	102
7. FIELD CULTIVATOR STANDARD SIMULATION.....	103
7.1 Model.....	103
7.2 Modal Analysis.....	112
7.3 Steady-State CFD Only Results.....	112
7.3 Transient Fluid-Structure Interaction Results.....	124
7.4 Conclusions.....	125

8.	ALTERNATIVE SOIL PROPERTY MEASUREMENT	128
8.1	Limitations of Soil Viscometer	128
8.2	Proposed Material Property Test	128
8.3	Conclusions	130
9.	CONCLUSIONS	132
9.1	Simulation Methodology.....	132
9.2	Soil Property Measurement.....	133
9.3	Rigid Flat Bar Test	133
9.4	Field Cultivator Standard Test	134
9.5	Soil Model Verification	135
9.6	Rigid Flat Bar Simulation	135
9.7	Field Cultivator Standard Simulation	136
9.8	Alternative Soil Property Measurement.....	137
9.9	Future Work	138
	APPENDIX.....	140
	BIBLIOGRAPHY	186

ACKNOWLEDGEMENTS

I would like to thank my advisor Dr. Adin Mann III for all of his guidance, help, and encouragement. I would like to thank my committee members for volunteering their time and providing me feedback through this process. I would also like to thank John Deere for funding the research and allowing me to use their test facilities. I would like to thank Brad Riesenberq, Carol Plouffe and Jim Schriver for their help in setting up and running the lab tests.

ABSTRACT

A new method of evaluating tillage tools using computational fluid dynamics is proposed. Steady-state CFD only and transient two-way fluid-structure interaction simulations were run to predict draft and vertical forces on a spring-reset field cultivator standard. Using CFD the soil was treated as a visco-plastic fluid using the Bingham-plastic material model. Lab tests were run using a rigid flat steel bar and a production field cultivator standard with 178 and 254 mm sweeps for comparison. The results indicate that the method can be used to reasonably predict the draft force to within three standard deviations of the average measured draft. The method was successfully used to determine which sweep size created the higher draft forces. The method also was able to predict the areas on the tool with the highest pressure related to the locations that exhibit the highest wear. Soil parameters were measured using a standard technique, but modified values were needed to get good agreement between measured and calculated forces. An alternate method of measuring soil properties using a flat steel bar was therefore proposed. Further work is needed to determine if the modified soil properties were correct, requiring the new soil property measurement technique, or if the CFD method needs to be modified.

1. INTRODUCTION

Currently, ground engaging tillage tools are developed by constructing parts and running physical tests either in a soil bin or in the field. Based on the results changes are made and new parts are constructed and retested. Design options are limited by the cost required to construct the parts and the time required to run tests. A new method of using computational fluid dynamics (CFD) to simulate ground engaging tools in soil is proposed. If successful, using CFD approach to design ground engaging tillage tools could reduce the time and cost required.

Throughout the history of farming various tools and machines have been developed to improve the effectiveness and speed of conditioning soil for improved crop growth. One important factor in evaluating these tools is the amount of power required to pull the tool, or implement, through the soil. The power requirement effects the size of tractor needed, the speed, and depth at which the tool can operated.

A common type of tool used to condition soil is a standard as shown in Figure 1.1. There are several types of standards based on the soil depth that they operate at and the type of soil conditions they are made for. Most agricultural implements have several standards mounted across the width of the machine. Each standard is typically made up of a rigid steel bar, referred to as the shank, which mounts to the frame of the implement and hangs below the frame with a steel blade mounted at the end that is pulled through the soil. Common blade types are sweep, point, and shovel and are designed to penetrate and breakup the soil. Modern day standards have spring reset mechanisms so that the sweep and shank can rotate up and over obstacles, such as large rocks, but reset back into the ground after clearing the obstacle. Spring reset standards are used on a number of different types of tillage tools including: field cultivators, chisel plows, mulch finishers, disc-rippers, mulch rippers, and mulch tillers.



Figure 1.1: Field cultivator spring reset standard

Consider the example of a field cultivator sweep from Figure 1.1 which will be studied in this dissertation. The work done by the sweep creates forces that are carried through the standard and into the implement frame. The forces can be divided into three components as illustrated in Figure 1.2. The force in the fore-aft direction is commonly referred to as the draft force. The vertical force is the amount of force the standard sucks into the ground or pushes up. The lateral force is the side-to-side force. These forces tend to be cyclic in nature and fatigue the implement frame. The sum of the forces from each individual standard is the total load on the hitch of the implement that connects the implement to the tractor.

Typically, tillage tools are developed by evolution rather than revolution. That is, current tool shapes are modified or created using welded steel plates and tested in the field or the lab. This method limits both the number and types of designs that can be evaluated due to the time and cost required. Although the shape of the tool may be modeled in three-dimensions on a computer, test parts must still be made and physically tested.

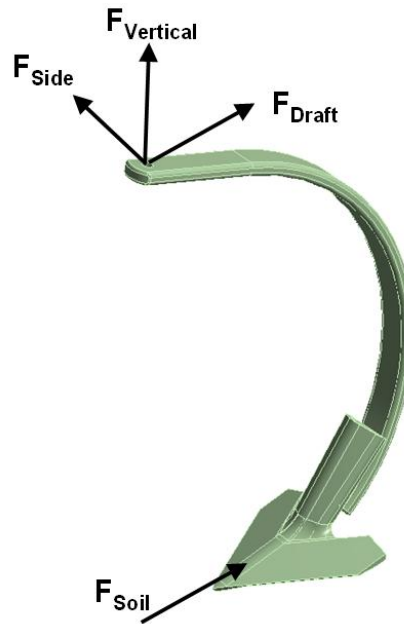


Figure 1.2: Free body diagram of field cultivator sweep and shank

Investigations have been made over a century in developing methods of measuring draft forces in lab and field conditions. John J. Thomas in 1869 described the principles of farm implements and the effect of draft for plows and cultivators (Thomas, 1869). A number of authors have investigated analytical methods of predicting the forces on tillage tools based on soil mechanics. More recently work has been done on developing numerical models for predicting draft loads based on laboratory or field test results. The latest work in this field is computer based simulations to predict static draft loads. Computer simulations may also be used to predict the amount of soil disturbance and the resulting trough or furrow. However, no known work has been done on predicting loads on production tillage tools using computational fluid dynamics and there is also no known work on predicting dynamic loads on spring reset tillage tools.

The benefit of predicting loads on tillage tools using computer simulations is that any number of tillage tool geometries can be evaluated in various types of soil conditions without the expense and time of building working prototypes. Currently, it can take several days to manufacture a rough weldment or weeks to order rapid prototype forgings or castings. In addition, testing in a soil bin can take several days to complete if different moisture levels are considered. In contrast, steady-state simulations can be completed in hours. Transient

analysis can be more time consuming and depending upon the size of the models could take days or weeks to run. Besides predicting the amount of power necessary to pull an implement with a known number of standards, being able to predict the dynamics of the loading can be used in predicting fatigue lives of the standards and the frame that the standards attach to. This is the reasoning behind the research presented here.

The approach taken for this research is to use a combination of finite element analysis (FEA) with computational fluid dynamics (CFD) to model the soil tool interaction of a spring reset field cultivator standard. The FEA model contains the structural components of the tool and the CFD domain represents the soil and in particular as a visco-elastic Bingham plastic.

The Bingham plastic material model was chosen for several reasons. The literature review showed that this model has been previously applied to soils. The model requires just two parameters, shear strength and viscosity. It was a desire of this research to use a material model that could be used with actual field soil conditions that could be obtained in-situ. As a part of this research a portable soil viscometer was constructed to measure the two material properties necessary for the model. The viscometer can be used in a soil bin or out in the field. The only other property necessary for the CFD model was density. However, the soil viscometer was developed for civil engineering purposes for use with static structures. As an addition to this research, a proposal for a more dynamic method of soil property measurement is included.

1.1 Benefits of Using FEA-CFD

One of the biggest weaknesses of using just FEA to simulate a tool moving through soil is modeling the domain. In the FEA model the entire length of soil mass that the tool will travel through during the simulation must be modeled. Considering a simulation running at 16.09 kph (10 mph) would require a domain 4.47 meters long for a one second run time. This could be prohibitively large if a somewhat refined mesh is used. Using CFD for the soil domain reduces the model to a window around the tool of interest. An analogy would be that using FEA would be like watching the tool pass by while standing in the field while using CFD would be like riding with the tool as it travels through the field.

Another benefit of using CFD for the soil domain is that the number of inputs required to characterize the soil is simplified to density, yield strength, and viscosity. Using

FEA requires that a more complicated material model with possibly a detailed stress versus strain curve with failure criteria be defined. To simulate soil failure once an element has reached the failure limit for stress or strain then that element is deleted and thus separating the mass. This can increase the sensitivity to mesh size and be computationally expensive.

Using FEA to model the spring reset standard allows the deflection of the standard to be simulated in a way that would not be easily replicated in just a CFD analysis. In CFD it is possible to develop equations that will replicate the movement of the mesh based on the resulting pressures but it is much more difficult to accomplish. This joint simulation is made possible by the ANSYS Workbench software package that supports the two-way interaction between the ANSYS FEA solver and the CFX CFD solver.

1.2 Detriments to Using FEA-CFD

One detriment to using CFD to model the soil domain is that the momentum of the tool is not included in the analysis. As shown in laboratory testing, as a tool disturbs the soil the forward momentum of the tool causes the soil to move in the same direction as the tool until the particle is tossed to the side and the tool passes by. In the CFD analysis the tool has no momentum because the tool is stationary and the soil flows around the tool. Consequently, the soil tends to build up in front of the tool rather than rolling forward and falling to the side. The repercussions of this will be discussed later.

Obviously using two codes rather than just one software package for the simulation introduces more chances for problems to arise. Care must be taken in setting up the models and defining the interfaces that the pressure and displacement data is transferred across. A finer detail is that the builds (build date/release level) of the ANSYS and CFX software must be the same for the two codes to interact.

1.3 Literature Review

For more than a century work has been done to understand the physics behind tillage operations. John J. Thomas wrote a book in 1869 describing how tillage equipment of the time worked and the effects of the ground forces on the implement (Thomas, 1869). His work was mostly based on observation and qualitative in nature. As the understanding of soil failure and soil-tool interaction has increased so has the level of detail in the analysis.

Some of the earliest developments in understanding soil failure were developed by Coulomb in 1776. He surmised that the shear strength of soil was made up of two components: cohesion and friction. Cohesion is the shear strength or bonding strength of the soil independent of any external applied pressure. Friction is the shear strength component that is relative to the applied pressure. Coulomb's law of soil shear strength is

$$\tau = C + \sigma_n \tan \phi, \quad (1.1)$$

where: τ = soil shear strength at failure

C = cohesion

σ_n = normal stress on the failure plane

ϕ = angle of internal friction

From the Coulomb's law of soil shear strength, various methods of evaluating the force of the soil acting on a wall or cutting tool have been developed. The basis for these formulations started out from infinite smooth vertical walls retaining a soil mass, such as a retaining wall. Coulomb developed one of the earliest such methods of calculating the soil force. He based his method on the idea that the weakest failure plane would most likely be the failure surface. Then he calculated the failure surface based on the internal friction, cohesion strength, and soil weight. The graphical representation of this development is shown in Figure 1.3. The resulting equation is

$$P = \frac{1}{2} \gamma z^2 \left[\frac{1 - \sin \phi}{1 + \sin \phi} \right] - 2Cz \left[\frac{1 - \sin \phi}{1 + \sin \phi} \right]^{\frac{1}{2}} \quad (1.2)$$

where: P = force of the soil acting on the wall

γ = soil specific weight

z = depth or height of the soil mass

C = cohesion

ϕ = angle of internal friction

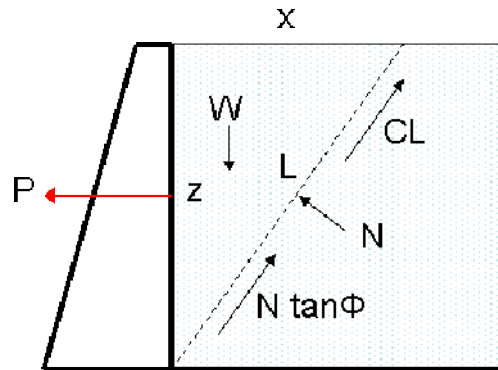


Figure 1.3: Representation of Coulomb's soil force development

The methodology developed by Coulomb has been applied to certain types of soil-tool interactions. These included wide tools such as bulldozer blades and plows where edge effects are small compared to the forces on the face of the tool because the width of the tools is large compared to the height. However, there are many types of tillage tools that do not satisfy the geometry assumptions.

Mohr, in 1882, showed that it is possible to show the two dimensional stress state on the failure plane even with known stress values that are not on the failure plane. The stresses on the failure plane can be determined by creating a graph of Mohr's circle with the values of cohesion and the principal stresses. The graph could also be used to calculate the internal friction angle of the soil and the angle of the failure plane. Figure 1.4 shows an example of the stress state on a triaxial soil sample and the corresponding Mohr's circle of the stress state.

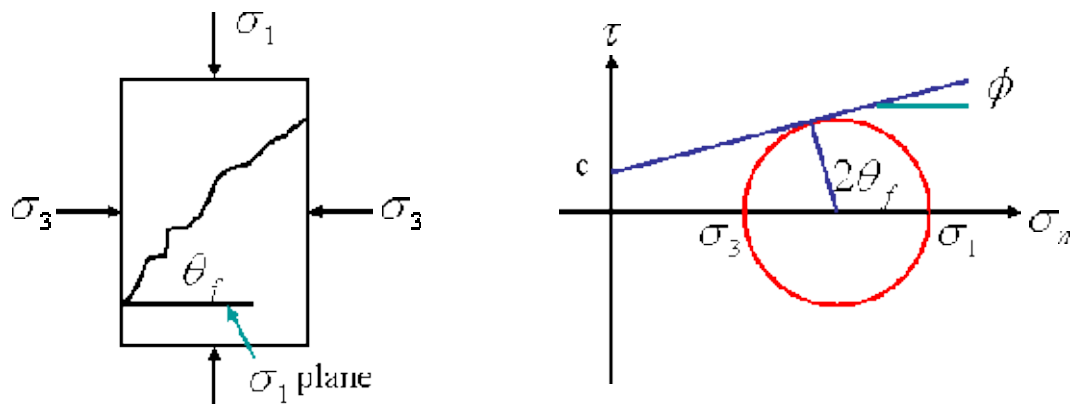


Figure 1.4: Mohr's circle of stresses for soil in failure

Prandtl developed an equation for determining the bearing capacity of smooth shallow footings. Directly below the footing is an active Rankine soil failure zone that moves downward and to the sides are passive failure zones that move up. Between the active and passive failure zones are radial shear zones. Prandtl surmised that if the weight of the soil were assumed to be negligible compared to the forces resulting from soil cohesion along the radial shear zone then the shape of the radial shear zone surface would be a log spiral (McKyes, 1989).

Combining the theories of Coulomb and Prandtl resulted in a two-dimensional model for calculating soil forces on tillage tools. The two failure zones in front of the tool have a surface shaped by the logarithmic spiral curve as mentioned before. Calculating the soil forces on the failure boundaries of the two zones and adding in the body forces can be used to calculate the force components on a tillage tool. Based on this theory, Reece developed a force equation for the total force on the tool (Shen and Kushwaha, 1998). Figure 1.5 illustrates the model and failure surface.

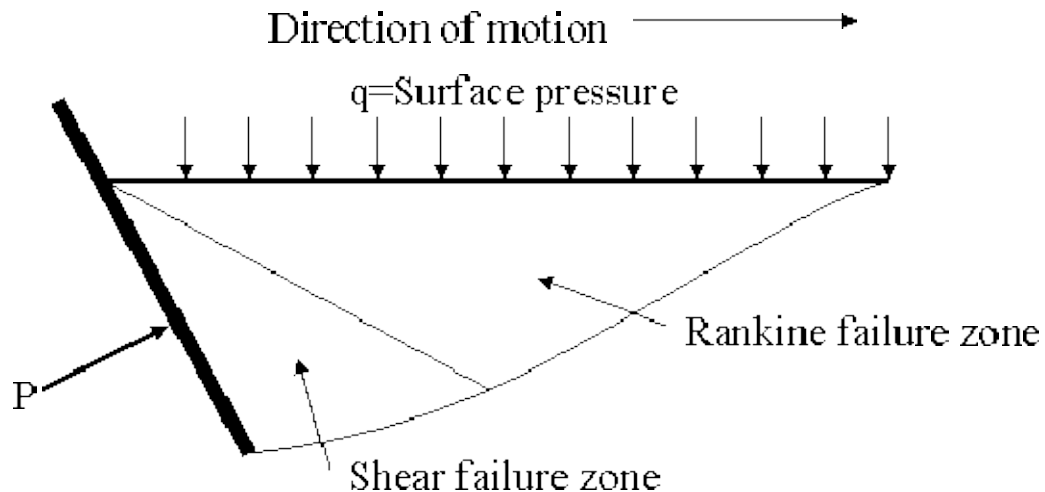


Figure 1.5: 2-d soil-tool model with logarithmic spiral failure zone

In 1956, Payne ran tests with flat steel blades of various height to width ratios and in several soil types and proved the necessity of specialized methods for narrow tools. For most tillage tool applications, these two dimensional based methods are not accurate where the tool width to depth ratio is less than ten. Payne also showed that the distance from the tool to

the forward failure plane changed with the tool width to depth ratio (McKyes, 1989). Based on his observations, Payne developed a three-dimensional model for predicting the draft and vertical forces on narrow tools with a width to depth ratio less than one. In developing his equations, he broke up the soil failure mass into three regions. Further experiments showed that the shape of the soil failure mass changed with the change in the shape of the tool. Others have developed their equations to address this shortcoming of Payne's equations.

Observations in the field have given way to lab experiments in controlled conditions that allowed for repetition. Soil bins were created in laboratories so that various soil parameters could be controlled to determine the effect on tillage tools. Willatt and Willis studied the effect of soil compaction and buildup on simple tines (Willatt and Willis, 1965). Others used grids of chalk drawn onto the soil to observe how soil breaks as a tool passes through. From these observations more tillage specific analytical models were developed to predict the stresses in the soil and the forces created on simple tool shapes. For example, Koolen and Kuipers developed various equations for predicting the draft of a plough as a function of soil moisture or speed (Koolen and Kuipers, 1983).

Stafford (1981) looked at the application of critical state soil mechanics as they apply to rigid tines. He performed laboratory experiments using narrow tines 40 mm wide and operating at 150 mm depth in a soil bin. A sandy loam and clay soil types were considered. He observed both the soil failure pattern on the surface and the draught force versus time for varying speeds, moisture levels, and rake angles. Two failure modes were observed, brittle and flow. He noted that flow failure was observed at higher speeds (5 m/s) for all moisture levels tested. The results lead to the idea of a failure coefficient or index, F , which is defined such that below the value soils would fail in brittle mode and above the index value soils would fail in flow mode.

Trying to predict the dynamics of soil-tool interaction have not received nearly the attention of predicting average draught forces. However, one such analysis was conducted by Upadhyaya et. al (1987). They used Fast Fourier transform and harmonic analysis techniques to understand and predict the dynamic loading of tillage tool draft. They found that the dominant frequency was tied to the soil-fracture mode. For their studies, they used a rigid flat bar operating at 50 mm depth. First they ran tests at two speeds and in two soils.

They were able to predict the force/time response based on the FFT results and the equation that was developed from their test data. The calculated dominant frequencies 7.75 Hz for Soil1A and 9.43 Hz for Soil2 at 0.22 m/s and 31.25 Hz for Soil1A and 19.86 Hz for Soil2 at 1.11 m/s. They also ran four additional tool systems to see the impact on the load frequency and the resulting draught forces. These included a sprung rigid tool, a tuned stiffness rigid tool, sinusoidal oscillation of a non-rigid tool, and non-sinusoidal oscillation of a rigid tool. They concluded that for many cases the load does vary in a periodic mode and at extremes the load could vary by +/- 50 percent of the mean draft value.

Glancey et. al (1989) looked at the dynamic loading characteristics of a chisel in tilled and untilled field conditions. They conducted tests in field conditions at operating depths of 100 and 200 mm. The operating speed varied between 0.8 and 3.2 km/h. The resulting measured load frequencies ranged from 0.81 Hz up to 11.15 Hz. The higher frequencies matched up with the higher operating speed but were not directly related to operating depth. The distance from the tool face to the fracture surface was inversely proportional to speed. The slower speeds created the largest distance to the fracture surface. A modal analysis of the chisel showed a first vibration of approximately 55 Hz indicating that the measured frequencies of the loading were due to the soil failure.

Most of the two and three-dimensional models were based on wide tools and were not valid for narrow tillage tools, as found by Payne. Also, these models did not account for the dynamic effects at speeds which are common to tillage practice. So Swick and Perumpral (1988) set out to update the quasi static equation previously developed by Perumpral et. al to account for the shear rate effect and friction at the soil-tool interface and apply it to narrow tillage tools. They developed a three step procedure for tines and tested it in a soil bin. First, they conducted laboratory tests to determine the relationship of shear rate on shear strength and the soil-tool friction values. Second, they modified the classical “slow moving” soil force equation to account for shear rate effects and the force of accelerating the soil mass. Third, the resulting equation was verified by running additional comparison tests in a soil bin. The soil failure mass accounted for the edge regions and broke the mass into a center wedge and two circular side wedges. Their analysis included four tool widths operating at 51, 102, and 152 mm of depth. Their model gave results for the narrow tools considered.

More advanced soil models have been developed for geotechnical purposes and even implemented into commercial finite element packages. These are used mostly for static analysis for slope stability and foundations. One example is the CAM Clay model developed by the Geotechnical Group at Cambridge University in 1958. This model is based on critical state soil mechanics, which basically says that “a soil is said to be in critical state when it undergoes large shear deformations at constant volume and constant shear and normal effective stress” (Karmakar, Sharma, Kushwaha, 2004). Rather than defining the failure stress state with Mohr’s circle, a three-dimensional stress state is developed with the critical state line (CSL) passing through it. Many variations of the basic Cam Clay model have been developed over the years. These models account for the stress history and any resulting softening or hardening of the soil. The model also takes into account the initial void ratio, compressibility, and swelling. The basic Cam-Clay model uses five parameters which are determined with various lab tests including triaxial and oedometer (PLAXIS V. 8). Other advanced models that include hardening and softening can use from five to fifteen parameters.

Wheeler and Godwin (1996) experimentally developed equations to predict the draught forces for single and multiple tines at speeds up to 20 km/h. Using previously developed equations by Godwin et. all for horizontal and vertical forces they created an additional equation that took into account both the number of tines and the spacing. The predictions were tested in both the lab, with a frictional soil, and in the field, with a cohesive soil. They were able to get good correlation for horizontal and vertical forces for both soil types. They also confirmed findings by Schuring and Emori that below a critical speed, inertial effects are negligible.

Using a glass sided soil bin, Fielke (1996) looked at the effect of the tillage tool cutting edge on the soil. In his experiments he used a 400 mm wide experimental sweep and varied the sharpness or bluntness of the leading edge and the effect on draught and soil fracture. He also compared the results with field results taken in two soil types (sandy loam and clay loam). The soil bin soil was prepared with a white grid that was visible from outside and the displacements of the soil were video recorded as the sweep was moved

through the soil. He found that the shape of the leading edge of the tillage tool had a strong effect on the measured draught forces.

Along the way various tools have been developed in the geotechnical community to measure and characterize the strength of soil. Such tools include the cone penetrometer and rotary shear vane. The cone penetrometer was developed to measure the level of compaction present in soil as a function of stress. The rotary shear vane was developed to measure the shear strength of soil. Both of these tools have been used extensively in laboratory and in-situ or field conditions.

Using a standard tine to predict the loads on tillage tools was proposed by Desbiolles et.al (1997). They investigated an approach where the tillage forces could be predicted based on two factors relating to soil strength and the tool geometry. The first step involved establishing relationships between a standard tine and various tool geometries under controlled soil conditions, such as in a soil bin. Five different tool types were considered including two subsoilers, chisel tine, disc, and mouldboard plow. The second step involved measuring the forces on the standard tine in a variety of field conditions. Collecting data with the standard tine in four soil conditions, they were able to predict the draught to within an average of 18 percent of the measured force.

Predicting tillage forces based on cone penetrometer readings was proposed by Desbiolles et. al (1999). In their research they compared the relationship between the cone penetration energy (P_e) and the soil strength factor (S). They collected cone penetrometer data in sandy-loam and clay soils. Draught data was collected for a 70mm wide standard tine. Using a regression analysis of the data, they were able to develop equations for sandy and clay soils as a function of soil type, geometry, tool width, working depth, and penetrometer energy.

One of the interesting observations made about soil at failure is that the soil appears to “flow”, as stated by Stafford and others. More clearly stated, prior to failure soil acts as a solid, however, once failure has been reached soil can act more like a fluid. Several investigations into this phenomenon have been made and have lead to comparing soil to a viscous fluid. Some viscosity models have been examined and include linear, power law, and hyperbolic sign function (Keedwell, 1984). Because of the solid/fluid dual nature the

Bingham Plastic model has been considered to model the non-Newtonian visco-plastic nature (Vyalov, 1986). Figure 1.6 graphically shows the visco-plasticity model. This model describes the shear stress as a function of the yield strength, viscosity, and shear rate.

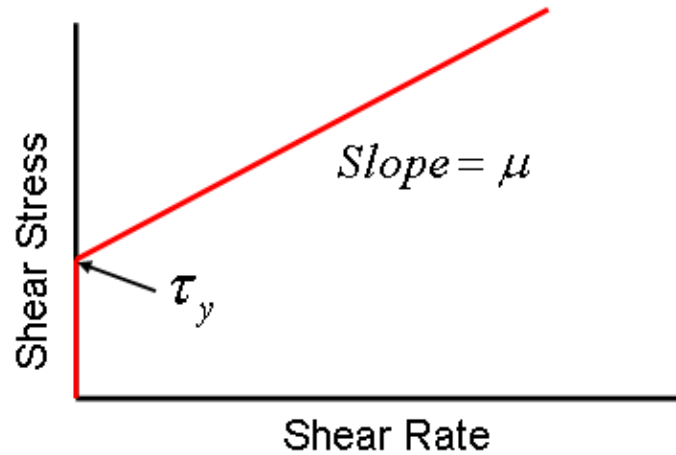


Figure 1.6: Bingham Plastic model

Two equations describe the two curves representing the Bingham plastic model. The first equation defines the value of shear stress as a function of yield and shear rate. The second equation defines the conditions for the shear rate for use in the first equation. The equations are:

$$\tau = \tau_y + \mu\dot{\gamma} \quad \text{when } |\tau| > \tau_y \quad (1.3)$$

$$\dot{\gamma} = 0 \quad \text{when } |\tau| \leq \tau_y \quad (1.4)$$

where: τ = shear stress (Pa),

$\dot{\gamma}$ = shear rate (s^{-1}),

τ_y = yield strength (Pa),

μ = plastic viscosity (Pa-s),

The advantage of this material model is its simplicity since only two parameters are required. In addition, these parameters can be easily obtained using a rotary shear vane. Soil parameters can be measured in the lab or in the field.

Zhixiong, Yaohua, and Junzheng (2001) looked at the stress strain behavior of clay and sandy soils under explosive loading to determine the soil mechanical properties. Soil

samples were prepared in a soil pit with a steel plate set on top. An explosive of ammonium nitrate fuel oil was detonated on top of the plate to create a one-dimensional stress wave. In their experiments they used piezoelectric crystal gauges buried at three depths to measure the soil stress. From the measured response they used a Lagrangian analysis method to develop a stress-depth-time surface. They concluded that both soil types exhibited fluid elastoplastic behavior from 0 to 20 cm in depth and viscoplastic behavior from 20 to 60 cm.

Jayasuriya and Salokhe (2001) reviewed the soil-tine models available at the time to organize the different approaches and determine what work need to be done. They considered eighteen different published works dating from 1952 to 1998 dealing with soil failure. The models covered a large range of tool types, soil types, and failure types. The models were organized into two groups: those that did not consider dynamic effects and those that did. They reviewed fourteen tillage force prediction models that did not account for dynamic effects and ten models that did account for dynamic effects. From their study they concluded that “the feasibility of applying theories in the area of laminar fluid flow mechanics to the behavior of wet clay under tool motion could be studied.” They thought that frictional-cohesive and partially saturated soil could be modeled as turbulent flow.

In addition to analytical models, numerical models have also been investigated. These have made use of finite element analysis (FEA) to predict static states of stress in the soil and the forces on simple tool shapes. Various elastic constitutive models have been investigated such as linear, nonlinear (bilinear and multi-linear), hyperbolic, and rate dependant. Plastic models have also been investigated including rigid, perfectly plastic and elastic-plastic. Properties for soil were measured using triaxial tests such as modulus of elasticity, Poisson’s Ratio, and stress/strain curves.

Shen and Kushwaha (1993) compared two and three-dimensional FEA models to soil bin results and looked at how the simulation time might be reduced. For the soil, they used a hyperbolic stress-strain model. The model was of a rigid flat bar 50 mm wide and operating at 100 mm depth. The 3-D model was half-symmetry. They created a FORTRAN based program and compared the run time results with a commercial code. Their results showed that although 2-D plane strain or plane stress models ran considerably faster, the 3-D model provided the most accurate results.

Shen and Kushwaha (1998) followed up their work with a book investigating various aspects of using FEA for soil-tool interaction. In their book they looked at various constitutive models for modeling soil, ways of simulating the soil-tool interface, various algorithms, and programming techniques. As part of their ongoing research they ran simulations with ADINA software that allowed for element birth and death. When a soil element reached the shear or tensile failure criteria then the element stiffness was greatly reduced so that the element did not contribute in any further iterations towards the forces on the tool.

Fielke (1999) compared the results for a two-dimensional FEA model with experimental and field results. His model was of the outside edge of an experimental sweep. Using NISA II software with the soil modeled as elastic-plastic with a Mohr-Coulomb failure criterion. The soil parameters were taken from direct shear and triaxial compression tests. In addition, the model included friction between the soil mass and the tool. Their work showed a large effect of Poisson's ratio when the soil does not remain in contact with the tool, as in the case of sweeps. He found that good correlation could be achieved between predicted draft and vertical forces with experimental data.

Mouazen and Nemenyi (1999a, 1999b, 1999c) looked at how tillage tool design could be affected using FEA. They used COSMOS/M software and modeled the soil as elastic-perfectly plastic with the Drucker-Prager criterion. The half-symmetry three-dimensional model was of a medium-deep subsoiler and the soil mass just ahead of it. They considered four tool geometries and one sandy loam soil type. The predicted pressures on the tool face were greatest near the bottom outside corners. Soil bin tests were then conducted and the predicted force values were compared. They found that the FEA models over predicted the forces by up to 20 percent. Vertical soil movement was also well predicted.

Rosa and Wolfsohn (1999) looked as using FEA to predict the draft loading of narrow tools at high speeds. Their material model was based on a hypoelastic using a variable Young's modulus and Poisson's ratio. They also ran laboratory tests in a soil bin to develop soil properties and to compare the analytical results with. They found that including inertial and viscous effects led to numerical instabilities. A viscoelastic model that included damping was able to make better average draft predictions.

Another method that has been used to look at dynamic soil-tool interaction is by using a hypoplastic stress-strain material model. Abo-Elnor used the Wolffersdorf version of the hypoplastic model that had been implemented into the ABAQUS finite element code to model fully drained sandy soil. A model of a simplified dozer blade was considered at various speeds (Abo-Elnor et.al, 2003, 2004). The blade was modeled as a rigid body with enforced displacements so no soil failure dynamics were observed in the results. Also, the results were not compared to any lab or field data.

Mouazen and Ramon (2002) used a combined numerical and statistical model to simulate a subsoiler in sandy loam soil. A FEM model was used to study the effects of varying the width of the tool, operating depth, and soil density on the reaction forces. The FEM model was run in COSMOS/DesignSTAR 1.0 software. The soil was modeled as Drucker-Prager elastic-perfectly plastic with Coulomb's criterion with friction between the soil and tool. Using the FEM results, multiple regression analyses were done to develop a formula to predict the draught forces for any combination of width, depth, and soil density. The predictor equation was compared to soil bin results and was found to have a small over-prediction in the draught force.

Renon, Montmitonnet, and Laborde (2005) used FEA to look at a rigid tine in soil but carried their analysis out to include large-deformations. The soil was modeled as a elastic-perfectly plastic. In their research, they considered several different numerical methods but did not compare predicted force values with experimental data. They also simulated triaxial tests using two and three dimensional models. The software used was Flac2D and FORGE3 and the FORGE3 software allowed the soil domain to be remeshed at each time step to reduce mesh distortion during the analysis.

Using discrete element modeling (DEM) to simulate soil-tool interaction was considered by Asaf, Rubinstein, and Shmulevich (2007). They simulated two-dimensional quasi-static in-situ tests representing plate/wedge sinkage and Grouser shear tests in cohesionless soil. Physical tests were run using plastic chips, glass beads, and sea sand for comparison and parameter estimation of the analytical models. An elastic-plastic material model was utilized with contact and friction. The models were able to reasonably predict the forces measured and parameter optimization methods were investigated.

Considering that soil failure has been considered to mimic a fluid and to address the dynamic visco-plastic behavior, Karamakar and Kushwaha considered using computational fluid dynamics (CFD) to simulate the soil to interaction (2005a). In their work they considered a flat simple bar in a soil “flow” modeled as a Bingham plastic. Karamakar and Kushwaha also constructed a bench top rotary viscometer to measure the shear strength of soils at various speeds as needed to calculate the viscosity of clay loam soil at various levels of moisture and compaction (2006a and 2006b). The measured values for shear strength and viscosity were then used in the CFD models. The CFD domain consisted of only the soil and did not include the vertical displacements of the soil ahead and around the tool or the resulting trough behind the tool. The major findings from their work dealt with the predicted relationships between tool face pressure to speed and draft force to speed (2005b). The model did not consider the soil disturbance, the resulting furrow, or dynamic effects.

1.4 Brief Overview of Finite Element Analysis

Finite element analysis reduces a structural domain to a finite number of elements that represent the stiffness of the actual structure. A stiffness matrix is developed for the model based on the assembly of the stiffness of the individual elements. Based on provided boundary conditions a system of equations can be developed and solved to determine the remaining displacements and reactions of the nodes in the model. From these displacements the resulting strains and stresses can be calculated. The basic FEA system of equations for a static analysis is (Chandrupatla and Belegundu, 1991),

$$[K][U] = [R] \quad (1.5)$$

where: $[K]$ = global stiffness matrix,

$[U]$ = displacement column matrix, and

$[R]$ = reaction column matrix.

To simulate a dynamic system, additional forces must be added to the above equation. These include inertia forces and damping forces. All of these forces are time-dependent.

The inertia forces account for accelerations that act on the mass. The damping forces are velocity dependent. The dynamic system of equations is represented by

$$[M][\ddot{U}] + [C][\dot{U}] + [K][U] = [R] \quad (1.6)$$

where: $[M]$ = mass matrix

$[\ddot{U}]$ = acceleration matrix

$[C]$ = damping matrix

$[\dot{U}]$ = velocity matrix

$[K]$ = stiffness matrix

$[U]$ = displacement matrix

$[R]$ = reaction matrix.

The mass matrix and stiffness matrix are calculated from the FEA mesh with the assigned material density. The damping matrix $[C]$ can be replaced with Rayleigh damping which takes the form of $\alpha [M] + \beta [K]$ (Bathe, 1996). The values of alpha and beta can be determined from a modal analysis using two damping ratios corresponding to two different vibration frequencies.

1.5 Brief Overview of Computational Fluid Dynamics

One of the earliest recognized developments in CFD is attributed to Richardson who in 1910 presented a point iterative method for solving Laplace's equation and the biharmonic equation to the Royal Society of London. He used his method to calculate the stress distribution in a dam. He later included relaxation in his method to take information from the previous step to update the unknown to improve convergence. Through World War II additional improvements were made in relaxation techniques.

The beginning of applying numerical methods to CFD problems is attributed to Courant, Friedrichs, and Lewy who published a paper in 1928. In their paper they discussed the solving of partial differential equations using numerical methods. The paper also discussed stability requirements for hyperbolic partial differential equations solved by

numerical methods. This paper was later republished in the IBM Journal of Research and Development in 1967 (Tannehill et. al., 1997).

One of the principal equations used in CFD and of fluids in motion is the continuity equation. Based on the conservation of mass, the continuity equation says the time rate of change of system mass is zero. In other words, the mass flow rate into the system minus the mass flow rate out of the system is equal to the rate of change of the mass in the system (control volume) (Robertson and Crowe, 1990).

Newton's second law of motion states that the time rate of change of the linear momentum of a system is equal to the sum of the forces acting on the system. The forces include pressure, gravitational, and viscous forces. If the system is divided into differential fluid elements the forces can be evaluated on the faces. The forces acting on a differential fluid element can then be expanded into Cartesian coordinates. The forces acting on each of the faces can be rewritten in terms of normal and shear stresses divided by the surface areas. To account for viscous forces constitutive relationships can then be written for Newtonian fluids and substituted into Newton's second law. The resulting three equations (X, Y, and Z directions) are known as the Navier-Stokes equations. The equations for compressible fluids are:

X dir:

$$\rho \frac{Du}{Dt} = \rho g_x - \frac{dP}{dx} + \frac{d}{dx} \left[\mu \left(2 \frac{du}{dx} - \frac{2}{3} \left(\frac{du}{dx} + \frac{dv}{dy} + \frac{dw}{dz} \right) \right) \right] + \frac{d}{dy} \left[\mu \left(\frac{du}{dy} + \frac{dv}{dx} \right) \right] + \frac{d}{dz} \left[\mu \left(\frac{dw}{dx} + \frac{du}{dz} \right) \right] \quad (1.7)$$

Y dir:

$$\rho \frac{Dv}{Dt} = \rho g_y - \frac{dP}{dy} + \frac{d}{dx} \left[\mu \left(\frac{du}{dy} + \frac{dv}{dx} \right) \right] + \frac{d}{dy} \left[\mu \left(2 \frac{dv}{dy} - \frac{2}{3} \left(\frac{du}{dx} + \frac{dv}{dy} + \frac{dw}{dz} \right) \right) \right] + \frac{d}{dz} \left[\mu \left(\frac{dv}{dz} + \frac{dw}{dy} \right) \right] \quad (1.8)$$

Z dir:

$$\rho \frac{Dw}{Dt} = \rho g_z - \frac{dP}{dz} + \frac{d}{dx} \left[\mu \left(\frac{dw}{dx} + \frac{du}{dz} \right) \right] + \frac{d}{dy} \left[\mu \left(\frac{dv}{dz} + \frac{dw}{dy} \right) \right] + \frac{d}{dz} \left[\mu \left(2 \frac{dw}{dz} - \frac{2}{3} \left(\frac{du}{dx} + \frac{dv}{dy} + \frac{dw}{dz} \right) \right) \right] \quad (1.9)$$

The continuity equation and the Navier-Stokes equations are the governing equations for CFD analysis. The unknowns that have to be solved for are P, u, v, and w. Various numerical methods have been developed to solve these non-linear, second-order, partial

differential equations. For the research reported in this paper ANSYS CFX 11.0 has been used for solving the fluid flow problem.

1.6 Overview of Fluid-Structure Interaction

The two previous sections gave brief overviews of finite element analysis (FEA) and computational fluid dynamics (CFD). Combining these two analytical methods allows for the simulation of more complex problems containing fluid-structure interaction or FSI. Examples of this type of problem include fluid sloshing in a tank, airplane wing flutter, and pumps. FSI analyses can have one-way or two-way interaction and can be static or transient.

The more common method of FSI is when displacements are predicted by a structural analysis in a solid domain and passed onto the fluid domain. Nodes of the fluid mesh at the interface between the two fields are moved accordingly. The CFD analysis is run to calculate the new pressures at the interface and pass the information back to the structural solver. The pressure loads are updated and the process is repeated. Referring to the equations for FEA, the pressure from the CFD analysis is applied to the area of the interface and is included in the load vector $[R]$ in either equation 1.5 or 1.6. Referring to the equations for CFD, the predicted displacements at the interface, from the FEA domain, are applied to update the fluid domain before the Navier-Stokes equations 1.6, 1.7, 1.8 are solved.

In one-way interaction, one field is run and then the other field is run with the information from the first field. An example would be running a CFD analysis of a fluid domain representing a tank of fluid with an applied acceleration. The resulting pressures on the domain would then be passed to the structural model of the tank and supports to determine the displacements and stresses on the structure.

In a two-way interaction, the process would be the same as the one-way interaction except that the process would be repeated so that both solid and fluid fields impact each other. The solutions are obtained for each field until the difference between the shared values at the interface (displacements and pressure/force) is less than some specified limit. Once convergence has been achieved or a maximum number of iterations has been reached, the analysis is complete for a static analysis. For transient analysis, once convergence has been achieved within a time step or the maximum number of iterations has been reached, the time step is incremented until the full time of the analysis has been reached.

1.7 Research Outline

The plan for this research project is as follows.

- Measure soil properties
- Soil bin testing of rigid flat bar
- Soil bin testing of spring reset field cultivator standard
- Modal analysis lab test of spring reset field cultivator standard
- CFD simulation to validate material model
- CFD simulation of rigid flat bar
- Structural and CFD simulation of spring reset field cultivator standard

2. SOIL PROPERTY TEST

In order to simulate the soil and tool interaction it is necessary to model the soil and the behavior of the soil under large deformations. As mentioned previously, numerous approaches have been studied to model soil properties. This paper focuses on treating the soil as a fluid using CFD. The relevant properties for a fluid analysis are density and viscosity. The Bingham-plastic model was chosen for this analysis and requires an extra parameter for soil strength. Soil properties can vary greatly depending upon composition, moisture, and compaction. Because of this variation, soil properties have to be measured for specific conditions that are to be analyzed.

A portable soil viscometer was designed and constructed to measure the required properties. The viscometer is a powered rotary soil shear vane with a motor controller to operate at predetermined speeds. The vane has four blades and is inserted vertically into the soil to be tested. A motorized drive system rotates the shaft of the vane at specified speeds while the torque on the shaft is recorded. The measured torque is converted to stress and the values are plotted against the rotational speed. A linear curve is fit to the data with the slope representing the viscosity. The y-axis intercept represents the yield strength. The operation of the rotary shear vane and conversion from torque to stress is based on ASTM standard D2573-01.

2.1 Soil Viscometer

A gearmotor was used to drive the viscometer along with a variable speed drive and a 100:1 speed reducer to achieve the range of speeds required. The viscometer drive train was attached to a welded aluminum base that was mounted to the tool carrier on the soil bin. The variable speed drive was remotely mounted so that the viscometer could be used at any location across the soil bin and controlled from the side of the bin.

The soil shear vane was a Geonor 55x110mm rotary vane. The speed reducer was a 100:1 right angle worm gear drive from Torque Transmission model SWB-5H with a hollow output shaft. The BLF360A-30 gearmotor and controller are from Oriental Motor and included a 30:1 gear reduction. The gearmotor has an output torque of 46 in-lbf and has a

output shaft speed range of 2.7 to 133 rpm. The controller was digital and allowed for the speed to be set to within one rpm. The gearmotor was accelerated and decelerated at a rate of 0.5 rpm/sec. The gearmotor and the right angle speed reducer were connected by a flexible coupler, Oriental Motor #MCL4015F06. A custom torque transducer was designed and manufactured from cold drawn steel bar with a calibrated shear bridge. The shear vane mounted to the torque transducer fit inside the hollow output shaft of the speed reducer with the torque transmitted through a 0.125 inch pin. The shaft speed was measured with a magnetic pickup and an 18 tooth timing wheel. The speed and torque were recorded on a Somat EDAQ data acquisition system controlled through a Compaq nw8240 laptop computer running the Somat TCE software. Figure 2.1 shows the viscometer attached to the tool plate in the soil bin.

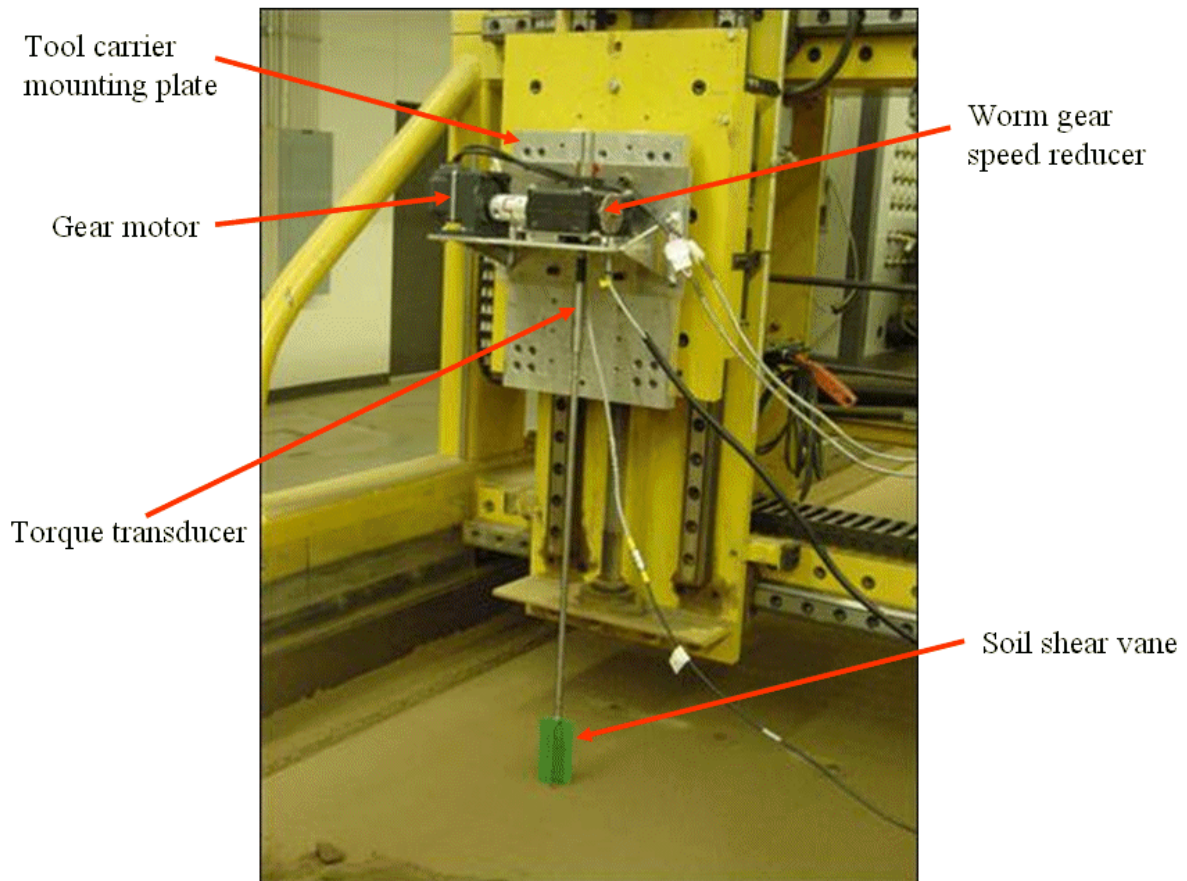


Figure 2.1: Soil viscometer mounted to soil bin tool plate

2.2 Experiment Setup

The lab tests conducted for this research were run at the John Deere soil bin facility. The soil (15% clay, 33% silt and 52% sand) was prepared to achieve a cone index of 200 (loose) and 1,100 (normal) kPa. The viscometer, rigid flat bar, and field cultivator standard were mounted to a tool plate on a carrier that can be driven at specified speed. The position of the tool plate can be controlled both across the width of the soil bin and also vertically.

The soil shear strength was calculated from the measured torque with the shear vane rotating at 0.027 rpm (0.17 deg/sec), within the range specified by ASTM D2573-01 Standard Test Method for Field Vane Shear Test in Cohesive Soil. To calculate the viscosity, the shear strength was also calculated from torque measurements taken at 0.053, 0.107, 0.213, 0.427, 0.853, and 1.333 rpm. The measured torque values were recorded to five significant digits. The shear strength (N/m²) was graphed against the rotating speed (rad/sec) and a linear curve was fit to the data with the slope representing the soil viscosity. The speeds were chosen based on the slowest speed achievable and then doubling the speed until the max motor speed was reached. The gearmotor and controller were chosen to maximize the range of speeds possible to see the shape of the relationship between shear stress and strain rate. The equation to calculate the shear strength is

$$(S_u)_{fv} = \frac{6T_{\max}}{7\pi D^3} \quad (2.1)$$

where T_{\max} is the maximum measured torque in N-m and D is the diameter of the shear vane in meters.

For each soil treatment the torque measurements were run at the seven speeds in three locations along the soil bin for replication, evenly separated along the length of the soil bin near the beginning (five meters), middle (ten meters), and end (15 meters). Soil treatments were run at two compaction levels, 200 kPa and 1,100 kPa and two moisture levels, 7.4% and 8.8% dry bulb (d.b.). The two compaction levels and the two moisture levels were used in the lab tests for the comparison runs of the rigid flat bar and the spring reset field cultivator standard. At each of the three positions along the soil bin the order that the seven speeds were tested was randomized. In addition, at each of the three locations measurements were

made in the soil bin, five penetrometer readings were taken across the width of the soil bin and one sample was taken to measure the moisture and density.

The seven shear strength tests were spaced evenly 288 mm apart with four samples taken on one side of the penetrometer readings and three taken on the other side of the penetrometer readings. Figure 2.2 shows the soil bin surface after all tests and samples had been run for the middle low moisture (7.4% d.b.) and low compaction (200 kPa) soil. The photograph shows the penetrometer holes down the middle and the shear vane holes on either side. The vane was inserted to a depth of about 152 mm so that the top of the vanes were approximately 50 mm below the surface. The calculated viscosity and shear strength properties were therefore averages over the depth of 52 to 152 mm.

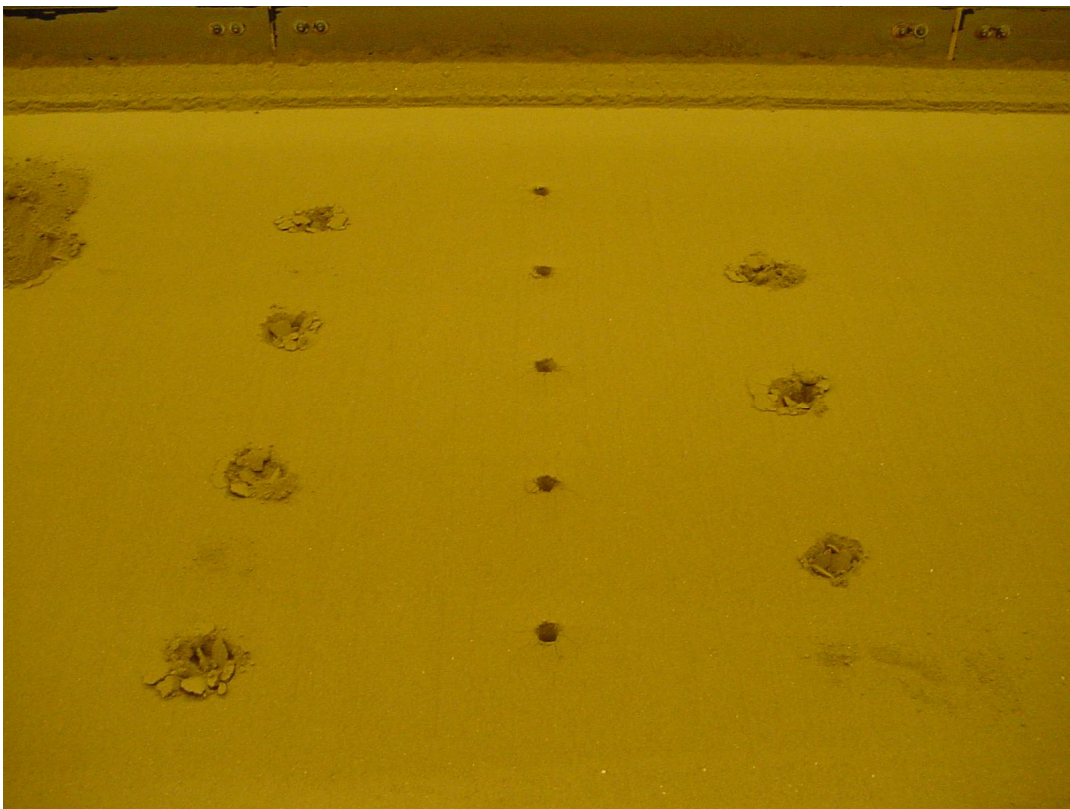


Figure 2.2: Soil bin surface with viscometer and penetrometer test holes

Figures 2.3 through 2.6 are examples of the penetrometer readings taken at the middle position in the soil bin from the soil surface down to 200 mm. The graphs for all of the positions and soil treatment levels are provided in the Appendix. The graphs show the variation in soil compaction both across the soil bin (Positions A-E) and through the depth of the soil.

The penetrometer and density readings in Table 2.1 show that there was variation both across the width of the soil bin and along the length of the soil bin. The results show that one side of the bin had consistently higher compaction. The third batch of readings taken near the end of the soil bin was consistently higher than the other two positions. At the high moisture (8.8% d.b.) level there appears to be a compacted layer just below the 150 mm depth. The viscometer was run at a single depth with the bottom of the rotary shear vane located at the 150 mm depth. Table 2.1 summarizes the measured density, moisture content, and average penetrometer measurements that were used in the computer simulations.

2.3 Results

For each soil treatment level and soil bin position the shear strength readings were graphed against the test run time in rad/sec. The resulting graphs for the measured data taken at the 10m position are shown in Figures 2.7 through 2.10. The graphs show the soil shear strength versus rotation angle for each of the shear vane test speeds and the residual strength of the soil after failure. The results were not consistent across all of the soil treatment levels for the change in strength at failure relative to speed. However, there did appear to be a difference between moisture levels. Typically failure occurred between 20 and 30 degrees of vane rotation. The slopes of the curves leading up to failure were similar for all speeds and for all conditions. This indicates that the soil is elastic and related to the soil shear strength independent of speed. This also indicates that the soil does not exhibit viscous behavior.

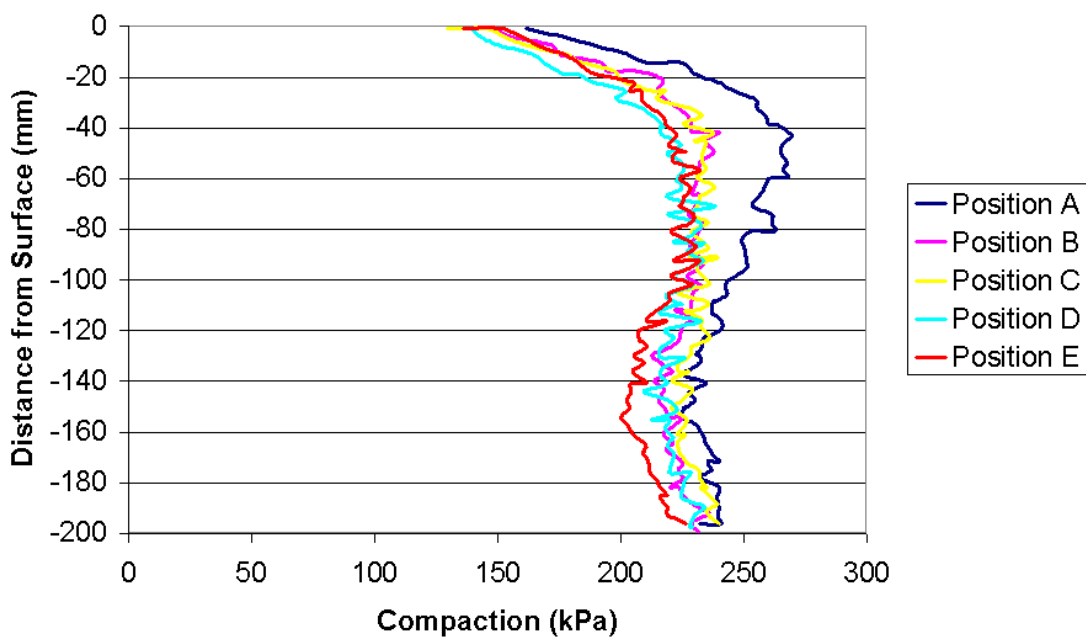


Figure 2.3: Penetrometer readings for middle position, low moisture (7.4% d.b.), low compaction (200 kPa)

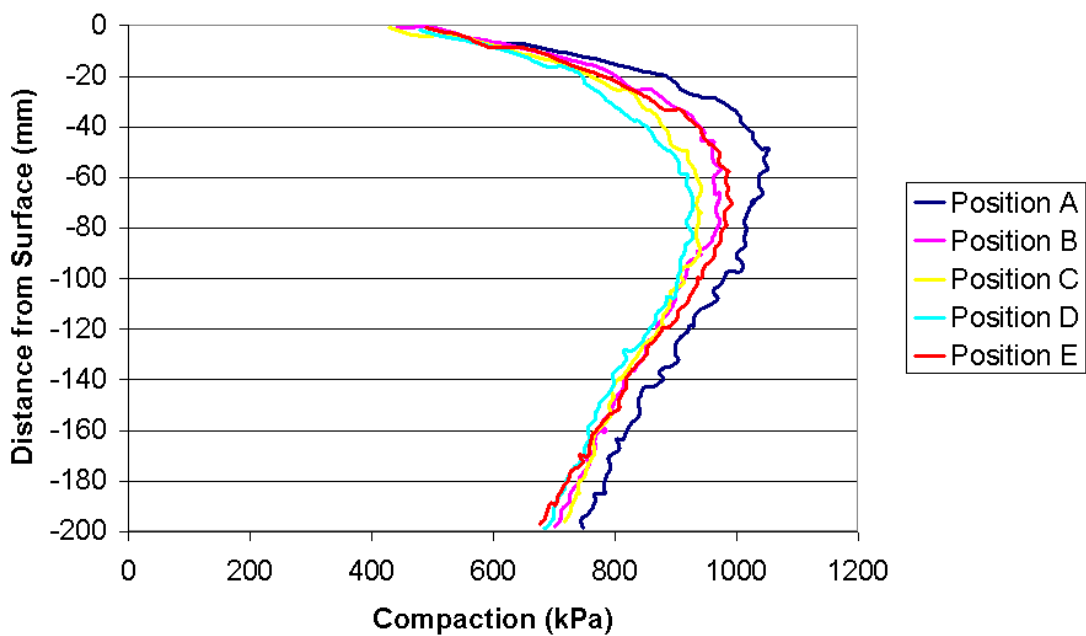


Figure 2.4: Penetrometer readings for middle position, low moisture (7.4% d.b.), high compaction (200 kPa)

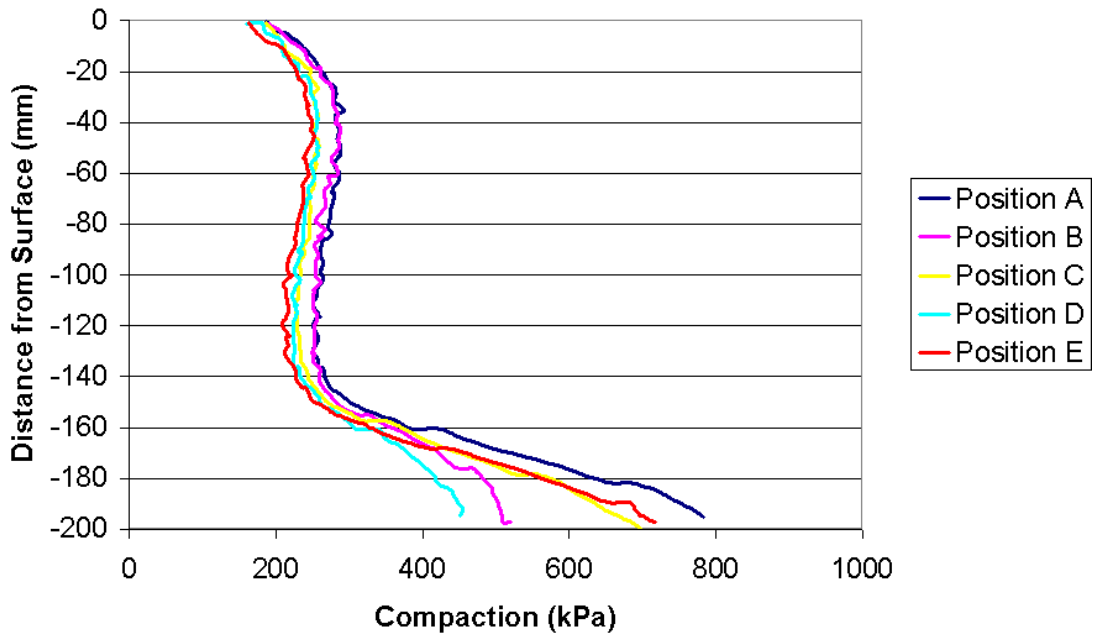


Figure 2.5: Penetrometer readings for middle position, high moisture (8.8% d.b.), low compaction (200 kPa)

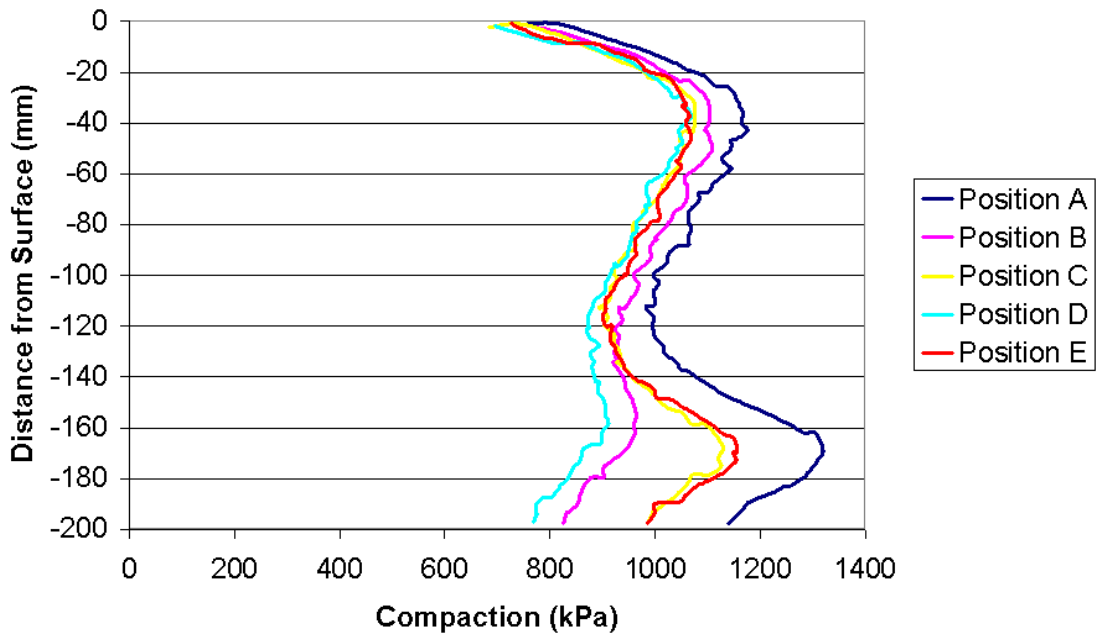


Figure 2.6: Penetrometer readings for middle position, high moisture (8.8% d.b.), high compaction (1,100 kPa)

Table 2.1: Penetrometer summary with density and moisture measurements

Moisture Level (d.b.)	Compaction Level (kPa)	Position Along Soil Bin (m)	Measured Moisture (d.b.)	Measured Density (kg/m ³)	Average Penetrometer Reading (kPa) Positions Across the Soil Bin Down to 150mm					
					A	B	C	D	E	Average
Low	Low-200	5	7.60%	1,330	230	211	206	192	196	207
		10	7.00%	1,380	241	220	220	212	210	221
		15	7.60%	1,330	292	265	255	245	238	259
		Average	7.40%	1,347						229
		Stdev	0.35%	29						27
Moisture Level (d.b.)	Compaction Level (kPa)	Position Along Soil Bin (m)	Measured Moisture (d.b.)	Measured Density (kg/m ³)	Average Penetrometer Reading (kPa) Positions Across the Soil Bin Down to 150mm					
					A	B	C	D	E	Average
Low	High-1100	5	7.20%	1,490	974	884	828	816	861	872
		10	7.00%	1,460	934	866	842	831	877	870
		15	7.80%	1,430	1036	957	895	894	938	944
		Average	7.33%	1,460						895
		Stdev	0.42%	30						42
Moisture Level (d.b.)	Compaction Level (kPa)	Position Along Soil Bin (m)	Measured Moisture (d.b.)	Measured Density (kg/m ³)	Average Penetrometer Reading (kPa) Positions Across the Soil Bin Down to 150mm					
					A	B	C	D	E	Average
High	Low-200	5	8.90%	1,290	234	216	212	215	212	218
		10	8.80%	1,300	265	261	241	233	226	245
		15	8.80%	1,320	262	249	233	231	243	244
		Average	8.83%	1,303						235
		Stdev	0.06%	15						15
Moisture Level (d.b.)	Compaction Level (kPa)	Position Along Soil Bin (m)	Measured Moisture (d.b.)	Measured Density (kg/m ³)	Average Penetrometer Reading (kPa) Positions Across the Soil Bin Down to 150mm					
					A	B	C	D	E	Average
High	High-1100	5	8.80%	1,430	995	909	883	860	902	910
		10	8.70%	1,390	1056	998	961	943	972	986
		15	8.80%	1,400	1015	935	918	914	950	946
		Average	8.77%	1,407						947
		Stdev	0.06%	21						38

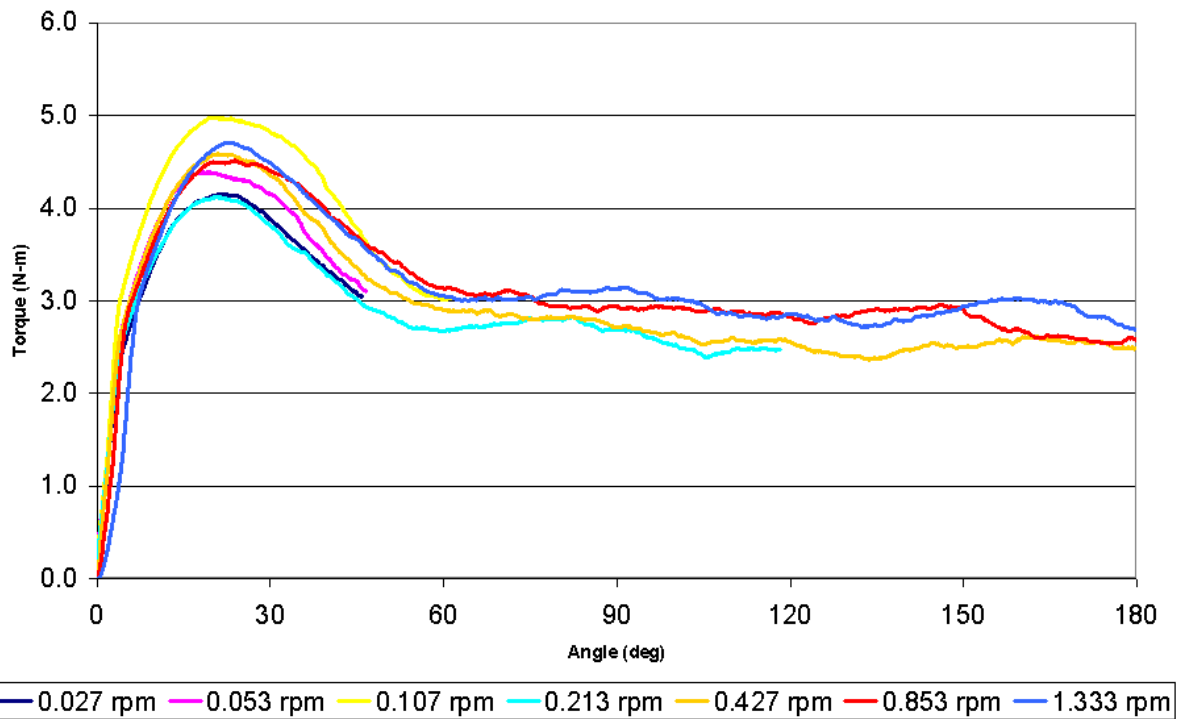


Figure 2.7: Measured torque versus time for middle position, low moisture (7.4% d.b.), low compaction (200 kPa)

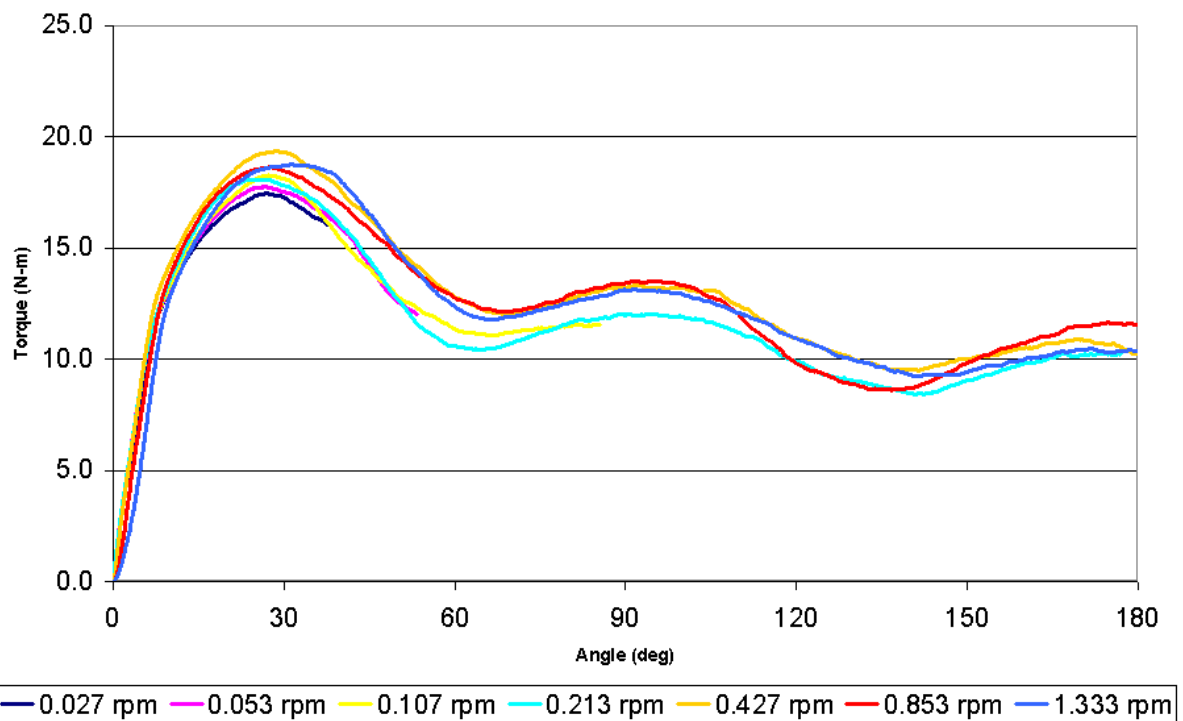


Figure 2.8: Measured torque versus time for middle position, low moisture (7.3% d.b.), high compaction (1,100 kPa)

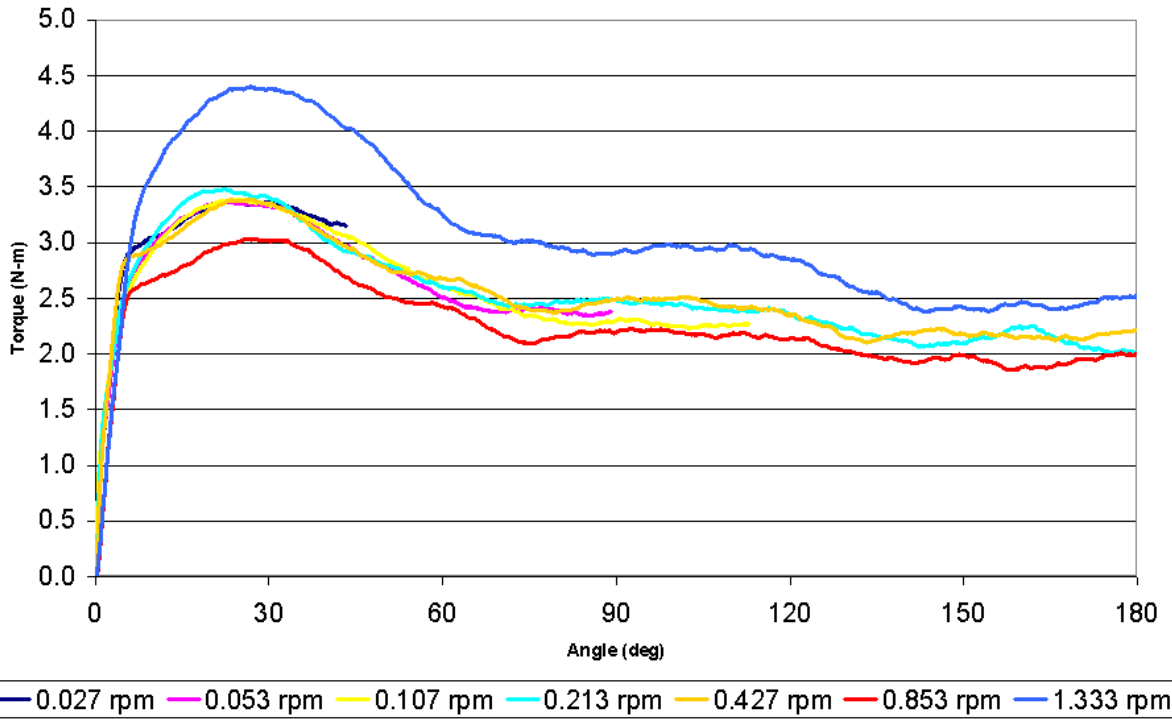


Figure 2.9: Measured torque versus time for middle position, high moisture (8.8% d.b.), low compaction (200 kPa)

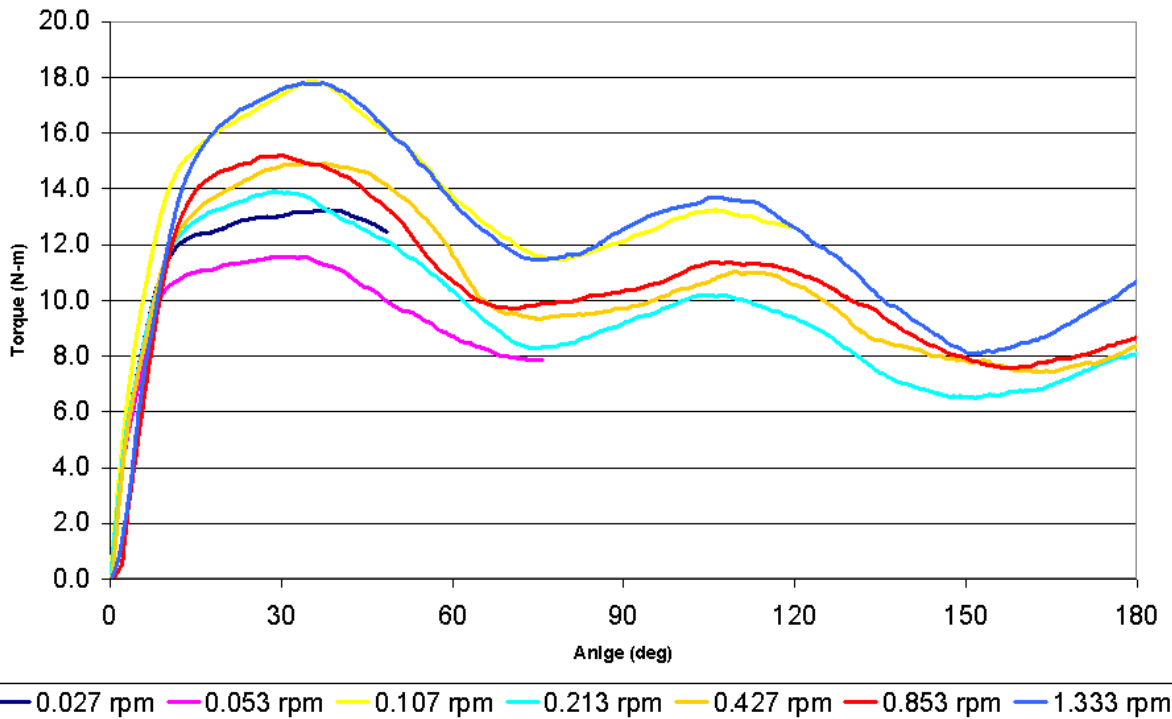


Figure 2.10: Measured torque versus time for middle position, high moisture (8.8% d.b.), high compaction (1,100 kPa)

The peak shear strength value at each speed was selected and plotted against the test speed or strain rate in radians per second. A linear equation was fit to the data for each of the four soil treatment levels. The data showed a strong linear relationship which matches results found by Lipscomb (1984). The graphs of the calculated shear strength (kPa) versus shear rate (rad/s) are shown in Figures 2.11 through 2.14. The graphs also show the linear curve fit to the data used to determine the shear strength and viscosity values for each soil treatment level. The Y-intercept represents the soil shear strength. The slope of the fit curve represents the viscosity. A summary of the tests results is shown in Table 2.2 with the measured density, and calculated values for shear strength and dynamic viscosity. The R values for the fit curves were low due to the large variation in results between the three repetitions. This variation was explored with a Tukey analysis presented later in the chapter.

The values given in the Table 2.2 were used in the simulations presented later in the paper. The levels of moisture and compaction closely match those used during the other laboratory tests for the flat bar and the spring reset standard. The results of those tests are presented in the following two chapters. The laboratory tests provide the conditions that the simulations attempt to reproduce.

Table 2.2: Summary of Viscometer Results

Moisture (d.b.)	Compaction (kPa)	Density (kg/m ³)	Shear Strength (Pa)	Dynamic Viscosity (Pa-s)
7.4%	200	1347	7,742	622
7.3%	1,100	1460	30,173	5,764
8.8%	200	1303	4,752	9,144
8.8%	1,100	1407	23,834	20,858

The density was higher for the treatments with high compaction. Also, the density was higher for the low moisture treatments than the high moisture treatments. Since water has a density lower than the sand and clay this makes sense. The shear strength was higher when the compaction level was high and the moisture level was low. However, the dynamic viscosity was highest at the high moisture and high compaction level.

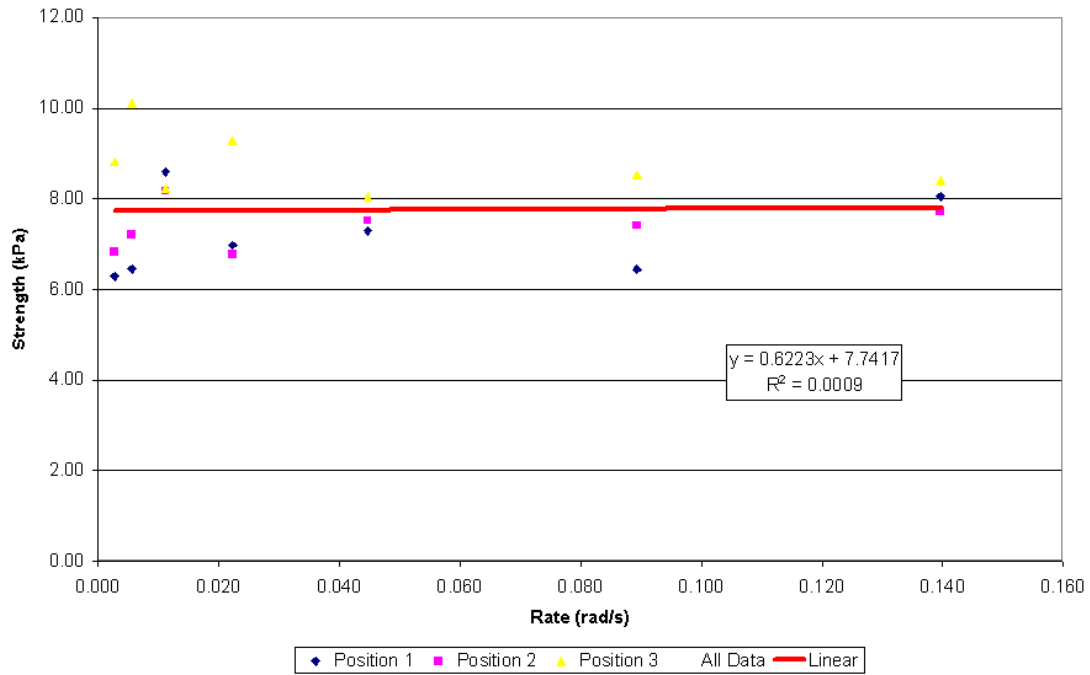


Figure 2.11: Shear strength versus shear rate, low moisture (7.4% d.b.), low compaction (200 kPa)

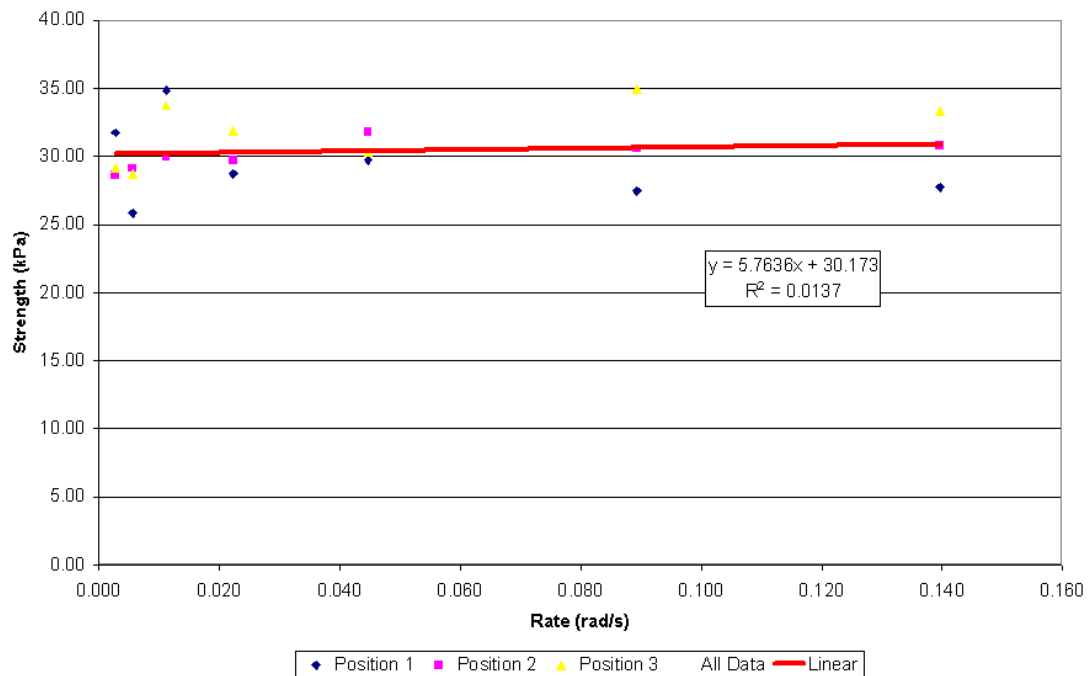


Figure 2.12: Strength versus shear rate, low moisture (7.3% d.b.), high compaction (1,100 kPa)

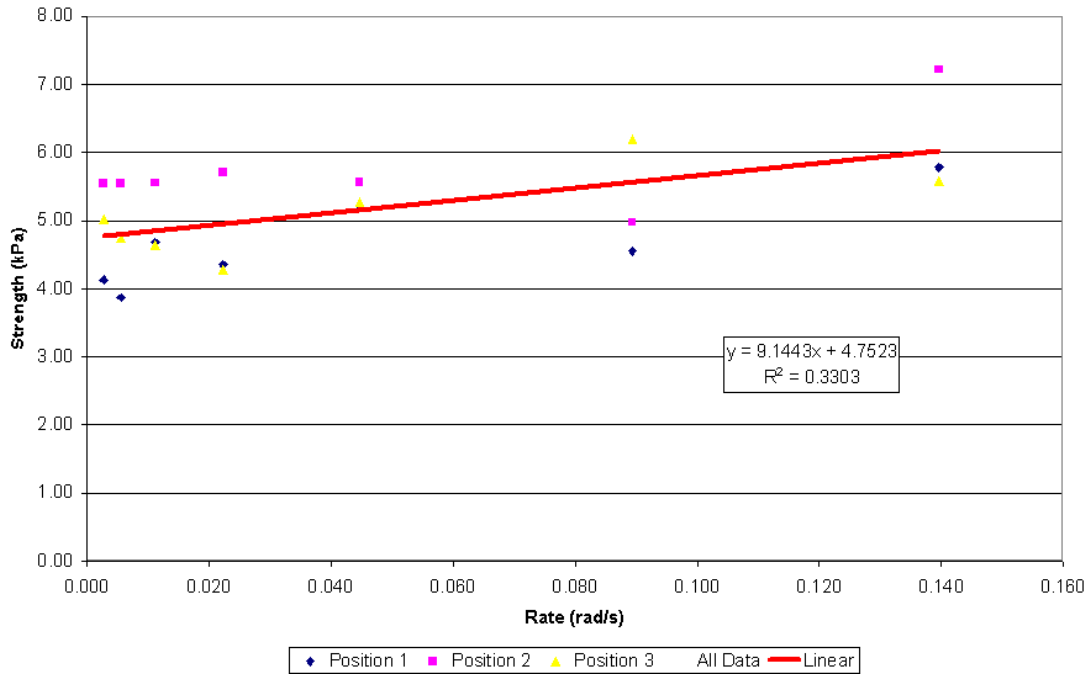


Figure 2.13: Strength versus shear rate, high moisture (8.8% d.b.), low compaction (200 kPa)

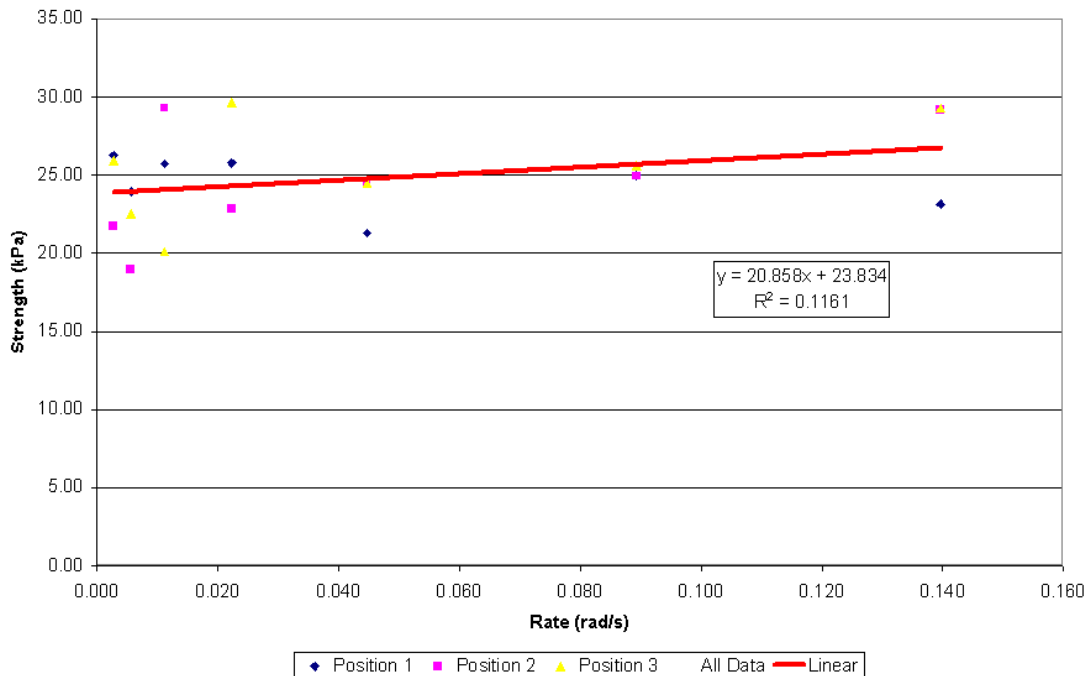


Figure 2.14: Strength versus shear rate, high moisture (8.8% d.b.), high compaction (1,100 kPa)

The measured soil properties were generally lower than those found by Karmakar and Kushwaha (2006a). In their testing, they ran their viscometer between 0.02 and 0.25 rpm with moisture levels from ten to twenty percent and compaction levels between 100 to 400 kPa. The clay content of their soil was about double and a slightly lower sand content (29% clay, 24% silt, and 47% sand). At the ten percent moisture level and low compaction (200 kPa), their measured viscosity was 145.8 kPa-s and the yield strength was 10.66 kPa.

2.4 Statistical Analysis

A linear ANOVA Tukey analysis of the shear stress data was run using Minitab software to determine if there was significant variation in the data from the soil property measurement tests. The data was analyzed for each of the four soil treatment levels to consider the variation in the measured shear strength versus the lateral position across the soil bin, the three positions along the length of the soil bin, and the test speed. An example of the full output from one of the analyses is shown in Figure 2.15. The summary of the rest of the analyses are provided in Figures 2.16 through 2.27. Ideally, there should be no statistically significant differences in the measured soil shear strength along the width or length of the soil bin. However, there should be statistically significant differences in the measured shear strength versus speed.

The analysis showed three combinations that did have statistically significant differences at the 95 percent confidence level. At the low moisture, low compaction level, the average shear strength at the 15m soil bin position had a statistically significant difference than the averages at the five and ten meter positions (Figure 2.15). At the high moisture, low compaction level, the average shear strength at the five meter soil bin position had a statistically significant difference than the ten meter position (Figure 2.21). Also, at the high moisture, high compaction level, the average shear strength at the zero millimeter position across the width of the soil bin had a statistically significant difference than the 720 mm position (Figure 2.25). For the three cases that did have statistically significant difference pairings, tables were created to illustrate the results (Table 2.3, Table 2.4, and Table 2.5). Cells in the tables that are filled indicate that there is no statistical significant difference between that pair.

An interesting result from the analyses was that for all four soil treatments there was no statistically significant difference in the measured shear values across the range of test speeds. The point of running the test at multiple speeds was to determine if a linear curve provided the best fit to the data with the slope being the viscosity used in the Bingham plastic soil model. This suggests several possibilities: more test samples are required to lower the standard error, tests need to be run at higher speeds closer to actual field test speeds, and the shear strength is independent of speed (non viscous). Further testing would help to clarify the results. Because the speeds used to measure the soil properties were significantly lower than actual field test speeds the test speeds may be too close together to show any statistically significant difference.

2.5 Conclusions

A soil viscometer was designed and constructed based on ASTM standard D2573-01 using a rotary shear vane. The soil viscometer was successfully used to measure the soil strength at seven speeds and at four soil treatment levels. The soil density was measured and the yield strength and viscosity were calculated from the measured torque to provide the three parameters necessary for using the Bingham-Plastic material model for the CFD analysis.

The shear vane results indicate that increased moisture lowered the shear strength of the soil but increased the viscosity. However, increased compaction resulted in higher shear strength and viscosity. The results also indicate that the soil does not show viscous behavior for the speeds tested but acts in a more elastic manner.

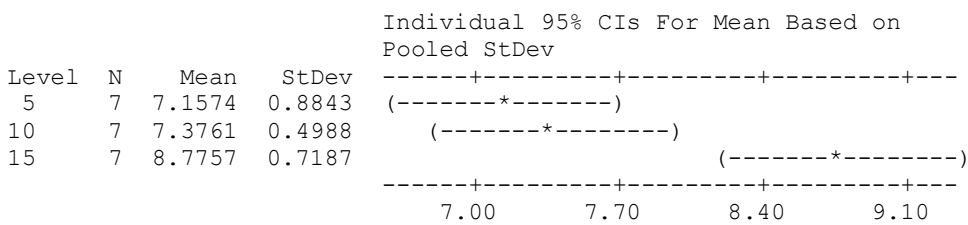
The Tukey analysis of the shear strength data showed that there were only three combinations of data that had statistically significant differences. The Tukey analysis also showed that there was no statistically significant difference in the measured shear strength versus speed. This may be attributed to the fact that the test speeds were very low compared with actual field test speeds. The test data points may be too close together to show statistical significant differences. Further testing at higher speeds would clarify this issue and verify that the slope of the strength versus speed data is linear.

The test method for the soil viscometer was based on the civil engineering standard developed for static structures. Limitations in the speeds that can be reasonably used with

the rotational soil viscometer suggest that alternate test methods of measuring soil properties may be required. An alternate method is suggested in Chapter 8. The test procedure also did not allow for soil dilation which is not representative of tillage tools.

Source	DF	SS	MS	F	P
Location	2	10.793	5.396	10.46	0.001
Error	18	9.284	0.516		
Total	20	20.077			

S = 0.7182 R-Sq = 53.76% R-Sq(adj) = 48.62%

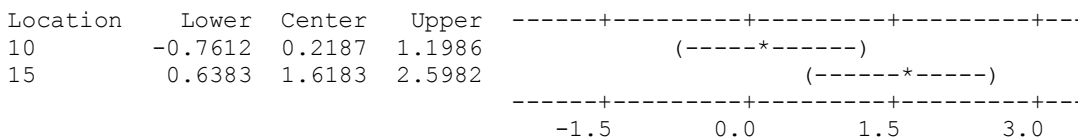


Pooled StDev = 0.7182

Tukey 95% Simultaneous Confidence Intervals
All Pairwise Comparisons among Levels of Location

Individual confidence level = 98.00%

Location = 5 subtracted from:



Location = 10 subtracted from:

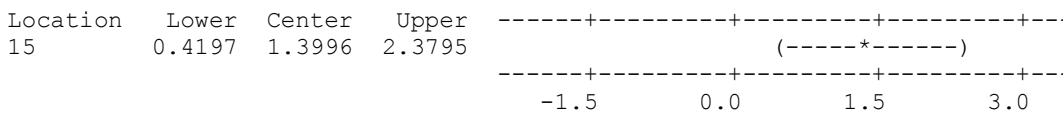
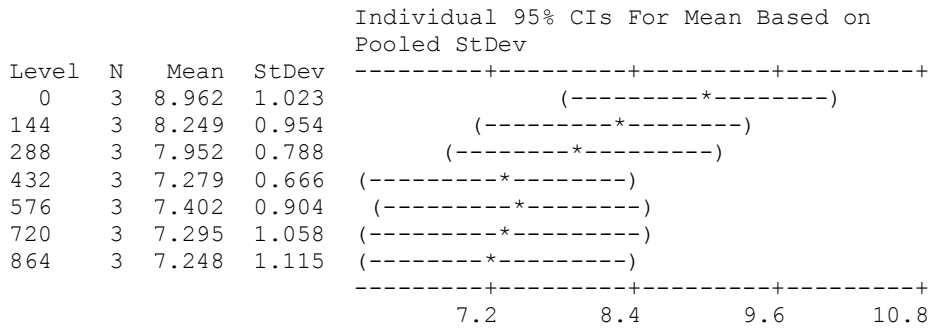


Figure 2.15: Tukey results – shear strength versus soil bin position, low moisture (7.4% d.b.), high compaction (200 kPa)

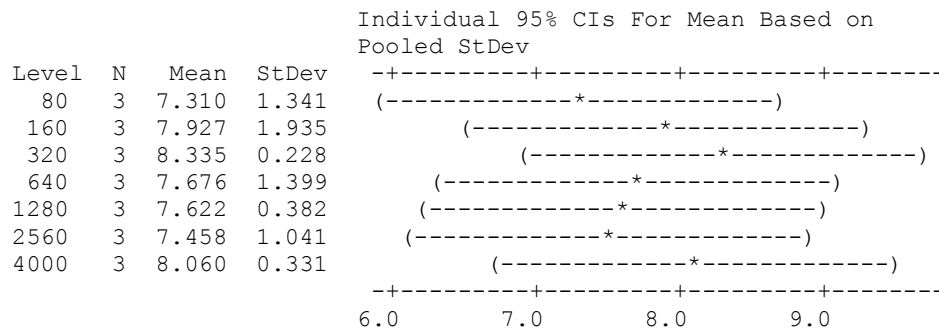


Pooled StDev = 0.941

Tukey 95% Simultaneous Confidence Intervals
All Pairwise Comparisons among Levels of Position

Individual confidence level = 99.58%

Figure 2.16: Tukey results – shear strength versus soil bin lateral position, low moisture (7.4% d.b.), low compaction (200 kPa)

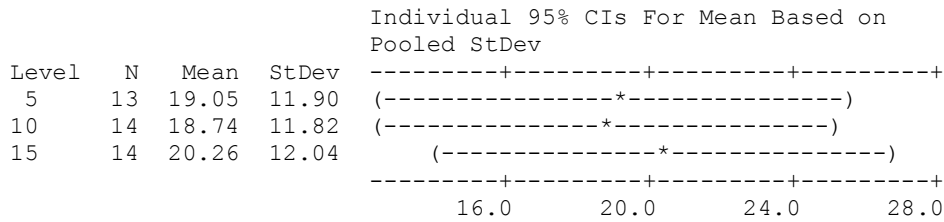


Pooled StDev = 1.127

Tukey 95% Simultaneous Confidence Intervals
All Pairwise Comparisons among Levels of Speed

Individual confidence level = 99.58%

Figure 2.17: Tukey results – shear strength versus rotational speed, low moisture (7.4% d.b.), low compaction (200 kPa)

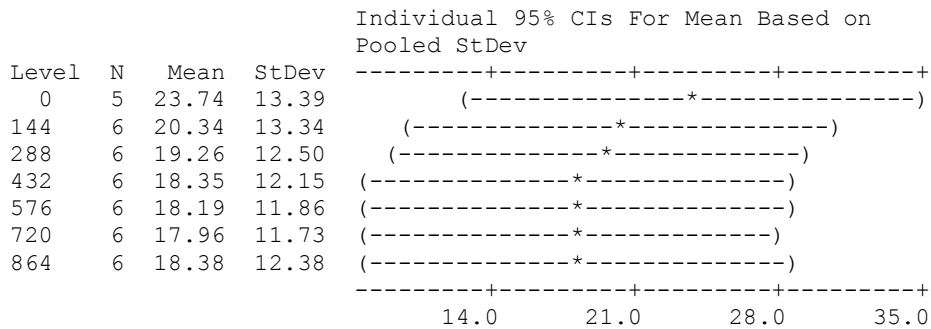


Pooled StDev = 11.92

Tukey 95% Simultaneous Confidence Intervals
All Pairwise Comparisons among Levels of Location

Individual confidence level = 98.05%

Figure 2.18: Tukey results – shear strength versus soil bin position, low moisture (7.4% d.b.), high compaction (1,100 kPa)

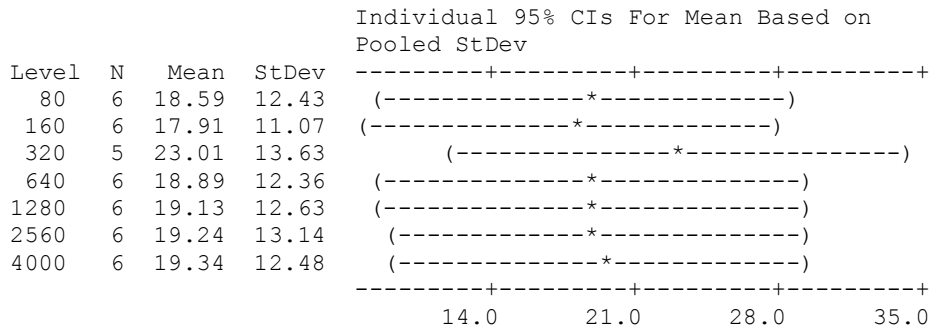


Pooled StDev = 12.46

Tukey 95% Simultaneous Confidence Intervals
All Pairwise Comparisons among Levels of Position

Individual confidence level = 99.64%

Figure 2.19: Tukey results – shear strength versus soil bin lateral position, low moisture (7.4% d.b.), high compaction (1,100 kPa)

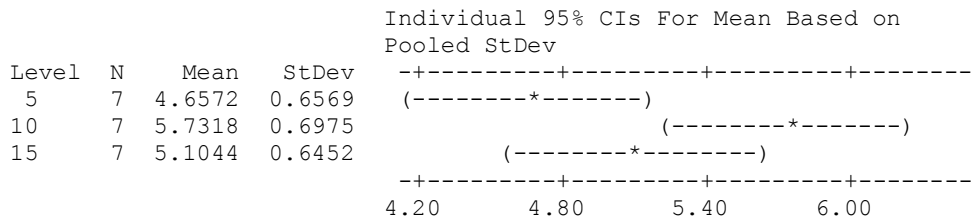


Pooled StDev = 12.52

Tukey 95% Simultaneous Confidence Intervals
All Pairwise Comparisons among Levels of Speed

Individual confidence level = 99.64%

Figure 2.20: Tukey results – shear strength versus rotational speed, low moisture (7.4% d.b.), high compaction (1,100 kPa)

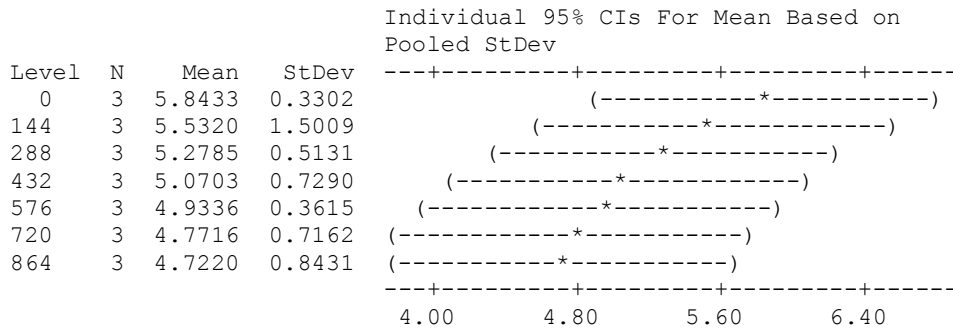


Pooled StDev = 0.6669

Tukey 95% Simultaneous Confidence Intervals
All Pairwise Comparisons among Levels of Location

Individual confidence level = 98.00%

Figure 2.21: Tukey results – shear strength versus soil bin position, high moisture (8.8% d.b.), low compaction (200 kPa)

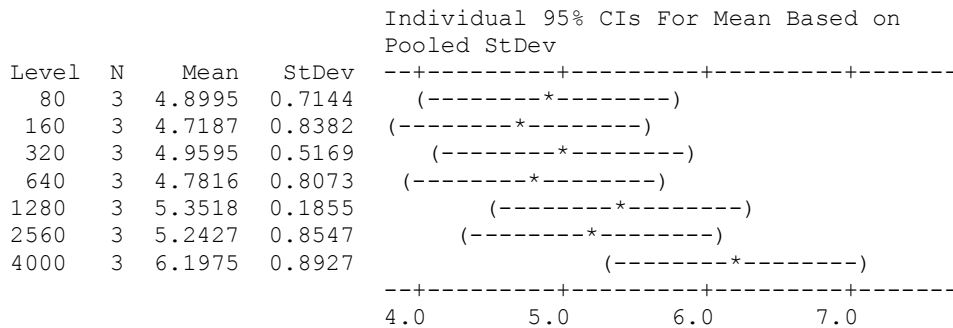


Pooled StDev = 0.8028

Tukey 95% Simultaneous Confidence Intervals
All Pairwise Comparisons among Levels of Position

Individual confidence level = 99.58%

Figure 2.22: Tukey results – shear strength versus soil bin lateral position, high moisture (8.8% d.b.), low compaction (200 kPa)

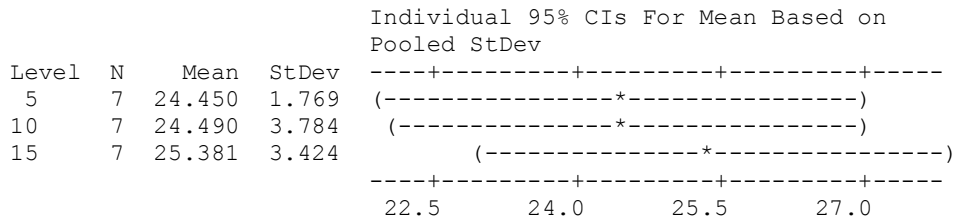


Pooled StDev = 0.7264

Tukey 95% Simultaneous Confidence Intervals
All Pairwise Comparisons among Levels of Speed

Individual confidence level = 99.58%

Figure 2.23: Tukey results – shear strength versus rotational speed, high moisture (8.8% d.b.), low compaction (200 kPa)

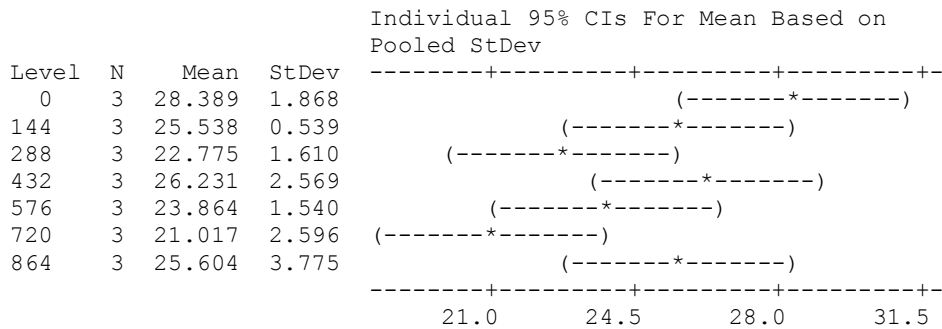


Pooled StDev = 3.118

Tukey 95% Simultaneous Confidence Intervals
All Pairwise Comparisons among Levels of Location

Individual confidence level = 98.00%

Figure 2.24: Tukey results – shear strength versus soil bin position, high moisture (8.8% d.b.), high compaction (1,100 kPa)

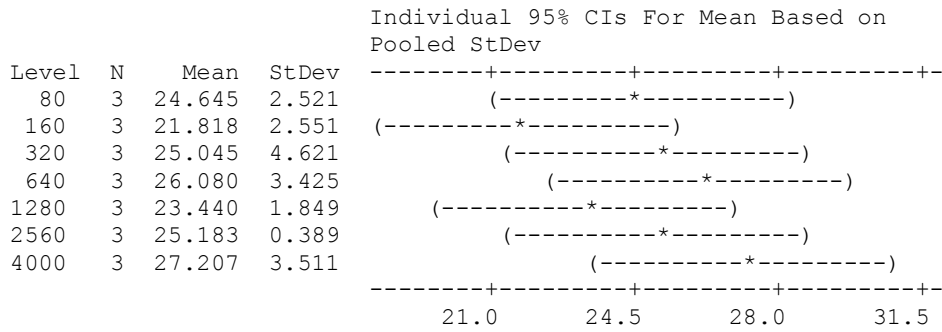


Pooled StDev = 2.278

Tukey 95% Simultaneous Confidence Intervals
All Pairwise Comparisons among Levels of Position

Individual confidence level = 99.58%

Figure 2.25: Tukey results – shear strength versus soil bin lateral position, high moisture (8.8% d.b.), high compaction (1,100 kPa)



Pooled StDev = 2.972

Tukey 95% Simultaneous Confidence Intervals
All Pairwise Comparisons among Levels of Speed

Individual confidence level = 99.58%

Figure 2.26: Tukey results – shear strength versus rotational speed, high moisture (8.8% d.b.), high compaction (1,100 kPa)

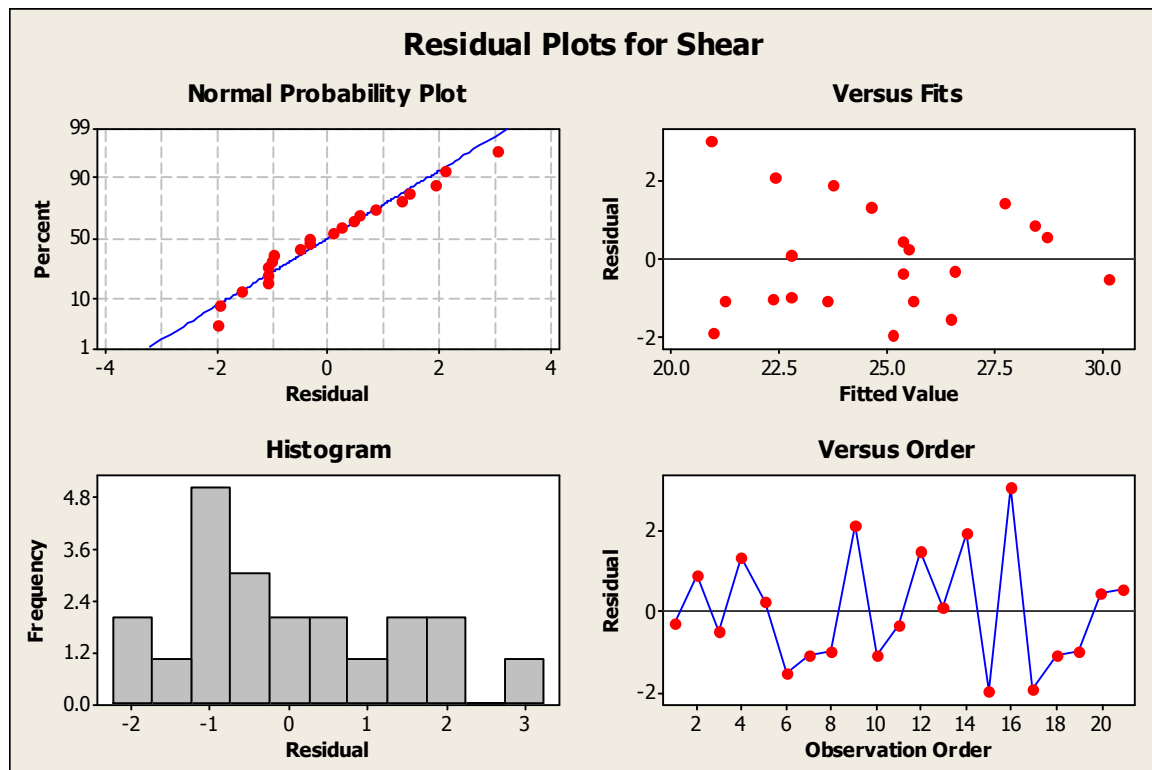


Figure 2.27: Tukey result plots – shear strength versus rotational speed, high moisture (8.8% d.b.), high compaction (1,100 kPa)

Table 2.3: Tukey results – shear strength versus soil bin position, low moisture (7.4% d.b.), low compaction (200 kPa) Filled in squares have no statistical difference

m	5	10	15
5			
10			
15			

Table 2.4: Tukey results – shear strength versus soil bin position, high moisture (8.8% d.b.), low compaction (200 kPa)

m	5	10	15
5			
10			
15			

Table 2.5: Tukey results – shear strength versus soil bin lateral position, high moisture (8.8% d.b.), high compaction (1,100 kPa)

mm	0	144	288	432	576	720	864
0							
144							
288							
432							
576							
720							
864							

3. RIGID FLAT BAR LAB TEST

The first step in developing the CFD procedure was to use simple geometry and compare to results from an actual physical test. A two inch wide flat steel bar was chosen for the simple tool shape similar to what was used by other authors in laboratory experiments (Stafford, 1981). The flat steel bar was mounted to a stiff structure and pulled through the soil at a soil bin while the draft forces were measured. The test depth, speed, and soil compaction were varied. The measured data was analyzed and the average draft force values plus or minus three standard deviations were calculated to use as the goal for the CFD simulation.

3.1 Test Setup

The flat bar was made from a 50.8 mm by 12.7 mm (2.0 in by 0.5 in) thick steel bar 203.2 mm (8 in) in length. The bar was mounted to a custom designed mounting with two half-inch carriage bolts. The mounting was relatively rigid and directly mounted to the soil bin tool carrier. The carrier was used to move the bar through the soil at predetermined treatment levels. Force measurements were made using four triaxial load cells (Model TRD-A-5K, Michigan Scientific) mounted between the tool plate and the shank mounting bracket. The twelve forces recorded by the data acquisition system are resolved in three orthogonal forces and moments around these axes.

The tests were run at twelve treatment levels: two depth, 51 and 102 mm (2 and 4 in), three speeds, 0.89, 1.79, and 2.68 m/s (2, 4, and 6 mph), and two compaction levels, 200 and 1,100 kPa. Three repetitions of each treatment level were run and analyzed. The runs were randomized for each group of repetitions and sorted into groups of three by soil treatment since three runs could be made before the soil had to be reconditioned. After the first repetition, a section of the trench was cleared of the loose soil by hand so that measurements could be made of the trench profile and pictures were taken. High speed video was also taken from above looking down at the tool and the soil disturbance in front of the tool.

The density of the soil was measured once at each compaction level. At the low compaction level, 200 kPa, the soil had a density of 1,760 kg/m³ with an average moisture

content of 9.15 percent taken from ten samples. At the high compaction level, 1,100 kPa, the soil had a density of 1,960 kg/m³ with an average moisture content of 9.2 percent taken from ten samples.

The tool carrier was a custom designed steel weldment made up of 6mm (0.25 inch) plate. The carrier also included a camera mount that allowed the use of a 30 frame-per-second color webcam to be used to record video of each test. The webcam was a Philips SPC900NC and was connected to an HP Compaq laptop to record the movie files. The camera was positioned above and in front of the tool to observe the soil fracture and shattering ahead of the tool. The setup is shown in Figure 3.1.

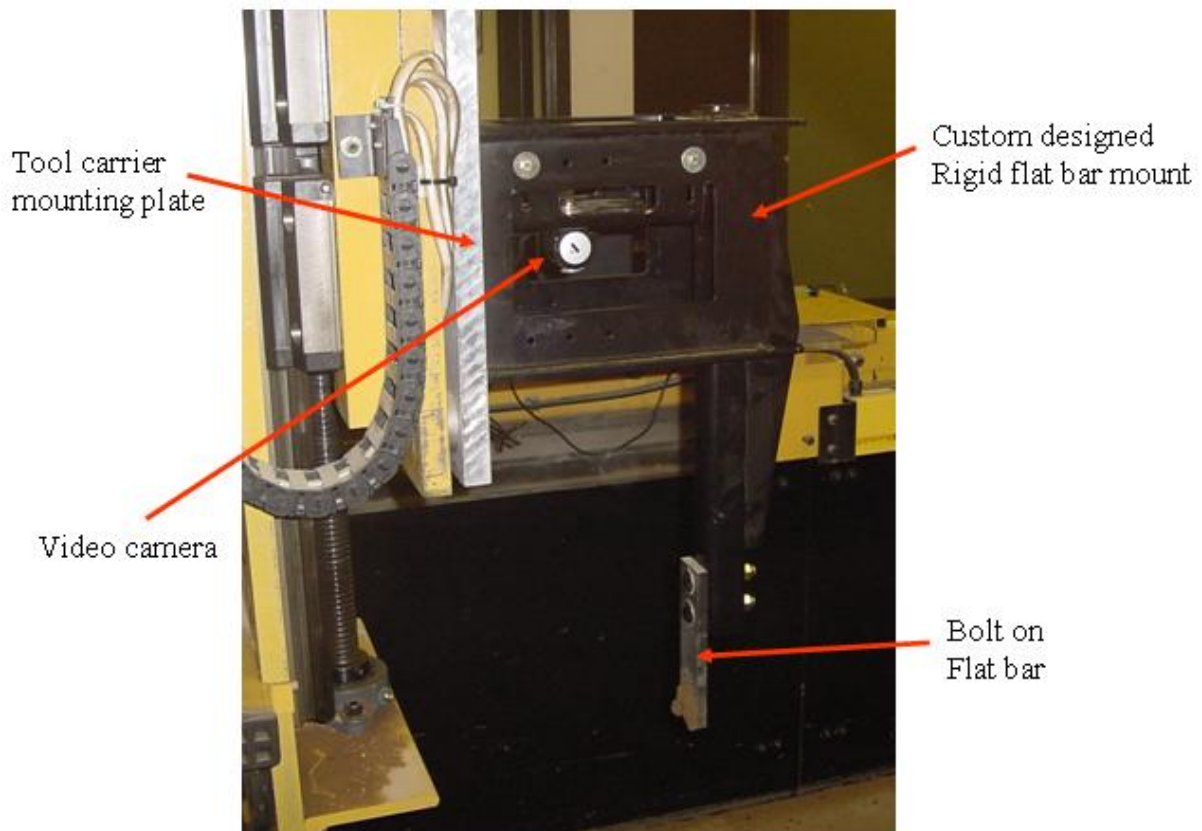


Figure 3.1: Rigid flat bar lab test Setup

Figure 3.2 shows how the trench was cleared of loose soil and dug out ahead to provide a clear image of the resulting trench profile. Clearing the loose soil away was carefully done by hand and by used soft brushes. A metal blade was used to remove the soil in front of the cleared area. A digital camera was then used to record the profile image. A tape measure was used to measure the width of the trench at the surface and the depth from the surface to the bottom.



Figure 3.2: Flat bar example trench profile with loose soil cleared away

3.2 Results

The videos captured by the webcam clearly showed how the level of compaction changed how the soil failed. At the low compaction level the soil exhibited flow failure resembling with the soil breaking up into small particles millimeters in size. At the high compaction level the soil exhibited brittle failure resulting in chunks of failed soil with some exceeding 100 mm in size. Examples taken from the test video are shown in Figure 3.3 and Figure 3.4.

Figure 3.5 and Figure 3.6 are examples of two time histories for the measured draft of two treatment levels. The operating depth and speed are the same and only the compaction level is different. The graphs give examples of the amount of repeatability that was measured and that the higher compaction level resulted in nearly a three times increase in average draft. All of the time histories are provided in the Appendix.

Table 3.1 summarizes the average measured draft and standard deviation for each of the twelve treatments. Figure 3.7 shows the mean and +/- three standard deviations for the average draft at each treatment level. Treatments at the low compaction level typically had lower variation in the average draft measurement between the three repeats. This might be explained by the higher level of variation in the compaction consistency as was shown in the soil viscometer experiment. The higher compaction level resulted in higher average draft values. The four inch depth resulted in higher average draft values than the two inch depth. Both of these observations make sense and are in agreement with previous work. Based on the statistical analysis only the compaction level resulted in average draft values that were statistically significant.



Figure 3.3: Image of soil failure, 51 mm depth, 2.68 m/s, low compaction (200 kPa)



Figure 3.4: Image of soil failure, 51 mm depth, 2.68 m/s, high compaction (1,100 kPa)

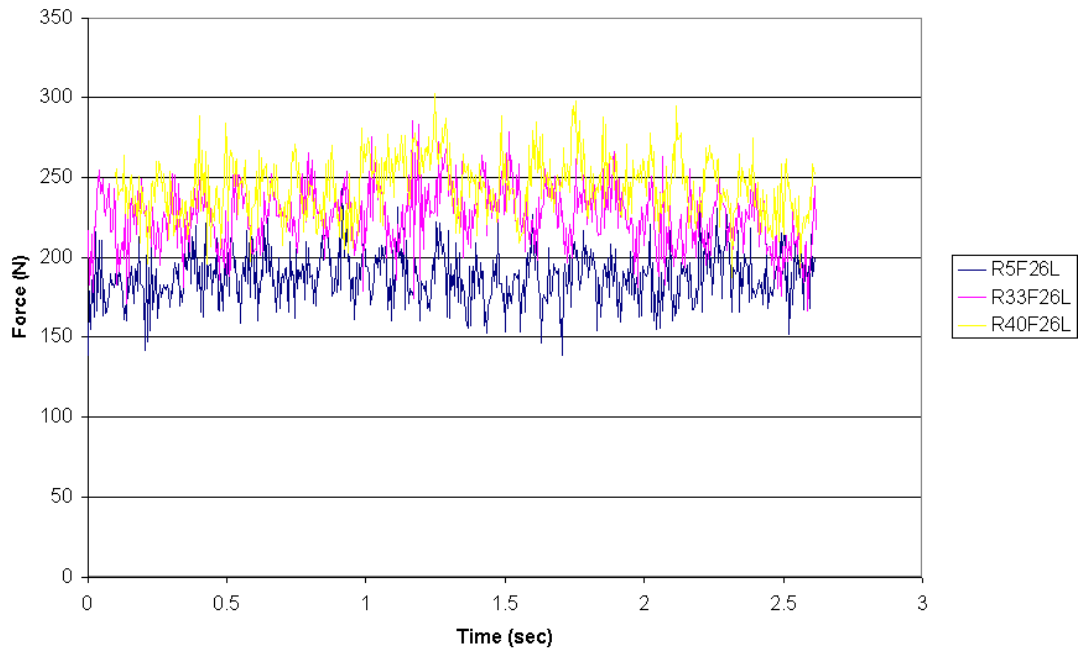


Figure 3.5: Measured draft, 51 mm depth, 2.68 m/s, low compaction (200 kPa)

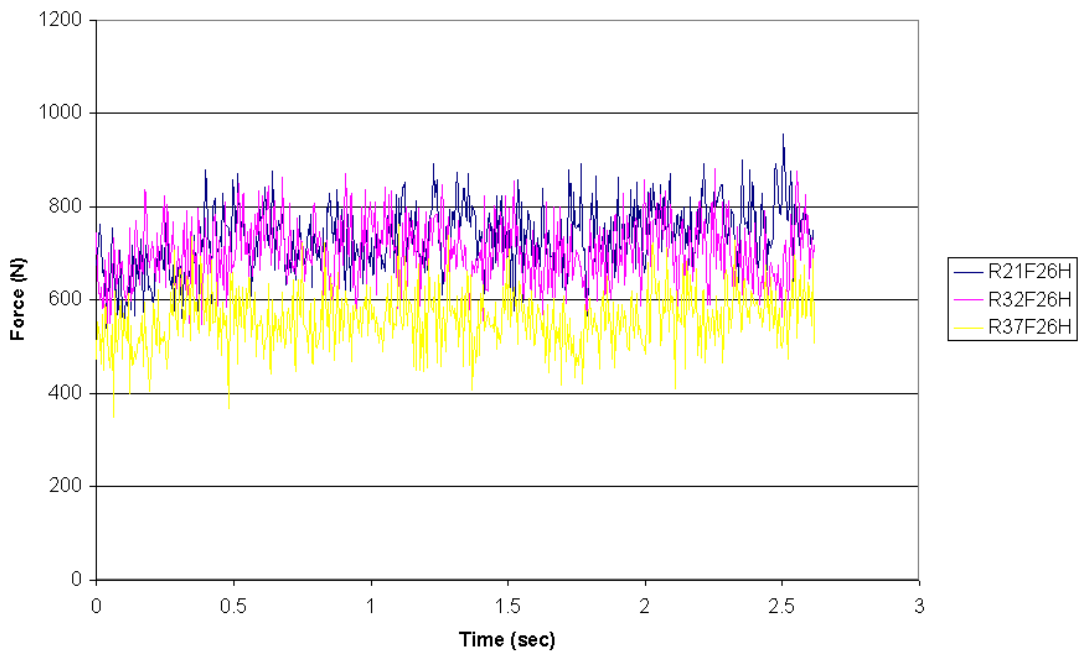
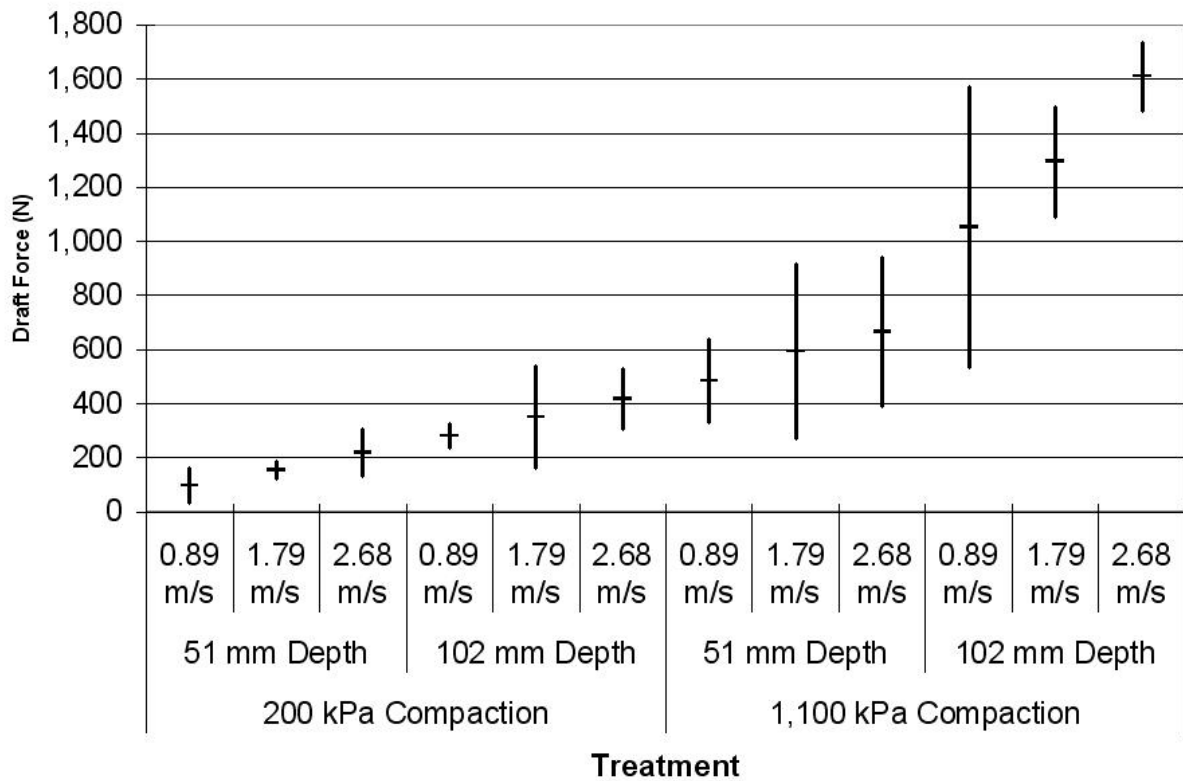


Figure 3.6: Measured draft, 51 mm depth, 2.68 m/s, high compaction (1,100 kPa)

Table 3.1: Summary of the draft forces for the rigid flat bar lab test

	Treatment	Depth (in)	Depth (mm)	Speed (mph)	Speed (m/s)	Compaction (kPa)	Draft (N)	
							Average	Stdev
1	D2S2L	2	50.8	2	0.89	200	98.04	21.17
2	D2S4L	2	50.8	4	1.79	200	153.26	10.50
3	D2S6L	2	50.8	6	2.68	200	219.14	29.00
4	D2S2H	2	50.8	2	0.89	1,100	483.50	50.81
5	D2S4H	2	50.8	4	1.79	1,100	594.27	107.33
6	D2S6H	2	50.8	6	2.68	1,100	665.62	92.47
7	D4S2L	4	101.6	2	0.89	200	280.98	15.53
8	D4S4L	4	101.6	4	1.79	200	350.50	62.63
9	D4S6L	4	101.6	6	2.68	200	416.53	36.90
10	D4S2H	4	101.6	2	0.89	1,100	1,053.70	172.53
11	D4S4H	4	101.6	4	1.79	1,100	1,295.17	67.68
12	D4S6H	4	101.6	6	2.68	1,100	1,609.90	42.25

**Figure 3.7: Average draft values and +/- 3 standard deviations for each treatment level**

3.3 Statistical Analysis

A regression ANOVA statistical analysis was conducted in Microsoft Excel on the test data to determine which variables were significant in predicting the draft force on the rigid flat bar. Scatterplots and correlation coefficients were created for each variable. Only the compaction level was strongly related to the draft. Based on the coefficients of determination, the operating depth explains 25.9 percent of the variability, the speed explains only four (4.0) percent of the variability, and the compaction level explains 56.5 percent of the variability in the draft. All three of the predictor variables had p-values lower than 0.05 meaning that all three variable were statistically significant at the 95 percent confidence level. The coefficient of determination from the regression analysis was 86.8 percent which shows that the three variables account for most of the variability in the draft load. Table 3.2 below has the results from the regression analysis. The full results of the regression analysis are provided in the Appendix. The resulting predictor equation is,

$$\text{Draft (N)} = -841.44 \text{ (N)} + 9.1068 \times \text{Depth (mm)} + 135.40 \times \text{Speed (m/s)} + 0.7779 \times \text{Compaction (kPa)} \quad (3.1)$$

Table 3.2: Regression analysis results for rigid flat bar test

	Intercept	Depth	Speed	Compaction
P-value	0.0000	0.0000	0.0027	0.0000
Coeff.	-841.4377	9.1068	135.4015	0.7779
Units	N	mm	m/s	kPa

Figure 3.8 shows a comparison of the draft force predicted by equation (3.1) and the test data that was shown in Figure 3.8. The predictor equation predicted draft force value was below the three standard deviation level for the lowest two speeds at the 51 mm depth and low compaction (200 kPa) levels. Similarly, the predictor equation predicted draft force was below the three standard deviation level for the highest speed, at 102 mm depth and high compaction (1,100 kPa) levels.

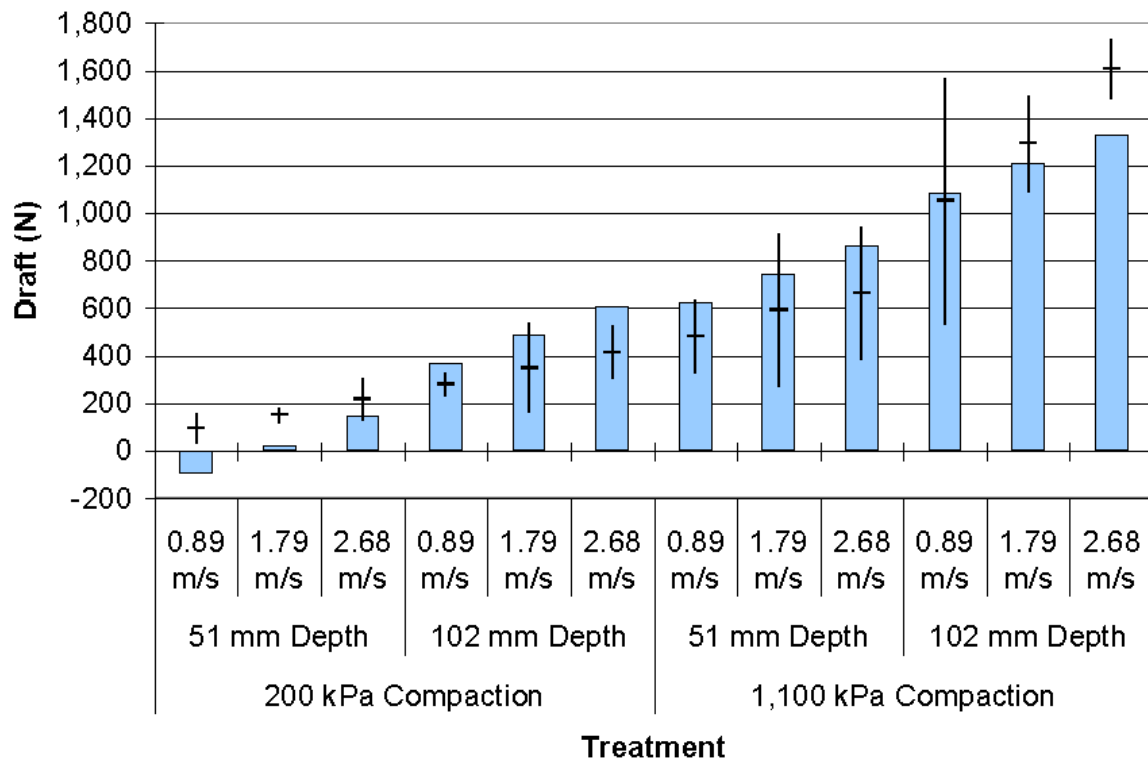


Figure 3.8: Predictor equation for draft force values compared to measured values

3.4 Conclusions

A 12.7 mm by 51 mm rigid flat steel bar was tested in a soil bin to measure the draft and vertical forces that occurred as the bar was pulled through soil. Twelve treatment levels were considered varying the tool speed, depth, and the soil compaction with three repeats of each. The data indicated that the variability in draft force was higher for the high compaction level and that in general the draft force increases with speed and soil compaction.

The average draft force values were evaluated to determine which treatment factors were statistically significant. All three variables were determined to be statistically significant at the 95 percent confidence level. A regression analysis was conducted to develop a predictor equation based on all three statistically significant variables. The predictor equation produced results that fell within the ± 3 standard deviations in all but 3 of the 12 test conditions. These predicted draft force values will be later compared to those predicted from CFD.

4. FIELD CULTIVATOR STANDARD LAB TEST

A soil bin lab test was conducted using a John Deere 200 lbf trip field cultivator standard with both a 178 and 254 mm sweep to measure the forces resulting from soil failure. The data was collected for later use in the development and validation of the simulation procedure. This particular standard and sweep combination were chosen because they represent a typical spring reset standard with high volume usage on a number of different machine types.

4.1 Setup

The standard assembly was mounted to the tool carrier on the soil bin. A Sony high speed video camera was mounted ahead of the sweep to the tool carrier to capture the soil failure in front of the sweep as it progressed through the soil. A bent sheet metal deflector was attached to the pivot casting so that fractured soil traveling up the shank would fall off to the sides and not block the high speed camera view. The video was captured at 500 fps and down sampled for viewing. The resulting videos were used to examine the soil failure mode and to look for connections between the soil failure rate and the load frequency. The sweeps used in the test were initially painted black. During actual usage the black paint is worn off by friction with the soil. Before testing began the sweeps were sandblasted to remove the paint to better simulate the scoured surface finish.

Thirty-two different treatment levels were considered in the test. Of those, eight were run with three repetitions and used for comparison with the simulation. The factors considered were sweep sizes of 178 and 254 mm (7 and 10 inch), speeds of 0.89, 2.68, and 4.47 m/s (2, 6, and 10 mph), depths of 76 and 152 mm (3 and 6 inches), soil compaction levels of 200 and 1,100 kPa (29 and 160 psi), and soil moisture levels of 6.9% and 8.3% d.b.. The repeated treatment levels used the 178 mm sweep at 2.68 m/s and varied the depth, compaction, and moisture levels. The 178 mm sweep at 2.68 m/s was chosen because this combination is the most common in actual tillage usage. The full list of runs were randomized by repetition and then paired for runs using the same level of compaction and moisture since the soil bin width would accommodate two runs before the soil had to be

reconditioned. Because of the difficulty and time required to change the moisture level of the soil, the higher moisture level runs were completed first and then the soil was allowed to dry out before running the low moisture treatment levels.

For each test run the loads were recorded at a frequency of 200 Hz in the draft, vertical, and lateral directions with four load cells connecting the mounting plate on the test rig to the tool carrier. The forces were recorded in pounds to three decimal places or six significant digits. A string pot was mounted to the standard bucket with the string running through the spring to the pivot casting so that the spring deflection could be measured. The data recorder was started after the test rig was up to the desired speed and stopped before the test rig had to decelerate. As mentioned previously, high speed video was recorded showing the soil failure and deflection as the standard and sweep passed through the bin. After each run was finished photos were taken of the disturbed soil. When both runs were completed for the soil treatment level the soil was tilled, smoothed, and compacted according to the next pair of test runs.

Figure 4.1 shows the field cultivator standard assembly mounted to the test rig in the soil bin. Penetrometer readings were taken at five positions across the width of the soil bin once for each of the two compaction levels at the high moisture level. The resulting readings are shown in Figure 4.2 and Figure 4.3. At the low compaction level of 200 kPa, Figure 4.2, the compaction across the soil bin was fairly consistent. The graph also shows that the compaction level is consistent to the about the lowest test depth of 152 mm. At the high compaction level of 1,100 kPa, Figure 4.3, the desired compaction level is not reached until about a depth of 60 mm. Figure 4.3 also shows that the actual average compaction level is closer to 1,000 kPa.

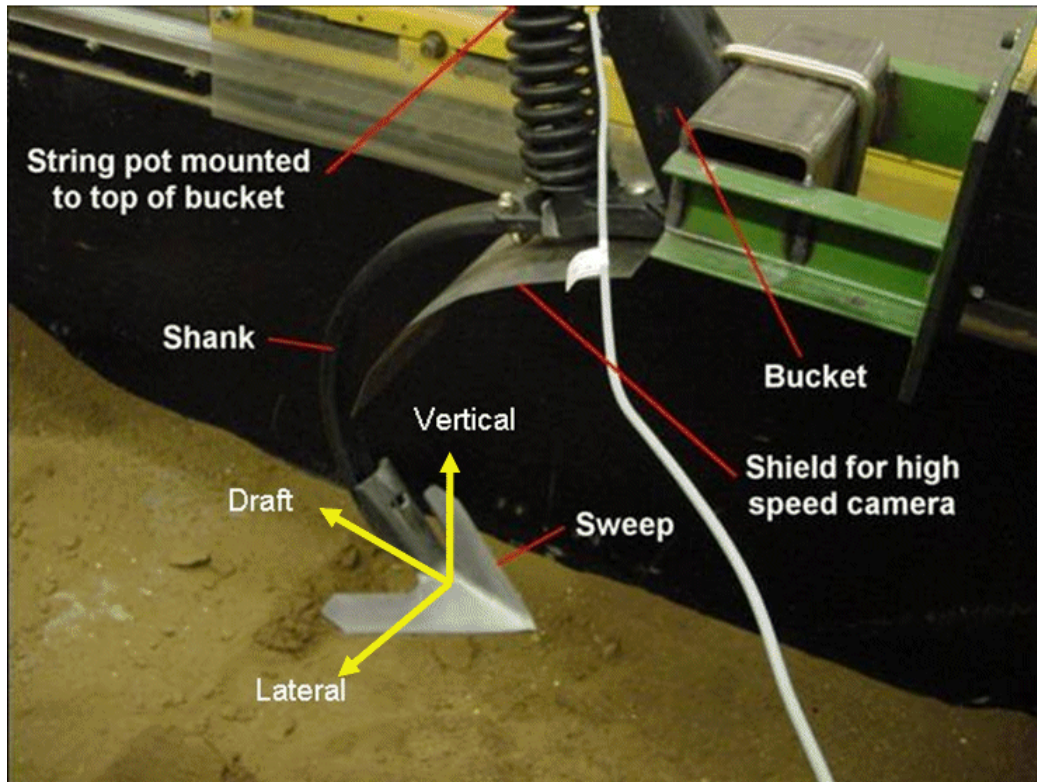


Figure 4.1: Field cultivator standard soil bin test setup

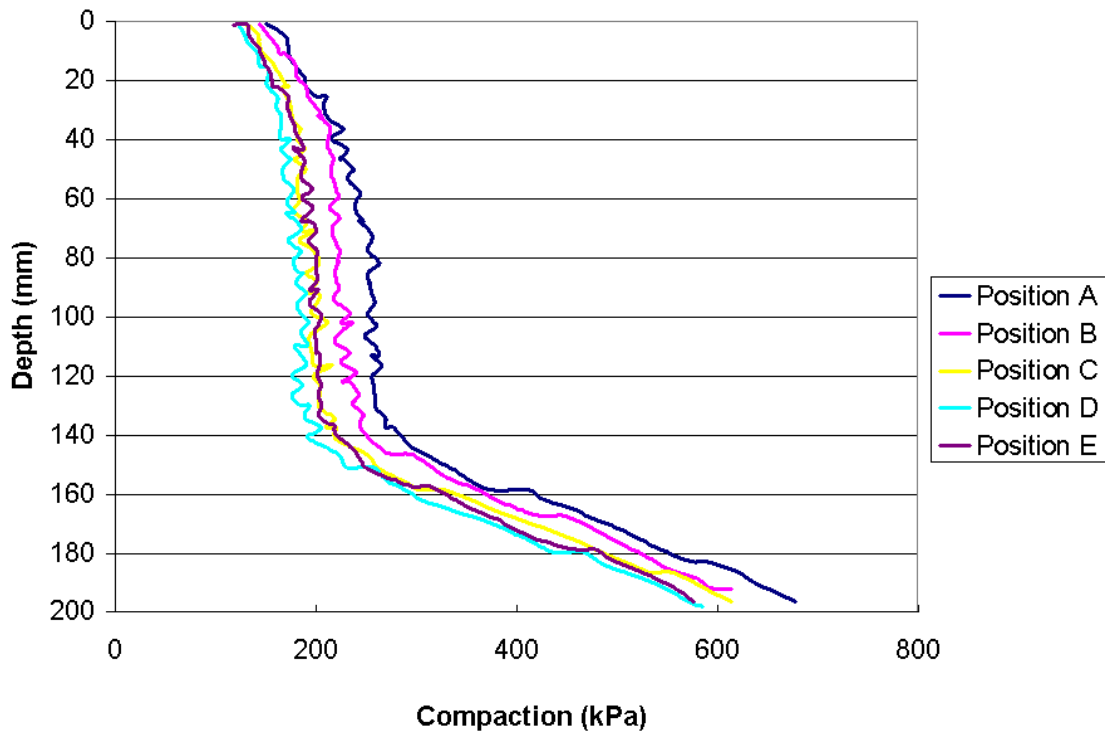


Figure 4.2: Penetrometer readings, high moisture (8.3% d.b.), low compaction (200 kPa)

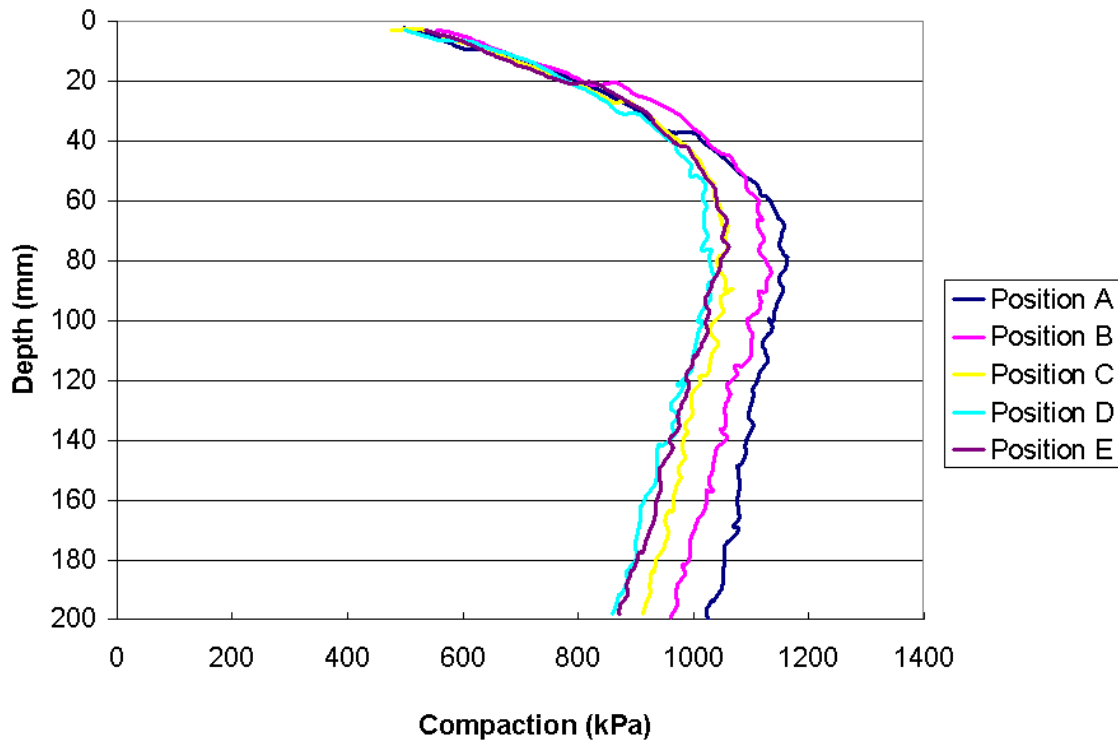


Figure 4.3: Penetrometer readings, high moisture (8.3% d.b.), high compaction (1,100 kPa)

4.2 Results

After the runs were completed the recorded load and spring deflection data were analyzed for statistical significance. For each of the runs the average and standard deviation was calculated from the time history data. For the runs that were repeated, the average of the individual run averages and the standard deviation of the averages were also calculated. Figure 4.4 and Figure 4.5 are still images taken from the high speed video. The images show the different soil failure modes when the soil compaction is low or high. At the low compaction level the soil fails in a fluid manner like sand. At the high compaction level the soil fails like a brittle material in chunks. Figures 4.6 through 4.8 show one second time segments of the measured forces to show the variation in response of the seven inch sweep at 152 mm at the high compaction and moisture levels but at the three different speeds. All of the graphed time histories are provided in the Appendix.

It is worth noting that by comparing Figures 3.5 and 3.6 with Figures 4.6 through 4.8, the forces with the sweep have a periodic variation and that the period of the variation is

much longer than that for the rigid bar. Table 4.1 provides a summary of the average and standard deviation draft and vertical forces for all of the treatment levels of the field cultivator soil bin test.

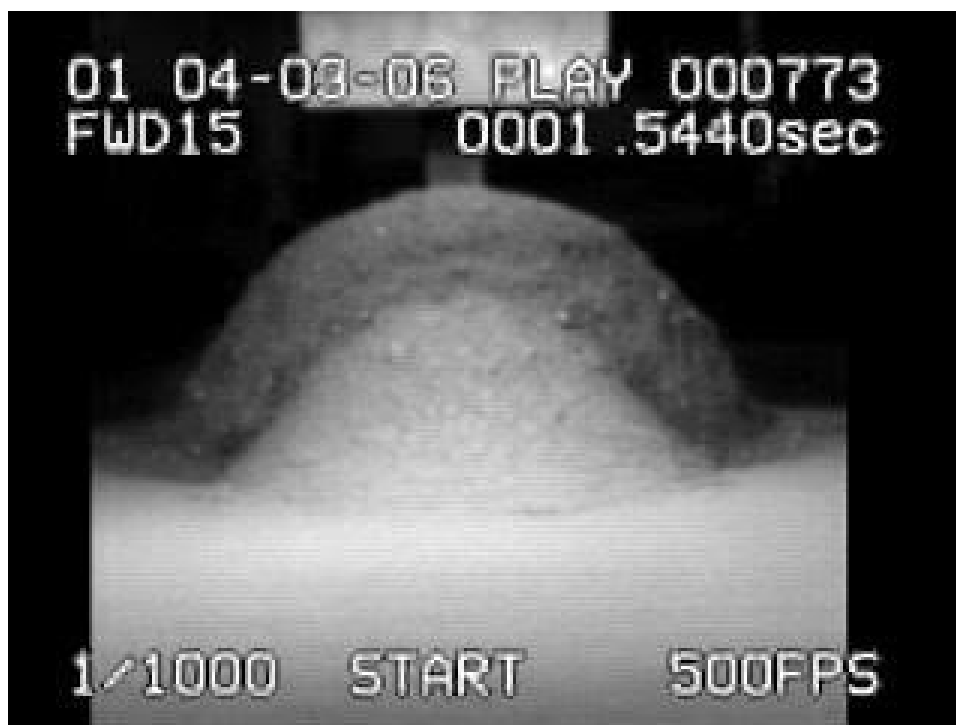


Figure 4.4: Soil bin test – 178 mm sweep, 2.68 m/s, 76 mm depth, high moisture (8.3% d.b.), low compaction (200 kPa)



Figure 4.5: Soil bin test – 178 mm sweep, 2.68 m/s, 76 mm depth, high moisture (8.3% d.b.), high compaction (1,100 kPa)

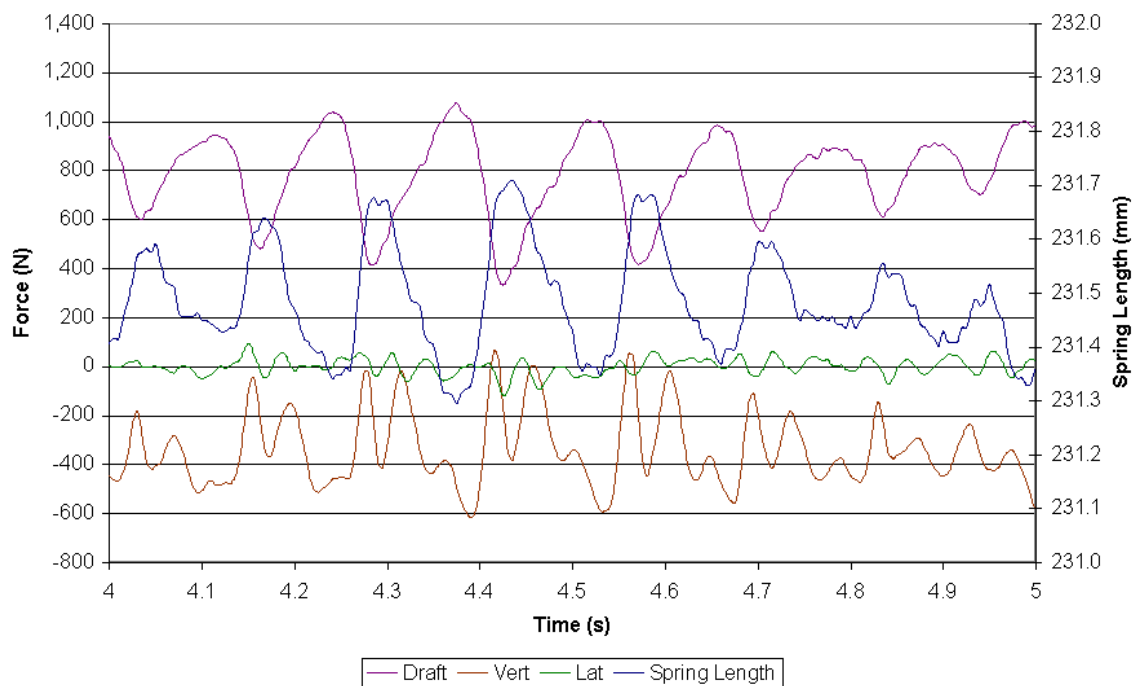


Figure 4.6: Run #1 time history results – 178 mm sweep, 0.89 m/s, 152 mm depth, high moisture (8.3% d.b.), high compaction (1,100 kPa)

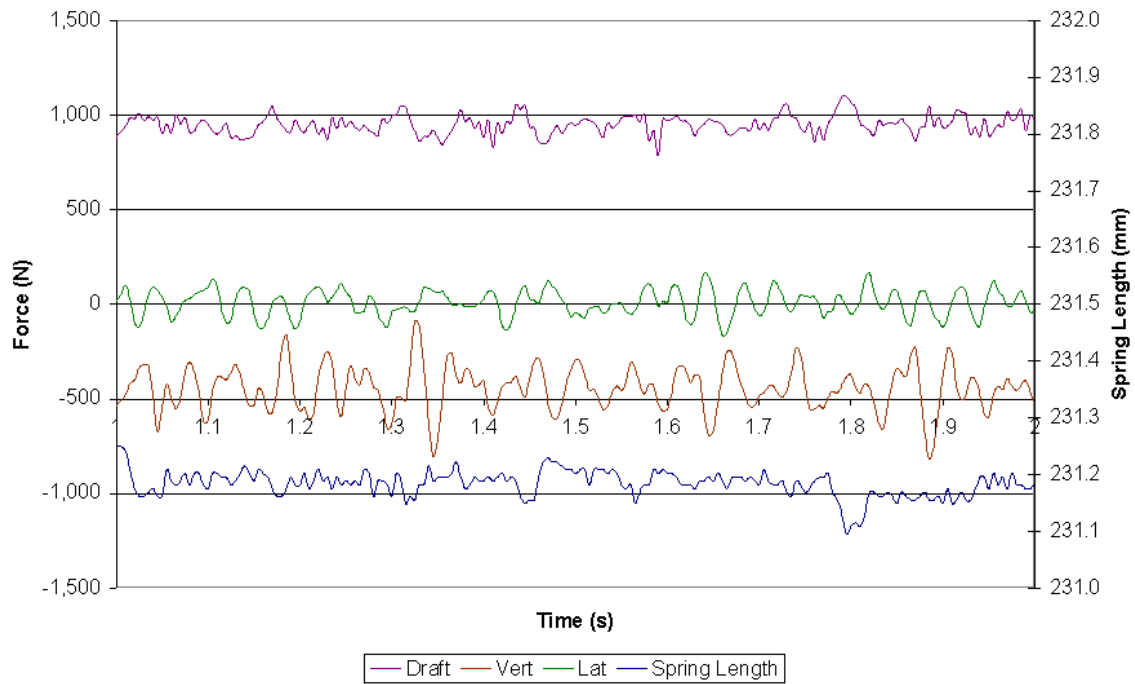


Figure 4.7: Run #16 – 178 mm sweep, 2.68 m/s, 152 mm depth, high moisture (8.3% d.b.) , high compaction (1,100 kPa)

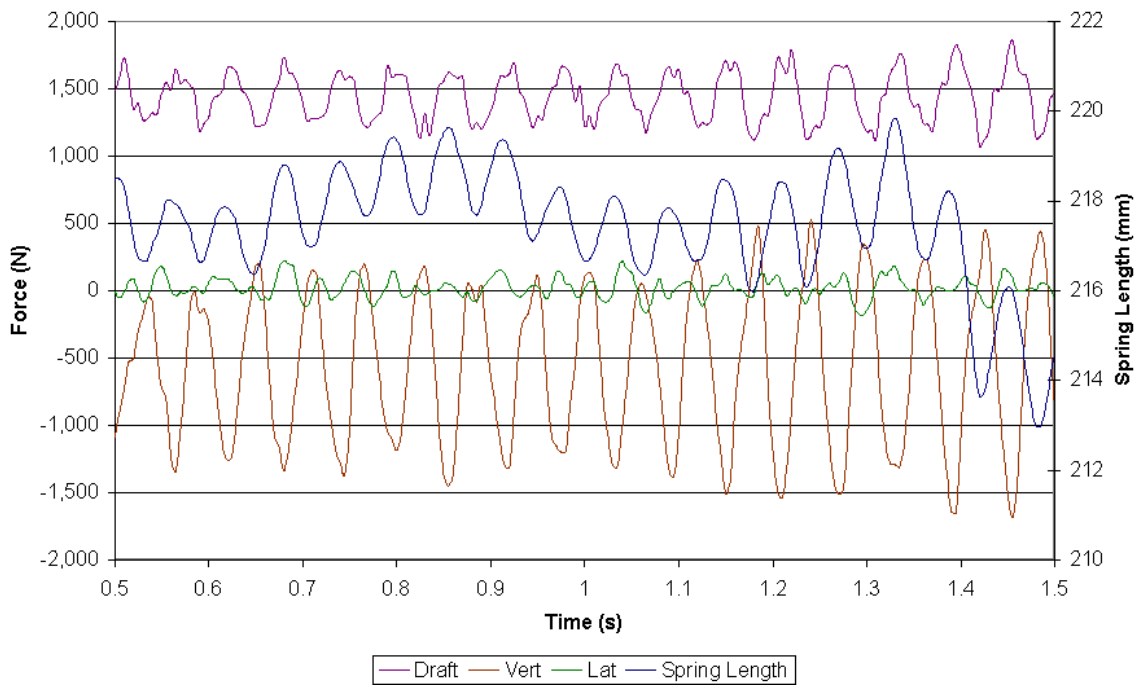


Figure 4.8: Run #111 – 178 mm sweep, 4.47 m/s, 152 mm depth, high moisture (8.3% d.b.) , high compaction (1,100 kPa)

Table 4.1: Summary of draft and vertical forces for field cultivator standard

Treatment #	Treatment Name	Sweep (in)	Sweep (mm)	Speed (mph)	Speed (m/s)	Depth (in)	Depth (mm)	Comp (H/L)	Moisture (H/L)	Draft		Vertical	
										Average (N)	Stdev (N)	Average (N)	Stdev (N)
1	W7S6D3LL	7	177.8	6	2.68	3	76.2	L	L	114.2	2.0	-48.8	0.5
2	W7S6D3LH	7	177.8	6	2.68	3	76.2	L	H	187.2	2.9	-59.4	0.3
3	W7S6D3HL	7	177.8	6	2.68	3	76.2	H	L	160.4	3.1	-49.8	0.4
4	W7S6D3HH	7	177.8	6	2.68	3	76.2	H	H	617.1	5.2	-54.0	6.2
5	W7S6D6LL	7	177.8	6	2.68	6	152.4	L	L	305.7	5.3	-165.9	2.8
6	W7S6D6LH	7	177.8	6	2.68	6	152.4	L	H	434.9	4.5	-206.8	2.3
7	W7S6D6HL	7	177.8	6	2.68	6	152.4	H	L	424.0	1.8	-214.0	0.4
8	W7S6D6HH	7	177.8	6	2.68	6	152.4	H	H	1,094.2	29.3	-509.8	14.6
9	W7S2D3LL	7	177.8	2	0.89	3	76.2	L	L	65.8	NA	-32.0	NA
10	W7S2D3LH	7	177.8	2	0.89	3	76.2	L	H	107.6	NA	-31.0	NA
11	W7S2D3HL	7	177.8	2	0.89	3	76.2	H	L	96.6	NA	-17.3	NA
12	W7S2D3HH	7	177.8	2	0.89	3	76.2	H	H	299.2	NA	4.4	NA
13	W7S10D3LL	7	177.8	10	4.47	3	76.2	L	L	237.1	NA	-103.7	NA
14	W7S10D3LH	7	177.8	10	4.47	3	76.2	L	H	353.8	NA	-257.0	NA
15	W7S10D3HL	7	177.8	10	4.47	3	76.2	H	L	330.3	NA	-109.8	NA
16	W7S10D3HH	7	177.8	10	4.47	3	76.2	H	H	844.7	NA	-158.0	NA
17	W7S2D6LL	7	177.8	2	0.89	6	152.4	L	L	175.7	NA	-111.2	NA
18	W7S2D6LH	7	177.8	2	0.89	6	152.4	L	H	229.6	NA	-116.7	NA
19	W7S2D6HL	7	177.8	2	0.89	6	152.4	H	L	270.8	NA	-134.5	NA
20	W7S2D6HH	7	177.8	2	0.89	6	152.4	H	H	772.8	NA	-386.9	NA
21	W7S10D6LL	7	177.8	10	4.47	6	152.4	L	L	593.9	NA	-282.8	NA
22	W7S10D6LH	7	177.8	10	4.47	6	152.4	L	H	600.6	NA	-257.0	NA
23	W7S10D6HL	7	177.8	10	4.47	6	152.4	H	L	831.1	NA	-365.0	NA
24	W7S10D6HH	7	177.8	10	4.47	6	152.4	H	H	1,575.3	NA	-585.4	NA
25	W10S6D3LL	10	254	6	2.68	3	76.2	L	L	172.1	NA	-82.2	NA
26	W10S6D3LH	10	254	6	2.68	3	76.2	L	H	234.2	NA	-76.9	NA
27	W10S6D3HL	10	254	6	2.68	3	76.2	H	L	195.0	NA	-66.1	NA
28	W10S6D3HH	10	254	6	2.68	3	76.2	H	H	774.7	NA	-100.9	NA
29	W10S6D6LL	10	254	6	2.68	6	152.4	L	L	361.0	NA	-204.0	NA
30	W10S6D6LH	10	254	6	2.68	6	152.4	L	H	527.3	NA	-253.7	NA
31	W10S6D6HL	10	254	6	2.68	6	152.4	H	L	595.8	NA	-288.8	NA
32	W10S6D6HH	10	254	6	2.68	6	152.4	H	H	1,183.9	NA	-498.5	NA

Figure 4.9 shows the average draft force and \pm three standard deviations for the eight treatments that were repeated. Figure 4.10 shows the average vertical force and \pm three standard deviations for the eight treatments that were repeated. These treatments were used for the comparison with the simulation. Figure 4.9 shows that seven of the eight repeated treatments had relatively small standard deviations in the average measured draft load, where the standard deviation is highest at the high compaction (1,100 kPa) and high moisture (8.3% d.b.).

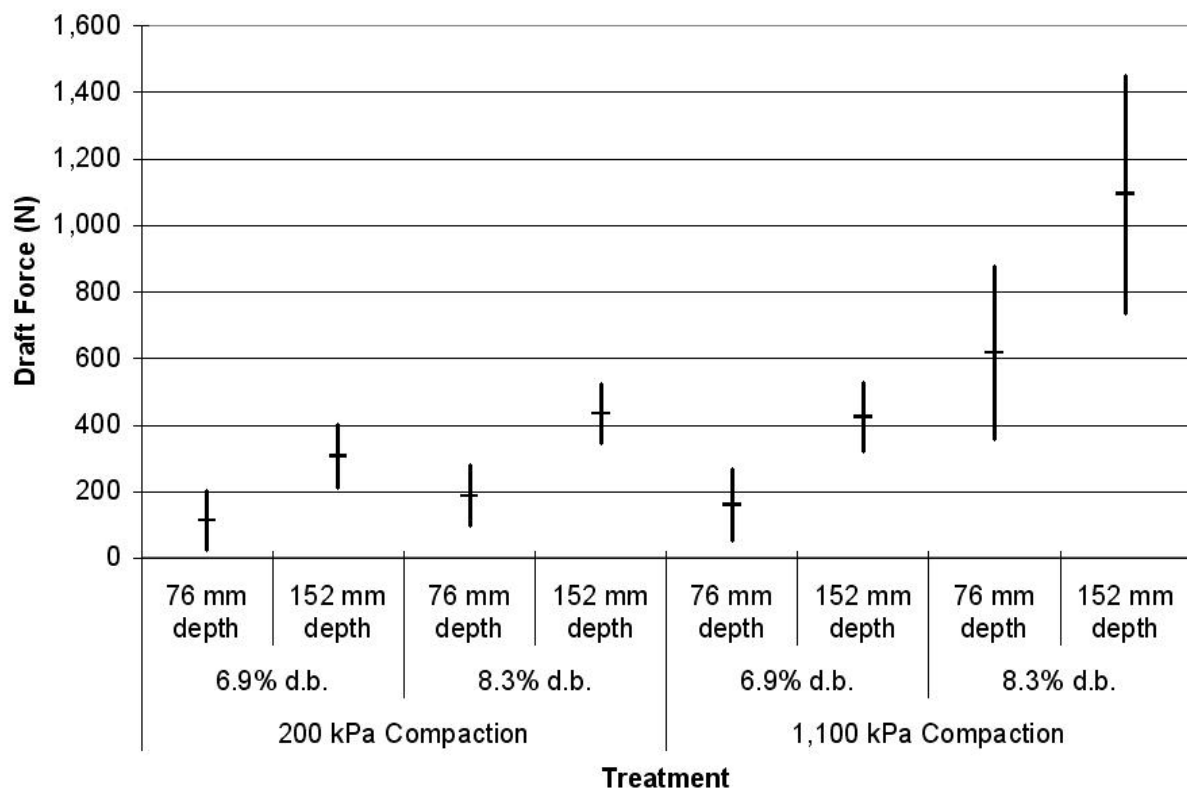


Figure 4.9: Field cultivator standard - average draft force values and \pm 3 standard deviations for repeated treatment levels with 178 mm sweep and 2.68 m/s

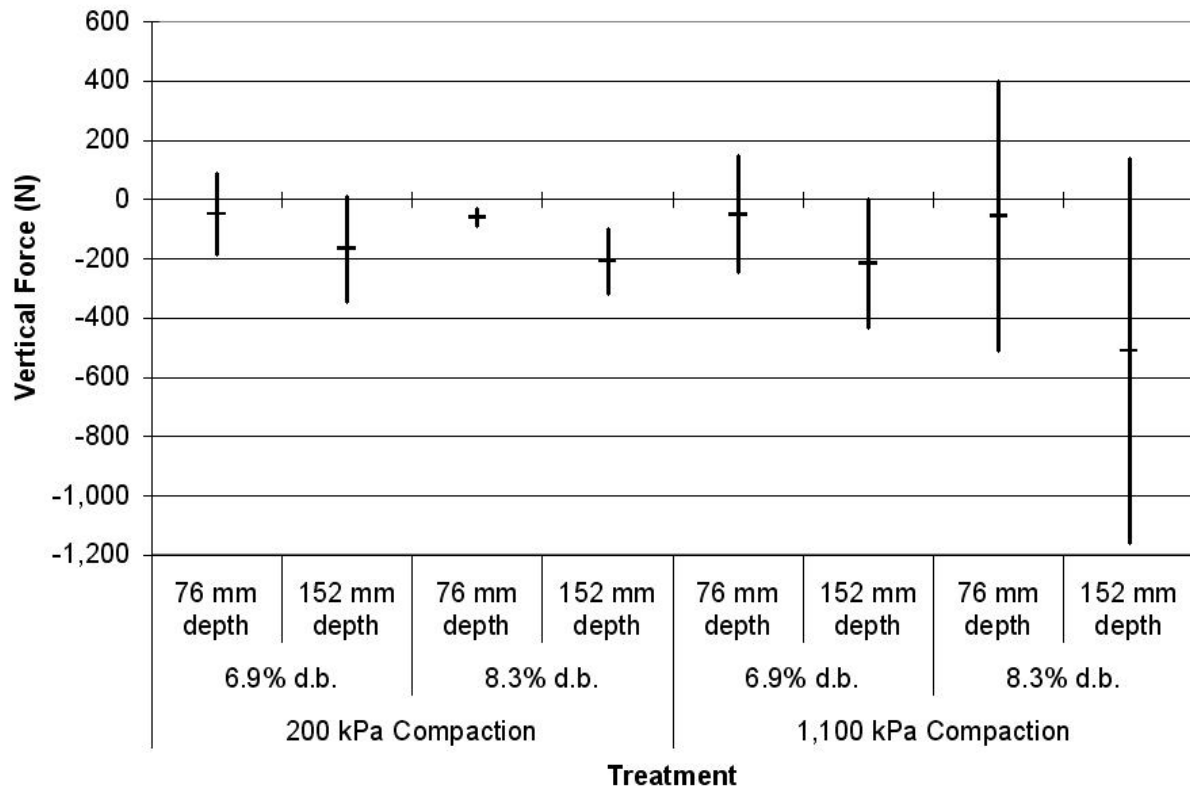


Figure 4.10: Field cultivator standard - average vertical force values and +/- 3 standard deviations for repeated treatment levels with 178 mm sweep and 2.68 m/s

4.3 Statistical Analysis

A statistical analysis was conducted on the data to determine which independent variables were significant in predicting the draft and vertical loads. Scatter plots were created and a multiple regression analysis was carried out with backward elimination by eliminating the variables with the highest P-value greater than 0.10 one at a time starting with the variable that had the highest P-value. Based on the literature review (Mouazen and Ramon, 2000) an additional variable of speed squared was added to the independent variables. After the initial regression analysis the speed variable was dropped with a P-value of 0.6701. The second variable that was dropped was sweep width with a P-value of 0.1599. The remaining four variables all had P-values lower than 0.10 and were all statistically significant in relation to the draft load. However, reducing the number of variables did not improve the coefficient of determination which was 75.0 percent.

Table 4.2 shows the P-values for each iteration of the regression analysis and the resulting coefficients for the predictor equation (4.1). Based on the ANOVA analysis shown in Table 4.2, the predictor equation for the draft load is,

$$\begin{aligned} \text{Draft (N)} = & -2,088.1 \text{ (N)} + 20.794 \times \text{Speed}^2 \text{ (m}^2\text{/s}^2\text{)} + 3.6287 \times \text{Depth (mm)} \\ & + 0.36447 \times \text{Compaction (kPa)} + 225.18 \times \text{Moisture (\% d.b.)} \end{aligned} \quad (4.1)$$

A similar analysis was carried on the data for the vertical loading. In the first pass of the regression analysis the speed squared variable was dropped with a P-value of 0.7118. In the second pass the sweep width variable was dropped with a P-value of 0.4383. The remaining four variables all had P-values that were below 0.1 and were all statistically significant in relation to the vertical loads at the 95 percent confidence level. The coefficient of determination for the resulting predictor equation was only 65.6 percent.

Table 4.3 shows the P-values for each iteration of the regression analysis and the resulting coefficients for the predictor equation. Based on the ANOVA analysis, the predictor equation for the vertical load is,

$$\begin{aligned} \text{Vert (N)} = & 699.58 \text{ (N)} - 43.608 \times \text{Speed (m/s)} - 2.5354 \times \text{Depth (mm)} - 0.093739 \\ & \times \text{Compaction (kPa)} - 53.250 \text{ Moisture (\% d.b.)} \end{aligned} \quad (4.2)$$

Figure 4.12 shows the predicted values of the vertical force versus the measured values. The predictor equation was able to predict the average vertical force to within +/- three standard deviations of the measured data in seven of the eight treatments.

An additional regression analysis was performed on the vertical force with just the measured draft load as the predictor variable. The regression analysis showed that the draft variable is statistically significant at the 95 percent confidence level with no intercept. Table 4.4 shows the P-values for each iteration of the regression analysis and the resulting coefficient for the predictor equation. Based on the ANOVA analysis, the predictor equation for vertical load is,

$$\text{Vert (N)} = -0.39058 \text{ Draft (N)} \quad (4.3)$$

Figure 4.13 shows the predicted values of the vertical force versus the measured values. The predictor equation was able to predict the average draft to within +/- three standard deviations of the measured data for all eight treatments.

The full tabular results for all of the regression analyses are provided in the Appendix.

Table 4.2: Regression analysis P-values and final coefficients for field cultivator draft loads

	Intercept	Sweep	Speed	Speed^2	Depth	Compaction	Moisture
Iteration#1	0.0000	0.2304	0.6701	0.4437	0.0000	0.0000	0.0000
Iteration#2	0.0000	0.1599		0.0000	0.0000	0.0000	0.0000
Iteration#3	0.0000			0.0000	0.0000	0.0000	0.0000
Coeff.	-2,088.1			20.794	3.6287	0.36447	225.18
Units	N	mm	m/s	m^2/s^2	mm	kPa	% d.b.

Figure 4.11 shows the predicted values of the draft force versus the measured values. The predictor equation was only able to predict the average draft force to within +/- three standard deviations of the measured data in three of the eight treatments.

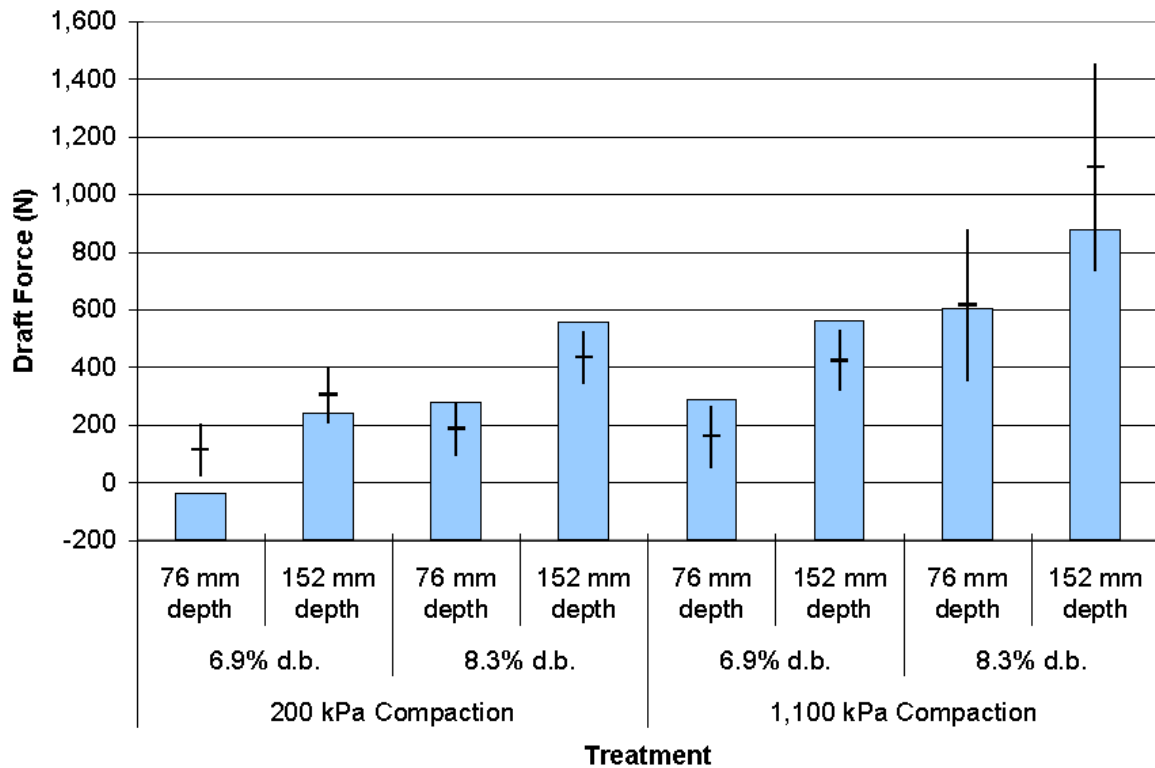


Figure 4.11: Predictor equation for draft force values compared to measured values

Table 4.3: Regression analysis P-values and final coefficients for field cultivator vertical loads

	Intercept	Sweep	Speed	Speed ²	Depth	Compaction	Moisture
Iteration#1	0.0002	0.3990	0.6434	0.7118	0.0000	0.0035	0.0091
Iteration#2	0.0001	0.4383	0.0018		0.0000	0.0032	0.0084
Iteration#3	0.0001		0.0017		0.0000	0.0030	0.0081
Coeff.	699.58		-43.608		-2.5354	-0.093739	-53.250
Units	N	mm	m/s	m ² /s ²	mm	kPa	% d.b.

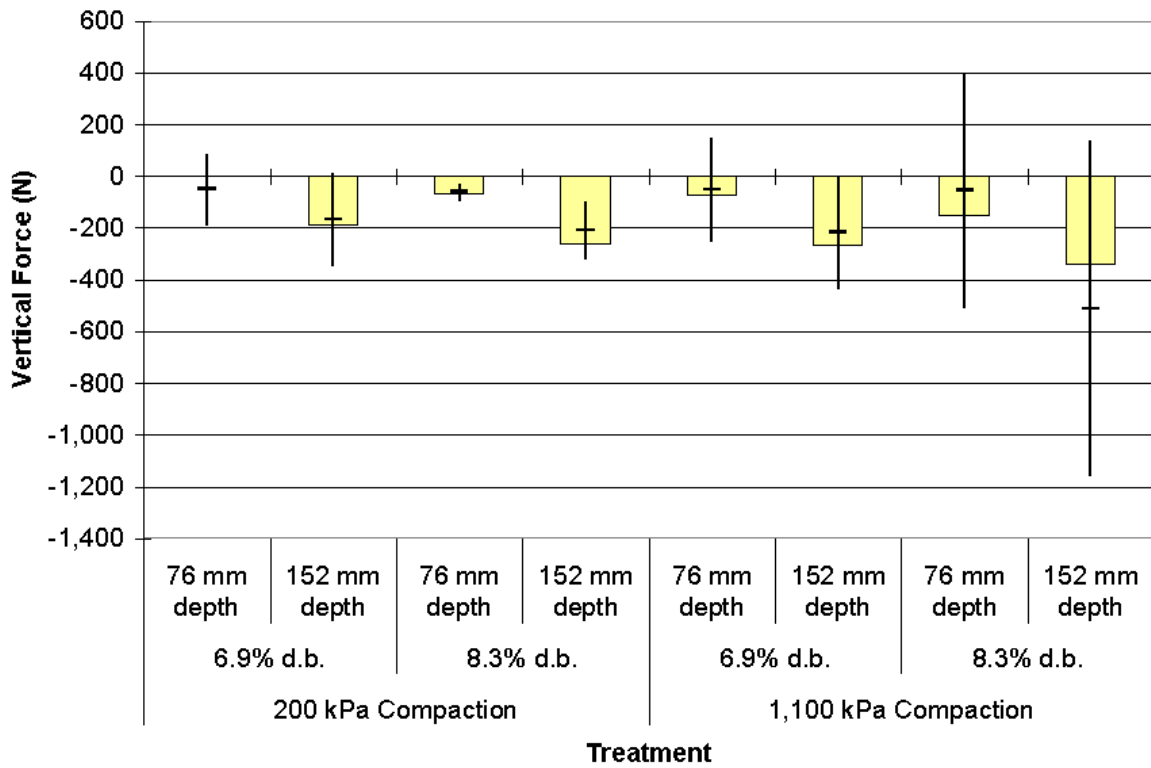


Figure 4.12: Predictor equation for vertical force values compared to measured values

Table 4.4: Regression analysis P-value and final coefficient for field cultivator vertical loads as a function of the draft loading

	Intercept	Draft
Iteration#1	0.9860	0.0000
Iteration#2		0.0000
Coeff.		-0.39058
Units	N	N

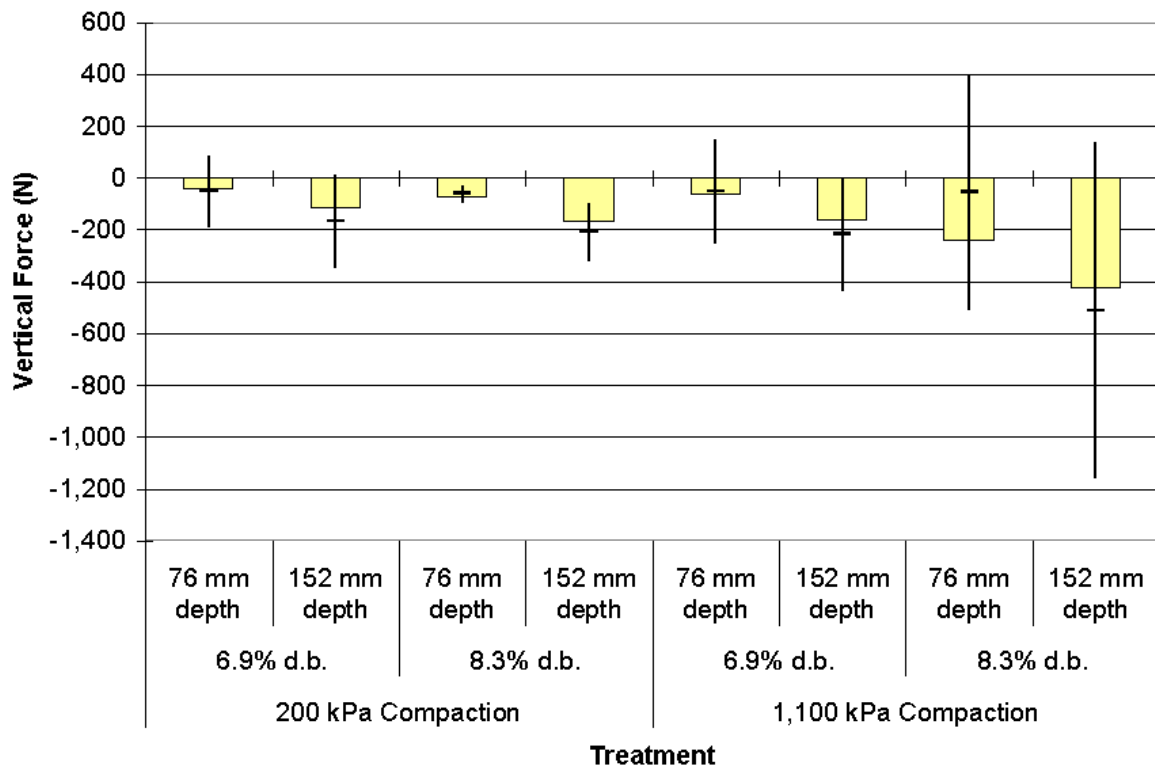


Figure 4.13: Predictor equation for vertical force as a function of measured draft force values compared to measured values

4.4 Modal Analysis

The field cultivator standard was mounted to a rigid structure of four by four steel tubing mounted to the floor. Accelerometers were mounted to an aluminum block which was then glued to the bottom of the sweep next to the shank. One accelerometer was mounted in the fore-aft direction and the other in the vertical direction. A large metal mallet was used to rap the end of the sweep to induce vibration in the standard assembly. The accelerometers were connected to a Somat Edaq data acquisition system and controlled by a laptop computer. The acceleration time histories were recorded at a frequency of 1,000 Hz. Figure 4.14 and Figure 4.15 show the test stand setup and the location of the accelerometers.



Figure 4.14: Modal analysis test stand for field cultivator standard



Figure 4.15: Accelerometer mounting to field cultivator standard

Several tests were run and three tests with no double hits or noise were analyzed to calculate the natural frequency of the assembly. The calculated natural frequency of the field cultivator standard was 22.6 Hz and was consistent for all three tests. The natural frequency value was also used to correlate with the structural FEA model later on. The vibration data was also used to calculate the damping of the spring reset standard to also use in the structural FEA model. An example of a partial time history is shown in Figure 4.16. Table 4.5 shows the damping calculations.

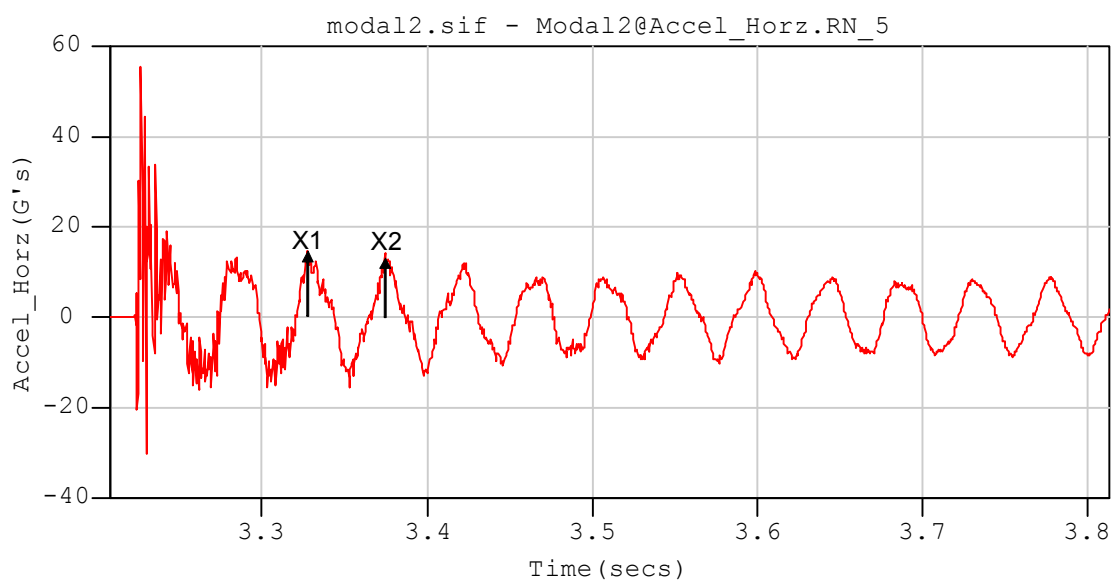


Figure 4.16: Time history of vibration data from accelerometer

The equations for calculating the damping from the measured accelerometer data are:

$$\delta = \ln(X1 / X2) \quad (4.1)$$

$$\xi = \frac{\delta}{\sqrt{(4\pi^2 + \delta^2)}} \quad (4.2)$$

$$c = 2\xi\omega_n \quad (4.3)$$

$$\beta = 2\xi / \omega_n \quad (4.4)$$

where: δ = logarithmic decrement

ξ = damping ratio

ω_n = natural frequency (Hz)

c = damping

β = beta damping.

Table 4.5: Damping calculation for field cultivator standard

Run #	1	3	4	5	6	Average
X1 =	24.9200	21.5471	36.4987	26.5509	11.4312	
X2 =	21.9986	18.4617	32.1731	23.2979	9.8420	
Logarithmic decrement =	0.1247	0.1545	0.1261	0.1307	0.1497	
Damping ratio =	0.0198	0.0246	0.0201	0.0208	0.0238	0.0223
Natural frequency (wn) =	22	22	22	22	22	22
Damping c =	0.8730	1.0819	0.8832	0.9151	1.0479	0.9820
Beta =						0.0020

4.5 Frequency Analysis of Measured Draft Force

A frequency analysis was conducted on the measured draft force time history data to determine if there were common frequencies that occurred across treatments levels. A power spectral density analysis was run for each treatment using nCode's nSoft 2004 software. The data was then exported in ASCII format and imported into MicroSoft Excel for plotting. For each treatment level, the three frequencies with the highest RMS power were recorded. Figure 4.17 is an example of the plot from a power spectral density analysis and shows how the three frequencies were determined. Figure 4.18 compares the measured draft load frequencies from the soil bin tests by treatment level for the repeated treatment levels. Figure 4.19 shows the results for all treatment levels tested. Both figures include a line representing the natural frequency of the field cultivator standard.

Figure 4.18 shows that for the eight treatments that were repeated, at least one of the three highest power frequencies coincided between repetitions. The very low frequencies, less than one hertz, that appear in the graph indicate that random vibration was significant in the draft force time histories. The most common frequency across all treatments was around 14.8 Hz which indicates that the dominant frequency is a function of the standard and the tool carrier it was mounted to at the soil bin rather than the soil fracture/failure frequency.

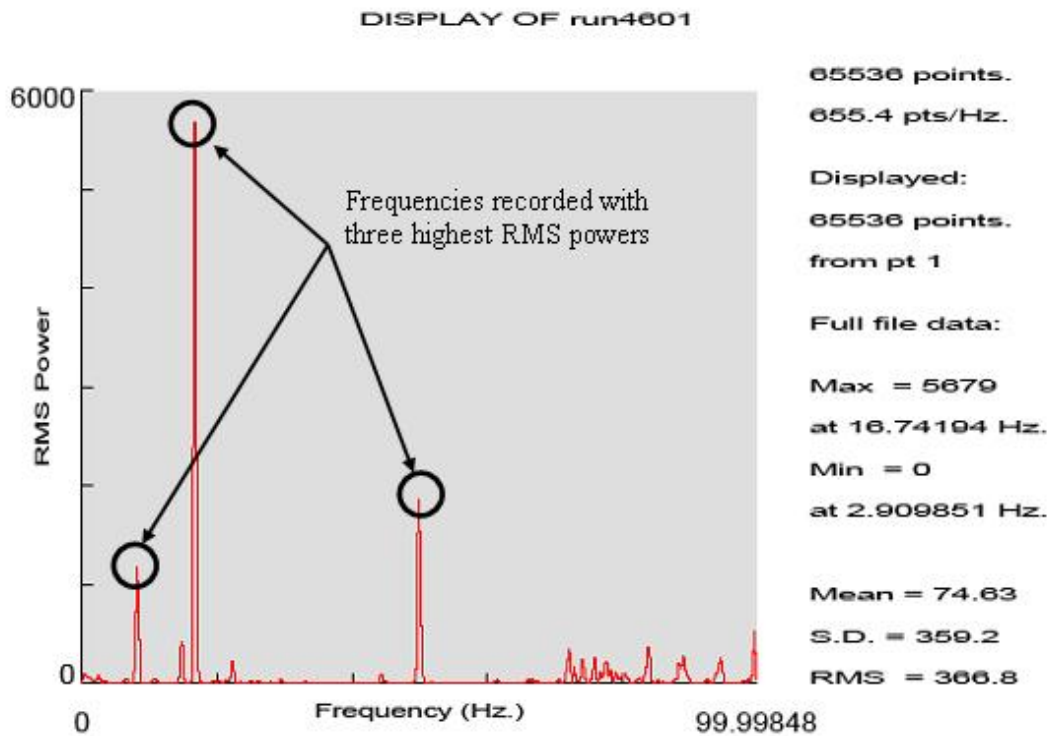


Figure 4.17: Example of power spectral density plot of measured draft forces

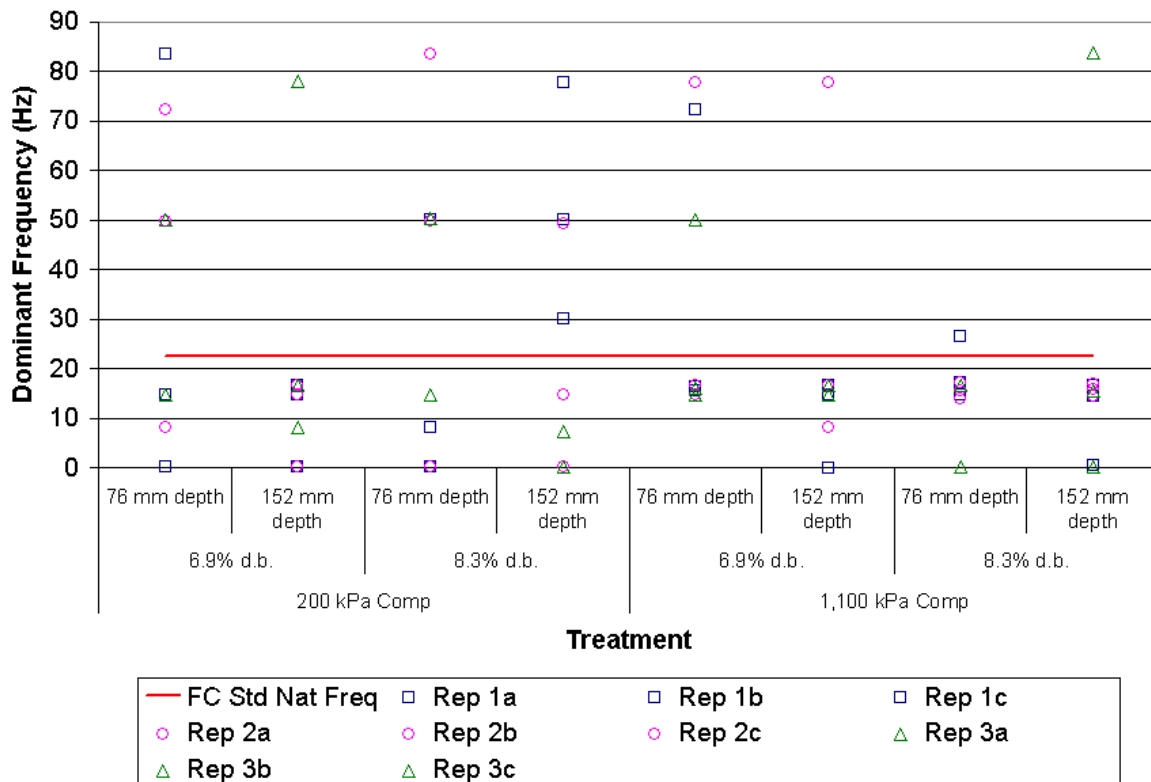


Figure 4.18: Dominant frequencies of measured draft forces for 176 mm sweep at 2.68 m/s

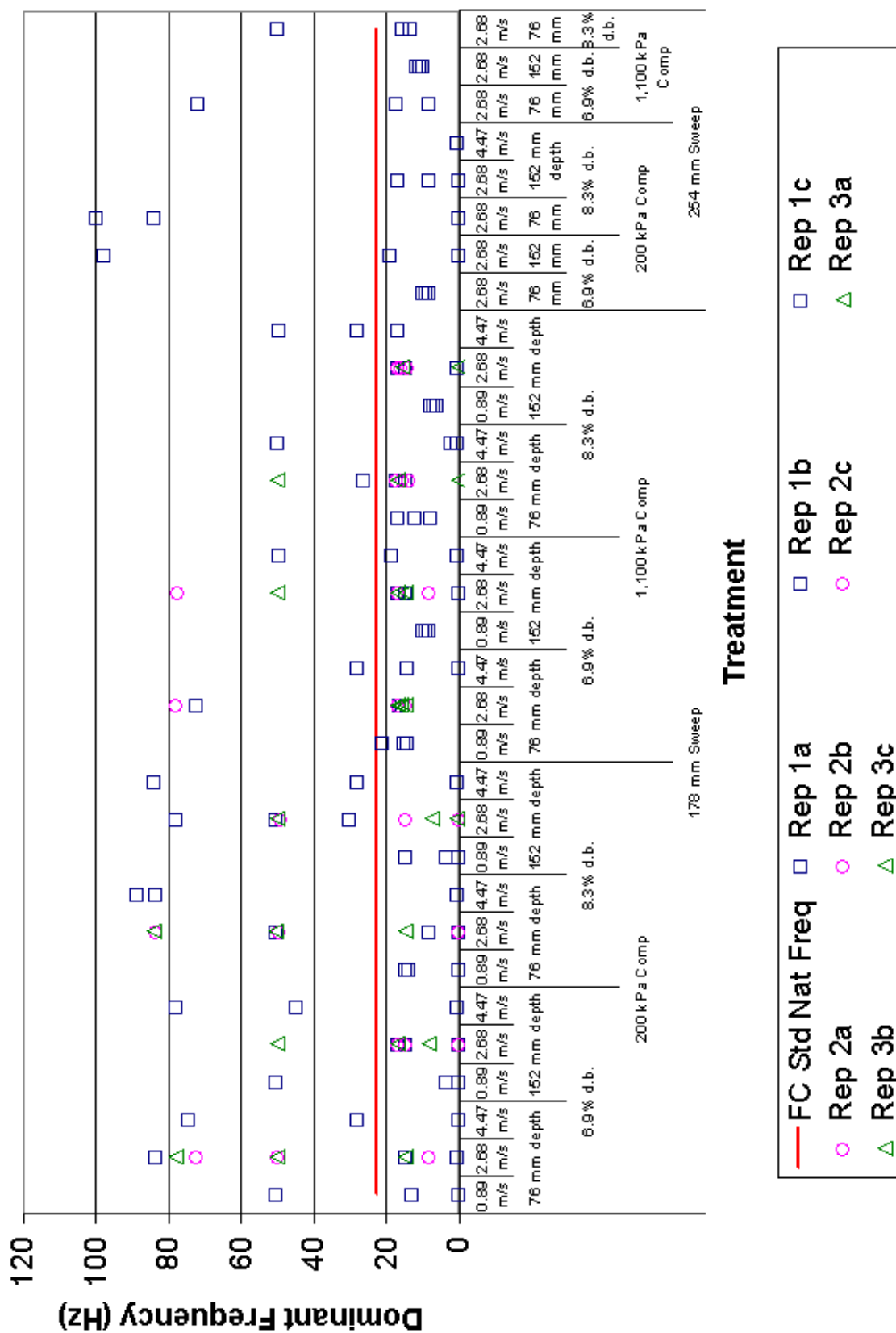


Figure 4.19: Dominant frequencies of measured draft forces for all treatments

An additional investigation was made to determine if the field cultivator standard stiffness influenced the frequency of the draft loads. To do this, a single example of the power spectrum density plot of the measured draft force from each treatment level was copied to Microsoft Excel. The first column contained the frequency and the second column contained the RMS power. In the third column the RMS powers were unitized by dividing the RMS power column by the maximum value. The frequency column and the unitized RMS power column were then plotted and compared in various ways to look for patterns. Unitizing the RMS Power values was necessary to make the overlaid data more viewable. Figure 4.20 shows the raw overlaid data to show how the difference in RMS Power levels makes unitizing the data necessary.

Plots were created to compare across speeds, soil conditions, test depths, and sweep size. Several plots are presented to illustrate the comparisons that were considered. Figure 4.21 through Figure 4.23 compare the 176 mm sweep at 76 and 152 mm depths for all four soil conditions at speeds of 0.89, 2.86, and 4.47 m/s respectively. Figure 4.24 compares the 254 mm sweep at 76 and 152 mm depth for all four soil conditions at 2.86 m/s. Figure 4.25 compares between the 178 and 254 mm sweeps at 76 and 152 mm depths but only for the soil condition with the high moisture level, 8.3% d.b., and the high compaction, 1,100 kPa.

All of the plots show random vibration occurred but there were several common harmonics that were visible. For the 176 mm sweep at 0.89 m/s a common frequency was found at about 3.5 Hz. For the 176 mm sweep at 2.86 m/s common frequencies were found at about 14, 15, and 17 Hz. For the 176 mm sweep at 4.47 m/s common frequencies were found at about 14, 25, and 28 Hz. For the 254 mm sweep at 2.86 m/s common frequencies were found at about 8, 15, and 17 Hz. A common frequency across all of the data occurred at about 50 Hz. It is not clear if this high frequency is related to the natural frequency of the test fixture.

The unloaded natural frequency of the standard assembly, 22.6 Hz, did not occur as a strong frequency in the data. One reason for this may be that the natural frequency was measured in the unloaded condition. Treating the soil and field cultivator standard as a spring mass system, the natural frequency is,

$$\omega = \sqrt{\frac{k}{m}} \quad (4.5)$$

where k is the equivalent stiffness (distance/force) and m is the equivalent mass. Assuming that the stiffness is primarily controlled by the structure of the standard and that the soil contributes to the mass, then the effect of the soil would be to increase the equivalent mass which will reduce the resonance frequency of the first mode.

As the sweep is loaded by the soil, the shank deflects rearward and slightly changes shape. This change in shape may also change the stiffness of the system and poses another possible reason for the difference between the loaded and unloaded frequencies. This effect could be studied by running a modal analysis on the deformed shank shape.

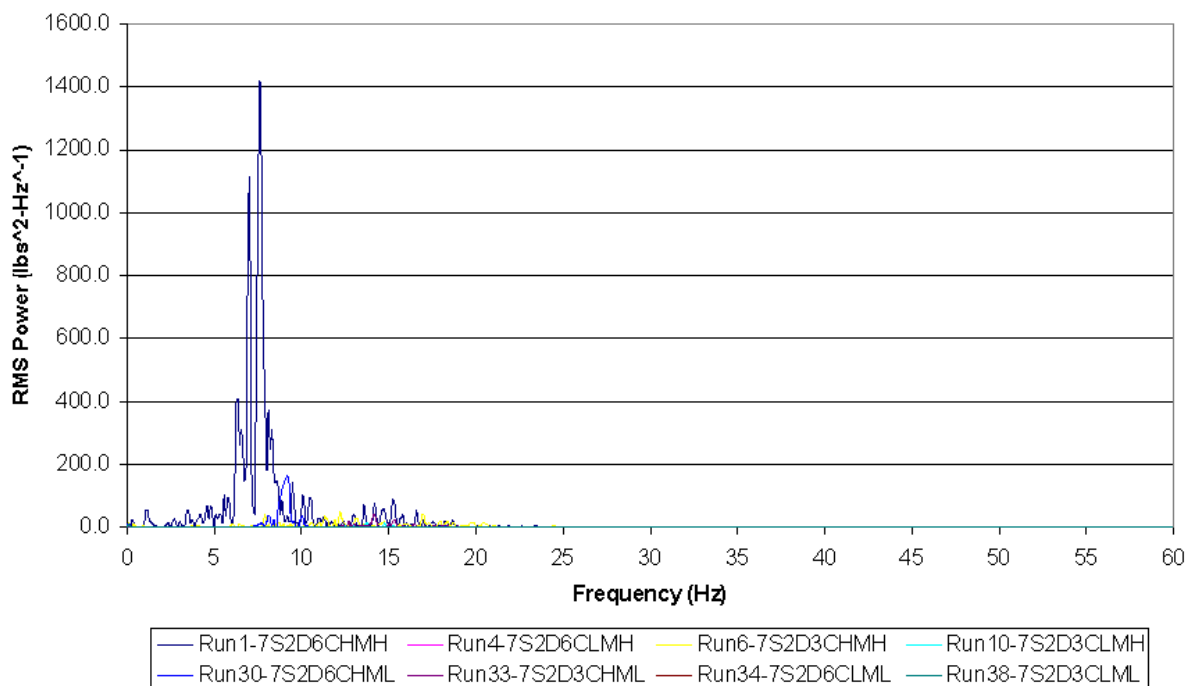


Figure 4.20: PSD plot for 178 mm sweep at 0.89 m/s, 76 & 152 mm depth, and all soil conditions

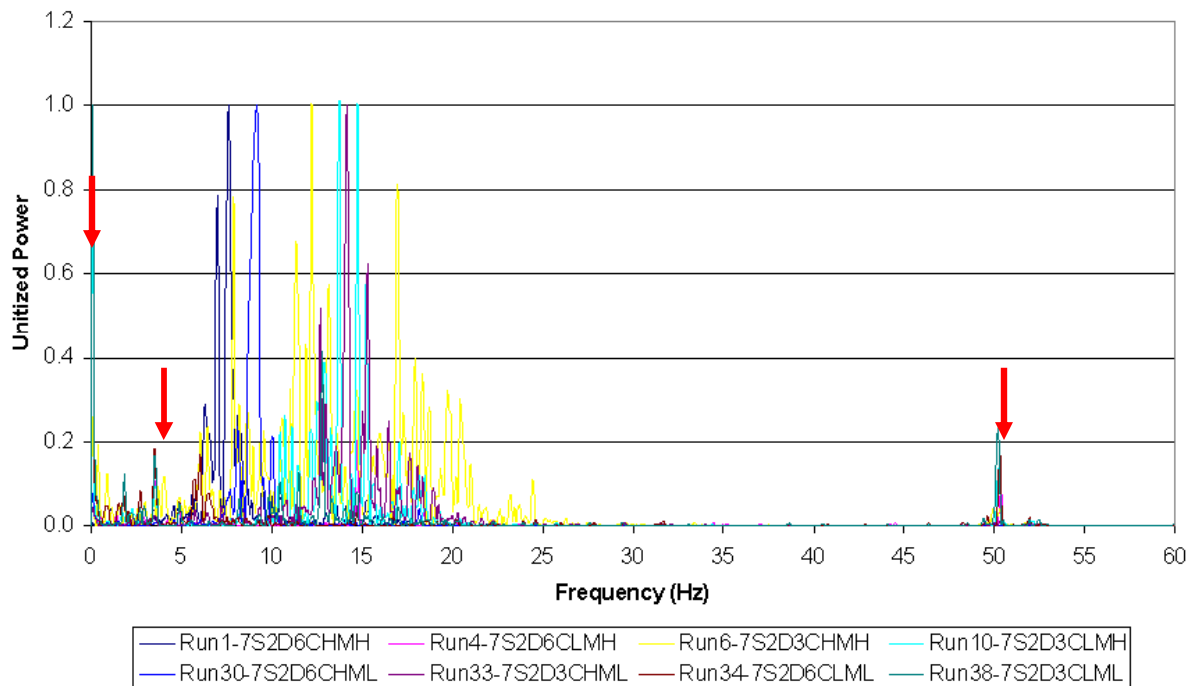


Figure 4.21: Unitized PSD plot for 178 mm sweep at 0.89 m/s, 76 & 152 mm depth, and all soil conditions

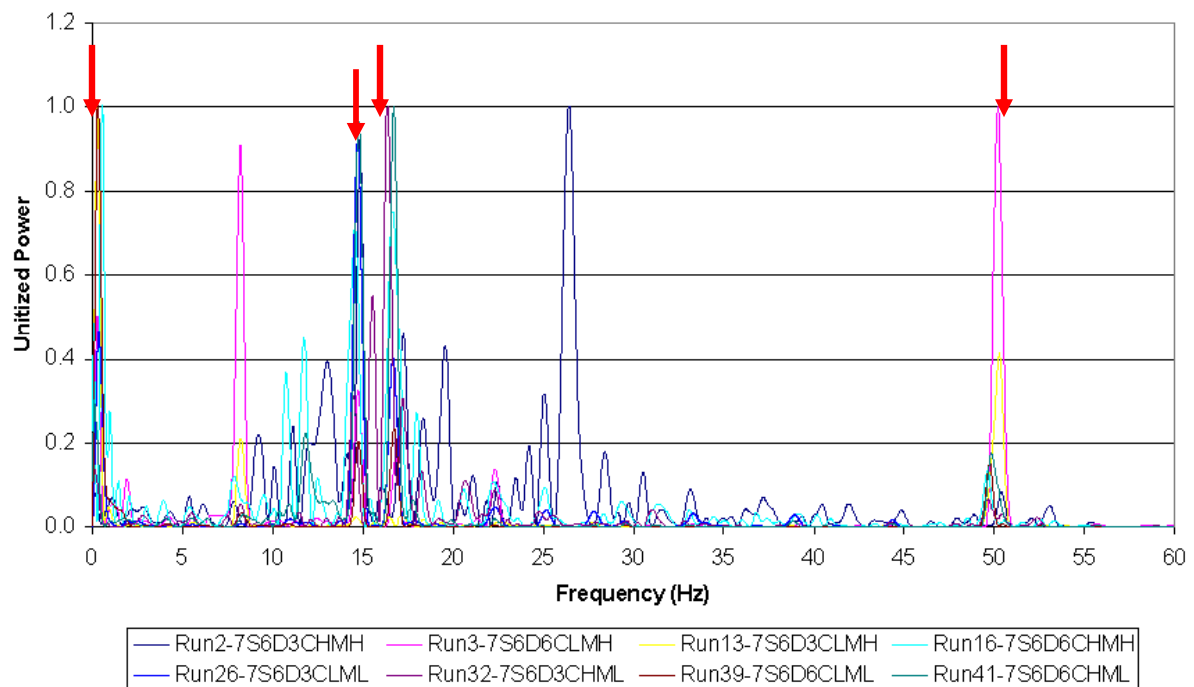


Figure 4.22: Unitized PSD plot for 178 mm sweep at 2.86 m/s, 76 & 152 mm depth, and all soil conditions

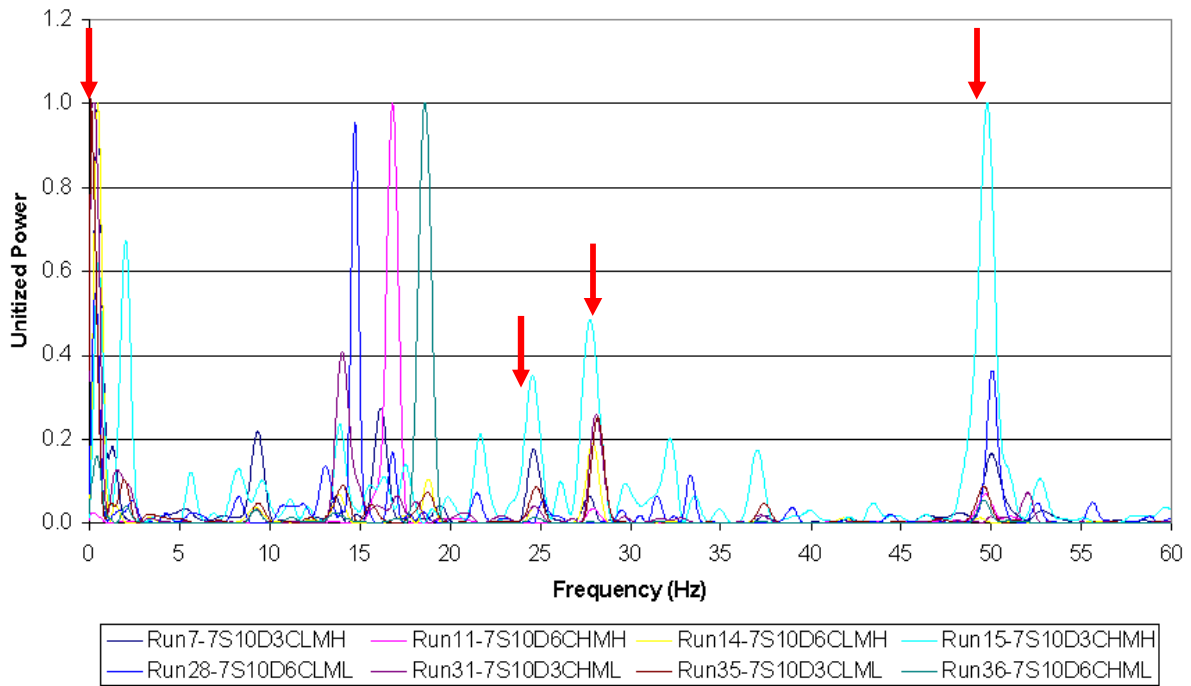


Figure 4.23: Unitized PSD plot for 178 mm sweep at 4.47 m/s, 76 & 152 mm depth, and all soil conditions

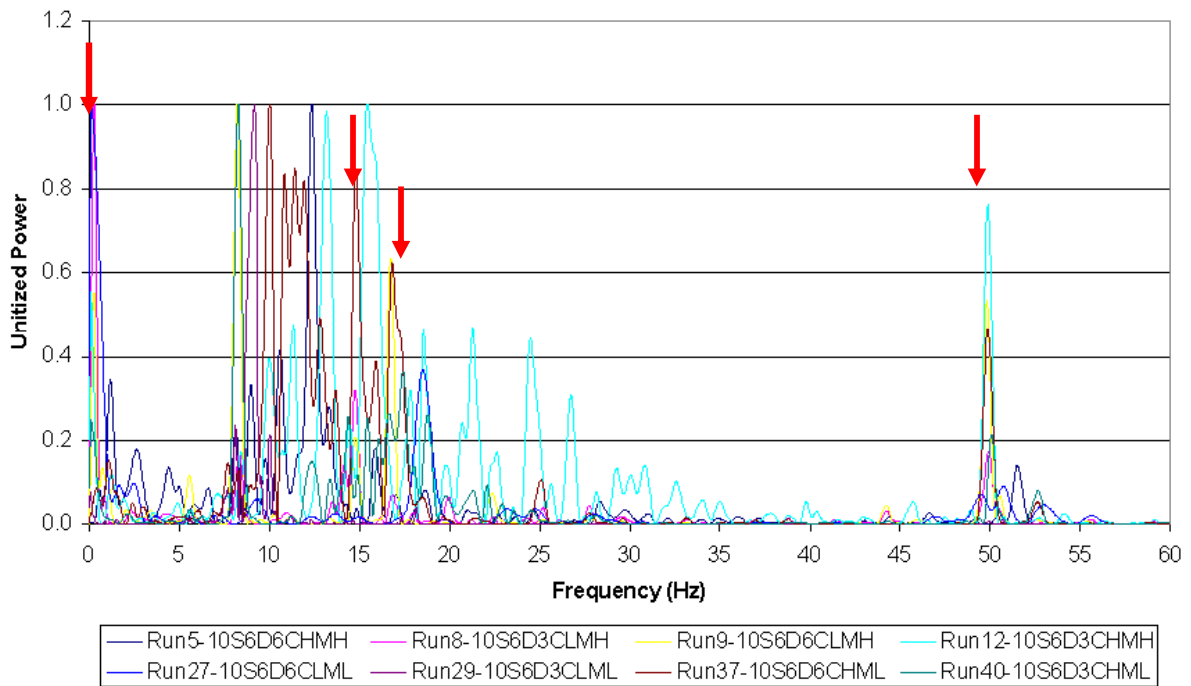


Figure 4.24: Unitized PSD plot for 254 mm sweep at 2.86 m/s, 76 & 152 mm depth, and all soil conditions

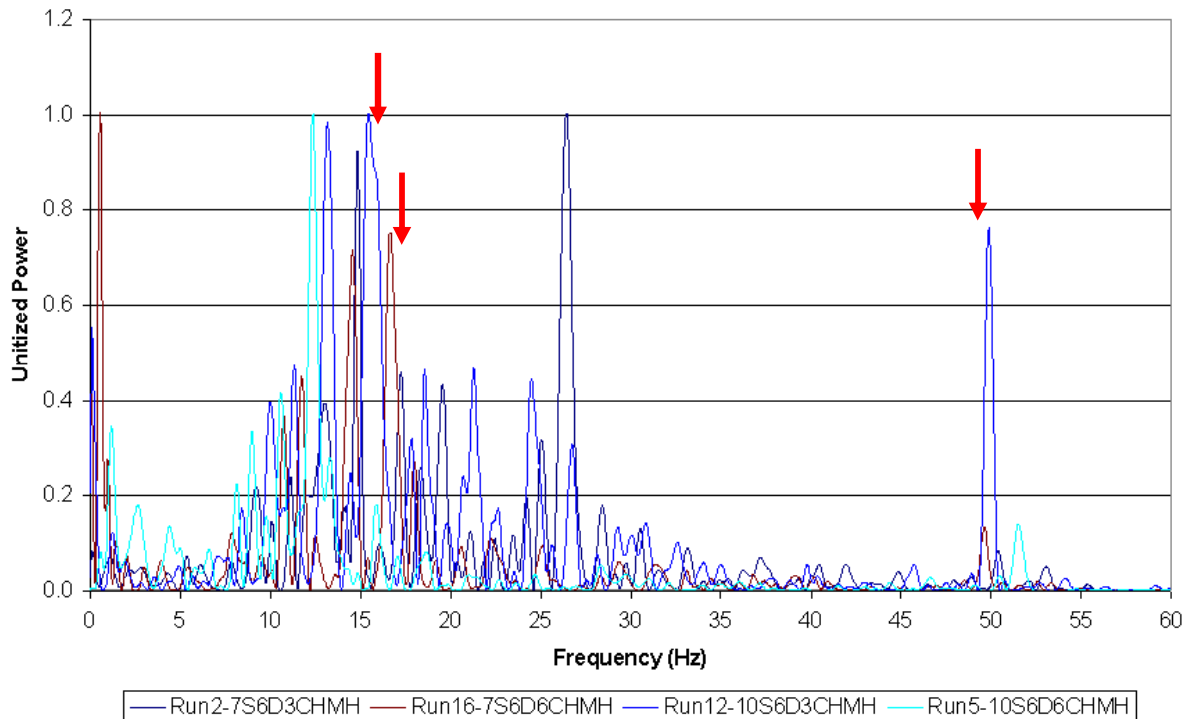


Figure 4.25: Unitized PSD plot for 178 & 254 mm sweep at 2.86 m/s, 76 & 152 mm depth, 8.3% d.b, and high compaction (1,100 kPa)

Attempts were also made to determine the dominant frequency of the load data by reviewing the high speed video that was taken during the test. The number of soil failures was counted and divided by the time over which the failures occurred. This method did not match the PSD data very consistently and was difficult to perform due to unclear soil failure surfaces. This was especially true for the low compaction soil which tended to fail in a flowing manner with no definitive failure surface. At higher speeds the fractured soil coming off of the sweep and shank obstructed the camera view of the soil failure surface. Table 4.6 shows a summary of six treatments and the comparison between the measured frequency data and the calculated frequency from the high speed video. This method could not be used with the rigid flat bar lab tests because the video camera was placed overhead. The fractured soil blocked the camera view making it impossible to count the fractured surfaces.

Table 4.6: Comparison of measured draft force frequency to high speed video frequency calculation

Sweep (mm)	Speed (m/s)	Depth (mm)	Compaction (kPa)	Moisture (% d.b.)	Measured Dominant Frequency	High Speed Video		
						Time (sec)	Fractures (#)	Calculated Frequency
178	0.89	152	1,100	8.3%	6-7	0.746	5	6.7
178	0.89	152	1,100	6.9%	8-10	0.746	8	10.7
178	2.68	76	1,100	6.9%	14-17	0.748	23	30.7
178	2.68	76	1,100	6.9%	14-17	0.746	24	32.2
178	2.68	152	1,100	8.3%	14-17	0.748	24	32.1
254	2.68	76	1,100	8.3%	13-15	0.746	21	28.2

The results in Table 4.6 show that the soil fracture rate is related to the dominant frequency of the draft force. For the two cases at the 0.89 m/s speed the ratio was approximately one-to-one. For the other load cases at the 2.68 m/s the ratio was about two-to-one. From these results it is not possible to tell whether the fracture rate is driving the draft force response frequency or the resonance response is driving the fracture frequency. Measuring the resonant frequency of the field cultivator standard with a load applied might show if the resonant frequency of the loaded structure matches the measured frequency of the draft loading. Conducting additional soil bin tests at different compaction levels would also help clarify if the structure stiffness drives the draft force frequency.

4.6 Conclusions

Soil bin tests were conducted using a 178 mm and 254 mm wide sweep with a spring reset field cultivator standard. Thirty-two treatments were considered and eight of the treatments were run with three repeats. The sweep width, speed, depth, soil compaction, and soil moisture were varied. The repeated runs were run with the 178 mm sweep at a speed of 2.66 m/s (6 mph) while just the depth, compaction, and moisture levels were varied.

The results for the repeated runs showed a fairly low level of variability in the draft force except for the treatment run at the higher depth, compaction, and moisture level. For both sizes of sweep the average ratio of vertical to draft force was forty percent. In predicting the draft load, the speed squared, depth, compaction, and moisture variables were all statistically significant at the 95 percent confidence level. In predicting the vertical load

the speed, depth, compaction, and moisture variables were all statistically significant at the 95 percent confidence level.

The natural frequency was experimentally determined for the unloaded field cultivator standard using accelerometers. The natural frequency was calculated to be 22.6 Hz. The accelerometer data was also used to calculate the damping of the spring reset standard for use in the fluid-structure analysis.

The analysis of dominant measured draft force frequencies showed that there was overlap in the repeated treatments. The most common frequency across all treatments was 14.8 Hz which may indicate that the draft force frequency is related more to the stiffness of the standard and the mounting than to the frequency of the soil failure. Common frequencies of around 14 to 15 Hz was found in the data for the 178 mm sweep at 2.86 and 4.47 m/s and for the 254 mm sweep at 2.86 m/s for all soil conditions. If this is the case, then in practice, predicting the load frequency would be related to the stiffness of standard and the implement structure stiffness, rather than the soil, which could be determined experimentally. The lower frequency of the draft force data compared with the natural frequency of the unloaded field cultivator standard may be attributed to the additional mass of the soil when treated as a spring-mass system or a change in the standards stiffness in the loaded condition.

An attempt was made at predicting the draft force frequency by counting the soil failure surfaces from high speed video recordings of the lab tests and dividing by the elapsed time. This method proved difficult but did show that the soil fracture rate was related to the dominant draft force frequency. This method was impossible to use at the low compaction level because the soil failed in a flowing manner with no distinct fracture surfaces. Additional testing would help to clarify the relationship.

5. CFD SOIL MODEL

As previously mentioned, the soil was modeled as a Bingham plastic for all of the simulation models. The values of density, yield strength and viscosity used in the simulations were measured and calculated as described in Chapter 2 and summarized in Table 2.2. To implement the visco-plastic model into the CFD software, equations were programmed into the software using the CFX expression language (CEL). The expressions were then referenced in the CFD material definition for the soil.

According to the Bingham plastic model the strain rate is zero until the soil shear stress reaches the yield strength. After yield is reached the soil shear stress and strain rate are directly proportional as a function of the viscosity. Because the slope of the shear stress versus strain rate is infinite until the yield strength is reached it is numerically impossible. To compensate for this a lower strain rate limit greater than zero is used to create a bilinear viscosity. Based on the recommendations of the CFX theory manual a low limit for the strain rate of 0.001 s^{-1} was used (2007).

$$\text{Visc} = \text{dynamic viscosity (Pa s)} \quad (5.1)$$

$$\text{Yield} = \text{yield strength (Pa)} \quad (5.2)$$

$$\text{LowLimit} = 0.001 \text{ (s}^{-1}\text{) lower strain rate limit} \quad (5.3)$$

$$\text{sstrnr} = \text{strain rate (s}^{-1}\text{)} \quad (5.4)$$

$$\text{Visceqn} = \text{Yield} / [\max(\text{sstrnr}, \text{LowLimit})] + \text{Visc (Pa s)} \quad (5.5)$$

Using the equations 5.1 through 5.5, five test models were created. The values of equations 5.1 and 5.2 were modified to see if the effects would come out as expected. The test values with the resulting range of dynamic viscosity and strain rates are provided in Table 5.1. The curves plotting the shear stress versus strain rate are shown in Figure 5.1. Note that for strain rates between zero and the LowLimit, the viscosity is equal to yield strength divided by the LowLimit value plus the measured dynamic viscosity. Above yield the viscosity is equal to Yield divided by the actual strain rate plus the measured dynamic

viscosity. This method proved to be numerically stable and easy to implement the different soil treatment levels that were used in the laboratory tests.

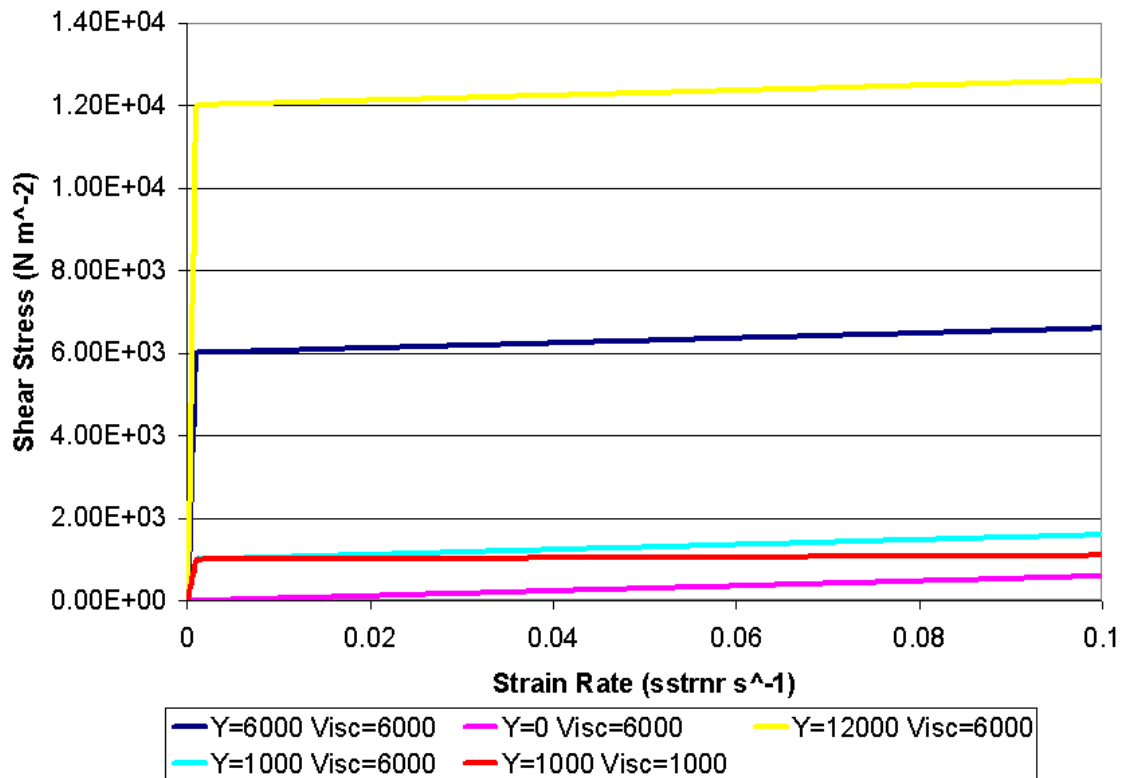


Figure 5.1: Shear stress versus strain rate for soil model test cases

5.1 Model

In order to test the soil model, a simple two dimensional model was created to simulate a concentric cylinder viscometer. In the model the outside of the domain is defined as a wall with no slip conditions. The inside diameter of the domain also was defined as a wall with no slip conditions and given a velocity of 0.001 m s^{-1} in the theta direction. The top and bottom cutting planes were defined with symmetry boundary conditions. The simulations were run as static with the solution allowed a maximum of 100 iterations with a convergence value of $1e-6$ for the RMS of the residuals for all of the governing equations across the entire domain. The solution timestep was chosen automatically by the software.

5.2 Results

Table 5.1 below shows the different Yield and Visc values considered and the resulting calculated dynamic viscosity and strain rate ranges across the gap between the inner and outer cylinders. Figures 5.2 through 5.6 show the dynamic viscosity profile for each of the five models. The models showed that the expressions created to model the visco-plastic behavior work correctly and can be applied to the rigid flat bar and the field cultivator standard simulations.

Table 5.1: Soil test model inputs and results

Model Name	Inputs		Dynamic Viscosity		Strain Rate (sstrnr)	
	Yield (N m ⁻²)	Visc (N s m ⁻²)	Min (N s m ⁻²)	Max (N s m ⁻²)	Min (s ⁻¹)	Max (s ⁻¹)
Model 1	6,000	6,000	7.160E+04	6.006E+06	7.624E-04	9.162E-02
Model 2	0	6,000	6.000E+03	6.000E+03	1.801E-02	2.765E-02
Model 3	12,000	6,000	1.261E+05	1.201E+07	7.421E-04	1.001E-01
Model 4	1,000	6,000	2.369E+04	6.511E+05	1.550E-03	5.655E-02
Model 5	1,000	1,000	1.193E+04	1.001E+06	7.624E-04	9.161E-02

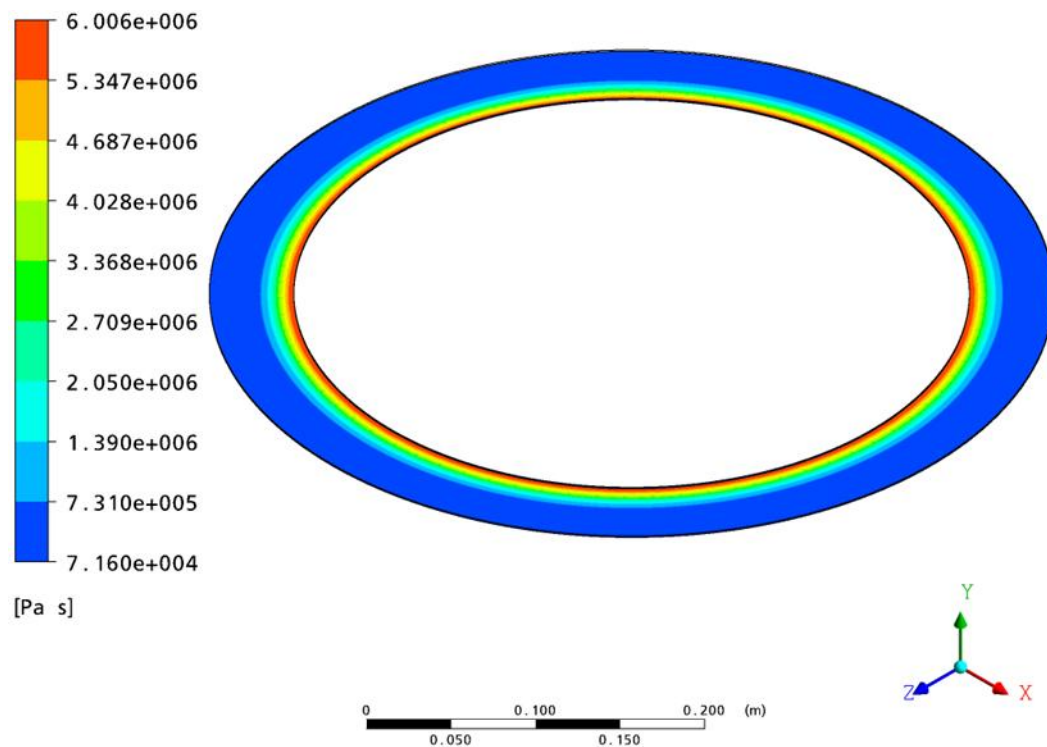


Figure 5.2: Model 1 dynamic viscosity plot (Yield=6,000 Pa, Visc=6000 Pa-s)

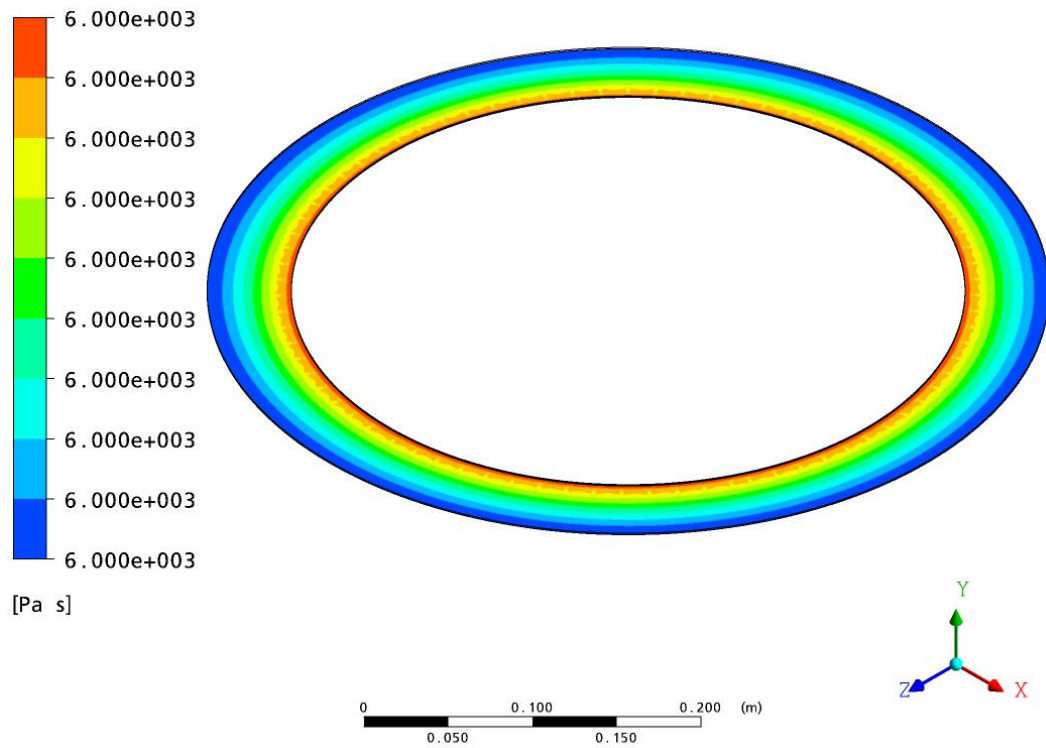


Figure 5.3: Model 2 dynamic viscosity plot (Yield=0 Pa, Visc=6,000 Pa-s)

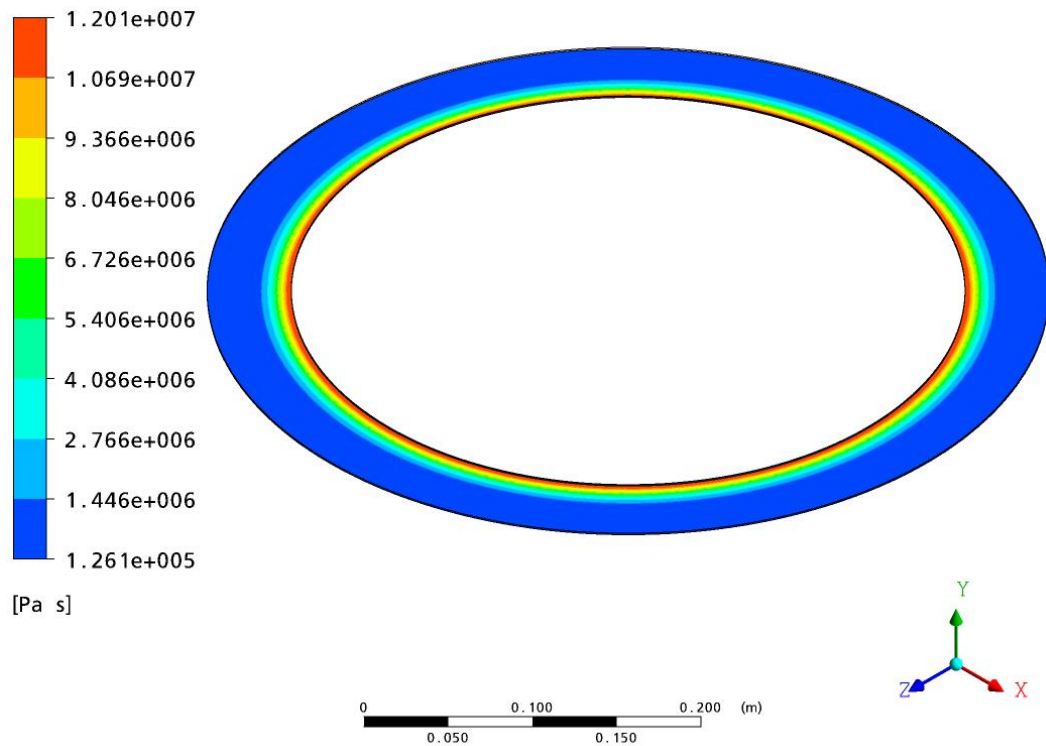


Figure 5.4: Model 3 dynamic viscosity (Yield=12,000 Pa, Visc=6,000 Pa-s)

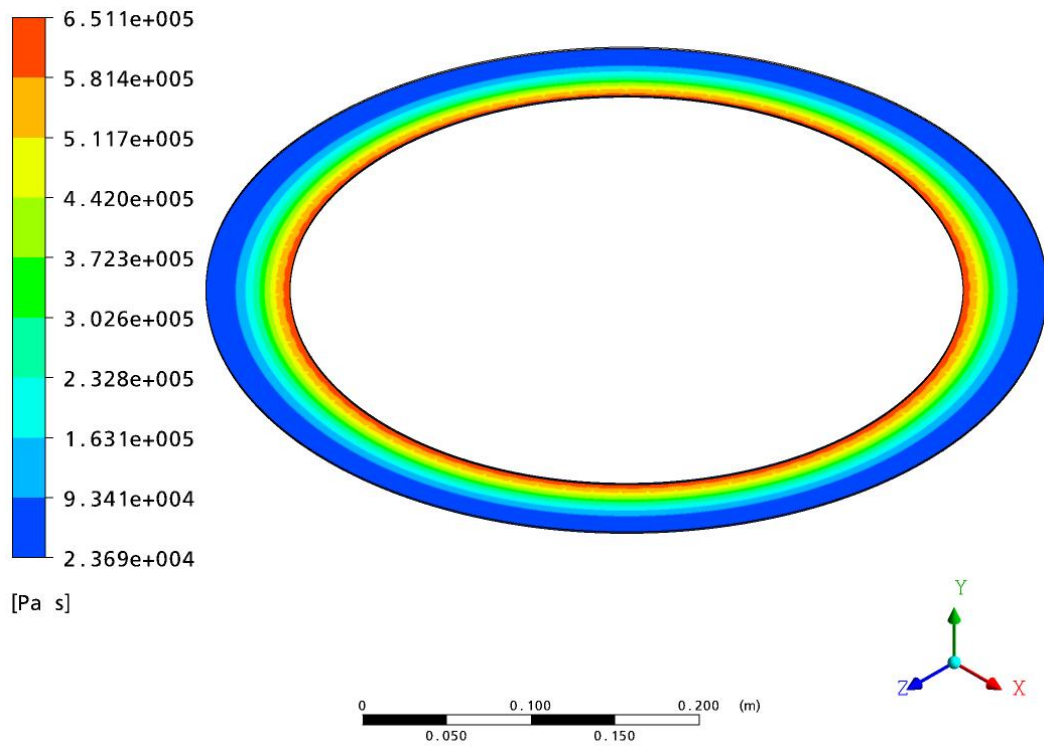


Figure 5.5: Model 4 dynamic viscosity (Yield=1,000 Pa, Visc=6,000 Pa-s)

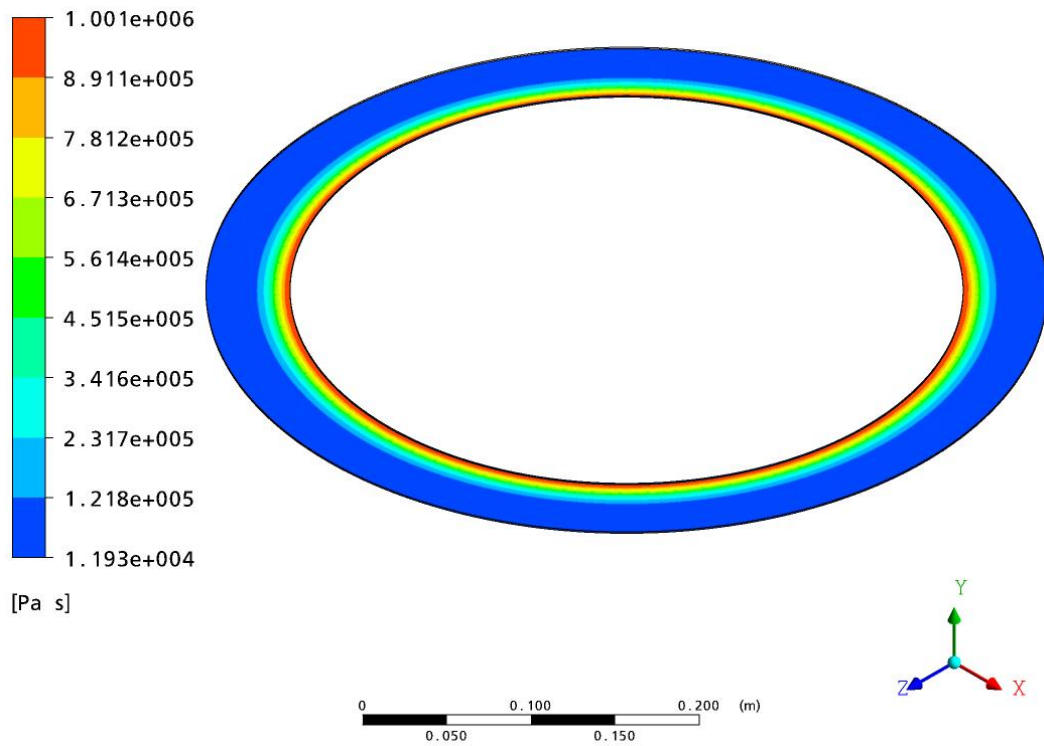


Figure 5.6: Model 5 dynamic viscosity (Yield=1,000 Pa, Visc=1,000 Pa-s)

5.3 Conclusions

The Bingham-Plastic material model was tested using a 2-d model of a concentric cylinder viscometer. The benefit of the test models was that the models are simple enough that the run times were very short. In addition, results for the two-dimensional models can be visually interpreted. The test models showed that the equations used to simulate the Bingham-Plastic model work correctly.

6. RIGID FLAT BAR SIMULATION

A steady-state CFD simulation was created for the rigid flat bar to develop the methodology and compare to the lab test results. Chapter 3 presented the actual lab test of the rigid flat bar. For this simulation the same parameters were varied and the calculated draft was compared to the measured data. This chapter presents the details of the model and the results. Lessons learned from this simulation were then applied to the final model of the spring reset field cultivator standard presented in the next chapter.

6.1 Model

The geometry for the simulation was created in ANSYS version 11.0 Design Modeler within the Workbench environment. The model was created as a half-symmetry to reduce the model size. A domain was chosen reasonably large so the walls would not significantly influence the flow. The domain size was 3 m long by 1.5 meter wide by 1.0 m deep with 0.5 m depth below the bottom of the bar. Figure 6.1 shows the domain. The domain was divided horizontally so that the mesh would have definite boundaries between the soil and air at the two test depths of 51 and 102 mm. The domain was divided between soil and air with equations that were programmed into the software using the CFX expression language (CEL) defining the element volume ratio between soil and air. The expressions were then referenced in the domain initialization and at the inlet. The equations allowed for the depth of the soil to be specified without requiring the domain to be divided. The equations to defining the volume ratios for each element in the domain are

$$\text{Height} = Y + \text{Offset} - \text{Depth} \quad (6.1)$$

$$\text{Vair} = \text{step}(\text{step}(\text{Height}/1 [\text{m}]) - 0.6) \quad (6.2)$$

$$\text{Vsoil} = 1 - \text{Vair} \quad (6.3)$$

where Y is the location on the vertical axis in the domain, Offset is the distance from the vertical axis to the bottom of the tool (m), Depth is the desired operating depth of the tool (m), Height is the vertical distance above the soil surface (m) (positive above the surface,

negative below the surface), V_{air} is the element volume ratio of air relative to the vertical location in the domain, and V_{soil} is the element volume ratio of soil relative to the vertical location in the domain. For locations in the domain below the soil surface the value of V_{air} is zero and the value of V_{soil} is equal to one. Above the soil surface the opposite is true.

This method allows for simple editing of the simulation input file to adjust the soil depth in the simulation. However, results will be improved at the soil surface if the domain is divided so that the mesh is divided at the desired soil depths. These equations were also used in the simulation of the field cultivator standard. The double step function in equation 6.2 changes the value of Height to either zero or one. The second step function is required because if the value of Height is equal to zero the first step function has a value of 0.5. The subtraction of 0.6 makes the sum become negative and the second step function makes the value of V_{air} go to zero at the surface when Height does equal zero. Equation 6.3 assures that the sum of the volume ratios does not round off to a value other than exactly one.

ANSYS

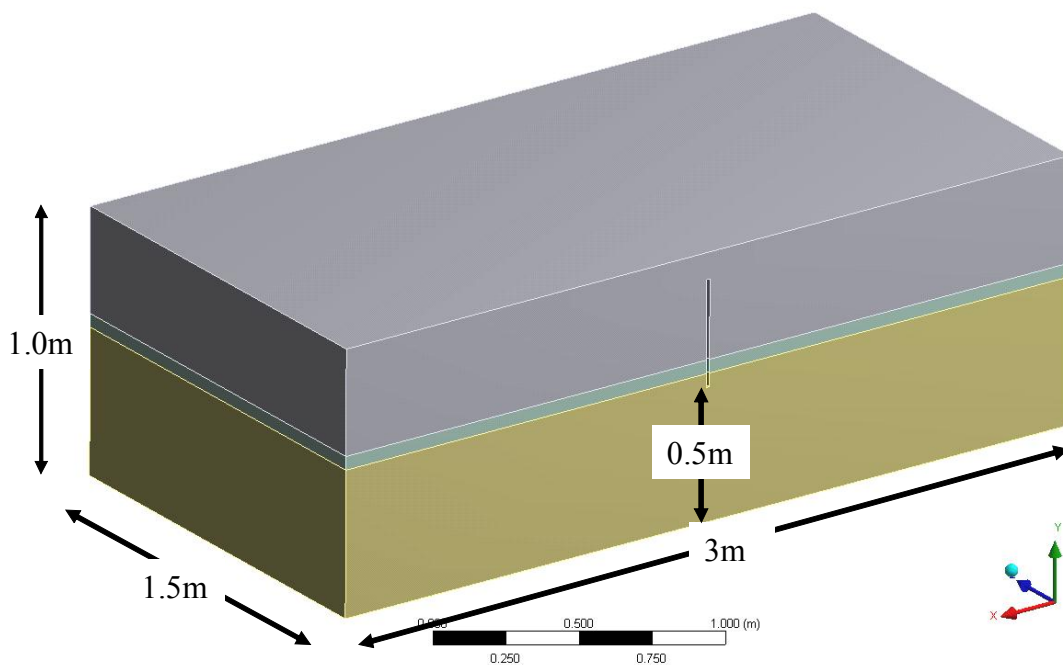


Figure 6.1: Rigid flat bar simulation domain

The full domain mesh is shown in Figure 6.2. Figure 6.3 shows a close-up of the mesh around the rigid flat bar with the mesh inflation layers for improved results on the

surface. The model contained 737,561 elements and 139,610 nodes. A mesh density of 0.006 mm was used on the surface of the flat bar. The mesh size was expanded in the remainder of the domain to a maximum element size of 50 mm. The mesh was made up of tetrahedron elements created in ANSYS Workbench Simulation and imported into ANSYS CFX pre-processor.

The boundary conditions were applied to the faces of the domain to replicate the actual lab test. Initially, a set of boundary conditions were determined that were reasonable and gave good results. The test speed was defined at the inlet and outlet. The half-symmetry cutting plane was defined as a symmetry boundary condition. The surfaces of representing the flat bar were defined with free slip conditions. The rest of the domain walls were also defined with free slip conditions.

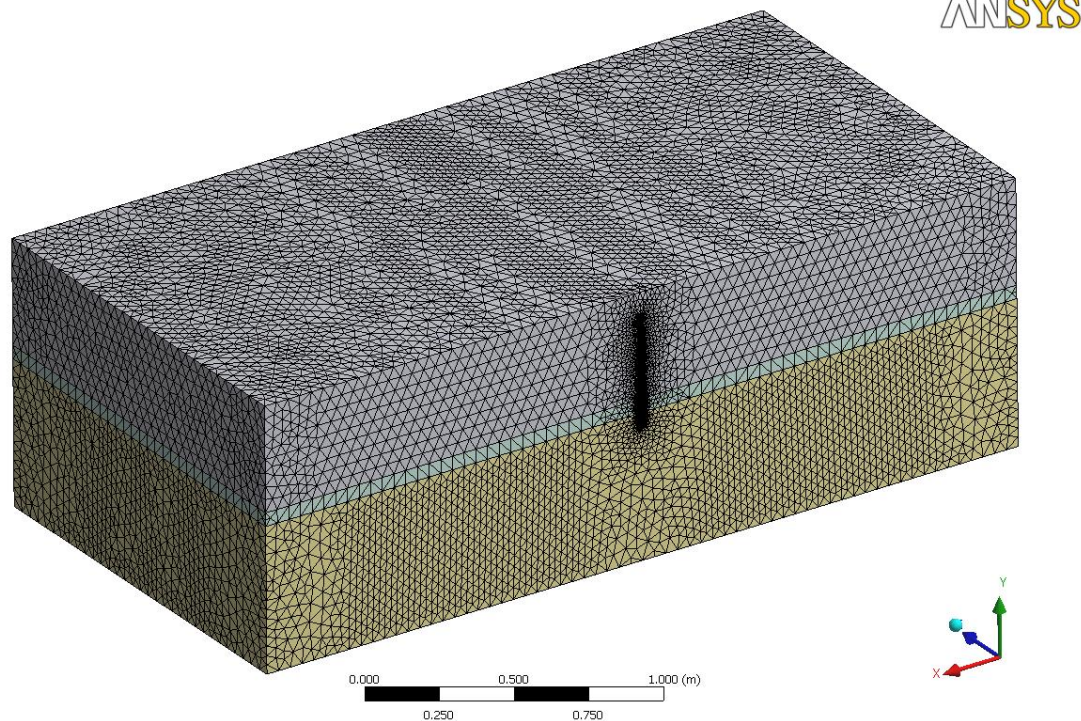


Figure 6.2: Rigid flat bar simulation mesh

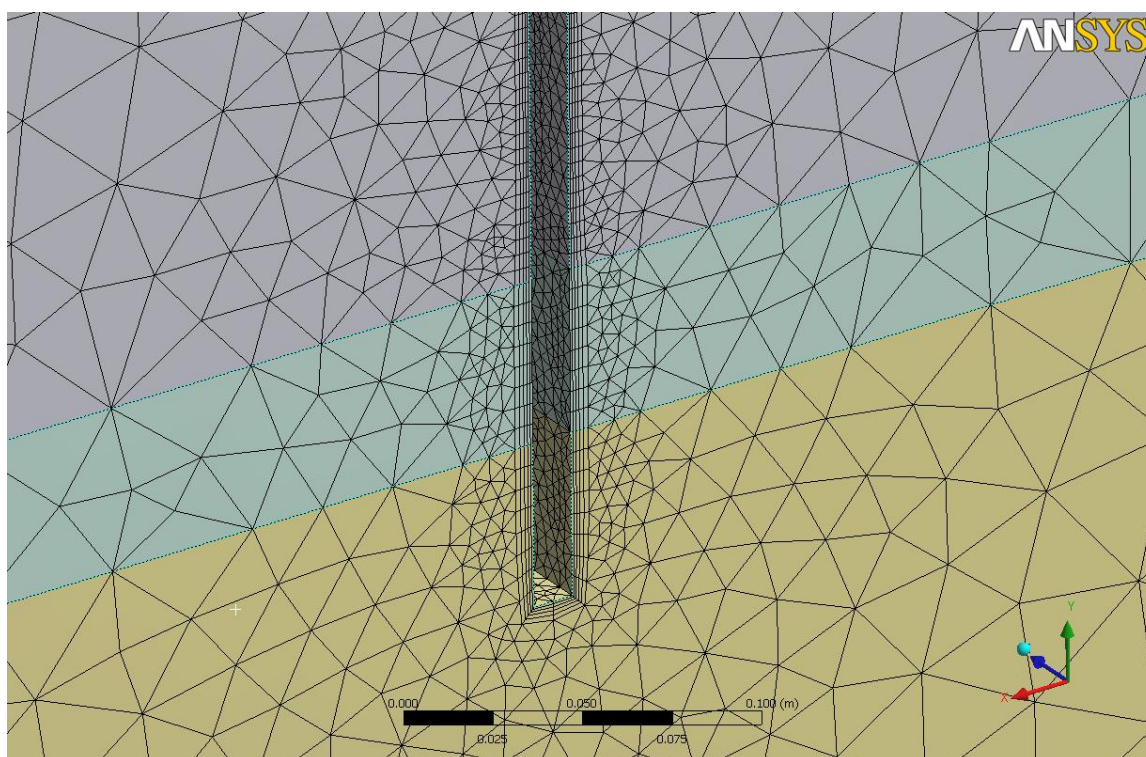


Figure 6.3: Close-up of rigid flat bar mesh

Table 6.1 shows the original development of the boundary conditions and the corresponding results. As the table shows, the results varied greatly depending on how the boundary conditions were defined. The basis for defining the speed at the inlet and outlet was in considering the domain a window moving with the bar through the soil. In such a case the “speed” of the soil moving into the domain would have to equal the speed out of the domain for conservation of mass to be maintained.

After the rigid flat bar simulations were completed, the steady-state field cultivator standard simulations were run. However, the results indicated that the same boundary conditions would not work. So, the boundary conditions were modified in a methodical manner and a new set of boundary conditions were determined. These new boundary conditions were then applied to the rigid flat bar simulations to make sure the conditions were “universal” for the two model types considered in this research.

Table 6.1: Rigid flat bar simulation original parameter table

Analysis Settings	Draft Force		Vertical Force		Max Tool Pressure Measured
	(N)	% Diff.	(N)	% Diff.	
300 iterations, buoyancy density = 1.184 kg/m ³	141	----	36	----	
buoyancy density = dens, pressure stabilized on tool face	1,785	1170%	227	529%	9.531E+05
divide dens/2	1,798	1180%	227	530%	9.586E+05
density = Dens, Rate Limit = 0.00001	1,754	1148%	232	545%	9.727E+05
Made top BC to opening 1 atm	1,788	1172%	220	512%	9.869E+05
change tool to only include front, side, bottom surfaces due to getting suction on back side of tool	crash		crash		crash
visc = visc/2	1,709	1116%	200	457%	9.073E+05
visc = visc, made top BC to opening (static press entrain) 1 atm	946	573%	124	244%	5.370E+05
made top BC to opening (opening pressure entrain) 1 atm	crash		crash		crash
top BC to opening (static press entrain 1 atm), made outlet to opening (static pressure 1 atm)	crash		crash		crash
Top BC to Wall (Free Slip) Inlet = Speed Outlet = Speed	1,709	1116%	15	-58%	8.651E+05
Yield_New = Yield/100	1,554	1006%	10	-71%	
Yield = Yield, Visc = Visc/100	134	-5%	5	-87%	5.782E+04

The final boundary conditions used were different at the outlet and top surfaces. The outlet was defined as a static pressure outlet with 0 Pa pressure. The top surface was defined as an opening, allowing fluid to enter or exit, with a pressure of 0 Pa defined. The amount of compaction and moisture level were accounted for in the material properties. The boundary conditions are illustrated in Figure 6.4.

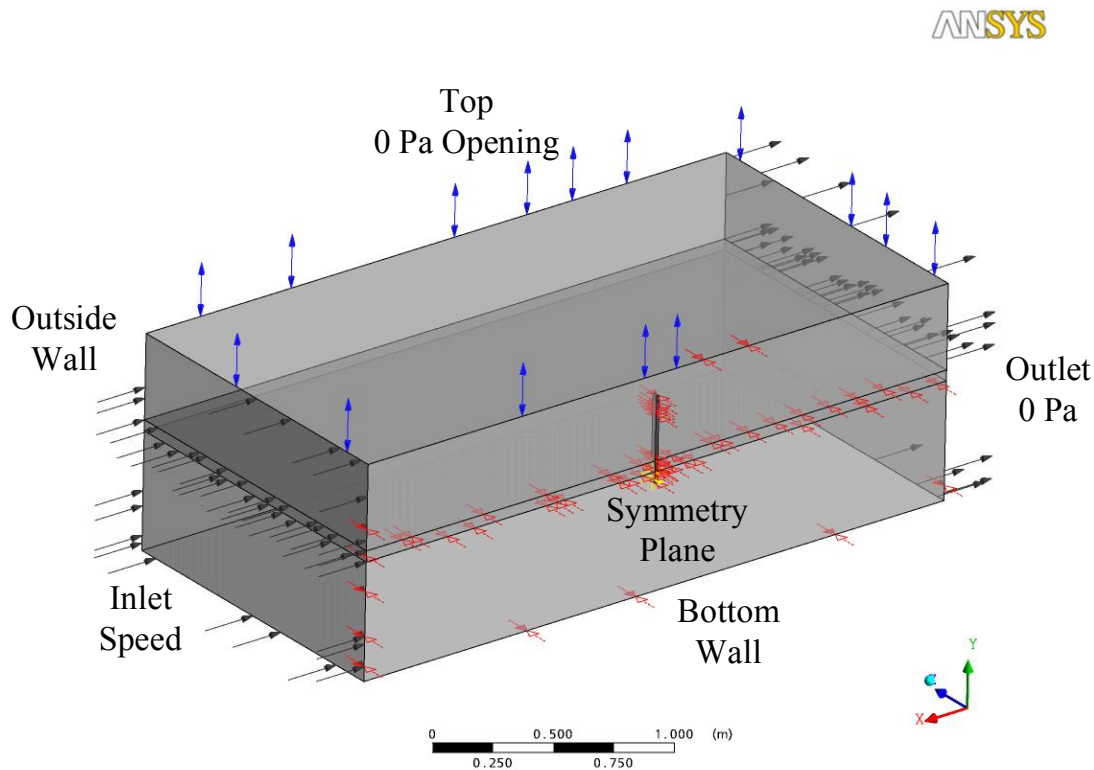


Figure 6.4: Rigid flat bar CFD domain boundary conditions

To implement the Bingham-plastic model into the CFD software, equations were programmed into the software using the CFX expression language (CEL). This is the same method used to verify the material models from Chapter 5. The expressions were then referenced in the CFD material definition for the soil. Air at 20 degrees Celsius was also included in the model from the software fluid library. While running the simulations it became apparent that changes to the material property values would be required to get results that matched the test results. Simulations were also run with the yield strength divided by factors of 2.0, 2.25, and 2.5 but 3.0 showed to provide the best correlation with the lab test results. Ultimately it was found that dividing the viscosity by 100 and the yield strength by a

factor of three yield the best results for both the rigid flat bar and the field cultivator simulations.

A possible reason for this difference in material properties may be due to differences between the material measurement method and the actual tests being simulated. The soil viscometer test was run with the shear vane beneath the soil surface so that the soil was contained and could not expand as failure occurred. The rigid flat bar and field cultivator tests disturbed the soil from the surface down so that soil expansion, dilation, could occur as the soil failed. By confining the soil, the viscometer tests may have forced the soil to appear to be stiff or stronger than if dilation were allowed to occur. Other published soil property data were based on static or near static measurements and were higher in value for both viscosity and strength than those that were measured or used in this dissertation.

Another difference between the viscometer test and the other lab test is the speed of the tests. The soil viscometer test was run at a maximum rotational speed of 1.333 rpm which equates to a shear vane tip speed of 0.004 m/s. This is 700 times slower than the common test speed of 2.68 m/s used in both the rigid flat bar and the field cultivator lab tests.

The simulation was run as a static analysis and launched from the CFX solver manager with parallel processing on a 64 bit Windows workstation with 8 Gb of RAM. The convergence was set at $1e-6$ with the number of iterations limited. Each treatment simulation was run to 100 iterations. Full convergence was not reached by any of the simulations but the forces in the draft direction were monitored during each run and did appear to reach convergence. Figure 6.5 is an example from one simulation to show the convergence of pressure on the bar face. The first two points were on the front side and the third point was on the back side. Figure 6.6 is an example from one simulation to show the convergence of the sum of the forces in the draft (X) direction.

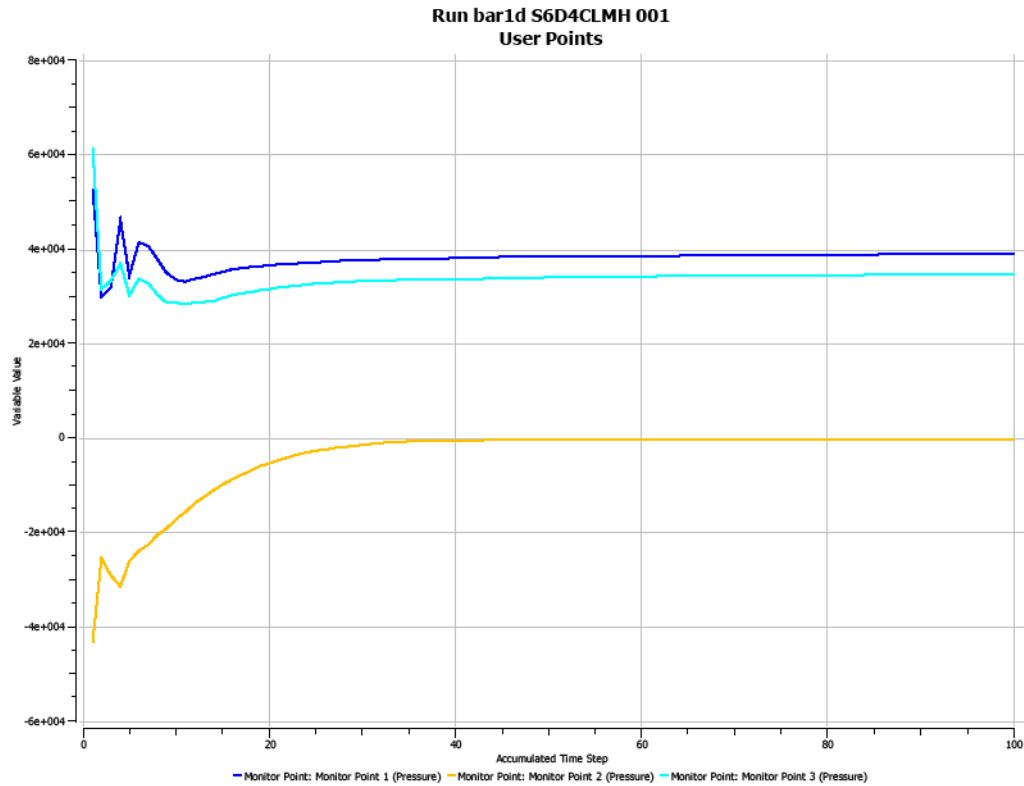


Figure 6.5: Rigid flat bar – example of pressure convergence on front and back of bar

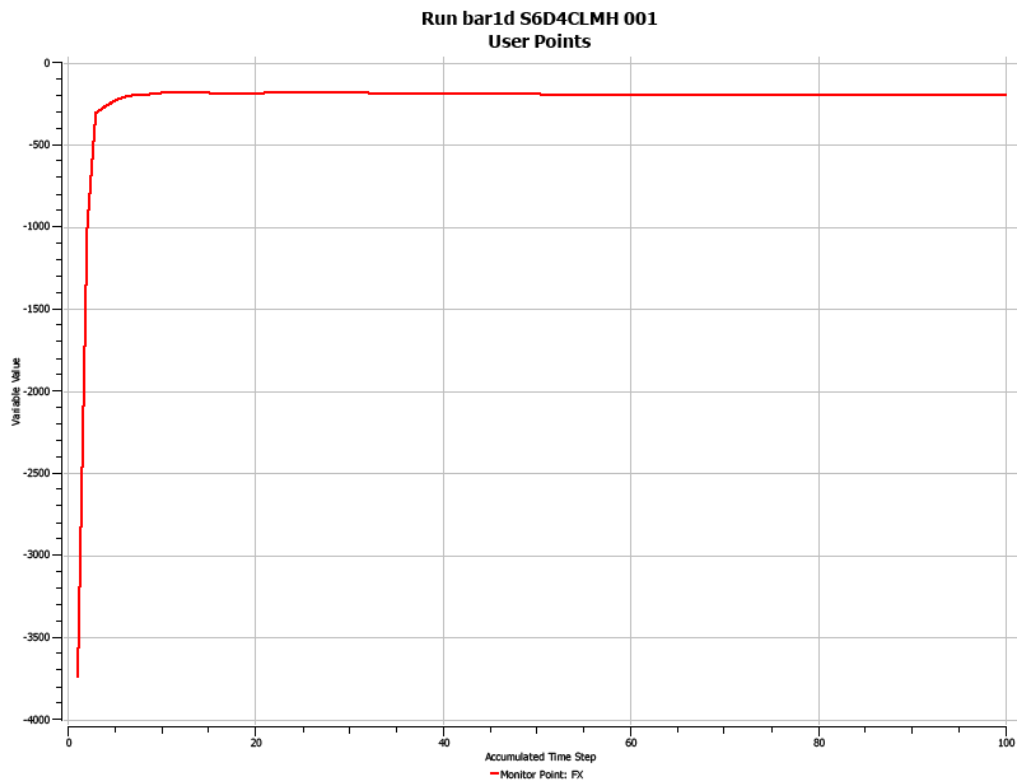


Figure 6.6: Rigid flat bar – example of draft force convergence

6.2 Results

Simulations were run at the twelve treatment levels from the lab test. Results were compared against the average measured draft with the +/- three standard deviations and the predictor equations and are presented in Figure 6.7 and Figure 6.8 with Yield divided by 2.0 and 3.0 respectively. Overall, the simulations were able to capture the trends in the draft loading. With the yield strength divided by 2.0, the predicted draft force fell within the +/- three standard deviations in only five of the twelve treatments.

The predictor equation was within three standard deviations in seven of the twelve treatments. With the yield strength divided by 3.0, nine of the twelve treatment levels, the predicted draft fell within +/- three standard deviations of the measured values. The predictor equation was within three standard deviations in seven of the twelve treatments. Of the three treatments that the predicted draft load did not fall within three standard deviations, one fell on the high side and two fell on the low side.

None of the runs reached the actual defined convergence tolerance over the entire domain. This was attributed to the abrupt interruption in the flow around the flat bar. However, the total draft force did show good convergence. The pressure at points on the front and back of the rigid flat bar were also monitored and also showed convergence. Each simulation took approximately 2.2 hours to run on a Windows 64 bit workstation with 8Gb of memory.

Figure 6.9 and Figure 6.10 show the density distribution in the domain for treatment D4S6L. An isosurface was defined at $1,200 \text{ kg/m}^3$ to show the soil surface and buildup on the front of the rigid flat bar. Figure 6.11 shows the pressure distribution on the flat bar with the maximum pressure of 89.07 kPa. The pressure value and distribution are comparable to results found by Karamakar and Kushwaha (2005b). Figure 6.12 shows the pressure in the soil on the surface. The distance in the fore-aft direction from the bar to where the pressure is equal to the strength of the soil is the predicted distance ahead of the bar that the soil would fail. The distance was measured from the pressure plots and included in Table 6.2. Table 6.2 summarizes the predicted maximum pressures on the bar face, and the predicted soil failure distance from the bar face.

Comparisons were attempted to the lab test data by measuring the distance from the flat bar face to the failure surface by taking measurements from the overhead recorded videos. There were only two runs where the failed soil did not block the view of the soil failure ahead of the tool. Images from the video are shown in Figures 6.13 and 6.14. The figures have been annotated to show the distance from the face of the bar to the edge of the soil failure surface. Figure 6.13 shows the failure distance of 114 mm compared with the predicted distance of 104 mm for the treatment with the speed of 0.89 m/s, depth of 102 mm, and compaction of 1,100 kPa. Figure 6.14 shows the failure distance of 127 mm compared with the predicted distance of 113 mm for the treatment with the speed of 1.79 m/s, depth of 102 mm, and compaction of 1,100 kPa.

Table 6.2: Rigid flat bar simulation max pressure and failure distance summary

Speed (m/s)	Depth (mm)	Compaction (kPa)	Predicted Max Pres (kPa)	Predicted Failure (mm)
0.89	51	200	34	33
1.79	51	200	55	89
2.68	51	200	73	100
0.89	102	200	37	24
1.79	102	200	60	111
2.68	102	200	79	133
0.89	51	1,100	134	78
1.79	51	1,100	179	87
2.68	51	1,100	220	92
0.89	102	1,100	149	104
1.79	102	1,100	197	113
2.68	102	1,100	240	117

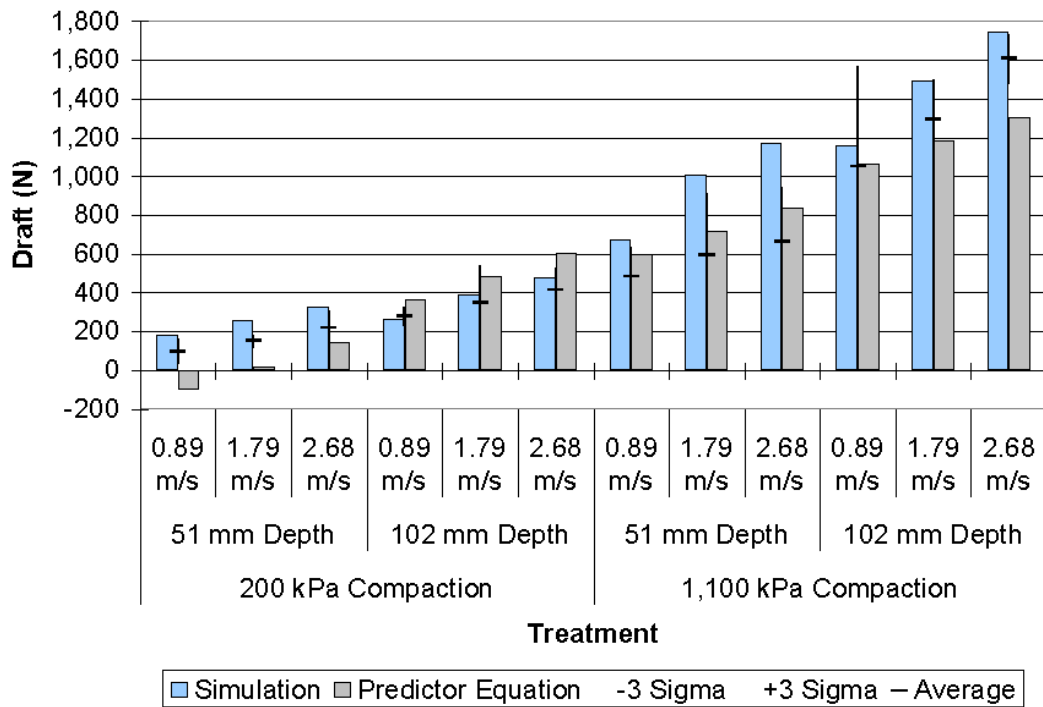


Figure 6.7: Rigid flat bar simulation – predicted draft by treatment with Yield/2.0 compared to measured average draft force and +/- 3 standard deviations

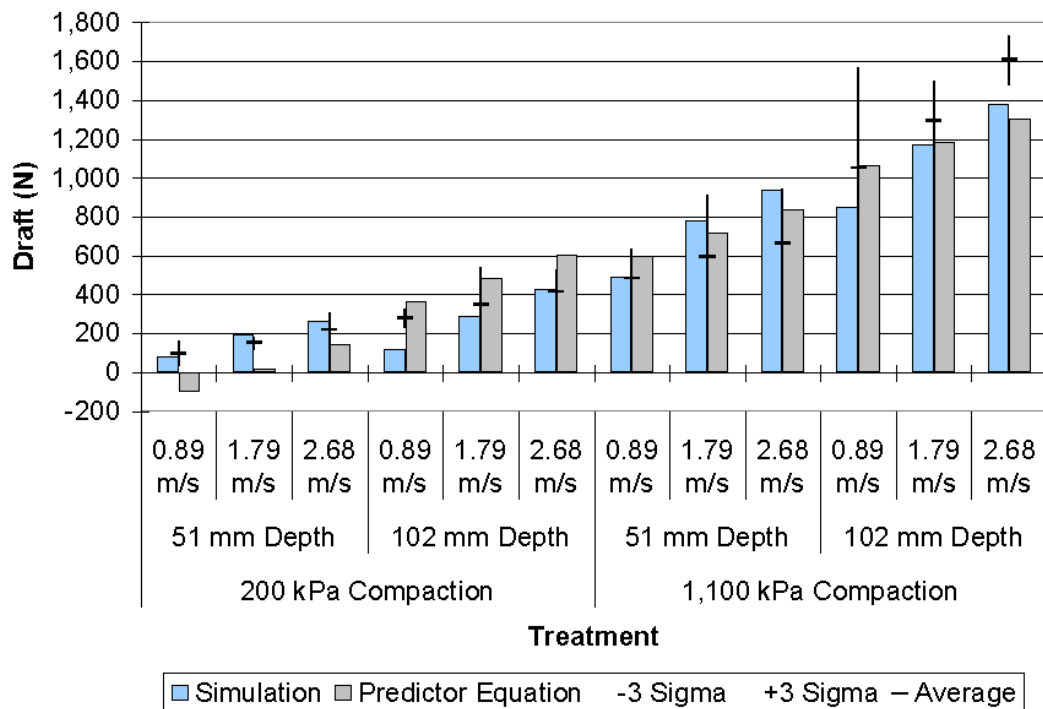


Figure 6.8: Rigid flat bar simulation – predicted draft by treatment with Yield/3.0 compared to measured average draft force and +/- 3 standard deviations

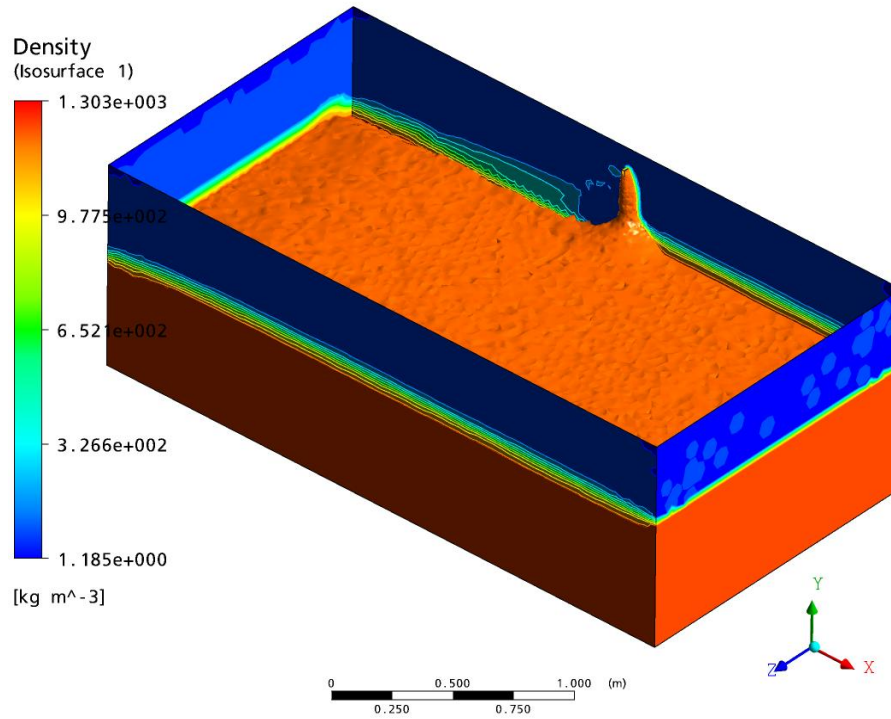


Figure 6.9: Rigid flat bar simulation – 2.68 m/s, 102mm depth, low compaction (200 kPa) - domain density

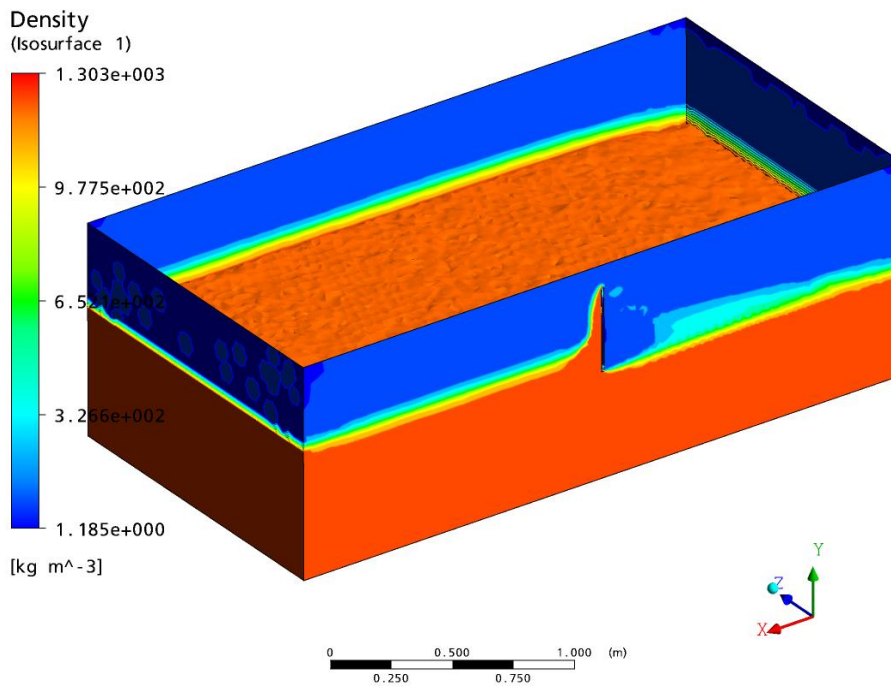


Figure 6.10: Rigid flat bar simulation – 2.68 m/s, 102mm depth, low compaction (200 kPa) - domain density

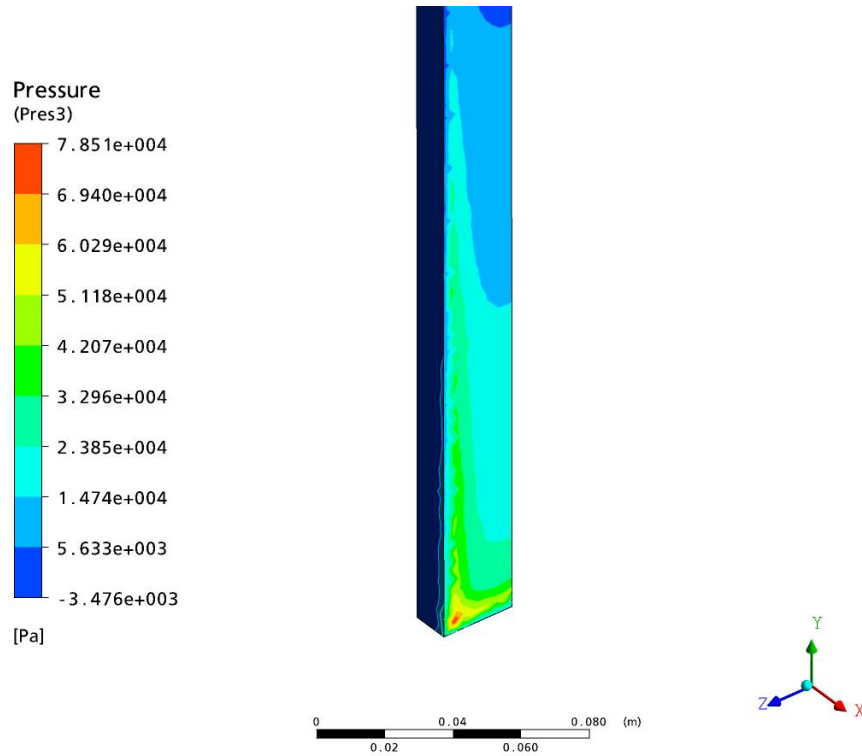


Figure 6.11: Rigid flat bar simulation – 2.68 m/s, 102mm depth, low compaction (200 kPa) –pressure on flat bar

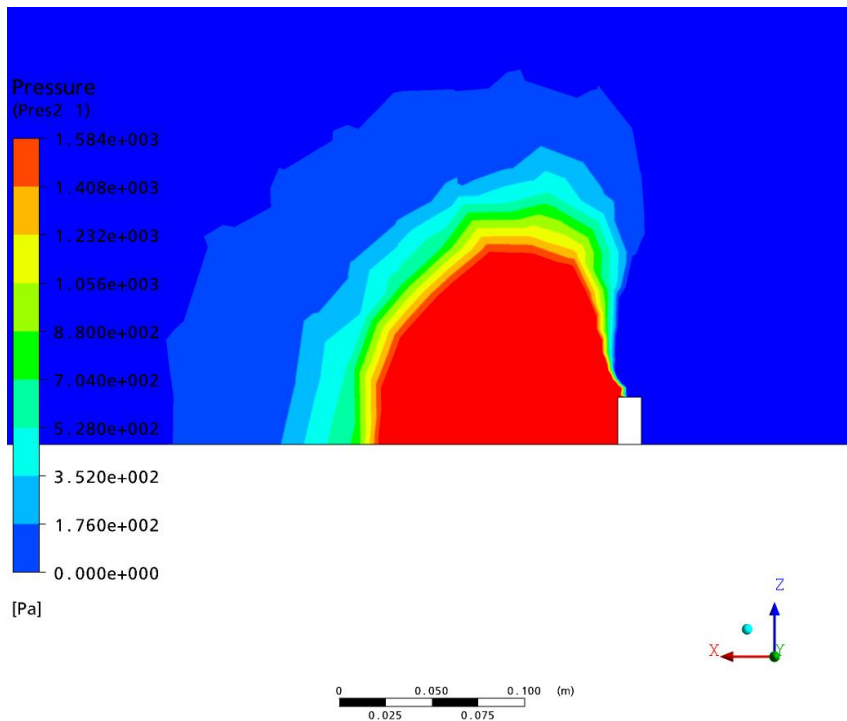


Figure 6.12: Rigid flat bar simulation – 2.68 m/s, 102mm depth, low compaction (200 kPa) soil pressure at the surface (top view)

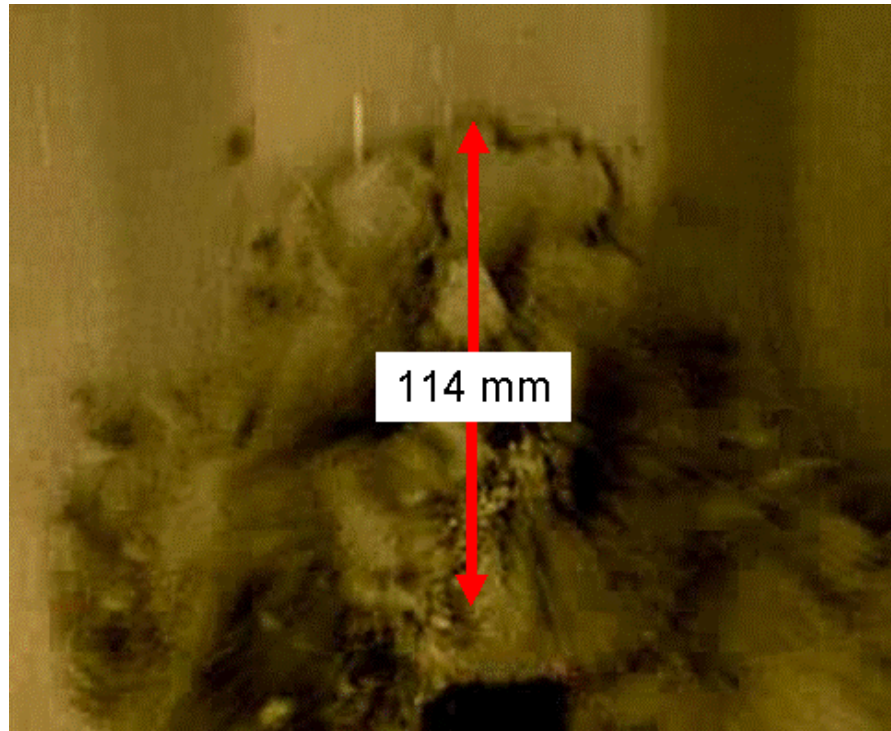


Figure 6.13: Rigid flat bar failure distance – 0.89 m/s, 102mm depth, high compaction (1,100 kPa)

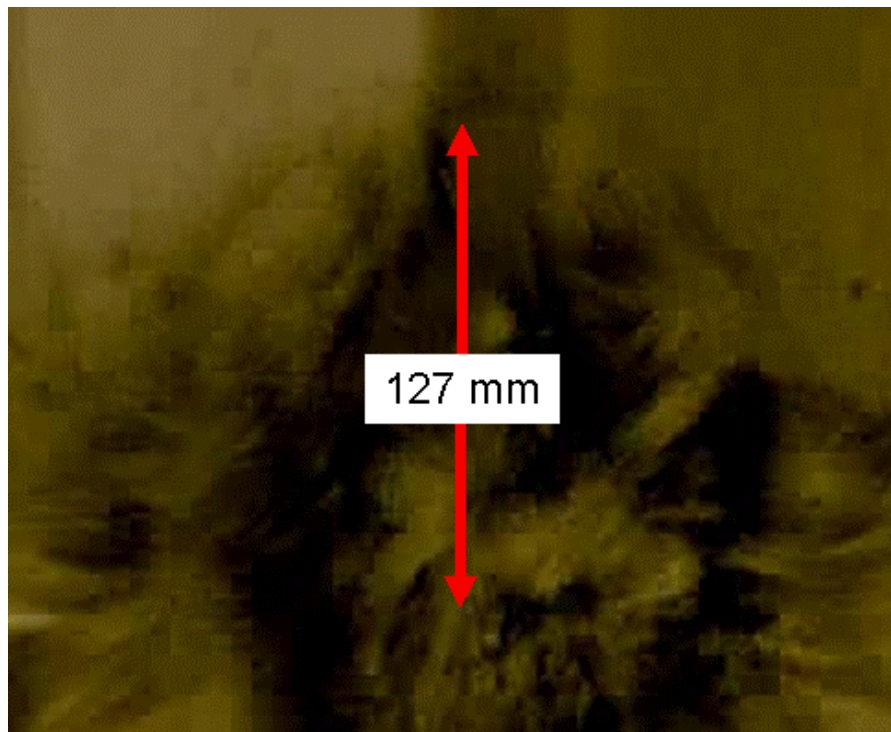


Figure 6.14: Rigid flat bar failure distance – 1.79 m/s, 102mm depth, high compaction (1,100 kPa)

6.3 Conclusions

A series of steady-state CFD simulations were run and compared to the soil bin results for the rigid flat bar. Overall, the simulations were able to show the trends in the draft loading. In nine of the twelve treatment levels, the predicted draft force fell within three standard deviations of the measured data.

Adjustments were required to the soil material parameters for the predicted forces to correlate with the measured data by dividing the viscosity by a factor of 100 and the yield strength by a factor of three. These adjustments were determined in an iterative process based on the field cultivator standard and the rigid flat bar simulations. There are several possibilities for this: the soil property measurement test may not be appropriate for this application, the measured soil properties are not good with viscosity not being a factor and dividing the shear strength by a factor of three was coincidental, or the simulation does not adequately represent the actual conditions being replicated. Running the simulation with viscosity removed from the Bingham-plastic model would clarify the impact of viscosity. Running the simulation with different bar geometries would help clarify the appropriateness of the soil parameters that were used.

An initial set of boundary conditions were developed based on trying various combinations and comparing the predicted draft and vertical forces with the average measured values. However, when the boundary conditions were applied to the field cultivator standard simulation the results did not match. Additional iterations were required and developed. The boundary conditions were verified in both simulations and across a range of operating conditions.

7. FIELD CULTIVATOR STANDARD SIMULATION

The main objective of this research was to predict the dynamic loads on a spring reset field cultivator standard. To accomplish this, both steady-state CFD and two-way interactive transient FEA-CFD analyses were run and the results were compared with the lab test results from chapter 4. The models were half-symmetry to reduce the model size and run times. The geometry was simplified to reduce small features that were not conducive to the meshing for both the FEA and CFD domains. Over the course of this research many iterations were run to determine the combination of parameters and boundary conditions that yielded the best and most consistent results.

7.1 Model

The structural model included the bucket, spring, pivot casting, pin, shank, adapter, and sweep. The bucket, pivot casting, pin, shank, adapter, and sweep were modeled with solid 10-node tetrahedron elements. The sweep, shank, and adapter were merged into one part in ANSYS Design Modeler so that there were no voids between the parts as required for the CFD model. The spring was modeled with a linear spring element with a spring rate of 22,766 N/m. The no-load position of the standard compresses the spring such that there is a preload of about 1,890 N which was included in the model. Figure 7.1 shows the meshed model with the boundary conditions.

A half-symmetry CFD domain was created around the structural model to simulate air and soil flowing by the standard. The CFD domain was 2.1 m wide, 4.5 m long, and 1.25 m high with 0.5 m below the bottom of the sweep. Figure 7.2 shows the CFD domain with the major dimensions. The domain was meshed with the ANSYS CFX mesher using tetrahedron elements. The domain mesh had 1,030,606 elements and 737,561 nodes. An inflation layer of elements was created on the face of the sweep and shank. Figure 7.3 shows the mesh of the entire domain. Figure 7.4 **Error! Reference source not found.** shows a close-up of the mesh around the field cultivator standard with the inflation layers.

Mesh
9/19/2007 8:31 AM

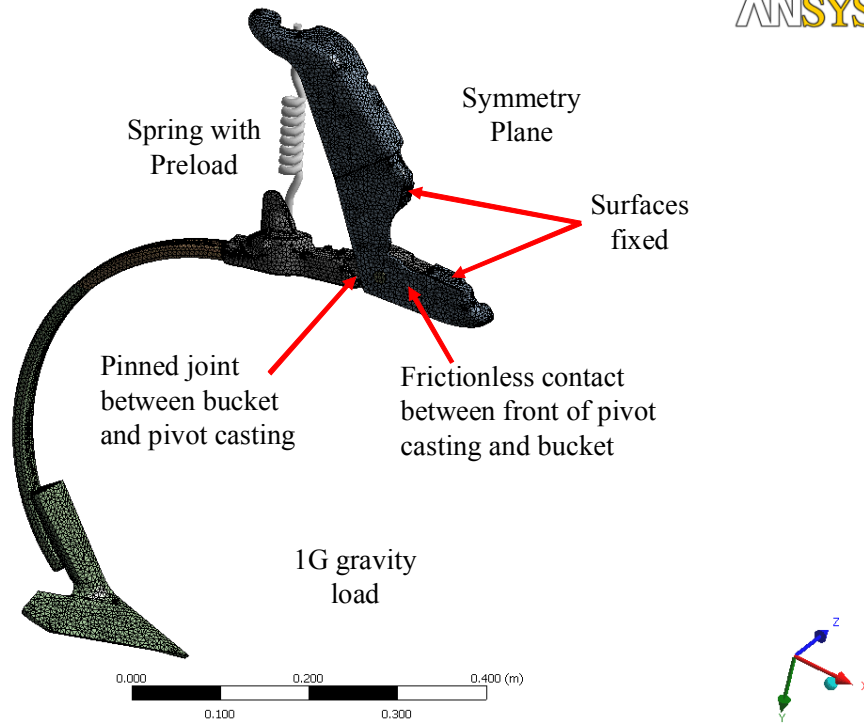


Figure 7.1: Field cultivator structural model

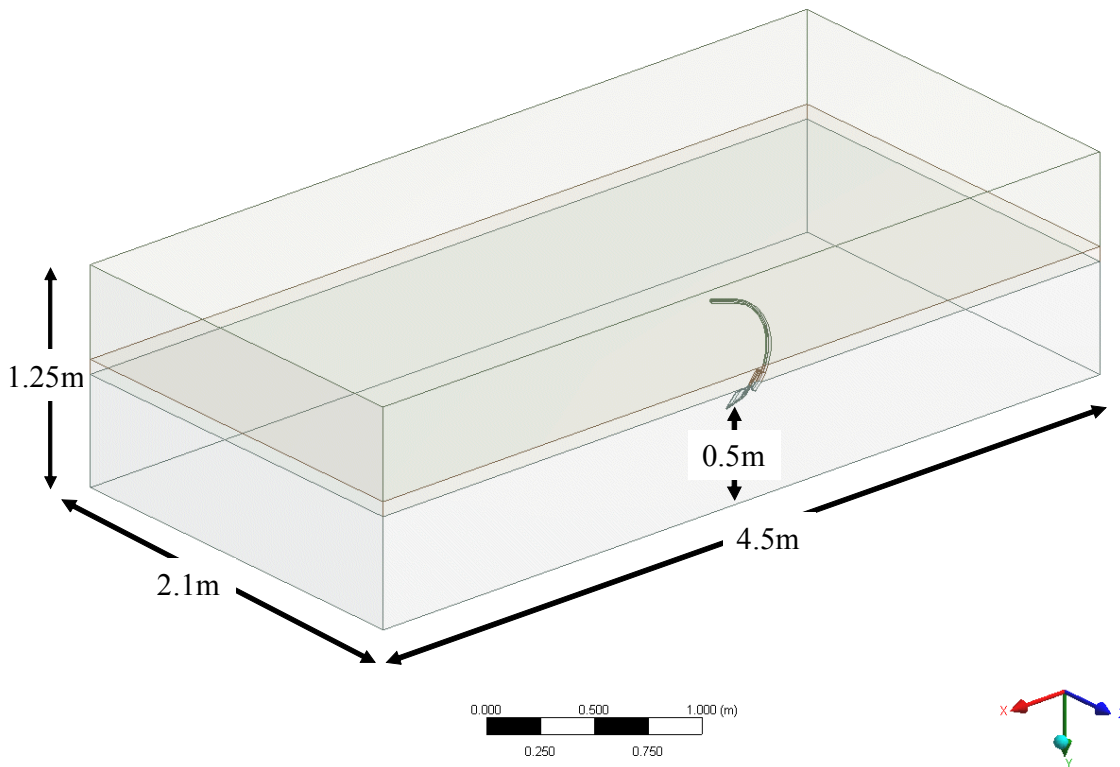


Figure 7.2: Field cultivator CFD domain

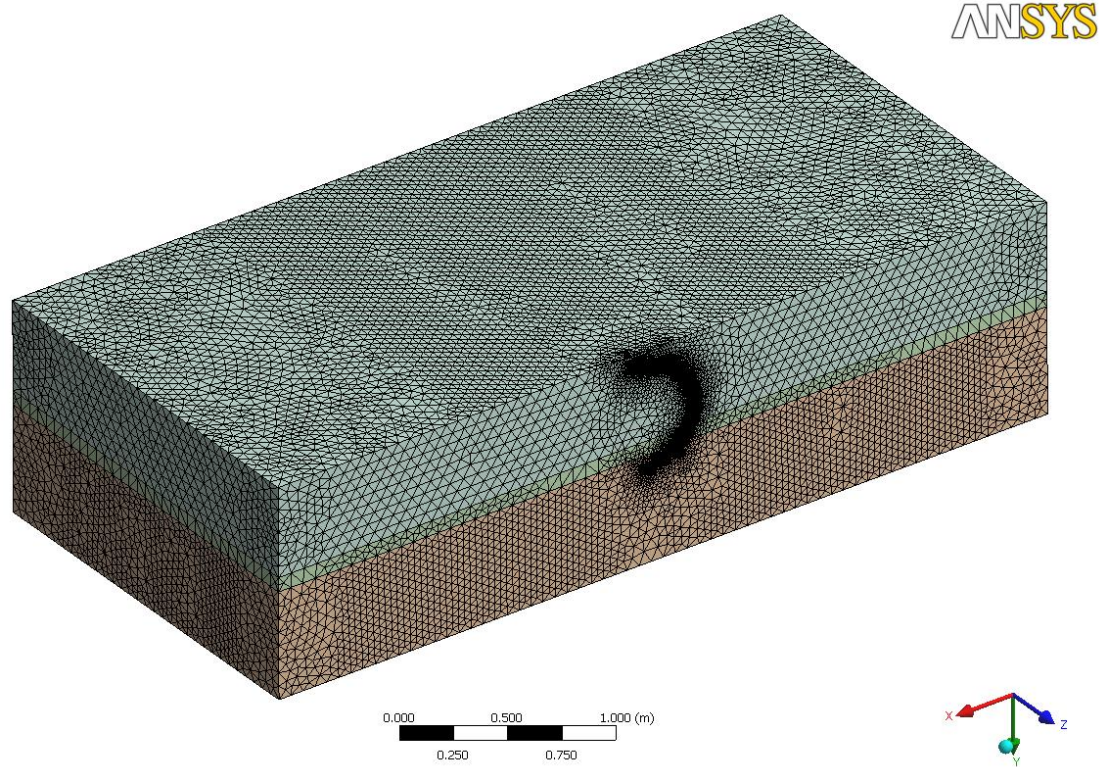


Figure 7.3: Field cultivator standard CFD domain mesh

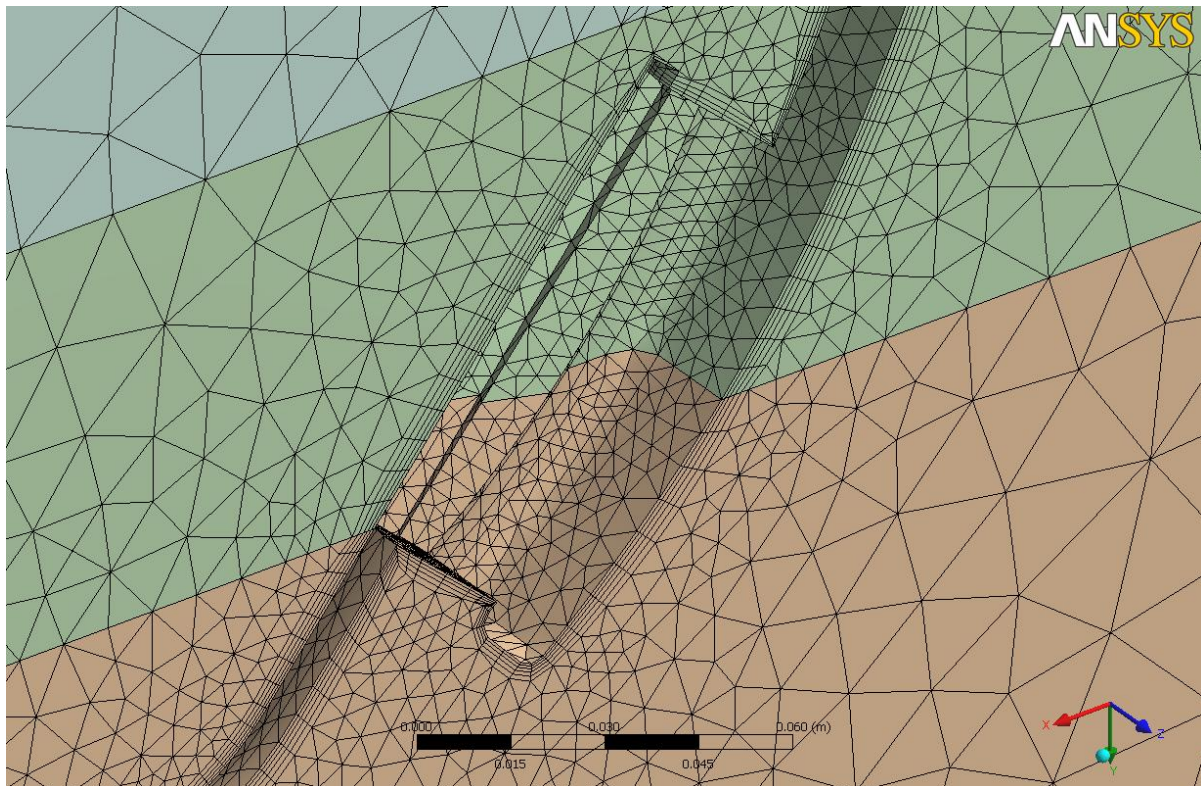


Figure 7.4: Field cultivator standard CFD domain mesh close-up

Many different parameters and boundary condition combinations were considered in this research. Table 7.1 lists many of the various combinations that were tried and the generalized outcome. The list of parameters that were adjusted included: viscosity, static versus transient analysis, number of iterations per time step, and number of time steps (transient analysis only). Initially, steady-state CFD only analyses were carried out to determine which combination of parameters and boundary conditions gave the best results. The number of iterations per step was set at 100 with the convergence set at $1e-6$. The pressure at several locations on the sweep and the total force in the draft and vertical directions were also monitored during the simulations. Figure 7.5 shows the CFD domain with the boundary conditions labeled.

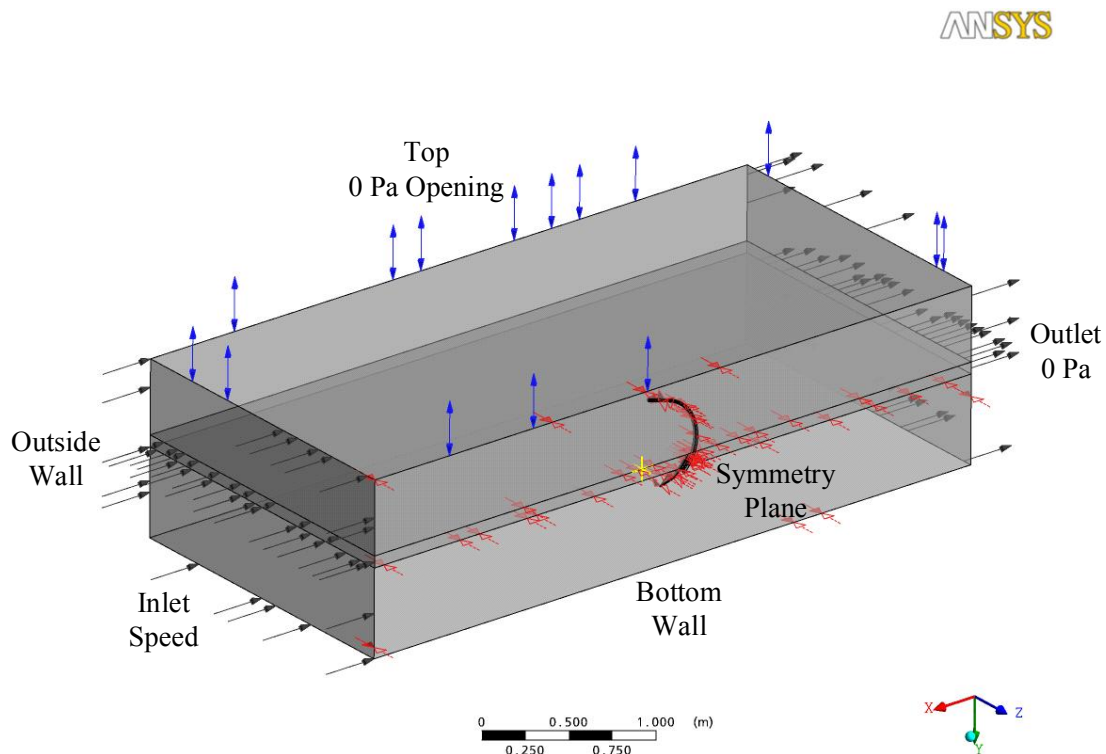


Figure 7.5: Field cultivator computational fluid domain boundary conditions

Different boundary conditions were tried on the inlet, outlet, and top surfaces to the domain. The inlet was defined with a specified pressure and with a specified speed. Ultimately, defining the speed at the inlet proved to be the best. At the outlet, definitions specifying the pressure or the speed were considered, as well as an opening. The best definition for the outlet was with a specified pressure with the supercritical option turned on

and an air pressure of 0 Pa. The top surface of the domain was considered as a wall with free slip and as an opening. Defining the top surface as an opening with a specified pressure of 0 Pa proved to be the with the inlet and outlet combinations. The bottom surface and outside surface were defined as walls with free slip. The sweep and shank were also defined as walls with free slip. The symmetry plane was defined as such.

Other methods were used to evaluate the results separately, from comparing the predicted forces. For example, some combinations of parameters and boundary conditions created suction, or negative pressure, on the back side of the sweep and shank which is not physically possible. Another method was to graph the pressures on the domain to see if there was any interaction between the soil disturbance around the sweep and shank and with the domain boundaries. This was a test to determine if the model domain was large enough. An example of this is shown later.

The material properties from Chapter 2 were modified as discussed in Chapter 6. Based on the results from the simulations and methodically varying the viscosity and yield strength, the viscosity was divided by a factor of 100 and the yield strength was divided by a factor of three. These same changes were shown to be appropriate for the rigid flat bar.

The effect on predicted draft and vertical forces was also examined in relation to mesh density and solver parameters. Table 7.2 shows the steady-state results of the same model of the 178 mm sweep at 2.68 m/s, 152 mm depth, low compaction (200 kPa), and 8.3% d.b. moisture levels. The table shows the effects of increasing the mesh size on the sweep and shank, the number of iterations, and whether the simulation was solved serially, one processor, or in parallel on two processors. The first column represents the baseline and how the results published in this dissertation were run. Figure 7.6 shows the locations on the model where forces were recorded from the CFD analysis. The shaded cells in the upper portion of Table 7.2 highlight what factor(s) was changed.

The results indicate that going from free-slip to no-slip wall conditions on the sweep, adapter, and shank has a large effect. The change is clearly seen in the draft force results as the pressure forces were reduced but the viscous forces increase considerably. The effect on the vertical forces was also dramatic. The viscous portion of the vertical force was negative or created suction.

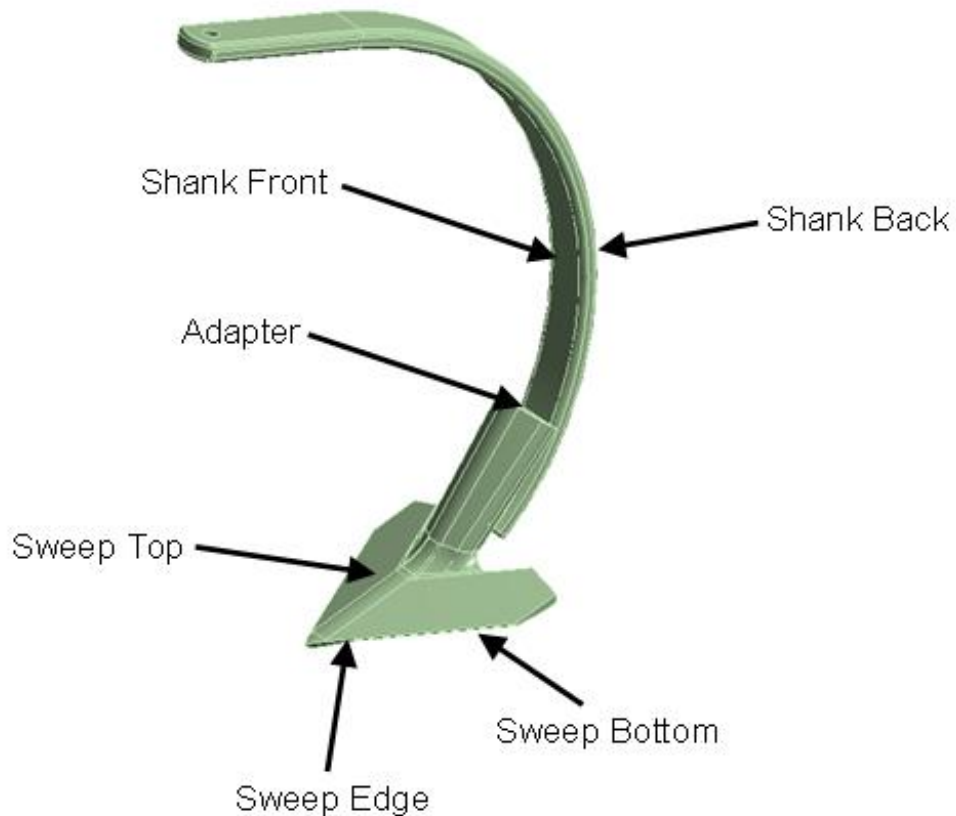


Figure 7.6: Locations monitored for CFD predicted forces

Increasing the number of iterations from 100 to 500 also impacted the predicted force results. Both the predicted draft and vertical forces were lower and the convergence of the forces was better. The use of 100 iterations for the published results was based trying to reach a balance between good convergence in all treatment conditions and run time.

Increasing the mesh density from between 0.003 to 0.006 m down to 0.002 m decreased the draft force prediction by three percent, while the vertical force prediction increased by three percent. Increasing the number of processors from one to two caused a one percent decrease in the predicted draft force and a ten percent increase in the predicted vertical force. Lowering the mesh size to just 0.001 m and using two processors resulted in a one percent increase in the draft force and a ten percent increase in the vertical force.

Table 7.2: Effects of mesh density and solver parameters on predicted draft and vertical forces

Mesh Size (m)	0.003-0.006			0.003-0.006			0.002			0.002			0.001		
	Force (N)	Draft	Vert	Force (N)	Draft	Vert	Force (N)	Draft	Vert	Force (N)	Draft	Vert	Force (N)	Draft	Vert
#Elements	1,030,606	1,030,606	1,030,606	1,030,606	1,030,606	1,030,606	1,595,368	1,595,368	1,595,368	1,595,368	1,595,368	3,825,278	3,825,278	3,825,278	3,825,278
Surface Condition	free-slip	no-slip	free-slip	no-slip	free-slip										
Viscosity	100	100	100	100	100	100	100	100	100	100	100	100	100	100	100
Yield Strength	100	100	100	100	100	100	100	100	100	100	100	100	100	100	100
# of iterations	1	1	1	1	1	500	1	1	1	1	1	2	2	2	2
#Processors	1	1	1	1	1	1	1	1	1	1	1	2	2	2	2
Run Time (hrs)	3.2	3.2	3.2	3.2	3.2	16.0	5.1	5.1	5.1	5.1	5.1	4.0	4.0	4.0	8.5
Pressure Force	Force (N)	Draft	Vert	Force (N)	Draft	Vert	Force (N)	Draft	Vert	Force (N)	Draft	Vert	Force (N)	Draft	Vert
Sweep Edge	11.4	6.2	-7.6	10.0	6.2	-4.6	18.6	18.6	-13.1	19.1	19.1	-13.3	25.8	25.8	-17.8
Sweep Top	58.5	43.7	95.7	58.4	43.7	77.7	59.8	59.8	94.7	60.4	60.4	95.6	59.9	59.9	93.1
Sweep Bottom	18.2	2.1	59.8	0.6	2.1	4.4	17.0	17.0	64.1	17.9	17.9	66.0	21.7	21.7	82.3
Adapter	0.1	0.2	0.8	0.2	0.2	0.5	0.7	0.7	0.5	0.9	0.9	0.5	2.2	2.2	-0.1
Shank Front	28.3	29.5	1.4	29.6	29.5	6.8	29.2	29.2	5.3	30.0	30.0	5.7	28.3	28.3	4.1
Shank Back	2.9	1.9	1.3	1.7	1.9	0.9	7.6	7.6	3.4	8.8	8.8	4.2	4.8	4.8	3.0
Sub-Total	119.4	83.6	151.4	100.5	83.6	85.7	132.9	132.9	154.9	137.1	137.1	158.7	142.7	142.7	164.6
Viscous Force	Force (N)	Draft	Vert	Force (N)	Draft	Vert	Force (N)	Draft	Vert	Force (N)	Draft	Vert	Force (N)	Draft	Vert
Sweep Edge	56.3	39.4	-33.6	56.2	39.4	-2.3	43.0	43.0	-27.5	42.9	42.9	-27.4	36.0	36.0	-21.4
Sweep Top	20.6	127.2	20.8	21.2	127.2	-33.3	19.3	19.3	25.3	19.3	19.3	25.4	17.6	17.6	25.6
Sweep Bottom	12.1	41.0	33.4	10.2	41.0	4.6	9.4	9.4	25.9	9.6	9.6	26.6	8.6	8.6	19.2
Adapter	0.0	0.2	0.0	0.0	0.2	0.2	0.2	0.2	-0.2	0.0	0.0	0.0	0.5	0.5	0.2
Shank Front	25.0	32.5	4.5	18.3	32.5	1.9	20.5	20.5	4.1	20.1	20.1	4.9	28.3	28.3	6.7
Shank Back	2.6	0.4	1.3	1.6	0.4	0.2	2.6	2.6	0.9	4.0	4.0	1.1	3.6	3.6	1.2
Sub-Total	116.6	240.7	26.4	107.5	240.7	-28.7	95.0	95.0	28.5	95.9	95.9	30.6	94.6	94.6	31.5
Total	236.0	324.3	177.8	208.0	324.3	57.0	227.9	227.9	183.4	233.0	233.0	189.3	237.3	237.3	196.1
% Diff.	----	37%	----	-12%	37%	-68%	-3%	-3%	3%	-1%	-1%	6%	1%	1%	10%

Table 7.3 shows the effect of the soil properties on the predicted draft and vertical forces. The table shows how changes to either viscosity, yield strength, or both. Although the soil property measurement test indicated that the soil may not be viscous but rather elastic, the steady-state CFD results in the table show that viscosity does significantly impact the results. Using both the viscosity and yield strength as measured resulted in significantly higher predicted draft and vertical forces. Removing viscosity from the soil material model and using the soil yield strength as measured resulted in a 26 percent reduction in predicted draft but only a modest four percent increase in predicted vertical force. Using the modified yield strength and no viscosity resulted in a 73 percent reduction in predicted draft force and a 55 percent reduction in the predicted vertical force.

Table 7.3: Effect of soil properties on predicted draft and vertical forces

Mesh Size (m)	0.003-0.006		0.003-0.006		0.003-0.006		0.003-0.006	
# Elements	1,030,606		1,030,606		1,030,606		1,030,606	
Surface Condition	free-slip		free-slip		free-slip		free-slip	
Viscosity	Visc/100		Visc/1		Visc=0		Visc=0	
Yield Strength	Yield/3		Yield/1		Yield/1		Yield/3	
# of iterations	100		100		100		100	
# Processors	1		2		2		2	
Run Time (hrs)	3.2		1.7		2.2		2.3	
Pressure Force	Draft Force (N)	Vert Force (N)						
Sweep Edge	11.4	-7.6	544.1	-333.5	8.4	-6.6	3.6	-2.6
Sweep Top	58.5	95.7	1,697.8	2,291.9	87.6	173.3	34.6	70.8
Sweep Bottom	18.2	59.8	317.7	717.9	0.5	-1.7	1.0	2.3
Adapter	0.1	0.8	70.0	1.7	0.2	0.1	0.1	0.1
Shank Front	28.3	1.4	1,956.3	153.8	39.2	2.6	9.1	1.2
Shank Back	2.9	1.3	1,447.4	368.8	2.9	0.4	1.3	0.6
Sub-Total	119.4	151.4	6,033.3	3,200.6	138.8	168.1	49.7	72.4
Viscous Force	Draft Force (N)	Vert Force (N)						
Sweep Edge	56.3	-33.6	3,215.7	-1,680.8	11.3	-8.8	3.9	-3.0
Sweep Top	20.6	20.8	845.9	714.7	16.5	11.1	6.8	7.1
Sweep Bottom	12.1	33.4	343.8	928.3	1.8	11.1	0.7	4.0
Adapter	0.0	0.0	8.3	8.1	-0.1	0.1	0.0	0.0
Shank Front	25.0	4.5	1,814.2	363.6	8.5	1.4	2.1	0.3
Shank Back	2.6	1.3	572.8	151.4	-2.9	1.6	0.2	0.0
Sub-Total	116.6	26.4	6,800.7	485.3	35.1	16.5	13.7	8.4
Total	236.0	177.8	12,834.0	3,685.9	173.9	184.6	63.4	80.8
% Diff.	-----	-----	5338%	1973%	-26%	4%	-73%	-55%

7.2 Modal Analysis

A modal analysis was run in ANSYS Workbench v11.0 to determine how well the structural model matched the stiffness of the actual field cultivator standard. The analysis was set up as two steps. In the first step, a static structural analysis was run to apply the spring preload and gravity loading to the structural model. Then the modal analysis was run on the preloaded model. The measured natural frequency from the testing presented in Chapter 4 was 22.6 Hz and the predicted value from the modal analysis was 19.2 Hz. Figure 7.7 shows the displacements of the natural frequency of the model.

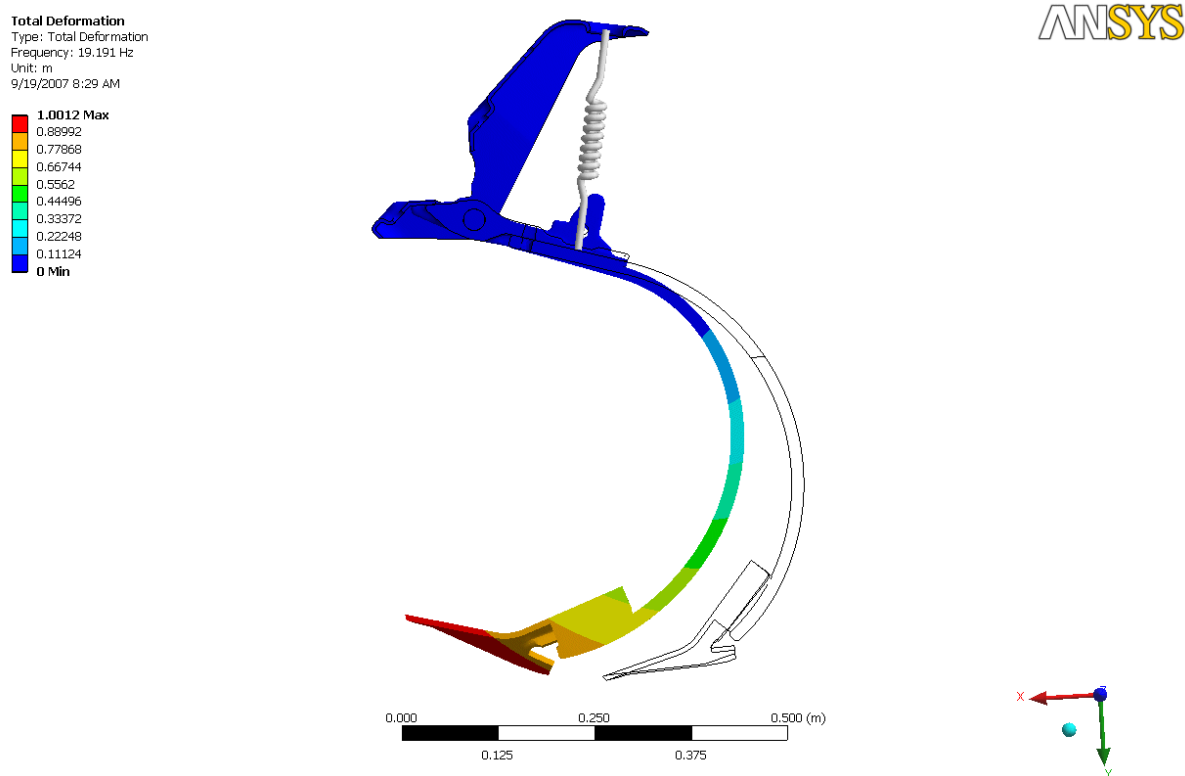


Figure 7.7: Field cultivator modal analysis – deformation

7.3 Steady-State CFD Only Results

Initially, only a steady-state CFD analysis was run to verify the boundary conditions and soil properties. Simulations were run to compare with the field cultivator test results in Chapter 4. Simulations were run for both of the sweep sizes and the same soil, speed, and

depth conditions. From the simulations the pressure was monitored at several locations on the sweep. In addition, the draft and vertical forces were monitored.

Several results are provided as an example from one steady-state CFD simulation involving a 178mm sweep operating at 152mm depth at the 8.3% d.b. moisture level and 1,100 kPa compaction levels. Figure 7.8 shows an example of the draft and vertical reaction force convergence throughout a steady-state simulation. Figure 7.9 show an example of the pressure convergence at three locations on the face of the sweep throughout the same steady-state simulation. Figure 7.10 and Figure 7.11 show density plots with an iso-surface created to clarify the surface of the soil. The figures show the soil flowing up the sweep and shank, as well as the trough formed behind the sweep and shank. Figure 7.12 and Figure 7.13 show the pressure distribution on the domain boundary. The fringe scale is set so that areas in red are above the modified yield strength of the soil to show where the soil would be flowing. Figure 7.13 shows a low pressure region between the sweep and the shank. This low pressure region occurs because the top of the sweep is higher than the adapter that connects the sweep to the shank and no soil flow occurs in this area.

Figure 7.14 shows the pressure distribution on the sweep and shank. The figure shows that the highest pressure occurs on the leading edge of the sweep. High pressures also occur at various locations on the sweep and shank. Figure 7.15 is a photo of a new and worn 254 mm sweep. Comparing Figure 7.14 with Figure 7.15 shows that the high pressure locations match up well with the locations that show the most wear on the sweep.

The draft and vertical forces predicted from the steady-state results were compared with the measured average and +/- three standard deviations. Figure 7.16 through Figure 7.21 show the draft and vertical force results for the treatments run with the 128 mm sweep at 0.89, 2.68, and 4.47 m/s. Figure 7.22 and Figure 7.23 show the draft and vertical force results for the 254 mm sweep at 2.68 m/s.

Overall, the results for the steady-state simulations compared well with the measured data. The results indicate that steady-state simulations can be used to compare sweep and shank geometry, predict the forces, and possibly predict high wear locations. A benefit of the steady-state simulations is simplified setup and reduced run time compared with the transient two-way fluid-structure interaction.

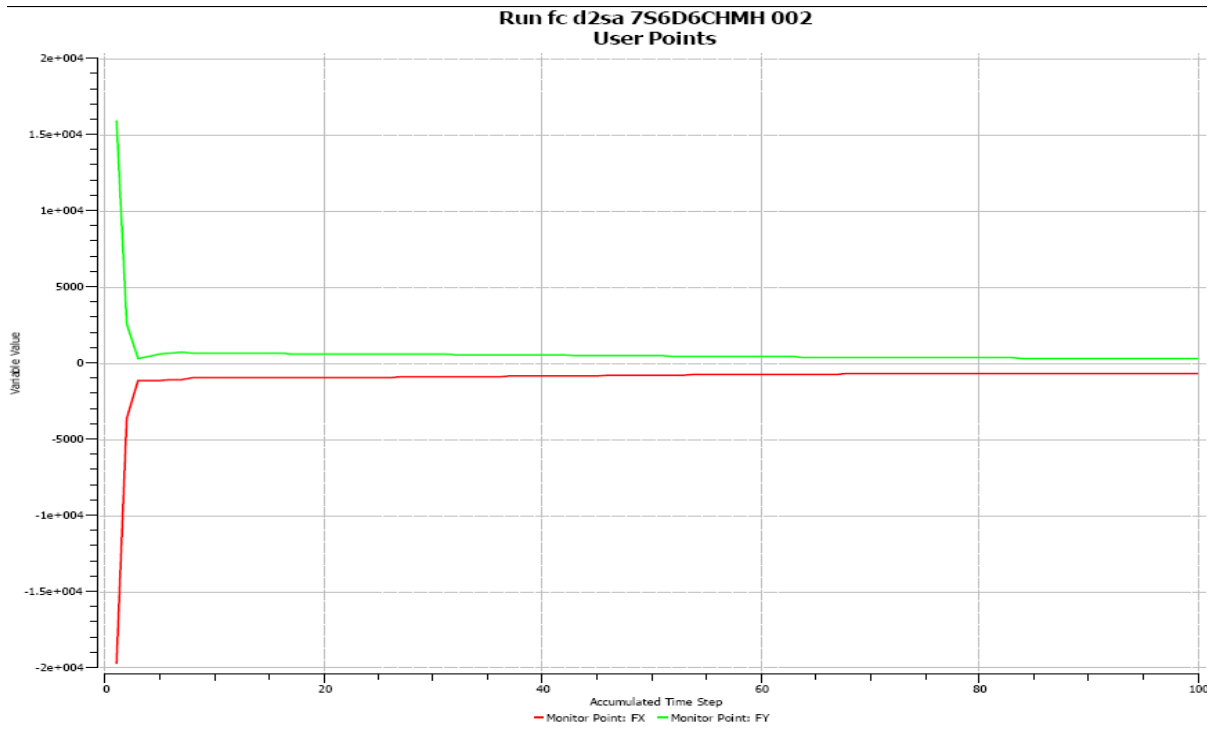


Figure 7.8: Field cultivator standard – example of reaction force convergence for steady-state CFD simulation

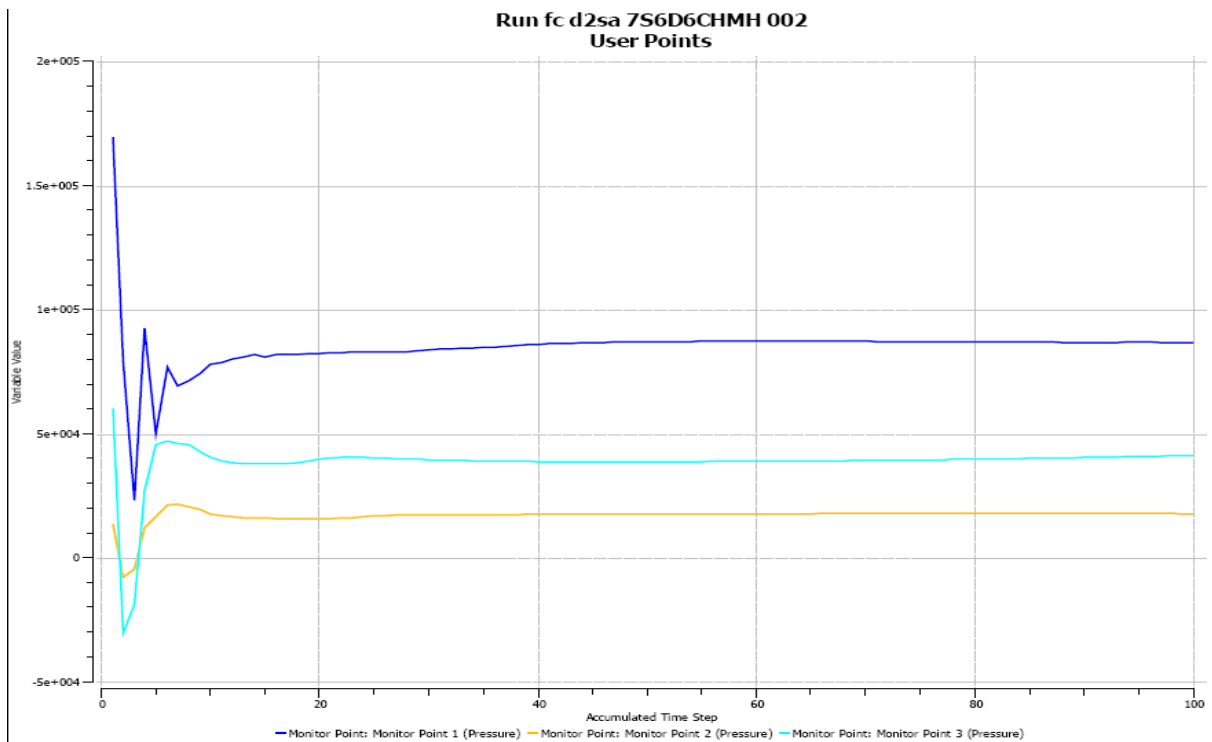


Figure 7.9: Field cultivator standard – example of pressure convergence for steady-state CFD simulation

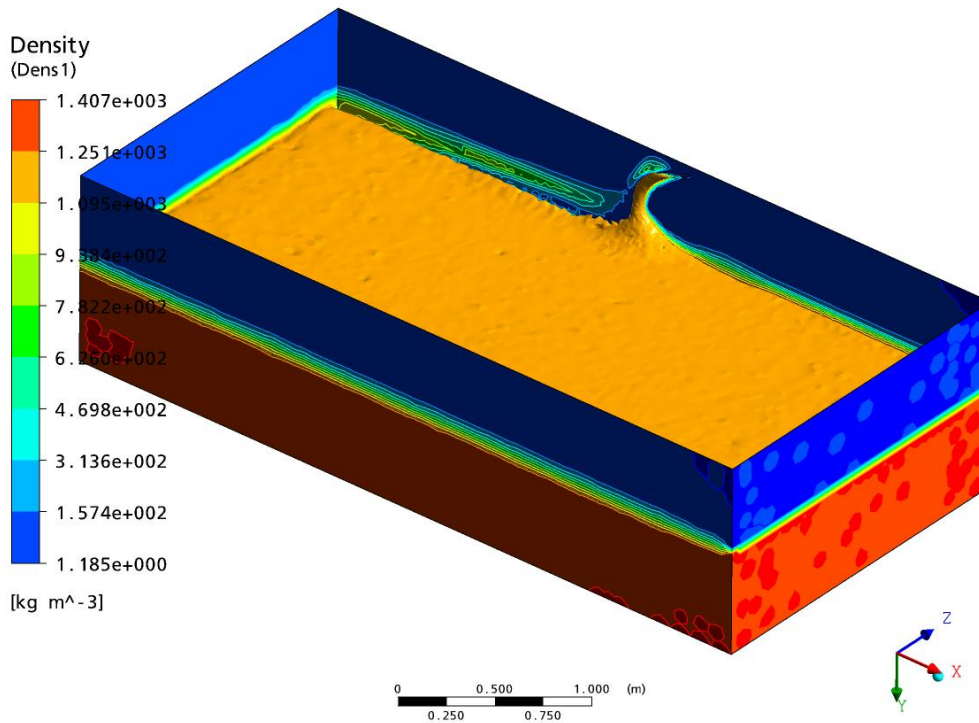


Figure 7.10: Field cultivator standard – example of density plot and iso-surface for steady-state simulation

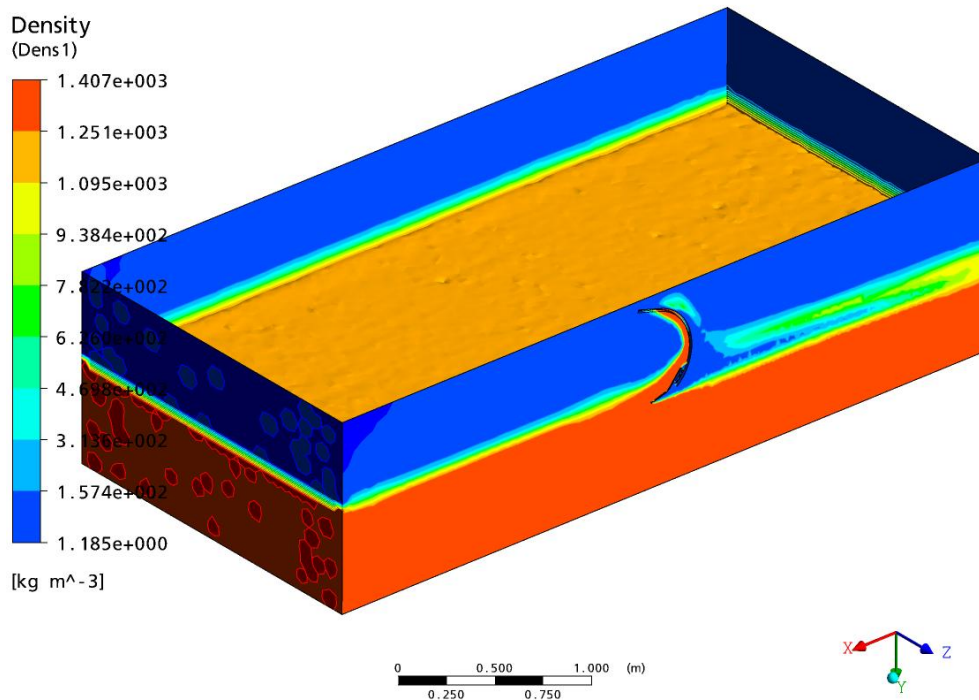


Figure 7.11: Field cultivator standard – example of density plot and iso-surface for steady-state simulation

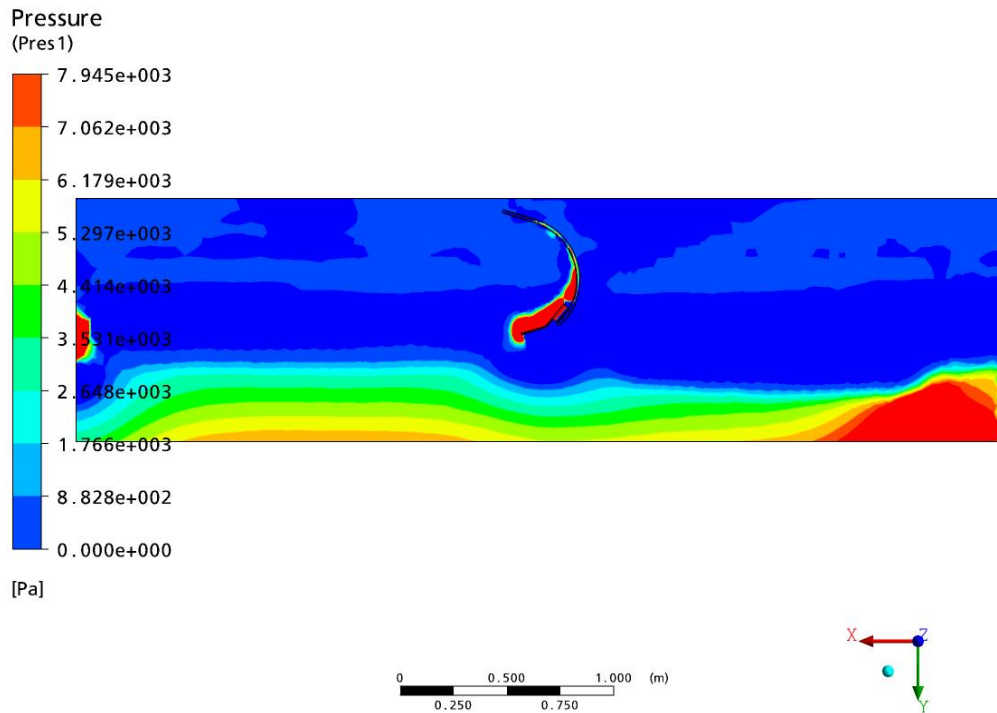


Figure 7.12: Field cultivator standard – example of pressure plot for steady-state simulation on the symmetry plane

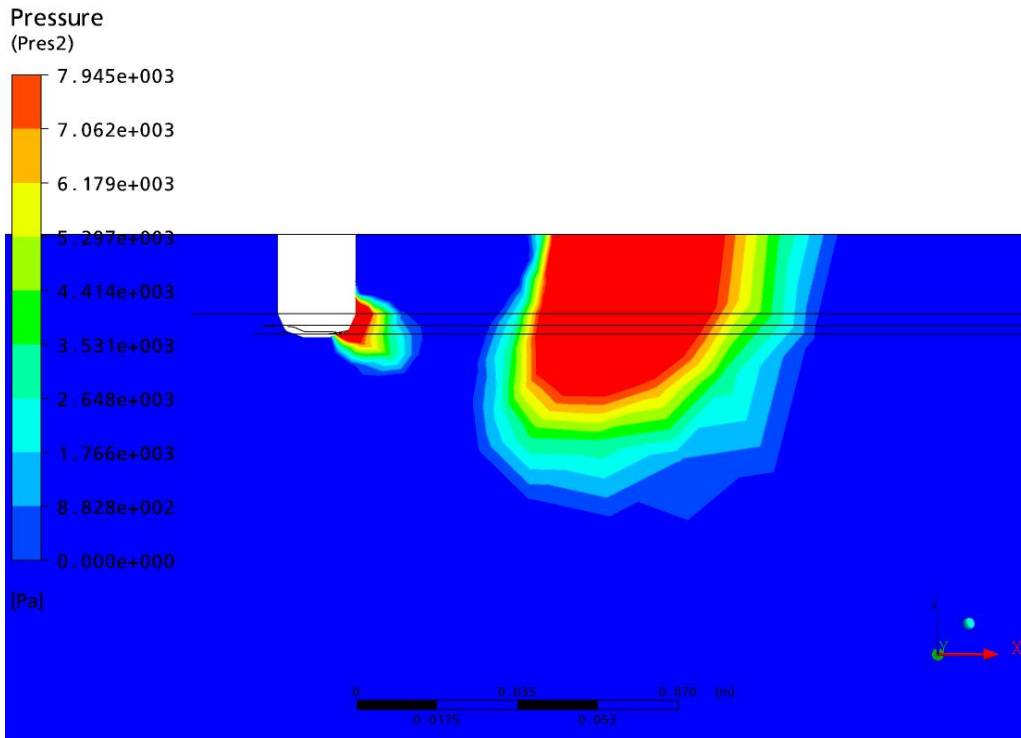


Figure 7.13: Field cultivator standard – example of pressure plot for steady-state simulation on the soil surface

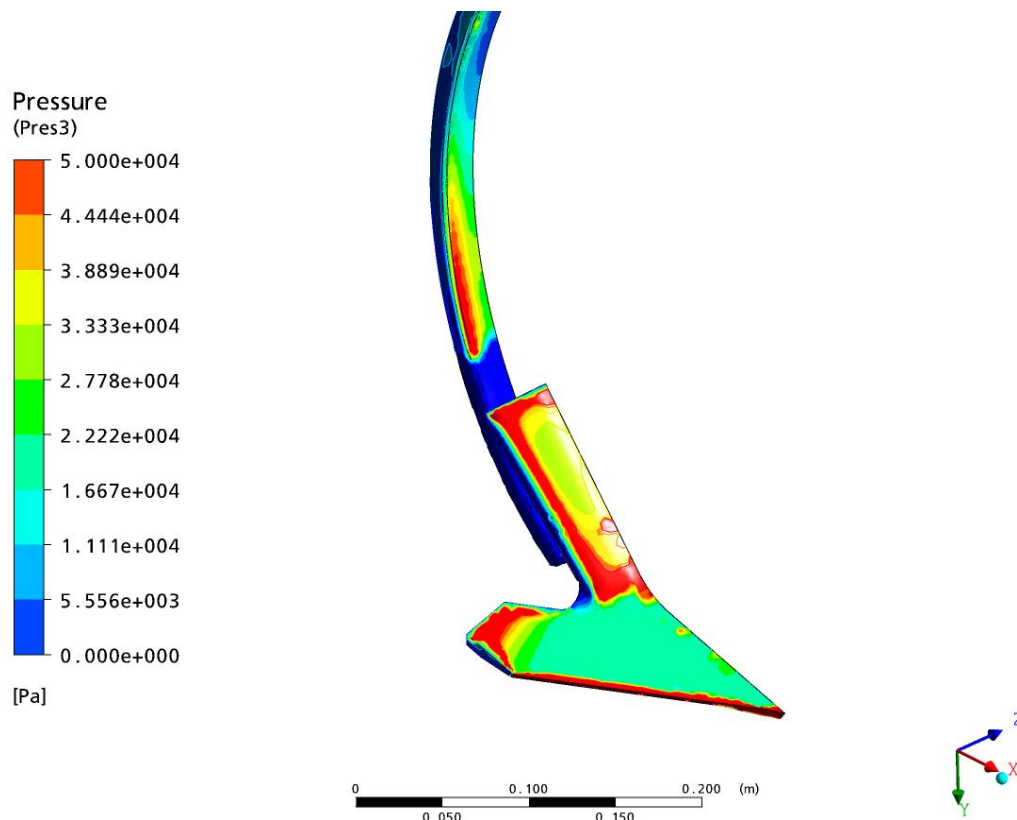


Figure 7.14: Field cultivator standard – example of pressure plot for steady-state simulation on the sweep and shank



Figure 7.15: Field cultivator standard – example of new and worn 254mm sweep

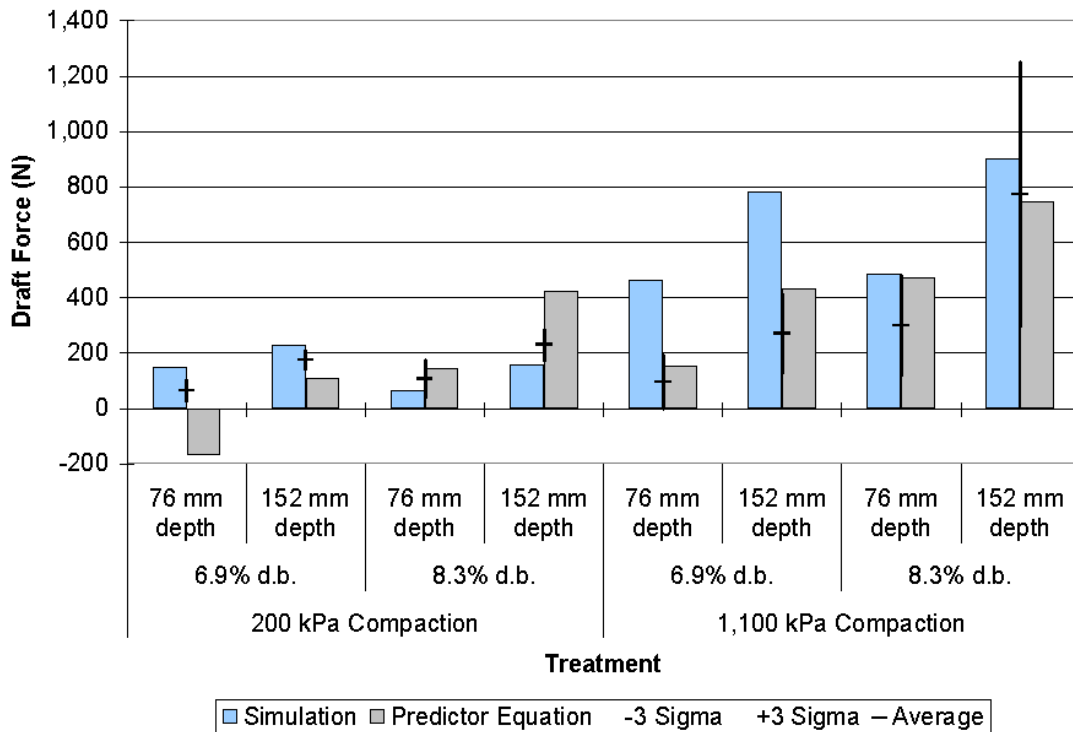


Figure 7.16: Field cultivator standard predicted versus measured draft force – 178 mm Sweep, 0.89 m/s

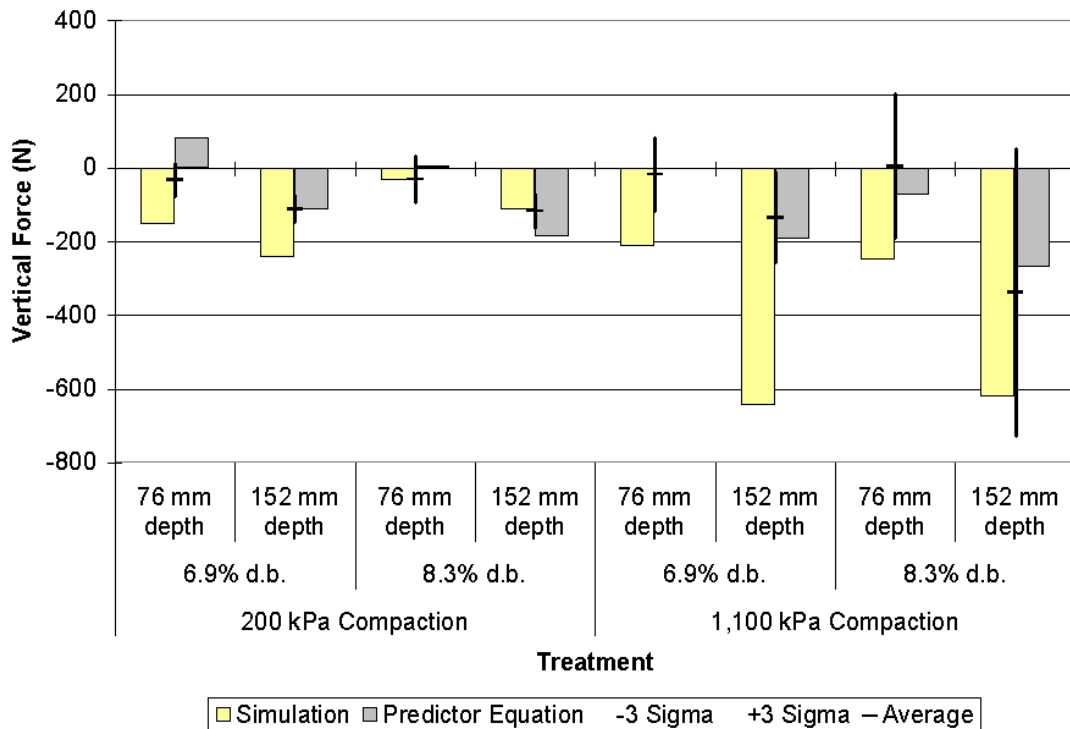


Figure 7.17: Field cultivator standard predicted versus measured vertical force – 178 mm Sweep, 0.89 m/s

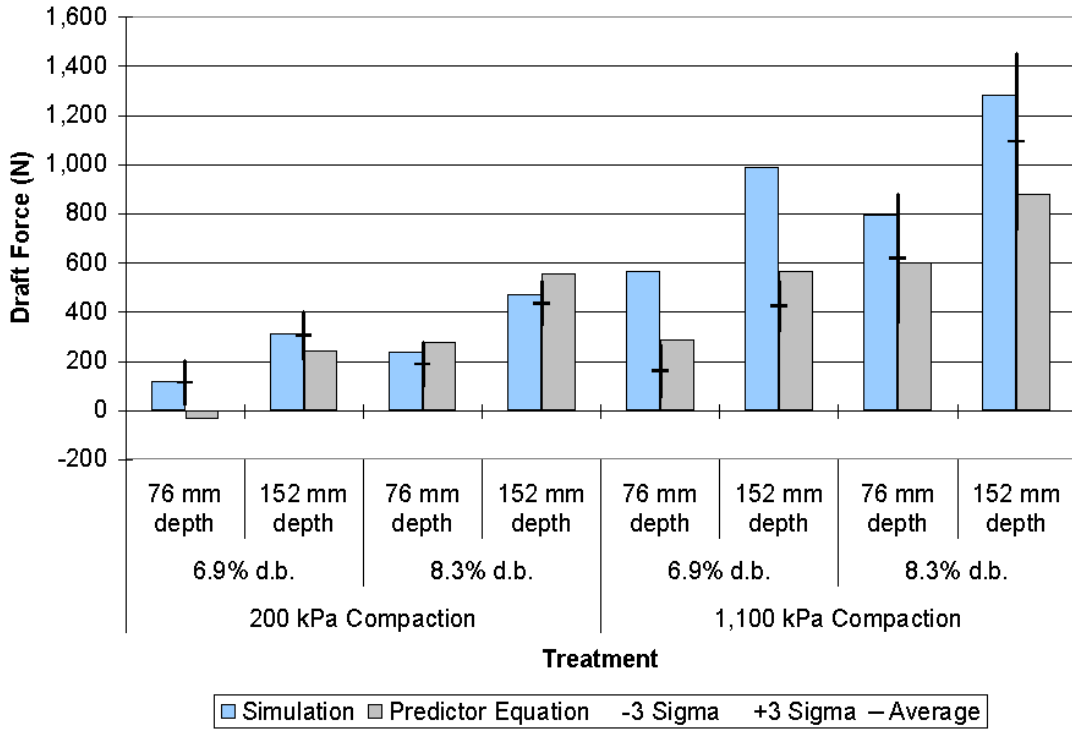


Figure 7.18: Field cultivator standard predicted versus measured draft force – 178 mm Sweep, 2.68 m/s

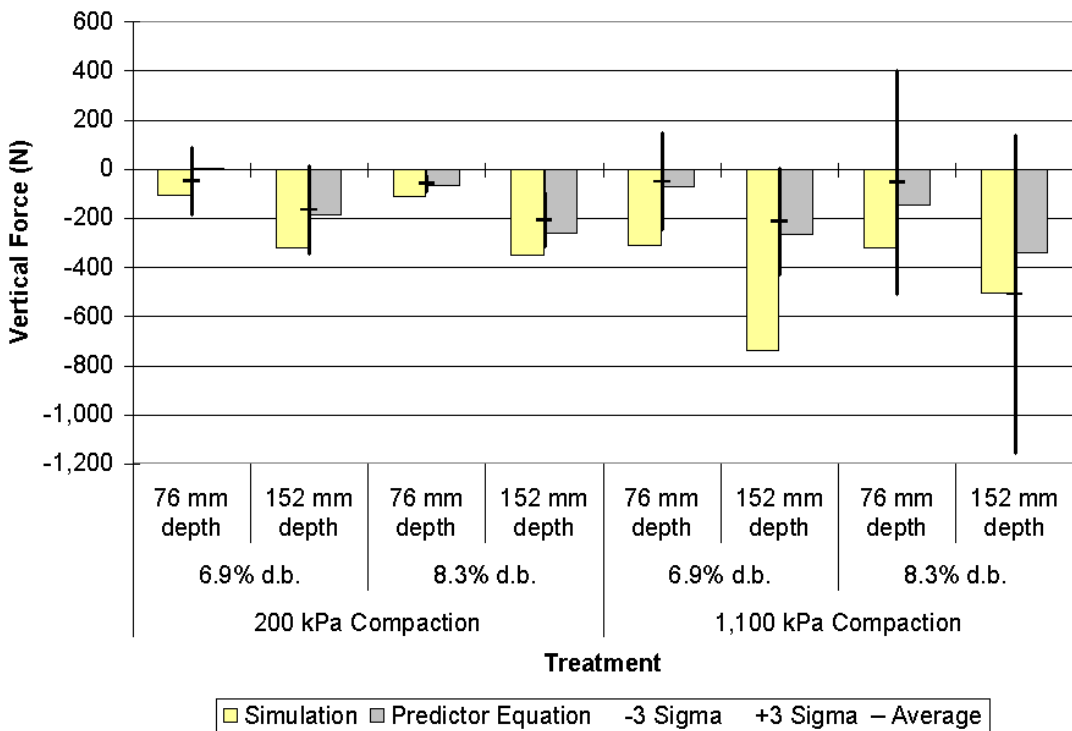


Figure 7.19: Field cultivator standard predicted versus measured vertical force – 178 mm Sweep, 2.68 m/s

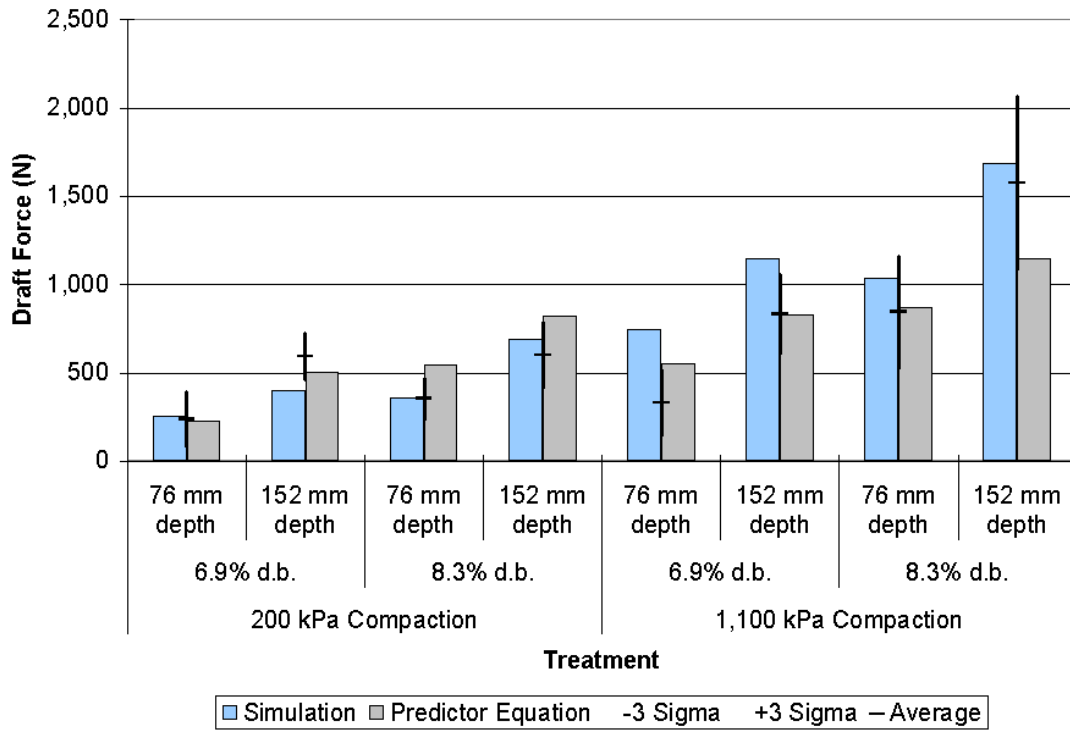


Figure 7.20: Field cultivator standard predicted versus measured draft force – 178 mm Sweep, 4.47 m/s

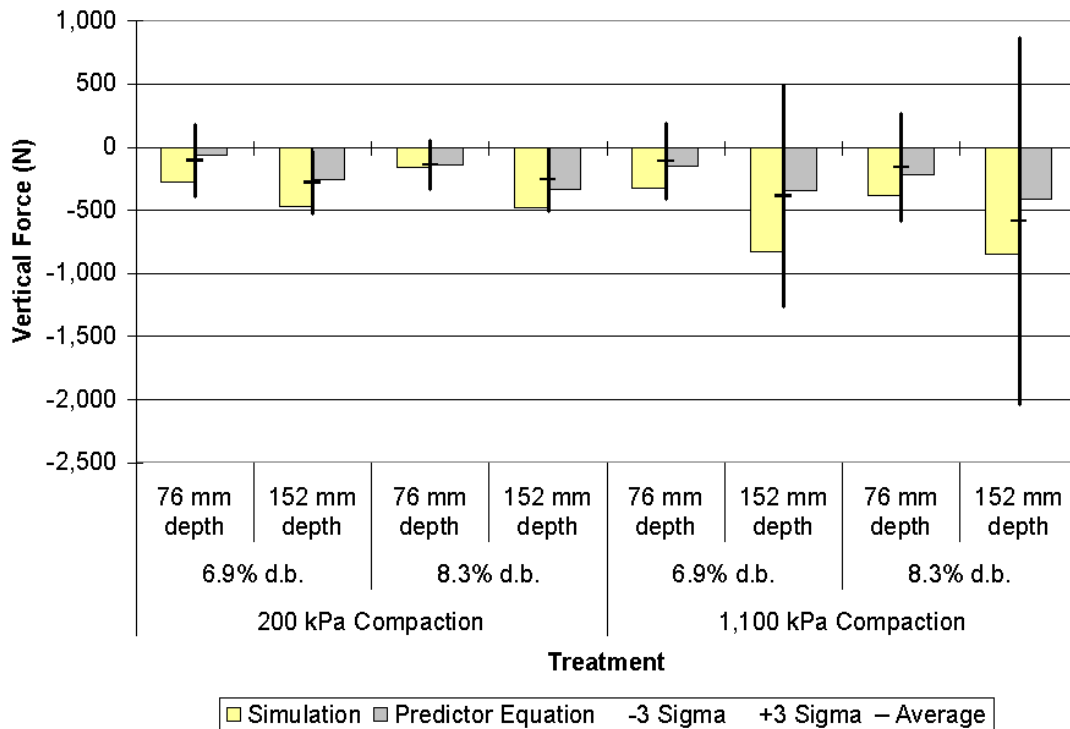


Figure 7.21: Field cultivator standard predicted versus measured vertical force – 178 mm Sweep, 4.47 m/s

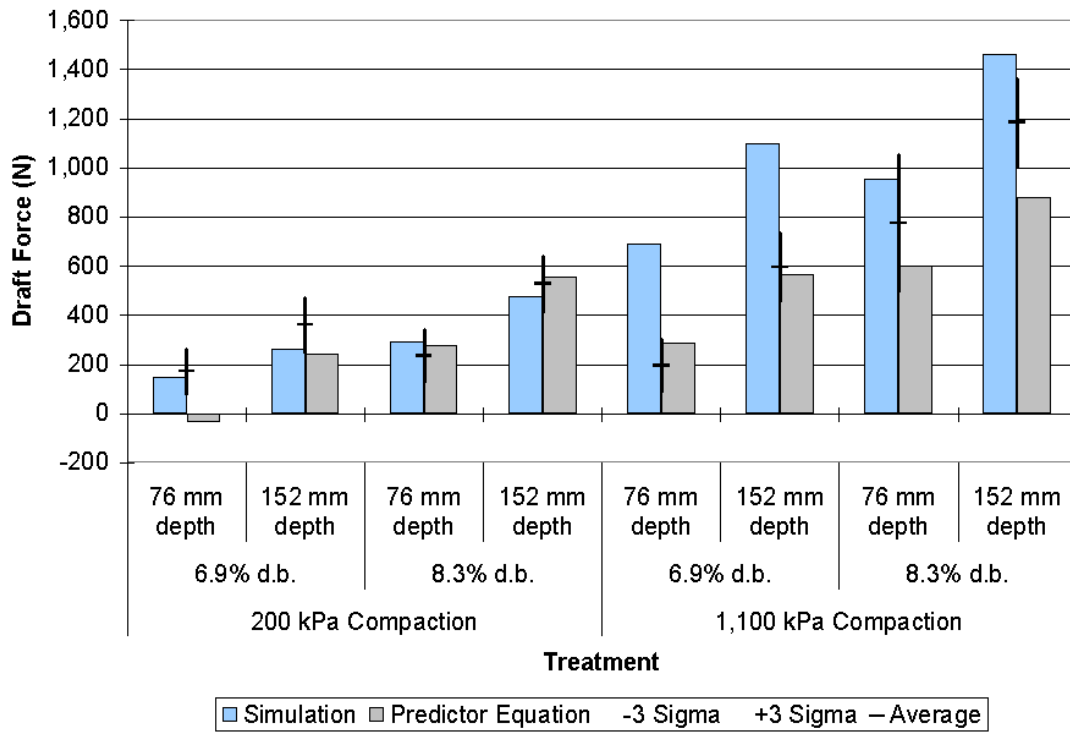


Figure 7.22: Field cultivator standard predicted versus measured draft force – 254 mm Sweep, 2.68 m/s

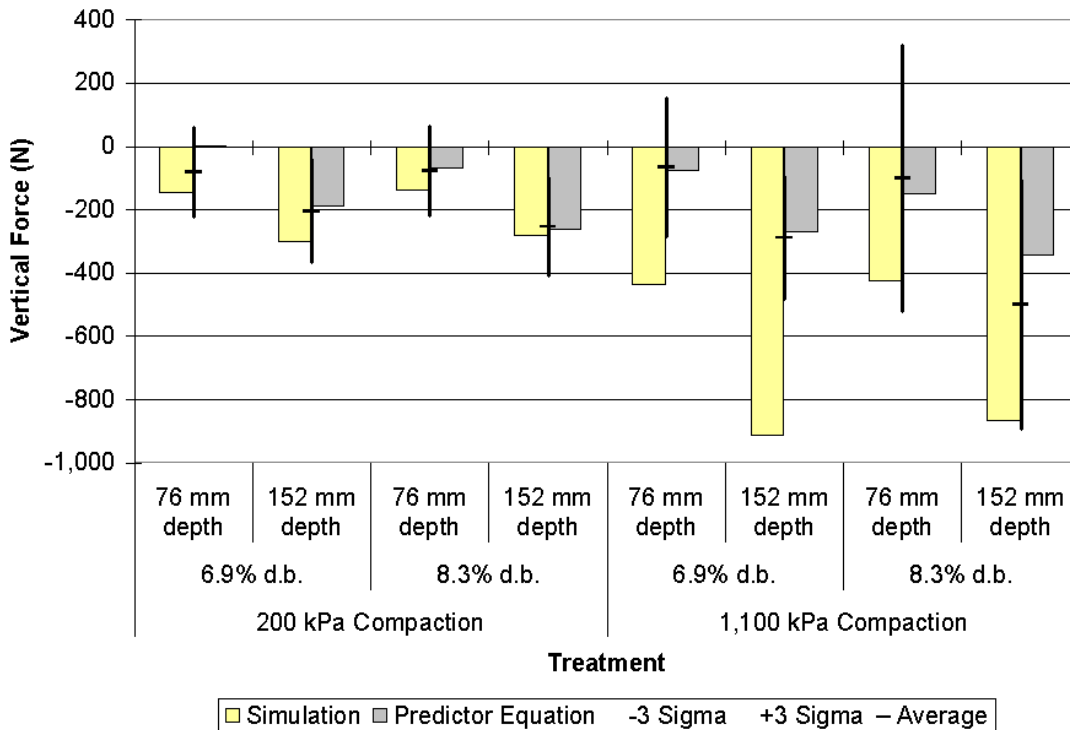


Figure 7.23: Field cultivator standard predicted versus measured vertical force – 254 mm Sweep, 2.68 m/s

For the 178 mm sweep at 0.89 m/s, the predicted draft force fell within three standard deviations of the measured draft loads in two of eight treatment levels and in three of eight for the vertical force. However, the trends were correct based on depth and compaction but did not match well for differences in moisture content. The predictor equation draft force fell within three standard deviations of the measured draft loads in four of eight treatment levels and in six of eight for the vertical force. However, for both the draft and vertical forces, the predictor equation predicted forces of opposite sign in one treatment each.

For the 178 mm sweep at 2.68 m/s, the predicted draft force fell within three standard deviations in six of the eight treatment levels and four out of eight for the vertical force. The trends were generally good. The predictor equation draft force fell within three standard deviations of the measured draft loads in four of eight treatment levels and in seven of eight for the vertical force. However, for both the draft and vertical forces, the predictor equation predicted forces off opposite sign in one treatment each.

For the 178 mm sweep at 4.47 m/s, the predicted draft force fell within three standard deviations in five of eight treatments and in all eight treatment levels for the vertical force. The trends matched very well. The predictor equation draft force fell within three standard deviations of the measured draft loads in five of eight treatment levels and in eight of eight for the vertical force.

For the 254 mm sweep at 2.68 m/s, the predicted draft force fell within three standard deviations of the measured data in five of the eight treatment levels and in six of the eight treatment levels for the vertical force. Again the trends matched very well. The predictor equation draft force fell within three standard deviations of the measured draft loads in five of eight treatment levels and in seven of eight for the vertical force. However, for both the draft and vertical forces, the predictor equation predicted forces off opposite sign in one treatment each.

One of the points of this research was to determine if this methodology could be used to compare different sweep shapes and predict the relative differences in draft and vertical forces. To determine the effectiveness of the approach, the differences between the average draft and average vertical forces were calculated for the measured and predicted data of the 178 mm and 254 mm sweeps. The predicted difference was then divided by the measured

difference in forces to determine the ratio of the predicted difference to the measured difference.

$$Ratio = \frac{(254mm_{predicted} - 178mm_{predicted})}{(254mm_{measured} - 178mm_{measured})} \quad (7.1)$$

Figure 7.24 shows the ratio between the predicted and measured differences in the draft and vertical forces between the 254 mm and 178 mm sweeps. A positive ratio means that the simulation correctly predicted which sweep had the higher force. A ratio of exactly one means that the simulation correctly predicted the difference in forces between the two sweep sizes. The figure shows that the simulation did consistently predict the differences between the two sweep sizes and the method can be used to predict between two designs. Care should be taken to make sure that the forces have converged by running the simulations to the number of iterations required to reach the desired convergence level.

For draft forces, the error in the simulation predicted difference was equally over and under predicted. The simulation incorrectly predicted which sweep had the higher draft force in one condition (152 mm depth, 6.9% d.b. and 200 kPa compaction). The predicted difference for the treatment of 76 mm depth, 8.3% d.b. and 1,100 kPa compaction matched the measured difference. Five of the treatment conditions had an error of less than 100 percent. One treatment condition had an error exceeding 200 percent.

For the vertical forces, the error was also equally likely to be over or under predicted. The simulation incorrectly predicted which sweep had the higher vertical force in three conditions. There were only two treatment conditions with an error less than 100 percent. Three conditions had errors that exceeded 200 percent or double the measured difference.

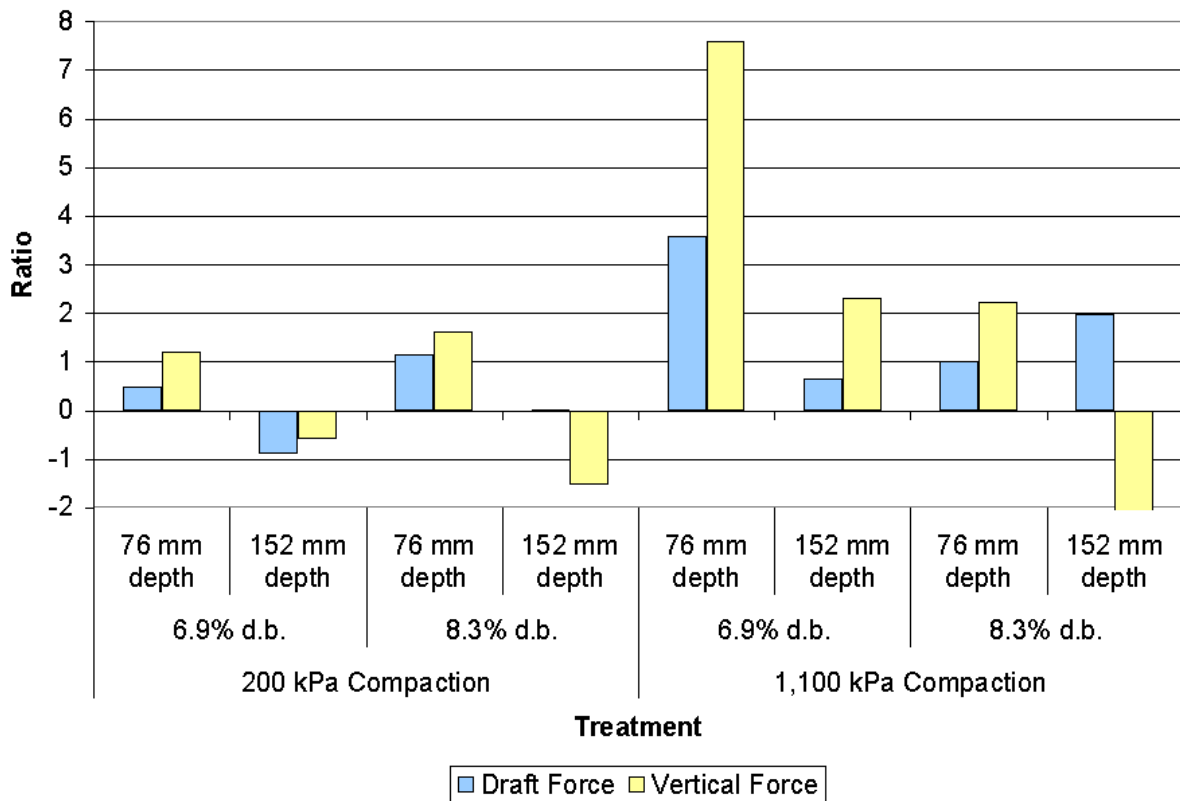


Figure 7.24: Field cultivator standard ratio of predicted to measured force differences between the 254 mm and 178 mm sweeps

7.3 Transient Fluid-Structure Interaction Results

A fully coupled two-way transient fluid-structure interaction analysis with the CFD and FEA models connected was set up. The purpose was to predict the dominant frequency of the predicted draft loading to compare with the measured data. To couple the structural and CFD codes, fluid-structure interfaces were defined in both models. The interfaces were broken up into several segments for the sweep, shank, and the adapter that connects them.

In the structural model, the fluid-structure interfaces were created as loads. In the CFD model, the fluid-structure interfaces were set up as boundary conditions. Additionally, the boundary conditions also allowed the definition of mesh movement based on displacements passed on from the structural model. At boundaries adjacent to the fluid-structure interfaces in the CFD model, the mesh motion was set as unspecified to allow the mesh to move as required.

No results were able to be obtained past the first time step. Several attempts were made to complete the simulation for one-second of time with a time step size of 0.005 seconds or 200 Hz to match the data collection rate used in lab tests. However, a couple of problems occurred in trying to complete this complex analysis.

One of the major problems with this type of analysis is the time due to the size of the problem. For this analysis the CFD model required the most time to solve. The CFD domain required a somewhat large number of elements to get convergence on the surface of the sweep and shank. Also, because of the split fluid between soil and air and the sharp corners of the geometry, getting good convergence requires more iterations within each time step. Based on a dual processor HP workstation with 8Gb or RAM each iteration required approximately two minutes. Based on a minimum of 100 iterations per time step at 200 Hz, the CFD analysis would require 667 hours without considering addition stagger iterations at each time step.

The problem that was most difficult was the degradation of the CFD domain elements as the structural model forced displacements onto the CFD mesh under load. Ultimately this problem killed the analysis. During the first time step the solvers would iterate with stagger steps until convergence was reached under the initial loading. During the second time step when the structural model passed meshed displacements to the CFD model the enforced displacements caused some elements to degrade to failure. Additional attempts were made to modify the mesh but none were successful. Test models with simpler geometry using all hexahedral elements were able to sustain large displacements without significantly degrading the mesh quality and were able to run to completion. However, the complex geometry made an all hexahedral mesh extremely difficult.

7.4 Conclusions

A CFD model was set up for the field cultivator standard with the 178 and 254 mm sweeps and shank. The CFD domain contained both soil and air. The depth of the soil was specified by the volume fraction at the inlet and initialization of the domain by the use of equations created in CFX Expression Language (CEL). The model was used for both steady-state and transient simulations.

The soil properties were modified as for the rigid flat bar simulation by dividing the measured values of viscosity by 100 and the yield strength by three. This was necessary to get the predicted forces to best correlate with the measured force data. This may suggest that either the soil property test was not appropriate for this application or soil moisture levels used or that the Bingham-plastic soil model cannot adequately simulate the behavior of cohesive soil and the adjustments made to the soil properties to improve the results were coincidental.

The effects on the predicted draft and vertical forces were considered for different mesh sizes, solver parameters, and soil properties. The tests validated the mesh density used for the simulations used to compare with the test data. The tests indicated that approximately 300 iterations would have improved the predicted force convergence although 100 iterations gave good convergence over a range of treatment simulations. Although the soil property test indicated that the soil may behave elastically and not viscous the tests showed that viscosity is a strong factor in the predicted draft force.

A structural finite element model was set up of the spring reset field cultivator assembly with preloaded spring. A modal analysis predicted a natural frequency of 19.2 Hz compared with 22.6 Hz that was measured. The structural model was also used in the two-way fluid-structure interaction transient simulations.

Steady-state CFD simulations were run at all of the treatment levels tested for in Chapter 4 to compare the predicted draft and vertical force values. Overall, the predicted force values and trends compared well with the measured data. The steady-state simulations showed good convergence on both pressure and force values. The simulation was able to predict which sweep size had the higher draft force in seven of eight treatment conditions. The simulation was able to predict which sweep size had the higher vertical force in five of eight treatment conditions. In addition, the simulation also showed the potential ability to predict high wear locations and run with a typical run time measured in hours.

A transient two-way fluid-structure interaction simulation was set up and run to attempt to predict the dynamic loading of the field cultivator standard. However, results were not able to be obtained due to convergence and element distortion problems. A high enough quality mesh was not able to be constructed in a reasonable manner that could

withstand the deformations passed to the CFD simulation from the structural FEA simulation. Based on the limited simulation results, the run time for a full analysis would potentially require weeks to complete a transient analysis with only a one-second time duration. Even the simulation did work, the value of the added information would not justify the time required.

8. ALTERNATIVE SOIL PROPERTY MEASUREMENT

As mentioned in previous Chapters 6 and 7, the soil properties measured with the soil viscometer in Chapter 2 had to be modified for the predicted forces from the simulations to correlate with the lab tests. Several factors were proposed to explain this difference: the lack of soil expansion during the soil viscometer test, the relatively slow test speeds of the shear vane relative to the test speeds of the rigid flat bar and field cultivator tests, and the results from the shear vane property test not be used for this type of simulation. In order to improve the quality of the soil property test a new test standard is proposed.

8.1 Limitations of Soil Viscometer

The soil viscometer used to measure the properties for this research was developed for civil engineering applications for use in static or near static applications. ASTM Standard D 2573-01 specifies the shape of the shear vane and the rotational speed to determine the soil shear strength. The standard specifies a test range of 0.005 to 0.034 rpm. The standard also specifies that the shear vane be below the surface where soil expansion can not occur.

The calculated soil viscosity was based on running the soil viscometer test at a variety of speeds and calculating the slope of the shear strength plotted against the rotation speed. The soil viscometer used in this research operated over a speed range of 0.027 to 1.333 rpm. With the 55 mm diameter shear vane at 1.333 rpm, the maximum tip speed was only 0.0038 m/s. This is approximately 700 times slower than a typical tillage speed of 2.86 m/s (6 mph). Simply increasing the speed of the shear vane is not likely to yield good results. To achieve a tip speed of 2.86 m/s with the 55 mm shear vane would require operating at about 1,000 rpm. At this speed the soil would fail quickly and any real differences between the soil shear strength at useful test speeds would be indistinguishable. The soil property test results also indicated that the soil did not show viscous behavior.

8.2 Proposed Material Property Test

A proposed test is to use the rigid flat bar for calculating the soil shear strength and viscosity based on the test depth and the measured draft force using equations developed from the tests results reported in Chapter 3. The shape of the bar would be specified as 12.7

x 101 mm (0.5 x 2.0 inches) as used in previous research and in the rigid flat bar lab test from Chapter 3. The test would be run at three or more speeds and at the depth representative of the actual tool operating depth being simulated. Three or more samples should be collected at each speed and soil treatment level. The data would be plotted with the draft force versus the speed. A linear trendline would be fitted to the data to determine the Y-intercept and slope for each soil depth and soil treatment or condition. Figure 8.1 shows the plotted data from the Chapter 3 test results with the trendlines displayed.

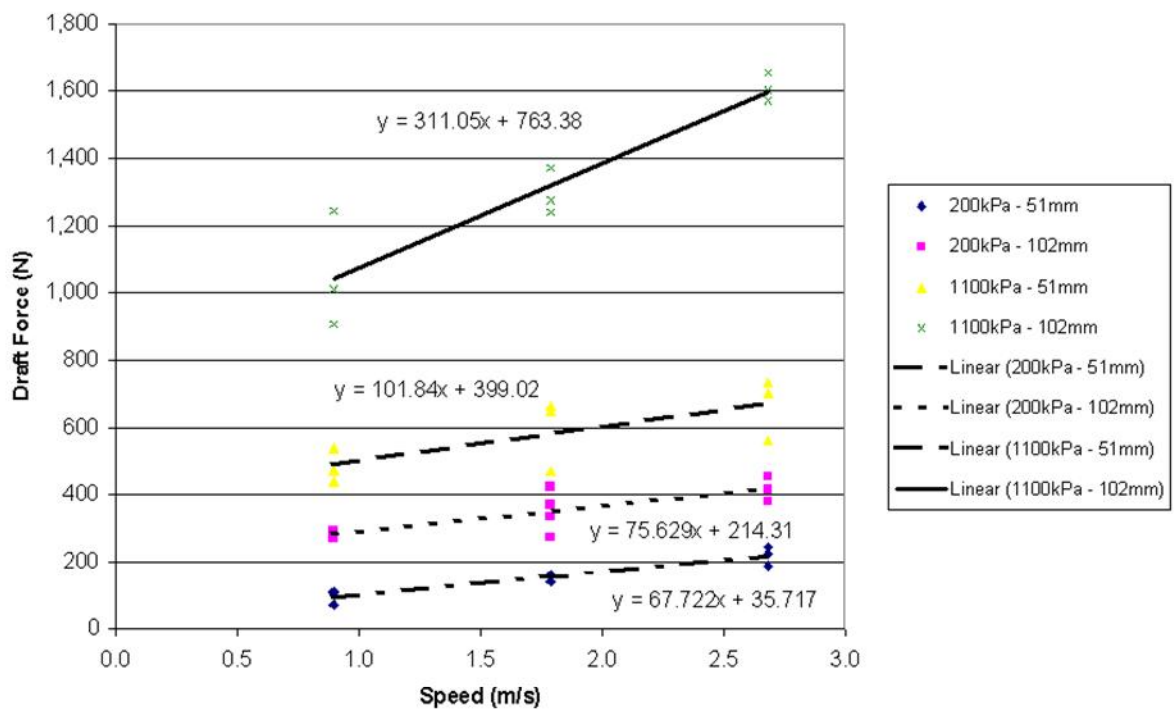


Figure 8.1: Rigid flat bar draft versus test speed

A multiple regression analysis was run on the data from Chapter 3 for the flat bar to determine the coefficients for the shear strength equation and for the viscosity equation recommended for this standard. The equations relate the draft force, depth, and the slope of the draft force versus speed. The output from the regression analysis is provided in the Appendix. The two predictor equations are:

$$\text{Shear Strength (Pa)} = 5,446.5 \text{ (Pa)} - 65.7 \times \text{Depth (mm)} + 19.2 \times \text{Draft (N)} - 17.7 \times \text{Slope (Ns/m)} \quad (8.1)$$

$$\text{Viscosity (Pa-s)} = 162.6 \text{ (Pa-s)} - 1.2 \times \text{Depth (mm)} + 0.4 \times \text{Draft (N)} - 0.3 \times \text{Slope (Ns/m)} \quad (8.2)$$

A sample spreadsheet has been created to use in future soil property tests and is presented in Figure 8.2. The spreadsheet has spaces to record the test information, test conditions, test speed, and the average measured draft force for each test run. The spreadsheet includes a graph to plot the draft force versus speed data. Once the data has been plotted a line can be drawn through the data to determine the Y-intercept and the slope to use in the soil property calculations. At the bottom of the spreadsheet are places to record the Y-intercept and slope into formulas to calculate the soil shear strength and viscosity.

Additional testing is recommended to further refine the equation coefficients and to test the validity and accuracy of the equations. However, this method of determining the material properties for use in CFD simulations is easily adaptable to use in both the lab and field conditions. The main benefits of this method are that the test can be run at representative speeds used in actual farming practices and is simple to use.

8.3 Conclusions

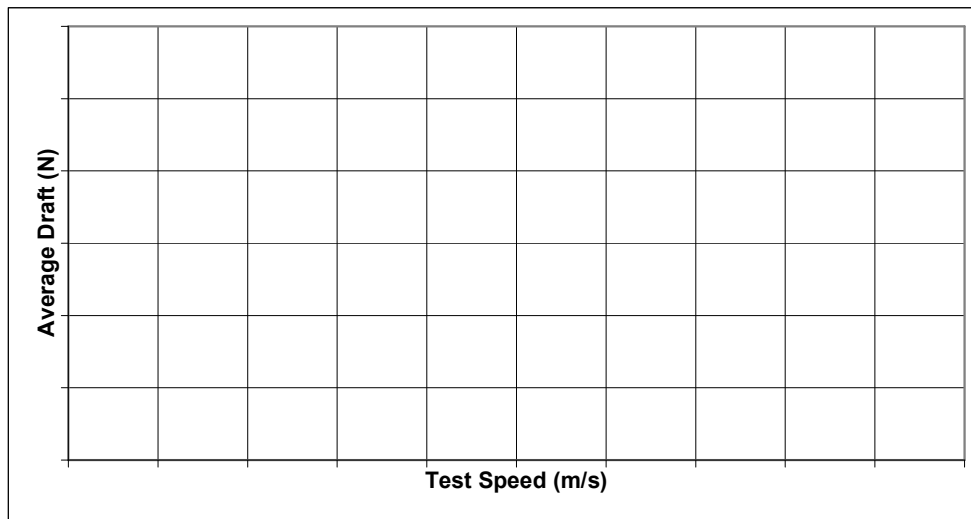
The soil viscometer used to measure the soil properties necessary for the CFD simulation is limited and does not reflect ground engaging tool applications in two ways. First, the test is run below the soil surface where no expansion of the soil can take place as failure occurs. Second, the test speed range of the soil viscometer is well below that of actual farming practices.

An alternate method of calculating soil properties for use in CFD simulations is proposed to address some of the shortcomings of using the shear vane viscometer. The basis for the method is from measuring the draft force on a 12.7 mm x 102 mm steel bar forced through the soil. The measured draft force, test speed, and depth are used in equations developed to calculate the soil strength and viscosity. The equations are based on a regression analysis of the test data discussed in Chapter 3 for the rigid flat bar lab test. The main benefits of the proposed test are ease of use, the ability to measure soil properties at the realistic farming speeds, and the soil is failed in a manner similar to ground engaging tools used in farming practice. Additional testing is recommended to further refine the equations.

Test Date:
 Tester:
 Test Location:
 Test Condition Description:

Soil Moisture (% d.b.):
 Soil Compaction (kPa):
 Test Depth (mm):

Test #	Test Speed (m/s)	Average Draft (N)	Test #	Test Speed (m/s)	Average Draft (N)
1			11		
2			12		
3			13		
4			14		
5			15		
6			16		
7			17		
8			18		
9			19		
10			20		



Soil Shear Strength Calculation

Depth		x 65.7 =	+	5446.5	
Y-intercept		x 19.2 =		-	
Slope		x 17.7 =		+	
Soil shear strength				-	
				Pa	

Soil Viscosity Calculation

Depth		x 1.2 =	+	162.6	
Y-intercept		x 0.4 =		-	
Slope		x 0.3 =		+	
Soil shear strength				-	
				Pa-s	

Figure 8.2: Soil property test sheet

9. CONCLUSIONS

Currently tillage tools are developed by creating physical prototypes and testing them either in a lab or in field tests to determine the resulting forces generated. This process conducted in the physical domain is both time consuming and limits the number of tool shapes that can be evaluated. A better method is proposed by using numerical simulations using computational fluid dynamics. The goal would be to use computer simulations that allow low cost evaluation of tillage tools so that more designs could be evaluated, more complex shapes could be evaluated, in less time and at less expense.

9.1 Simulation Methodology

The purpose of this research is to determine if it is possible to use computational fluid dynamics (CFD) to simulate tillage tools moving through soil for use in tillage tool development. Both steady-state and two-way fluid-structure interaction simulations were considered. The research was focused on predicting the draft and vertical forces on a field cultivator standard. Several steps were taken to carry out and validate the proposed method.

Simulating ground engaging tools such as a field cultivator standard could be done using FEA, CFD, or discrete element analysis (DEA). CFD was chosen because the domain needed to simulate a field only had to be large enough to not influence the flow around the tool. This allowed for a smaller model size and consequently shorter run times. Using FEA or DEA would have required modeling the entire length of a field. The CFD approach allows interaction with the structure to be included using two-way fluid-structure interaction.

The Bingham-plastic model was chosen to simulate the properties of soil for the CFD simulations. This model was chosen because it represents the behavior of soil well and only requires two properties versus other more complicated structural material models. The required properties are soil shear strength and viscosity. To measure these properties, a shear vane soil viscometer was developed and used.

9.2 Soil Property Measurement

A soil viscometer was designed and constructed based on ASTM standard D2573-01 using a rotary shear vane. The soil viscometer was successfully used to measure the soil strength at seven speeds and at four soil treatment levels. The soil density was measured and the yield strength and viscosity were calculated from the measured torque to provide the three parameters necessary for using the Bingham-Plastic material model for the CFD analysis.

The shear vane results indicate that increased moisture lowers the shear strength of the soil but increased the viscosity. However, increased compaction resulted in higher shear strength and viscosity. The results also indicate that the soil does not show viscous behavior for the speeds tested but acts in a more elastic manner.

The Tukey analysis of the shear strength data showed that there were only three combinations of data that had statistically significant differences. The Tukey analysis also showed that there was no statistical significant difference in the measured shear strength versus speed. This may be attributed to the fact that the test speeds were very low compared with actual field test speeds. The test data points may be too close together to show statistical significant differences. Further testing at higher speeds would clarify this issue and verify that the slope of the strength versus speed data is linear.

The test method for the soil viscometer was based on the civil engineering standard developed for static structures. Limitations in the speeds that can be reasonably used with the rotational soil viscometer suggest that alternate test methods of measuring soil properties may be required. The test procedure also did not allow for soil dilation which is not representative of tillage tools. An alternate method is suggested in Chapter 8.

9.3 Rigid Flat Bar Test

A 12.7 mm by 51 mm rigid flat steel bar was tested in a soil bin to measure the draft and vertical forces that occurred as the bar was pulled through soil. Twelve treatment levels were considered varying the tool speed, depth, and the soil compaction with three repeats of each. The data indicated that the variability in draft force was higher for the high compaction level and that in general the draft force increases with speed and soil compaction.

The average draft force values were evaluated to determine which treatment factors were statistically significant. All three variables were determined to be statistically significant at the 95 percent confidence level. A regression analysis was conducted to develop a predictor equation based on all three statistically significant variables. The predictor equation predicted draft force value was below the three standard deviation level for the lowest two speeds at the 51 mm depth and 200 kPa compaction levels. Similarly, the predictor equation predicted draft force was below the three standard deviation level for the highest speed, at 102 mm depth and 1,100 kPa compaction levels.

9.4 Field Cultivator Standard Test

Soil bin tests were conducted using a 178 mm and 254 mm wide sweep with a spring reset field cultivator standard. Thirty-two treatments were considered and eight of the treatments were run with three repeats. The sweep width, speed, depth, soil compaction, and soil moisture were varied. The repeated runs were performed with the 178 mm sweep at 2.66 m/s (6 mph) while just the depth, compaction, and moisture levels were varied.

The results for the repeated runs showed a fairly low level of variability in the draft force except for the treatment ran at the higher depth, compaction, and moisture level. For both sizes of sweep the average ratio of vertical to draft force was forty percent. In predicting the draft load, the speed squared, depth, compaction, and moisture variables were all statistically significant at the 95 percent confidence level. In predicting the vertical load, speed, depth, compaction, and moisture variables were all statistically significant at the 95 percent confidence level.

The natural frequency was experimentally determined for the unloaded field cultivator standard using accelerometers. The natural frequency was calculated to be 22.6 Hz. The accelerometer data was also used to calculate the damping of the spring reset standard for use in the fluid-structure analysis later on.

The analysis of measured draft force dominant frequencies showed that there was overlap in the repeated treatments. The most common frequency across all treatments was 14.8 Hz which may indicate that the draft force frequency is related more to the stiffness of the standard and the mounting than to the frequency of the soil failure. Common frequencies of around 14 to 15 Hz were found in the data for the 178 mm sweep at 2.86 and 4.47 m/s and

for the 254 mm sweep at 2.86 m/s for all soil conditions. If this is the case, then in practice, predicting the load frequency would be related to the stiffness of standard and the implement structure stiffness, rather than the soil. Both stiffness values could be determined experimentally. The lower frequency of the draft force data compared with the natural frequency of the unloaded field cultivator standard may be attributed to the additional mass of the soil when treated as a spring-mass system or a change in the standards stiffness in the loaded condition.

An attempt was made at predicting the draft force frequency by counting the soil failure surfaces from high speed video recordings of the lab tests and dividing by the elapsed time. This method proved difficult but did show that the soil fracture rate was related to the draft force dominant frequency. This method was impossible to use at the low compaction level because the soil failed in a flowing manner with no distinct fracture surfaces. Coupled with the conclusion that the draft force variation is related to the natural frequency of the field cultivator standard, these results suggest that the vibration of the standard drives the frequency of soil failure rate, rather than the soil fracture rate driving the vibration. Additional testing would help to clarify the relationship.

9.5 Soil Model Verification

The Bingham-Plastic material model was tested using a 2-d model of a concentric cylinder viscometer. The benefit of the test models was that the models are simple enough that the run times were very short. In addition, results for the two-dimensional models can be visually interpreted. The test models showed that the equations created in CFX Expression Language (CEL) used to simulate the Bingham-Plastic model work correctly.

9.6 Rigid Flat Bar Simulation

A series of steady-state CFD simulations were run and compared to the soil bin results for the rigid flat bar. Overall, the simulations were able to show the trends in the draft loading. In nine of the twelve treatment levels, the predicted draft force fell within three standard deviations of the measured data.

Adjustments were required to the soil material parameters for the predicted forces to correlate with the measured data by dividing the viscosity by a factor of 100 and the yield

strength by a factor of three. These adjustments were determined in an iterative process based on the field cultivator standard and the rigid flat bar simulations. There are several possibilities for this: the soil property measurement test used may not be appropriate for this application, the measured soil properties were not good with viscosity not being a factor and dividing the shear strength by a factor of three was coincidental, or the simulation does not adequately represent the actual conditions being replicated. Running the simulation with viscosity removed from the Bingham-plastic model would clarify the impact of viscosity.

An initial set of boundary conditions were developed based on trying various combinations and comparing the predicted draft and vertical forces with the average measured values. However, when the boundary conditions were applied to the field cultivator standard simulation the results did not match. Additional iterations were required and developed. The boundary conditions were verified in both simulations and across a range of operating conditions.

9.7 Field Cultivator Standard Simulation

A CFD model was set up for the field cultivator standard with the 178 and 254 mm sweeps and shank. The CFD domain contained both soil and air. The depth of the soil was specified by the volume fraction at the inlet and initialization of the domain by the use of equations created in CFX Expression Language (CEL). The model was used for both steady-state and transient simulations.

The soil properties were modified as for the rigid flat bar simulation by dividing the measured values of viscosity by 100 and the yield strength by three. This was necessary to get the predicted forces to best correlate with the measured force data. This may suggest that either the soil property test was not appropriate for this application or the soil moisture levels used or that the Bingham-plastic soil model cannot adequately simulate the behavior of cohesive soil and the adjustments made to the soil properties to improve the results were coincidental.

The effects on the predicted draft and vertical forces were considered for different mesh sizes, solver parameters, and soil properties. The tests validated the mesh density used for the simulations run to compare with the test data. The tests indicated that approximately 300 iterations would have improved the predicted force convergence although 100 iterations

gave good convergence over a range of treatment simulations. Although the soil property test indicated that the soil may behave elastically and was not viscous the tests showed that viscosity is a strong factor in the predicted draft force.

A structural finite element model was set up of the spring reset field cultivator assembly with preloaded spring. A modal analysis predicted a natural frequency of 19.2 Hz compared with 22.6 Hz that was measured. The structural model was also used in the two-way fluid-structure interaction transient simulations.

Steady-state CFD simulations were run at all of the treatment levels tested for in Chapter 4 to compare the predicted draft and vertical force values. Overall, the predicted force values and trends compared well with the measured data. The steady-state simulations showed good convergence on both pressure and force values. The simulation was able to predict which sweep size had the higher draft force in seven of eight treatment conditions. The simulation was able to predict which sweep size had the higher vertical force in five of eight treatment conditions. In addition, the simulation also showed the potential ability to predict high wear locations and run with a typical run time in measured in hours.

A transient two-way fluid-structure interaction simulation was set up and run to attempt to predict the dynamic loading of the field cultivator standard. However, results were not able to be obtained due to convergence and element distortion problems. A high enough quality mesh was not able to be constructed in a reasonable manner that could withstand the deformations passed to the CFD simulation from the structural FEA simulation. Based on the limited simulation results, the run time for a full analysis would potentially require weeks to complete a transient analysis with only a one-second time duration. Successfully running the transient FSI simulation may also help clarify the relationship between the structure resonant frequency, the soil fracture frequency, and the draft load frequency.

9.8 Alternative Soil Property Measurement

The soil viscometer used to measure the soil properties necessary for the CFD simulation is limited and does not reflect ground engaging tool applications in two ways. First, the test is run below the soil surface where no expansion of the soil can take place as

failure occurs. Second, the test speed range of the soil viscometer is well below that of actual farming practices.

An alternate method of calculating soil properties for use in CFD simulations is proposed to address some of the shortcomings of using the shear vane viscometer. The basis for the method is from measuring the draft force on a 12.7 mm x 102 mm steel bar forced through the soil. The measured draft force, test speed, and depth are used in equations developed to calculate the soil strength and viscosity. The equations are based on a regression analysis of the test data discussed in Chapter 3 for the rigid flat bar lab test. The main benefits of the proposed test are ease of use, the ability to measure soil properties at the practical farming speeds, and the soil is failed in a manner similar to ground engaging tools used in farming practice. Additional testing is recommended to further test the equations.

9.9 Future Work

CFD produced results to simulate tillage tools in soil that could be matched to measured draft and vertical forces on a field cultivator standard with a sweep. Steady-state simulations were used. The estimated time to complete such an analysis would be one to two days for set-up, solving, and post-processing. This process could be used to compare different sweep/shank designs in a time that is beneficial and an improvement over current physical test methods. The simulation also provides detailed information not readily obtained from physical testing such as the load created by the sweep versus the shank and the possibility of predicting where the high wear areas will occur.

However, additional work is necessary to improve and further validate the methodology presented. The primary concern is that to match experimental data, the soil properties were varied. It is critical that work be performed to validate the modified soil parameters and validate the CFD model for soils.

The proposed method of soil property measurement needs to be further validated and adjusted with additional soil bin test data. More tests need to be run at different speeds and depths and with more soil variations to determine if this approach is viable. If proven, this method of calculating soil strength and viscosity would be an improvement of the soil viscometer using the rotational shear vane. The proposed test method also needs to be run in actual field conditions to determine if the method produces valid results.

Additional tool shapes need to be analyzed using the method described to determine if the same boundary conditions can be applied. In particular, the method needs to be applied to tools that operate at greater soil depths such as rippers and sub-soilers. The field cultivator standard that was investigated as a part of this research operates at a relatively shallow 150 mm. Deep tillage tools can operate at well over twice that. At that greater depth soil shatters less and is kept somewhat contained, similar to the way soil fails with the rotating soil viscometer.

Successfully running a transient two-way fluid structure interaction may clarify the relationships between system stiffness, soil failure, and draft loading frequencies. Using either simpler tillage tool shapes to allow for easier mesh creation or using a better mesh creation tool would help overcome some of the issues discussed in this dissertation for doing this type of analysis. Distributed computing systems would also help reduce the long run times.

More simulations of different tool shapes compared with actual tool wear will also help determine if this method of ground engaging tool simulation can help predict locations of highest wear. The benefit of this is that tool shapes can be optimized to improve the useful life of the tool and allow material to be removed that does not improve or degrade the overall life.

APPENDIX

The Appendix contains data from the lab tests and statistical analysis output not included in the body of the document. The figure and table numbers are separated by the chapters the information was referenced in.

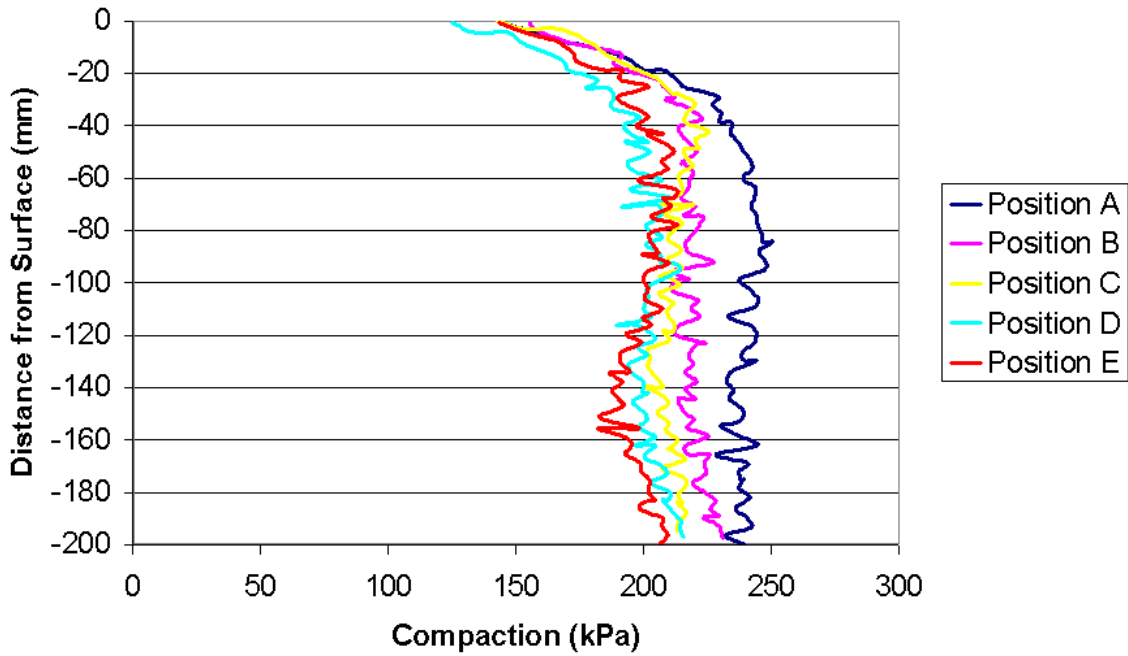


Figure A1.1: Penetrometer readings for 5m position, low moisture (7.4% d.b.), low compaction (200 kPa) from viscometer test

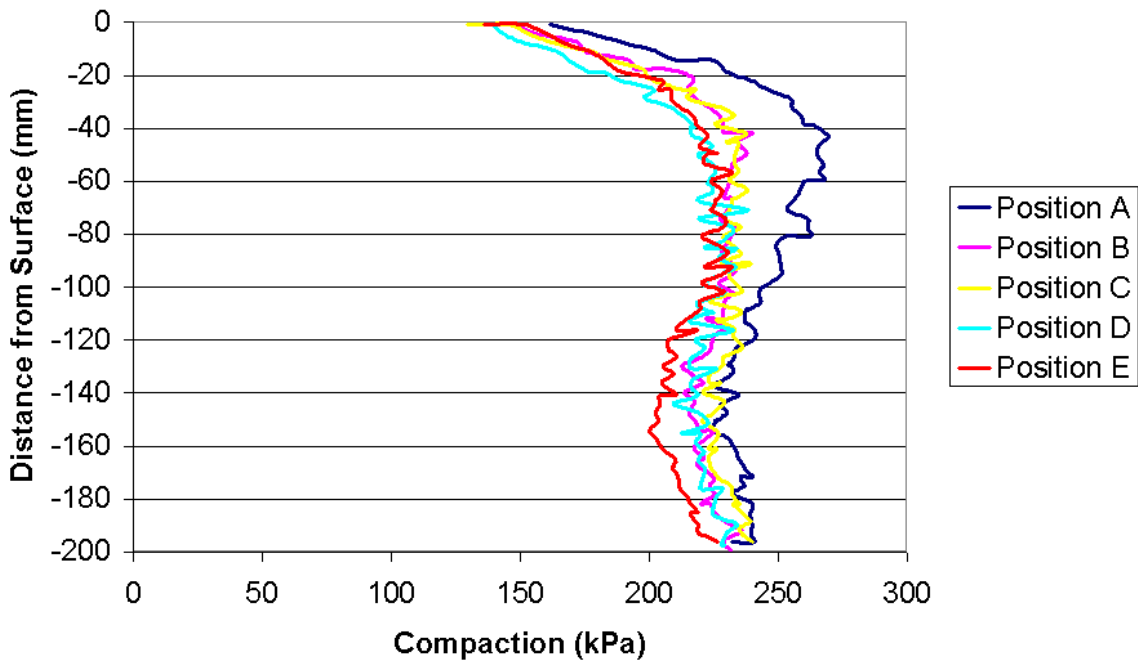


Figure A1.2: Penetrometer readings for 10m position, low moisture (7.4% d.b.), low compaction (200 kPa) from viscometer test

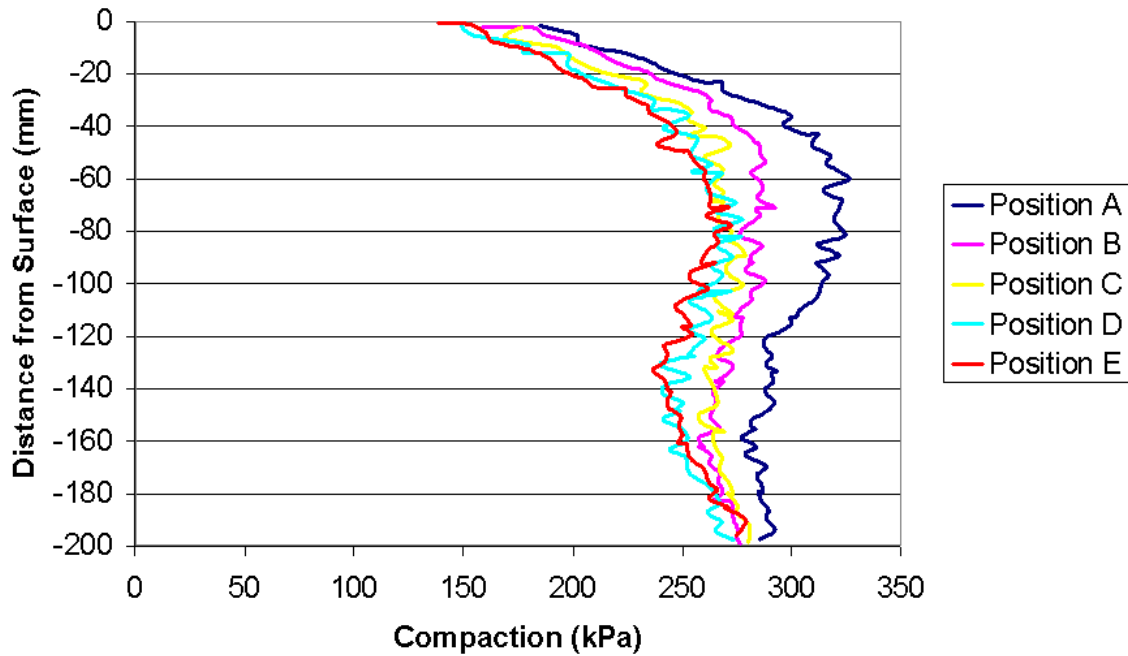


Figure A1.3: Penetrometer readings for 15m position, low moisture (7.4% d.b.), low compaction (200 kPa) from viscometer test

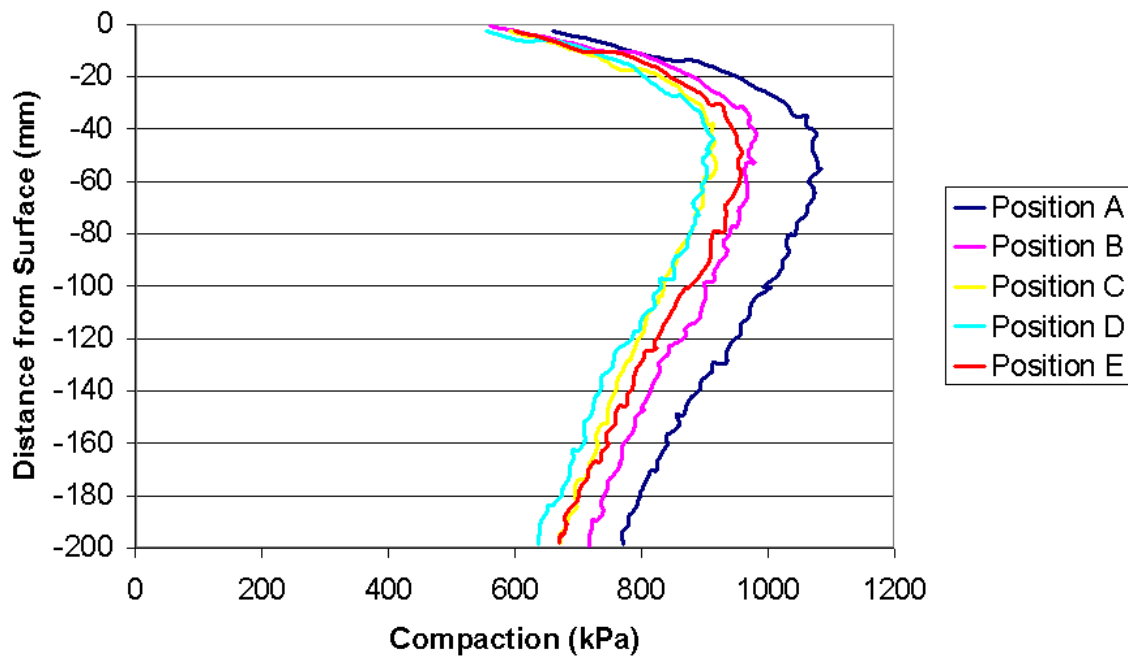


Figure A1.4: Penetrometer readings for 5m position, low moisture (7.4% d.b.), high compaction (1,100 kPa) from viscometer test

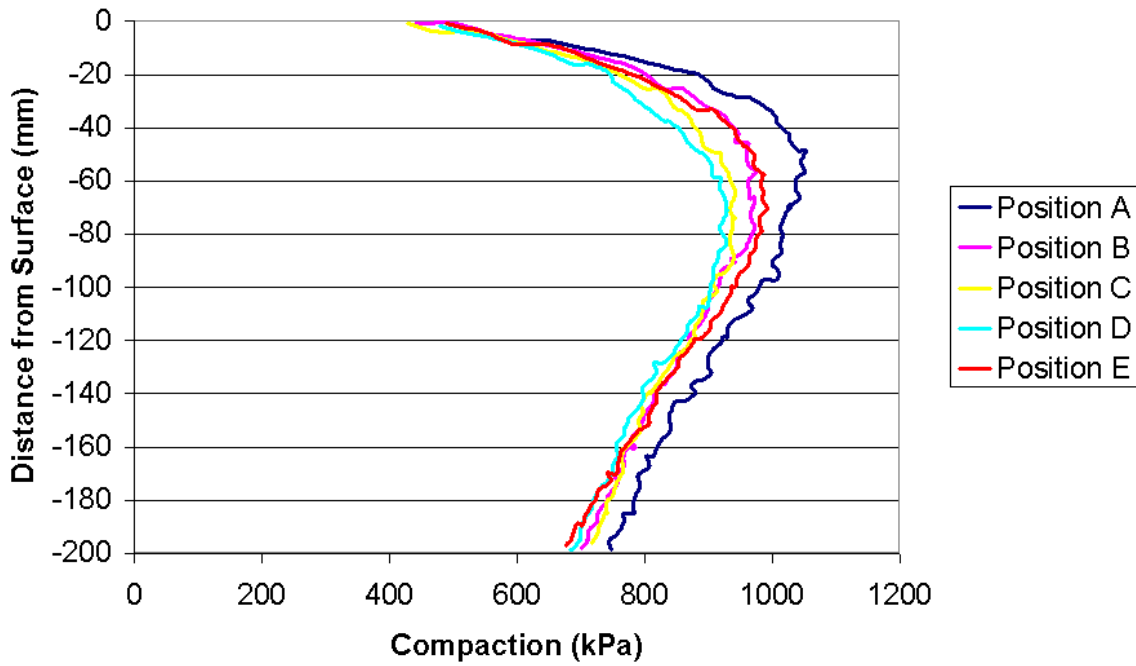


Figure A1.5: Penetrometer readings for 10m position, low moisture (7.4% d.b.), high compaction (1,100 kPa) from viscometer test

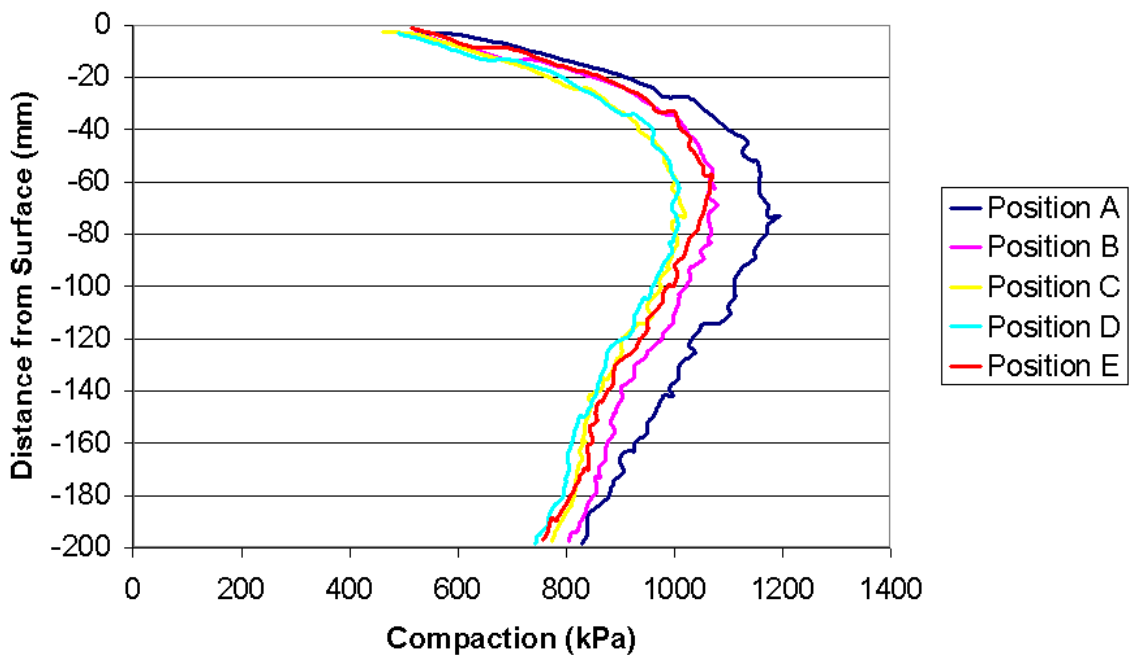


Figure A1.6: Penetrometer readings for 15m position, low moisture (7.4% d.b.), high compaction (1,100 kPa) from viscometer test

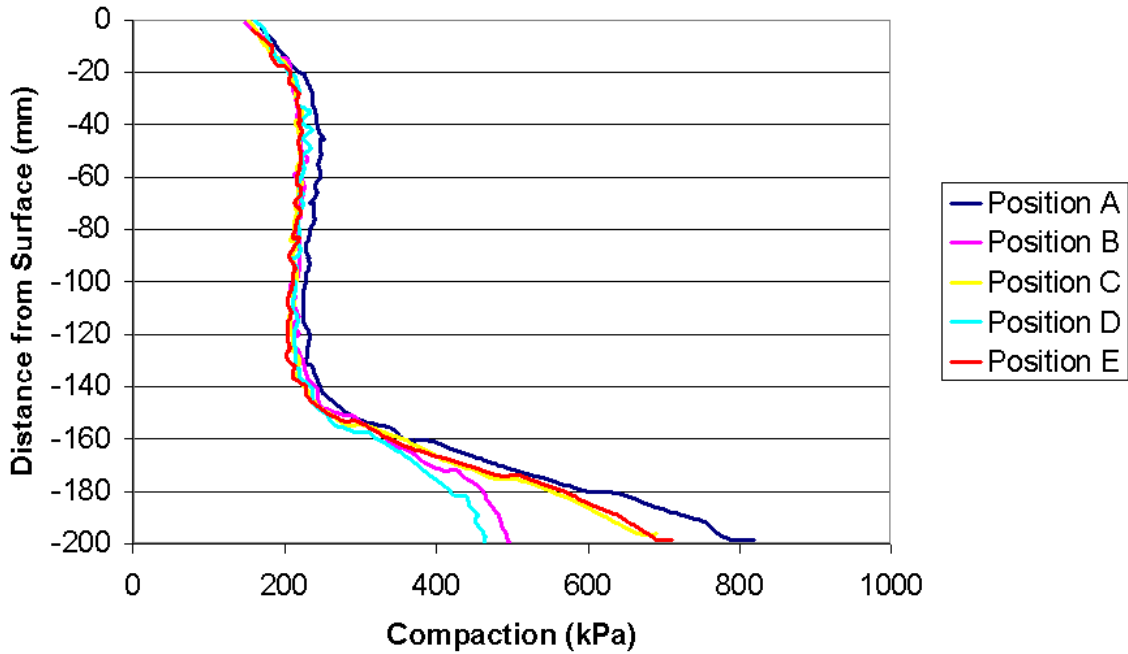


Figure A1.7: Penetrometer readings for 5m position, high moisture (8.8% d.b.), low compaction (200 kPa) from viscometer test

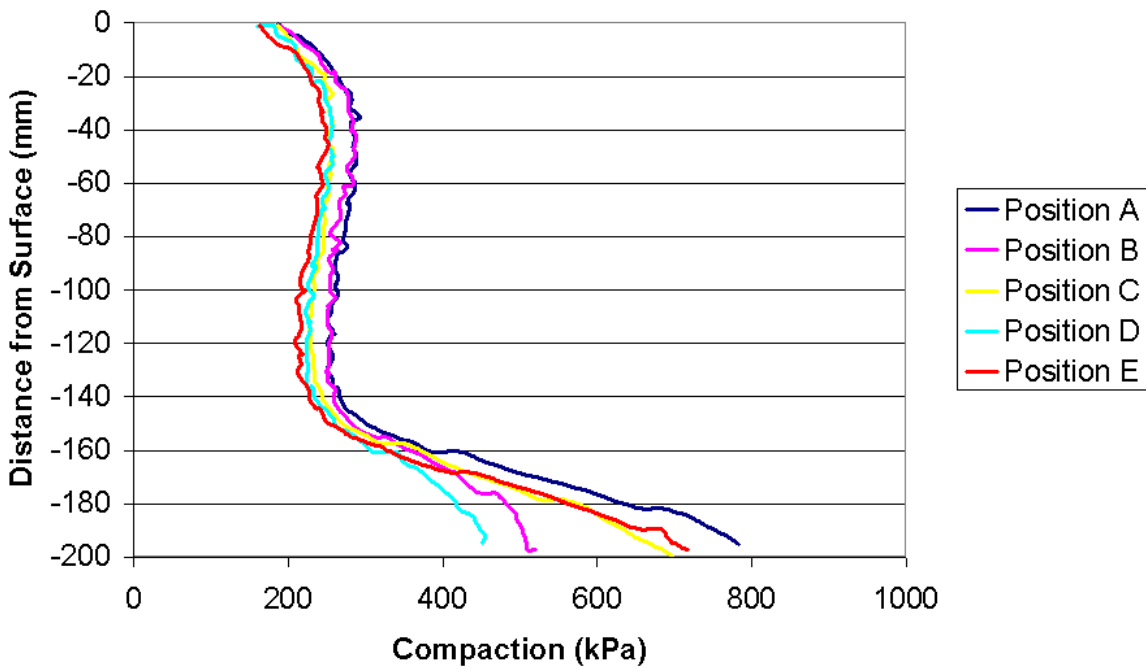


Figure A1.8: Penetrometer readings for 10m position, high moisture (8.8% d.b.), low compaction (200 kPa) from viscometer test

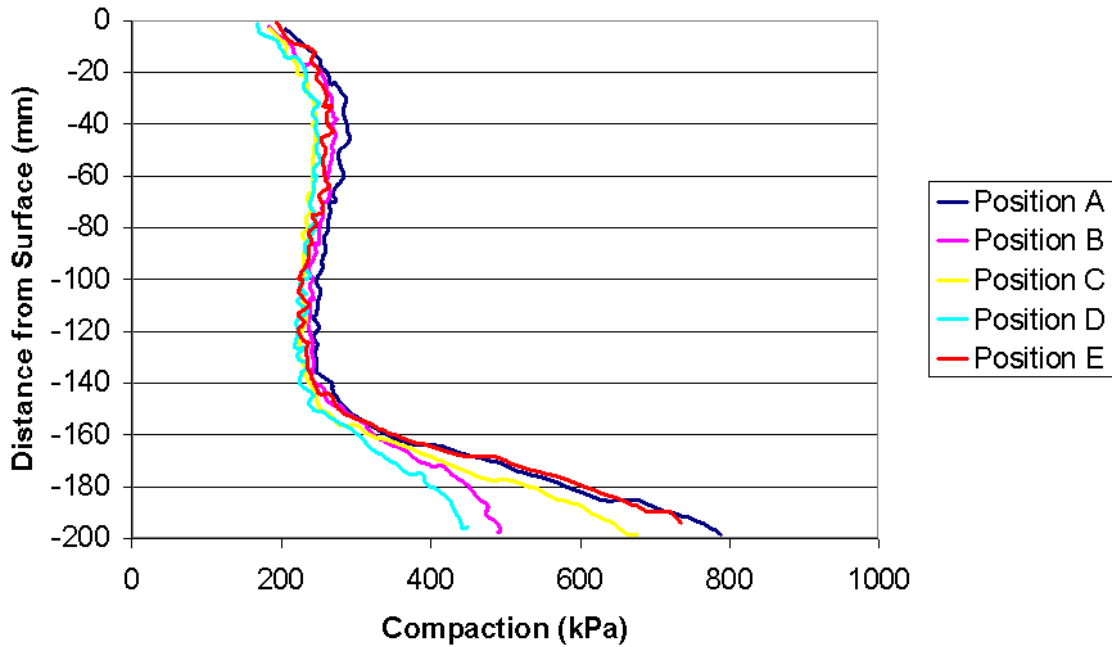


Figure A1.9: Penetrometer readings for 15m position, high moisture (8.8% d.b.), low compaction (200 kPa) from viscometer test

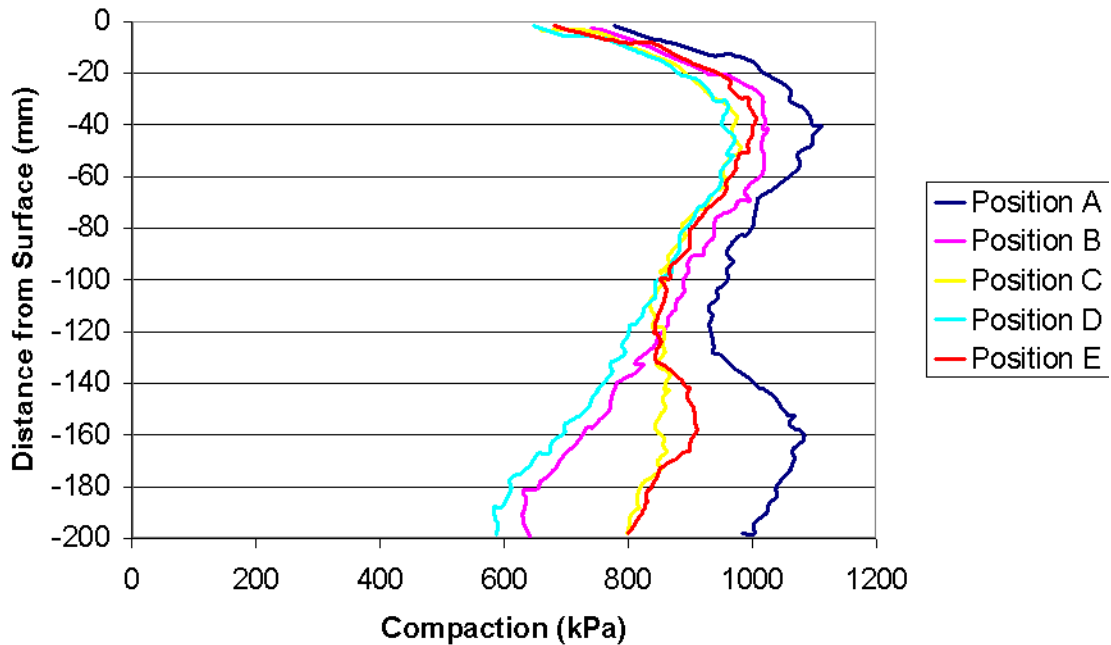


Figure A1.10: Penetrometer readings for 5m position, high moisture (8.8% d.b.), high compaction (1,100 kPa) from viscometer test

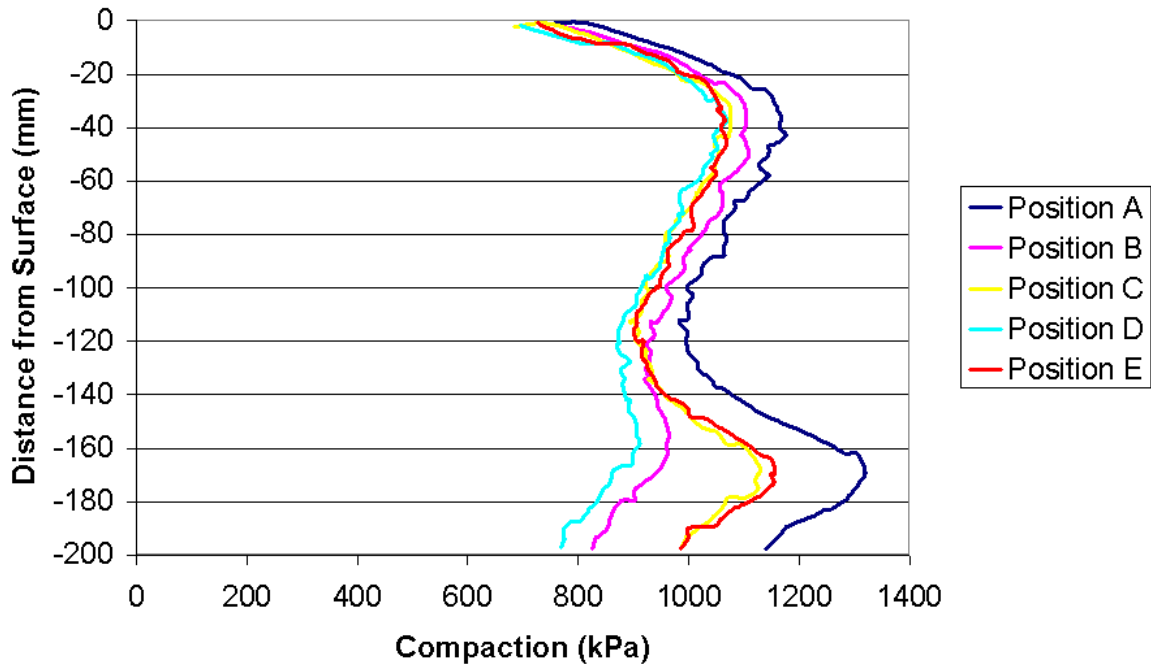


Figure A1.11: Penetrometer readings for 10m position, high moisture (8.8% d.b.), high compaction (1,100 kPa) from viscometer test

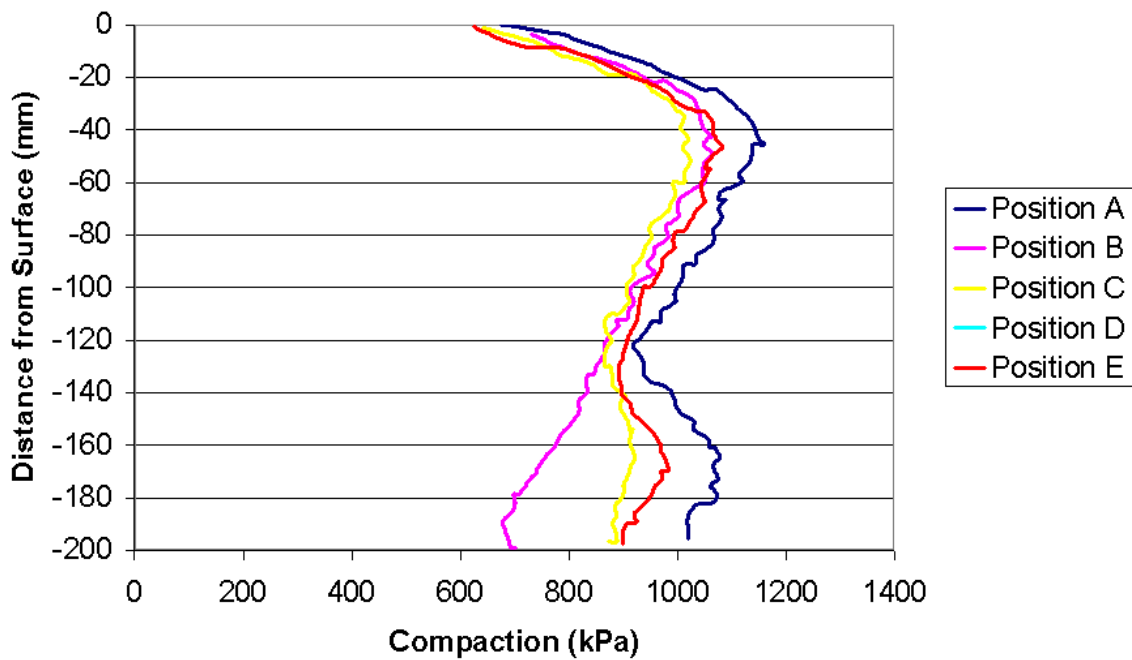


Figure A1.12: Penetrometer readings for 15m position, high moisture (8.8% d.b.), high compaction (1,100 kPa) from viscometer test

Table A1.1: Viscometer run sheet and measurements for low moisture (7.4% d.b.)

#	Compaction (kPa)	Moisture (% d.b.)	Soil Treatment	Bin Position (m)	Location	Motor Speed (rpm)	Shaft Speed (rpm)	Shaft Speed (rad/s)	Torque (N-m)	Shear (kN/m ²)
1	200	7.43	1	5	A	320	0.107	0.011	5.2415	8.60
2	200	7.43	1	5	B	1280	0.427	0.045	4.4502	7.30
3	200	7.43	1	5	C	2560	0.853	0.089	3.9292	6.44
4	200	7.43	1	5	D	160	0.053	0.006	3.9361	6.45
5	200	7.43	1	5	E	4000	1.333	0.140	4.9109	8.05
6	200	7.43	1	5	F	640	0.213	0.022	4.2527	6.97
7	200	7.43	1	5	G	80	0.027	0.003	3.8314	6.28
8	200	7.43	1	10	A	320	0.107	0.011	4.9835	8.17
9	200	7.43	1	10	B	4000	1.333	0.140	4.7154	7.73
10	200	7.43	1	10	C	1280	0.427	0.045	4.5884	7.52
11	200	7.43	1	10	D	640	0.213	0.022	4.1266	6.77
12	200	7.43	1	10	E	2560	0.853	0.089	4.5178	7.41
13	200	7.43	1	10	F	80	0.027	0.003	4.1589	6.82
14	200	7.43	1	10	G	160	0.053	0.006	4.3949	7.21
15	200	7.43	1	15	A	160	0.053	0.006	6.1698	10.12
16	200	7.43	1	15	B	80	0.027	0.003	5.3826	8.83
17	200	7.43	1	15	C	320	0.107	0.011	5.0238	8.24
18	200	7.43	1	15	D	2560	0.853	0.089	5.1972	8.52
19	200	7.43	1	15	E	640	0.213	0.022	5.6628	9.29
20	200	7.43	1	15	F	1280	0.427	0.045	4.9048	8.04
21	200	7.43	1	15	G	4000	1.333	0.140	5.1185	8.39
22	1100	7.32	2	5	A	320	0.107	0.011	21.2569	34.86
23	1100	7.32	2	5	B	1280	0.427	0.045	18.1335	29.74
24	1100	7.32	2	5	C	4000	1.333	0.140	16.9176	27.74
25	1100	7.32	2	5	D	160	0.053	0.006	15.7585	25.84
26	1100	7.32	2	5	E	80	0.027	0.003	19.3669	31.76
27	1100	7.32	2	5	F	640	0.213	0.022	17.5286	28.75
28	1100	7.32	2	5	G	2560	0.853	0.089	16.7632	27.49
29	1100	7.32	2	10	A	1280	0.427	0.045	19.3819	31.78
30	1100	7.32	2	10	B	80	0.027	0.003	17.4788	28.66
31	1100	7.32	2	10	C	320	0.107	0.011	18.2972	30.01
32	1100	7.32	2	10	D	4000	1.333	0.140	18.7787	30.80
33	1100	7.32	2	10	E	2560	0.853	0.089	18.6580	30.60
34	1100	7.32	2	10	F	160	0.053	0.006	17.7712	29.14
35	1100	7.32	2	6	G	640	0.213	0.022	18.1075	29.69
36	1100	7.32	2	15	A	320	0.107	0.011	20.5890	33.76
37	1100	7.32	2	15	B	4000	1.333	0.140	20.3183	33.32
38	1100	7.32	2	15	C	80	0.027	0.003	17.8057	29.20
39	1100	7.32	2	15	D	640	0.213	0.022	19.4394	31.88
40	1100	7.32	2	15	E	2560	0.853	0.089	21.3211	34.96
41	1100	7.32	2	15	F	1280	0.427	0.045	18.5315	30.39
42	1100	7.32	2	15	G	160	0.053	0.006	17.5072	28.71

Table A1.2: Viscometer run sheet and measurements for high moisture (8.8% d.b.)

#	Compaction (kPa)	Moisture (% d.b.)	Soil Treatment	Bin Position (m)	Location	Motor Speed (rpm)	Shaft Speed (rpm)	Shaft Speed (rad/s)	Torque (N-m)	Shear (kN/m ²)
1	200	8.84	1	5	A	4000	1.333	0.140	3.5279	5.79
2	200	8.84	1	5	B	320	0.107	0.011	2.8576	4.69
3	200	8.84	1	5	C	2560	0.853	0.089	2.7760	4.55
4	200	8.84	1	5	D	160	0.053	0.006	2.3597	3.87
5	200	8.84	1	5	E	640	0.213	0.022	2.6551	4.35
6	200	8.84	1	5	F	1280	0.427	0.045	3.1833	5.22
7	200	8.84	1	5	G	80	0.027	0.003	2.5200	4.13
8	200	8.84	1	10	A	80	0.027	0.003	3.3818	5.55
9	200	8.84	1	10	B	1280	0.427	0.045	3.3929	5.56
10	200	8.84	1	10	C	2560	0.853	0.089	3.0350	4.98
11	200	8.84	1	10	D	320	0.107	0.011	3.3878	5.56
12	200	8.84	1	10	E	4000	1.333	0.140	4.4039	7.22
13	200	8.84	1	10	F	640	0.213	0.022	3.4836	5.71
14	200	8.84	1	10	G	160	0.053	0.006	3.3817	5.55
15	200	8.84	1	15	A	2560	0.853	0.089	3.7799	6.20
16	200	8.84	1	15	B	4000	1.333	0.140	3.4059	5.59
17	200	8.84	1	15	C	1280	0.427	0.045	3.2144	5.27
18	200	8.84	1	15	D	160	0.053	0.006	2.8909	4.74
19	200	8.84	1	15	E	80	0.027	0.003	3.0613	5.02
20	200	8.84	1	15	F	640	0.213	0.022	2.6087	4.28
21	200	8.84	1	15	G	320	0.107	0.011	2.8274	4.64
22	1100	8.81	2	5	A	80	0.027	0.003	16.0016	26.24
23	1100	8.81	2	5	B	1280	0.427	0.045	12.9918	21.31
24	1100	8.81	2	5	C	4000	1.333	0.140	14.1182	23.15
25	1100	8.81	2	5	D	640	0.213	0.022	15.7274	25.79
26	1100	8.81	2	5	E	320	0.107	0.011	15.6902	25.73
27	1100	8.81	2	5	F	2560	0.853	0.089	15.2386	24.99
28	1100	8.81	2	5	G	160	0.053	0.006	14.6006	23.94
29	1100	8.81	2	10	A	320	0.107	0.011	17.8580	29.29
30	1100	8.81	2	10	B	1280	0.427	0.045	14.9373	24.50
31	1100	8.81	2	10	C	640	0.213	0.022	13.9083	22.81
32	1100	8.81	2	10	D	80	0.027	0.003	13.2561	21.74
33	1100	8.81	2	10	E	2560	0.853	0.089	15.2015	24.93
34	1100	8.81	2	10	F	4000	1.333	0.140	17.7973	29.19
35	1100	8.81	2	10	G	160	0.053	0.006	11.5793	18.99
36	1100	8.81	2	15	A	640	0.213	0.022	18.0742	29.64
37	1100	8.81	2	15	B	160	0.053	0.006	13.7344	22.52
38	1100	8.81	2	15	C	2560	0.853	0.089	15.6295	25.63
39	1100	8.81	2	15	D	4000	1.333	0.140	17.8559	29.28
40	1100	8.81	2	15	E	80	0.027	0.003	15.8270	25.95
41	1100	8.81	2	15	F	1280	0.427	0.045	14.9515	24.52
42	1100	8.81	2	15	G	320	0.107	0.011	12.2688	20.12

Table A2.1: Rigid flat bar test data summary

Run #	Data #	Tool Type	Depth (in)	Depth (mm)	Speed (mph)	Speed (kph)	Comp. (H/L)	Comp. (kPa)	Draft Avg. (N)	Draft Stdev (N)
1	2	Bent	4	102	6	9.66	Low	200	----	----
2	4	Bent	4	102	2	3.22	Low	200	----	----
3	5	Flat	2	51	6	9.66	Low	200	187.57	16.72
4	6	Bent	2	51	4	6.44	High	1100	----	----
5	7	Bent	2	51	2	3.22	High	1100	----	----
6	8	Flat	4	102	2	3.22	High	1100	1010.82	108.11
7	9	Bent	2	51	6	9.66	Low	200	----	----
8	10	Bent	2	51	4	6.44	Low	200	----	----
9	12	Bent	4	102	4	6.44	Low	200	----	----
10	13	Flat	2	51	4	6.44	High	1100	647.77	71.06
11	14	Flat	2	51	2	3.22	High	1100	472.59	53.19
12	15	Flat	4	102	4	6.44	High	1100	1275.01	89.02
13	16	Flat	2	51	4	6.44	Low	200	161.12	12.85
14	17	Flat	4	102	6	9.66	Low	200	415.13	17.90
15	18	Flat	4	102	4	6.44	Low	200	335.04	14.27
16	19	Flat	4	102	4	6.44	Low	200	370.82	21.02
17	20	Flat	2	51	2	3.22	Low	200	108.13	10.34
18	21	Flat	2	51	6	9.66	High	1100	733.32	71.56
19	22	Flat	4	102	6	9.66	High	1100	1602.52	103.80
20	23	Flat	4	102	4	6.44	High	1100	1370.64	101.73
21	24	Flat	4	102	4	6.44	Low	200	422.57	16.50
22	26	Flat	4	102	6	9.66	Low	200	454.11	40.18
23	27	Flat	2	51	4	6.44	Low	200	141.34	12.22
24	28	Flat	4	102	2	3.22	High	1100	1243.62	137.79
25	29	Flat	2	51	2	3.22	High	1100	538.88	56.62
26	30	Flat	2	51	4	6.44	High	1100	664.33	69.94
27	31	Flat	4	102	6	9.66	High	1100	1655.36	97.77
28	32	Flat	2	51	6	9.66	High	1100	703.27	69.30
29	33	Flat	2	51	6	9.66	Low	200	225.24	19.53
30	34	Flat	4	102	2	3.22	Low	200	291.96	15.29
31	35	Flat	2	51	2	3.22	Low	200	112.28	11.71
32	36	Flat	4	102	2	3.22	High	1100	906.65	104.29
33	37	Flat	2	51	6	9.66	High	1100	560.26	64.14
34	38	Flat	2	51	4	6.44	High	1100	470.70	60.08
35	40	Flat	2	51	6	9.66	Low	200	244.61	19.32
36	41	Flat	4	102	2	3.22	Low	200	269.99	12.08
37	42	Flat	2	51	4	6.44	Low	200	157.33	13.50
38	43	Flat	4	102	6	9.66	High	1100	1571.84	102.75
39	44	Flat	4	102	4	6.44	High	1100	1239.86	89.63
40	45	Flat	2	51	2	3.22	High	1100	439.04	59.58
41	46	Flat	4	102	6	9.66	Low	200	380.35	16.23
42	47	Flat	4	102	4	6.44	Low	200	273.54	12.01
43	48	Flat	2	51	2	3.22	Low	200	73.71	7.78

Note: Run 18 was supposed to be R18F42L.

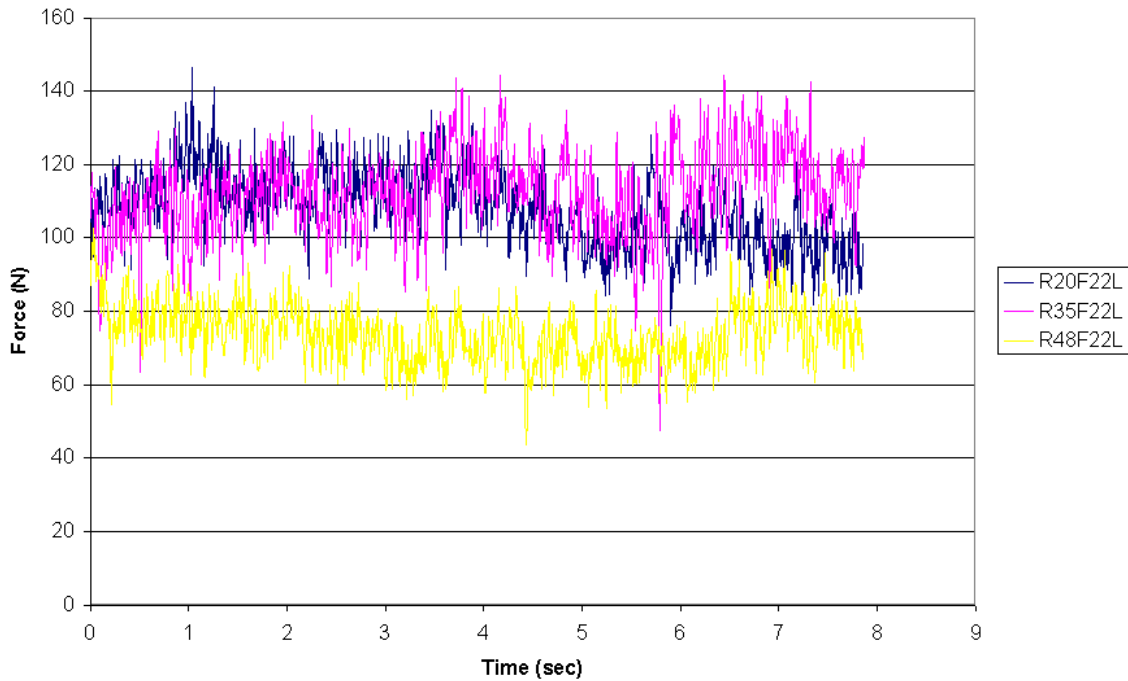


Figure A2.1: Rigid flat bar test – treatment #1 draft force time histories – 51 mm depth, 0.89 m/s, low compaction (200 kPa)

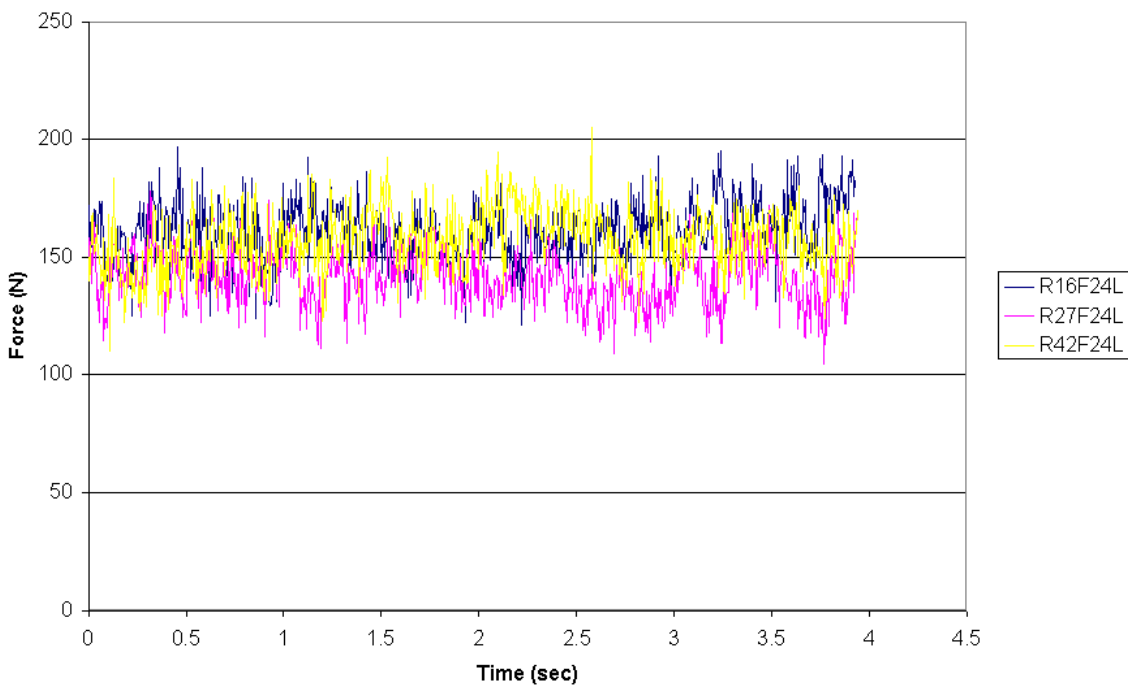


Figure A2.2: Rigid flat bar test – treatment #2 draft force time histories – 51 mm depth, 1.79 m/s, low compaction (200 kPa)

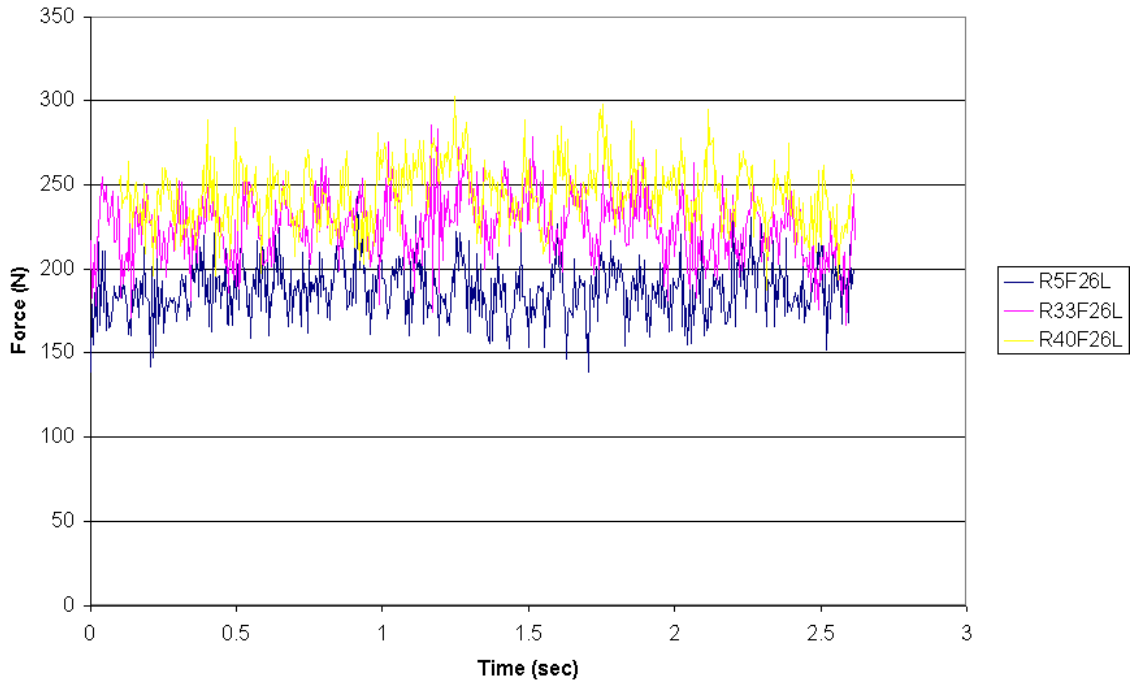


Figure A2.3: Rigid flat bar test – treatment #3 draft force time histories – 51 mm depth, 2.68 m/s, low compaction (200 kPa)

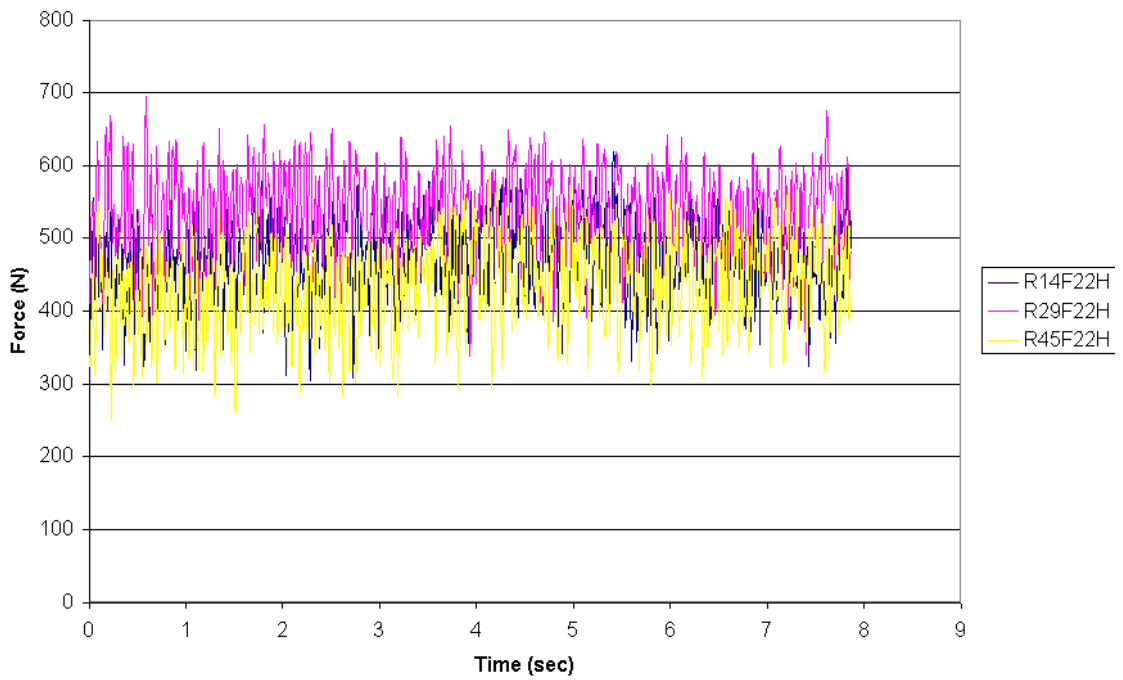


Figure A2.4: Rigid flat bar test – treatment #4 draft force time histories – 51 mm depth, 0.89 m/s, high compaction (1,100 kPa)

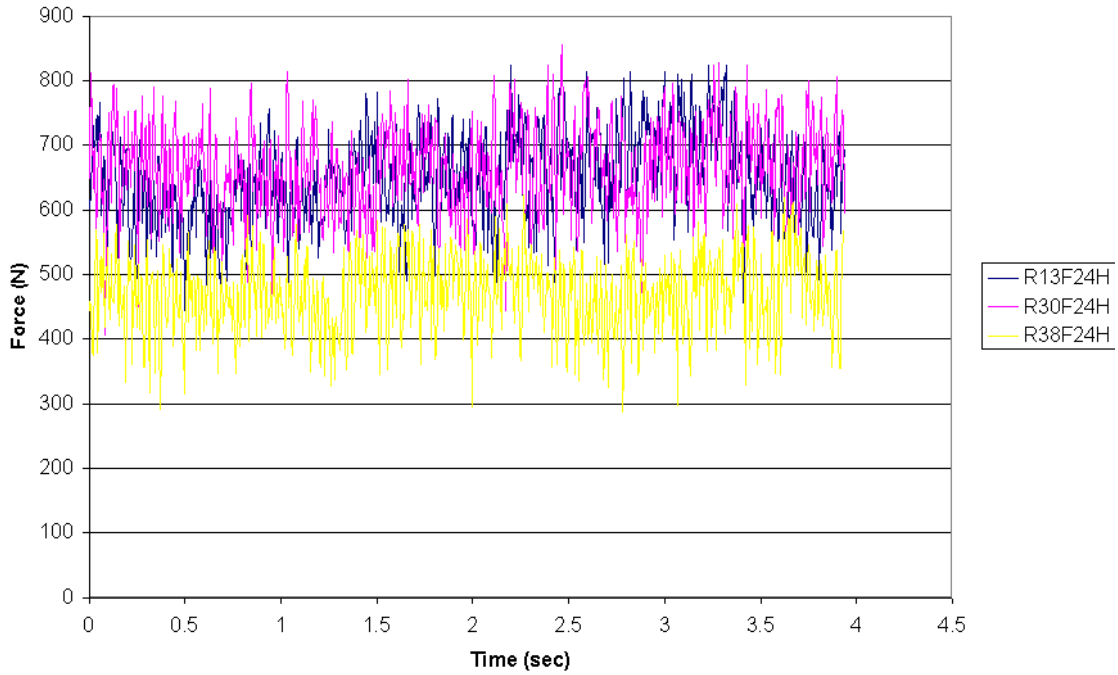


Figure A2.5: Rigid flat bar test – treatment #5 draft force time histories – 51 mm depth, 1.79 m/s, high compaction (1,100 kPa)

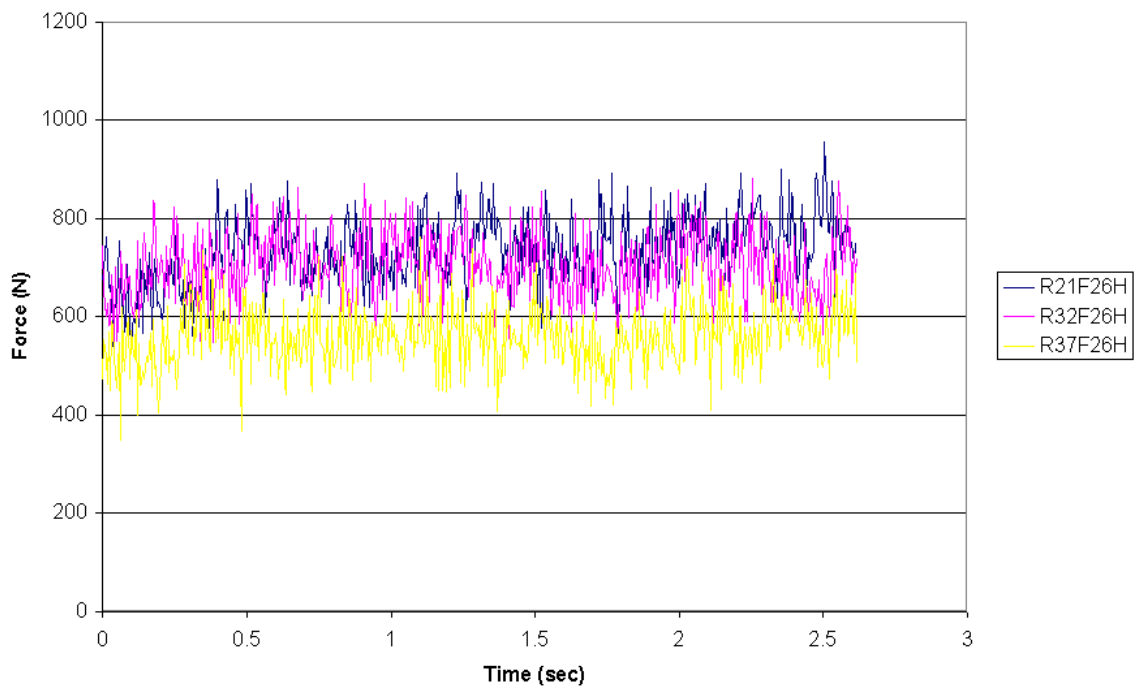


Figure A2.6: Rigid flat bar test – treatment #6 draft force time histories – 51 mm depth, 2.68 m/s, high compaction (1,100 kPa)

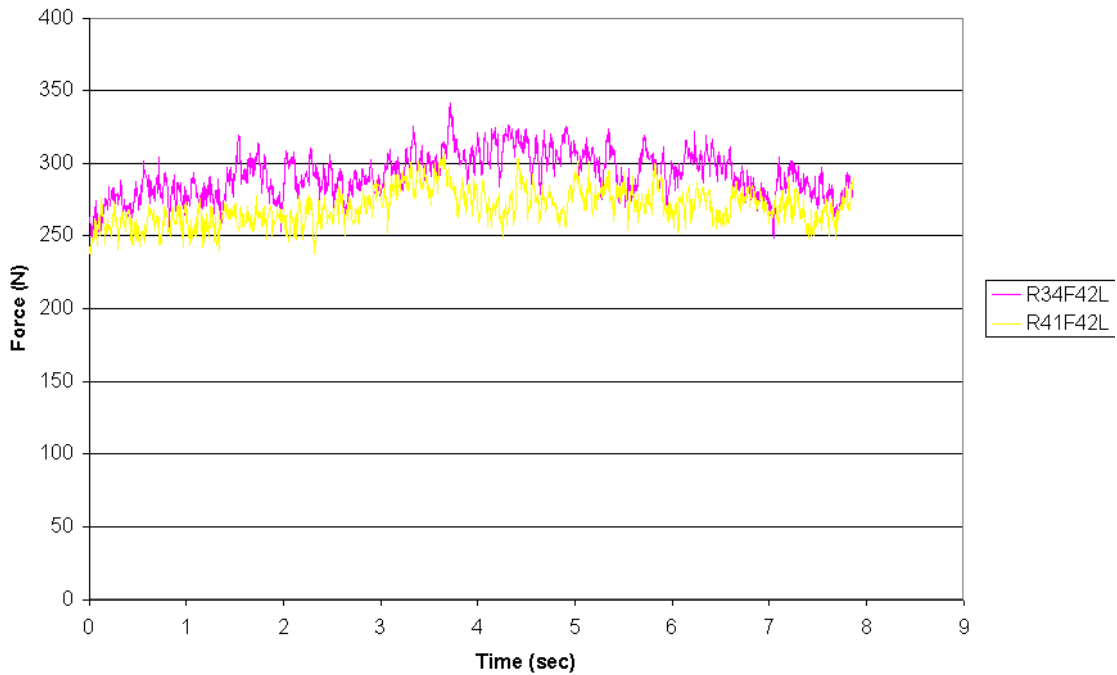


Figure A2.7: Rigid flat bar test – treatment #7 draft force time histories – 102 mm depth, 0.89 m/s, low compaction (200 kPa)

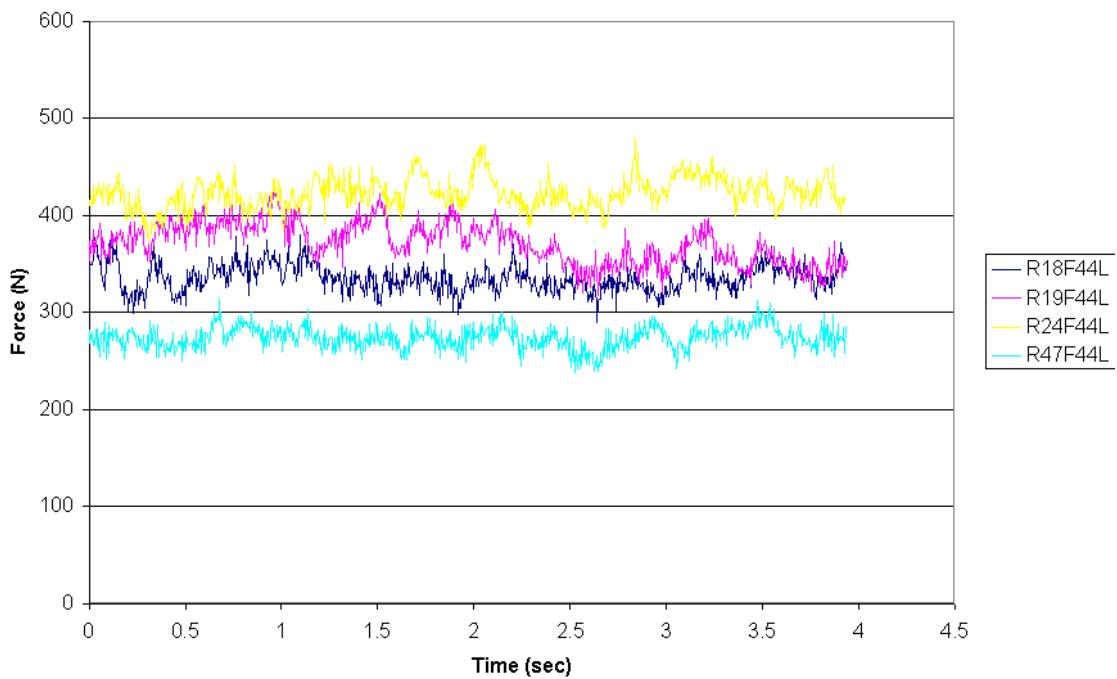


Figure A2.8: Rigid flat bar test – treatment #8 draft force time histories – 102 mm depth, 1.79 m/s depth, low compaction (200 kPa)

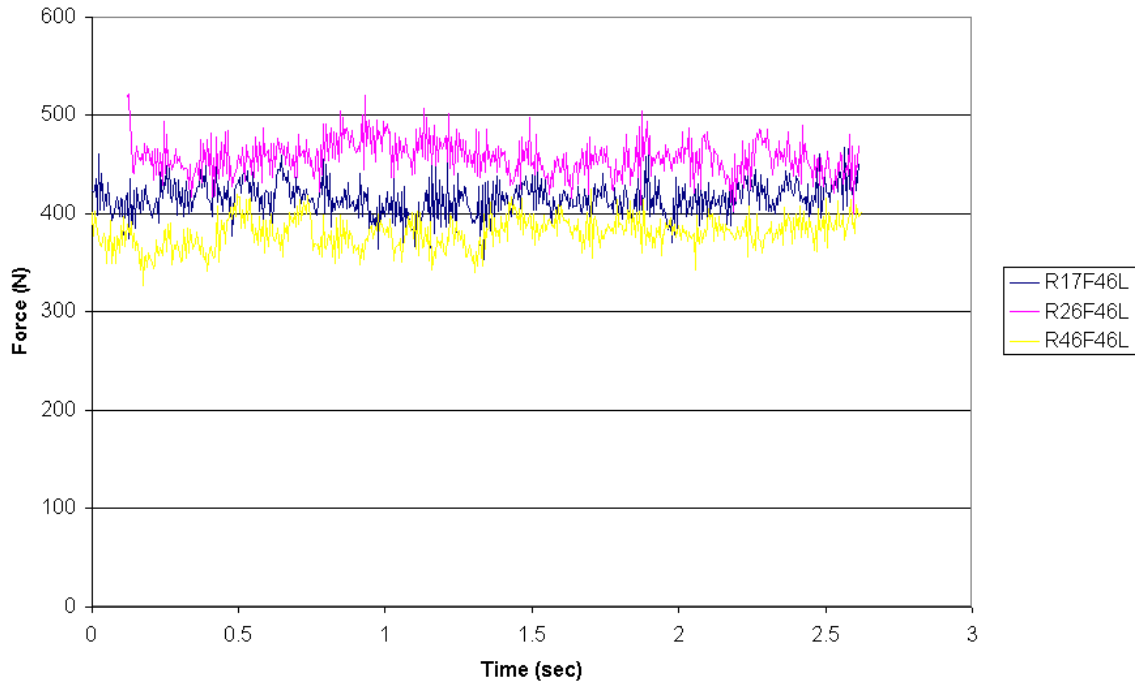


Figure A2.9: Rigid flat bar test – treatment #9 draft force time histories – 102 mm depth, 2.68 m/s, low compaction (200 kPa)

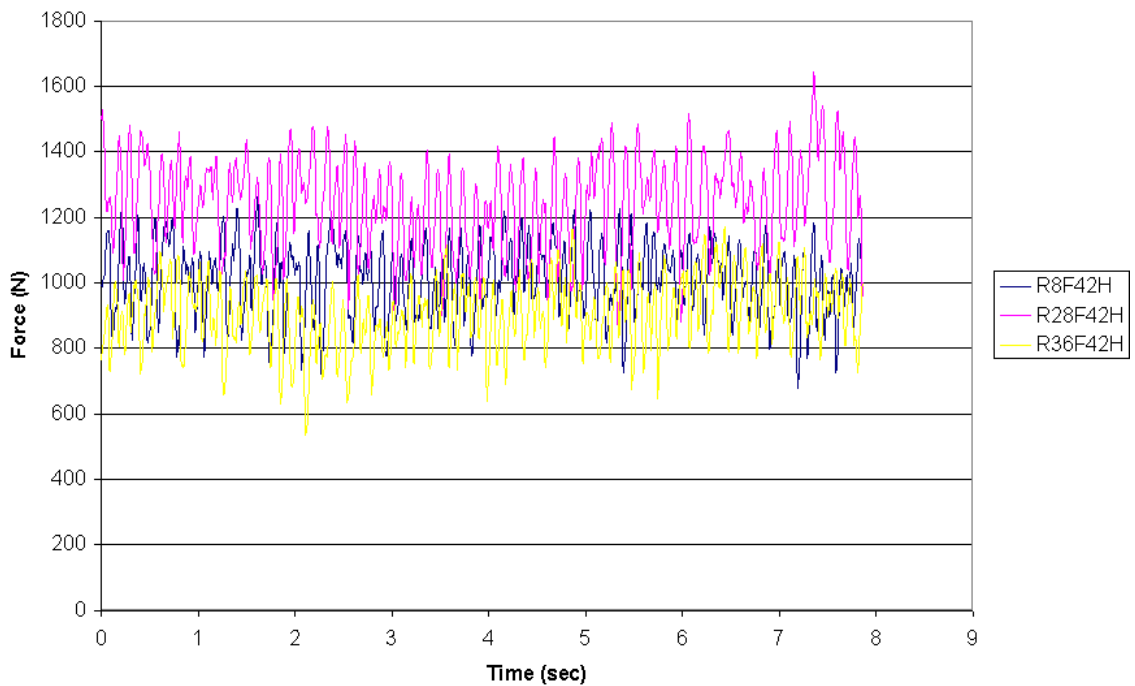


Figure A2.10: Rigid flat bar test – treatment #10 draft force time histories – 102 mm depth, 0.89 m/s, high compaction (1,100 kPa)

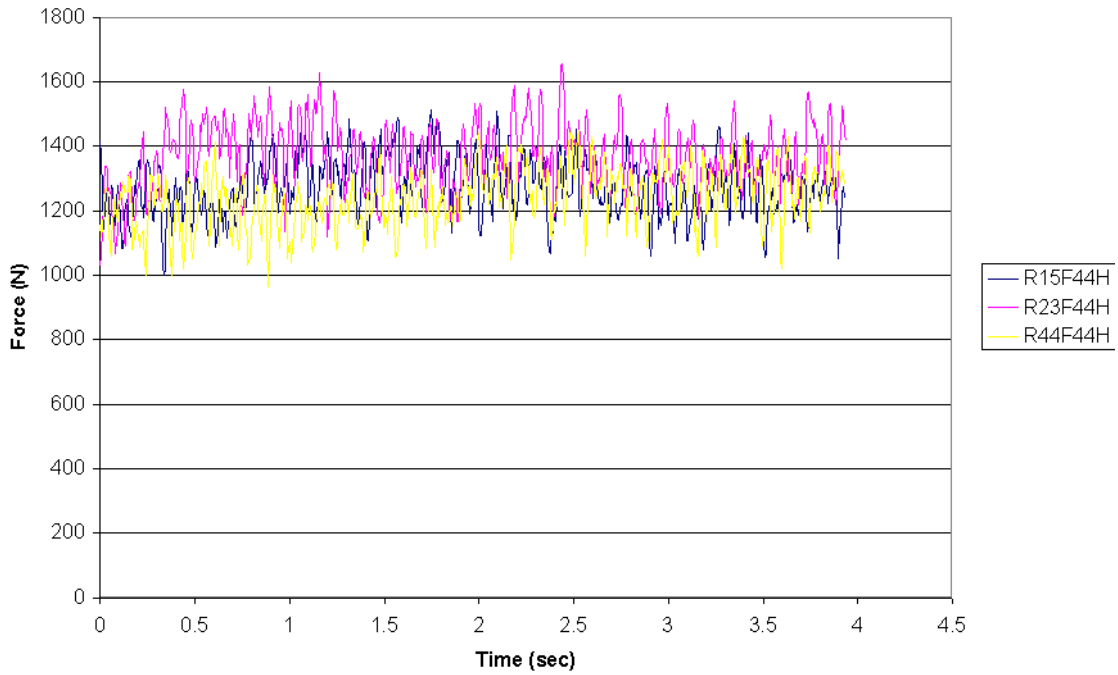


Figure A2.11: Rigid flat bar test – treatment #11 draft force time histories – 102 mm depth, 1.79 m/s, high compaction (1,100 kPa)

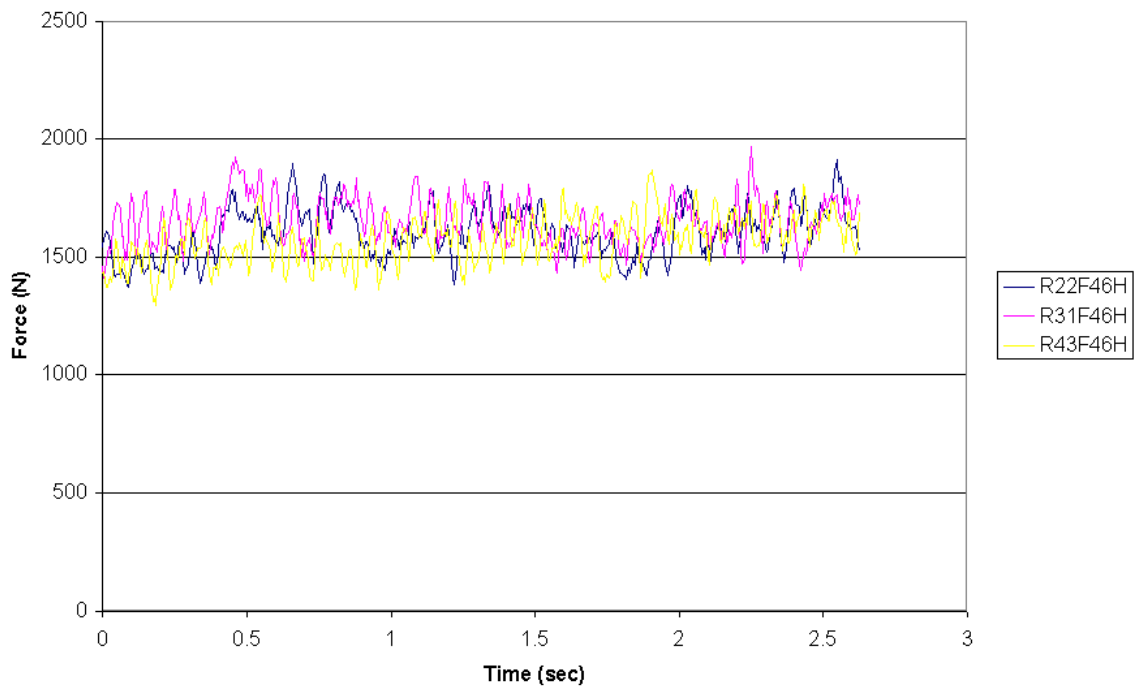


Figure A2.12: Rigid flat bar test – treatment #12 draft force time histories – 102 mm depth, 2.68 m/s, high compaction (1,100 kPa)

Table A2.2: Rigid flat bar test draft force regression analysis

Regression Statistics	
Multiple R	0.931542473
R Square	0.867771378
Adjusted R Square	0.866374945
Standard Error	177.8956142
Observations	36

ANOVA					
	df	SS	MS	F	Significance F
Regression	3	6345999.005	2245333	70.0017	3.77425E-14
Residual	32	1012699.186	31646.85		
Total	35	7658698.791			

	Coefficients	Standard Error	t Stat	P-value	Lower 95%	Upper 95%	Lower 95.0%	Upper 95.0%
Intercept	-841.4377066	126743.1191	-6.638922	1.73E-07	-1099.604991	-583.2704224	-1099.604991	-583.2704224
Depth	9.10683717	1.169001293	7.793941	6.82E-09	6.727696401	11.48597794	6.727696401	11.48597794
Speed	135.4014851	41.56359815	3.257694	0.002861	50.73920651	220.0637637	50.73920651	220.0637637
Comp.	0.77794256	0.065927184	11.80003	3.41E-13	0.643663281	0.912231839	0.643663281	0.912231839

Table A3.1: Field cultivator standard lab test load data summary

Run#	Sweep Width (in)	Sweep Width (mm)	Speed (mph)	Speed (m/s)	Depth (in)	Depth (mm)	Compaction Level (MPa)	Moisture Level (% dH)	Draft Avg. (kN)	Draft Sidev (kN)	Draft Max (kN)	Draft Min (kN)	Vertical Avg. (kN)	Vertical Sidev (kN)	Vertical Max (kN)	Vertical Min (kN)	Lateral Avg. (kN)
1	7	177.8	2	0.89	6	152.4	1100	8.3	772.8	159.2	1124.3	290.6	-336.9	130.2	80.6	-618.8	-3.0
2	7	177.8	6	2.68	3	76.2	1100	8.3	620.2	75.1	846.9	409.8	-76.2	145.6	367.5	-487.7	-7.4
3	7	177.8	6	2.68	6	152.4	200	8.3	451.7	30.3	544.4	342.7	-206.7	34.3	-108.2	-332.4	-10.5
4	7	177.8	2	0.89	8	152.4	200	8.3	229.6	19.1	283.9	170.7	-116.7	15.8	-64.4	-177.9	-0.3
5	10	254	6	2.68	6	152.4	1100	8.3	1163.9	59.7	1416.7	974.4	-456.5	131.0	9.3	-900.8	-40.0
6	7	177.8	2	0.89	3	76.2	1100	8.3	299.2	60.4	432.5	94.0	4.4	85.2	212.2	-191.7	0.8
7	7	177.8	10	4.47	3	76.2	200	8.3	353.8	39.2	443.5	222.8	-141.1	65.0	23.3	-314.7	-6.7
8	10	254	6	2.68	3	76.2	200	8.3	234.2	35.6	348.0	115.0	-76.9	47.3	63.6	-197.7	8.6
9	10	254	6	2.68	6	152.4	200	8.3	527.3	38.4	640.1	377.7	-253.7	52.1	-133.8	-407.4	-5.0
10	7	177.8	2	0.89	3	76.2	200	17.8	107.6	22.6	196.7	46.4	-31.0	21.1	68.5	-126.2	3.1
11	7	177.8	10	4.47	6	152.4	1100	8.3	1575.3	182.7	1913.9	1211.5	-585.4	483.7	315.1	-1617.9	-13.3
12	10	254	6	2.68	3	76.2	1100	8.3	774.7	93.7	984.3	508.9	-100.9	140.0	349.6	-490.8	-9.2
13	7	177.8	6	2.68	3	76.2	200	8.3	172.8	35.8	284.0	72.3	-59.3	47.4	96.2	-131.0	-8.3
14	7	177.8	10	4.47	6	152.4	200	8.3	800.6	61.3	811.4	434.1	-257.0	82.1	-61.3	-454.2	2.6
15	7	177.8	10	4.47	3	76.2	1100	8.3	844.7	105.9	1119.7	422.2	-158.0	142.3	388.1	-436.7	-2.3
16	7	177.8	6	2.68	6	152.4	1100	8.3	950.2	194.4	1428.2	197.6	-438.8	179.9	114.2	-1061.9	5.4
16	7	177.8	6	2.68	3	76.2	200	8.3	196.1	29.6	299.2	88.0	-55.3	43.5	64.1	-193.1	-1.3
19	7	177.8	6	2.68	6	152.4	200	8.3	413.0	29.6	488.0	314.6	-196.5	37.0	-86.0	-240.3	4.5
20	7	177.8	6	2.68	6	76.2	1100	8.3	1203.9	78.9	1424.0	978.9	-566.3	244.9	193.0	-1729.5	-14.5
21	7	177.8	6	2.68	3	152.4	1100	8.3	592.6	86.4	823.4	333.5	-62.5	145.5	392.0	-483.0	5.1
22	7	177.8	6	2.68	3	76.2	1100	8.3	638.4	99.4	937.9	362.2	-23.4	162.8	455.9	-530.5	-3.1
23	7	177.8	6	2.68	6	152.4	1100	8.3	1128.8	83.3	1395.4	834.3	-524.3	233.1	223.4	-1215.3	8.2
24	7	177.8	6	2.68	6	76.2	200	8.3	439.9	30.6	536.3	350.9	-217.1	38.7	-112.0	-340.6	-0.3
25	7	177.8	6	2.68	3	152.4	200	8.3	190.7	25.8	277.1	103.2	-60.6	45.6	108.9	-176.9	-0.3
26	7	177.8	6	2.68	3	76.2	200	6.9	124.1	31.4	222.8	33.5	-48.4	35.7	46.2	-153.4	-3.5
27	10	254	6	2.68	6	152.4	200	6.9	361.0	37.5	469.1	228.7	-204.0	54.5	-22.4	-362.5	-9.0
28	7	177.8	10	4.47	6	152.4	200	6.9	593.9	44.7	760.4	462.6	-282.8	81.9	-59.9	-448.2	-2.8
29	10	254	6	2.68	3	76.2	200	6.9	172.1	30.5	281.9	68.6	-82.2	47.2	76.1	-228.2	-9.8
30	7	177.8	2	0.89	6	152.4	1100	6.9	270.8	48.0	389.9	149.0	-134.5	40.9	-34.9	-257.9	3.0
31	7	177.8	10	4.47	3	76.2	1100	6.9	330.3	62.5	533.6	206.2	-108.8	94.1	160.3	-387.5	-3.1
32	7	177.8	6	2.68	3	76.2	1100	6.9	178.0	41.1	309.3	50.0	-47.8	70.4	179.7	-257.0	2.2
33	7	177.8	2	0.89	3	76.2	1100	6.9	96.6	32.1	178.9	-15.4	-17.3	32.9	94.4	-125.1	-1.0
34	7	177.8	2	0.89	6	152.4	200	6.9	175.7	12.0	207.7	119.7	-111.2	12.2	-64.2	-149.8	-1.9
35	7	177.8	10	4.47	3	76.2	200	6.9	237.1	52.4	438.7	138.0	-103.7	95.7	219.3	-386.6	-2.3
36	7	177.8	10	4.47	6	152.4	1100	6.9	831.1	74.6	1094.6	606.1	-365.0	292.7	256.1	-1091.3	-6.5
37	10	254	6	2.68	6	152.4	1100	6.9	595.8	46.8	744.9	459.5	-288.8	84.8	-70.9	-457.6	-12.9
36	7	177.8	2	0.89	3	76.2	200	6.9	65.6	13.2	119.9	31.9	-32.0	15.0	30.1	-65.5	-2.6
39	7	177.8	6	2.68	6	152.4	200	6.9	332.7	39.7	419.1	209.2	-179.7	55.4	-48.4	-325.9	1.0
40	10	254	6	2.68	3	76.2	1100	6.9	195.0	35.4	313.3	85.6	-86.1	72.7	166.9	-300.3	-3.8
41	7	177.8	6	2.68	6	152.4	1100	6.9	431.8	34.6	523.2	320.6	-215.8	76.7	-21.5	-399.9	-3.5
42	7	177.8	6	2.68	6	152.4	1100	6.9	418.2	36.9	543.2	311.7	-212.8	84.1	-54.7	-370.6	2.7
43	7	177.8	6	2.68	3	76.2	1100	6.9	154.9	34.5	245.3	65.2	-50.8	66.1	159.4	-273.9	-0.6
44	7	177.8	6	2.68	6	76.2	200	6.9	111.9	32.7	263.6	26.3	-46.6	50.4	77.1	-130.7	6.6
45	7	177.8	6	2.68	3	152.4	200	6.9	295.3	29.0	378.0	205.9	-182.4	45.9	-9.7	-296.6	8.3
46	7	177.8	6	2.68	6	152.4	200	6.9	288.1	27.7	368.4	216.3	-155.6	76.8	10.0	-324.5	4.8
47	7	177.8	6	2.68	3	76.2	200	6.9	106.5	24.7	186.9	26.8	-51.4	50.8	81.1	-187.2	8.9
48	7	177.8	6	2.68	6	76.2	1100	6.9	150.2	30.5	236.6	52.6	-50.8	60.5	125.3	-216.4	10.2
49	7	177.8	6	2.68	3	152.4	1100	6.9	422.0	31.8	528.2	306.1	-213.4	76.6	-5.6	-423.3	7.7

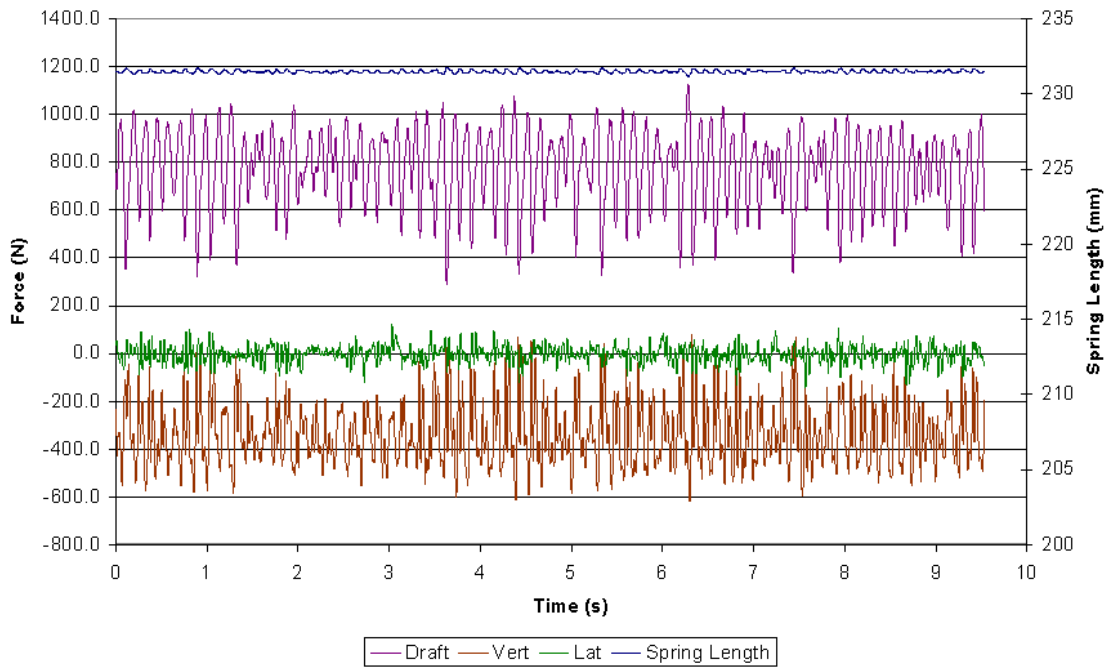


Figure A3.1: Field cultivator standard – run #1 time history results – 178 mm sweep, 152 mm depth, 0.89 m/s, high moisture (8.3% d.b.), high compaction (1,100 kPa)

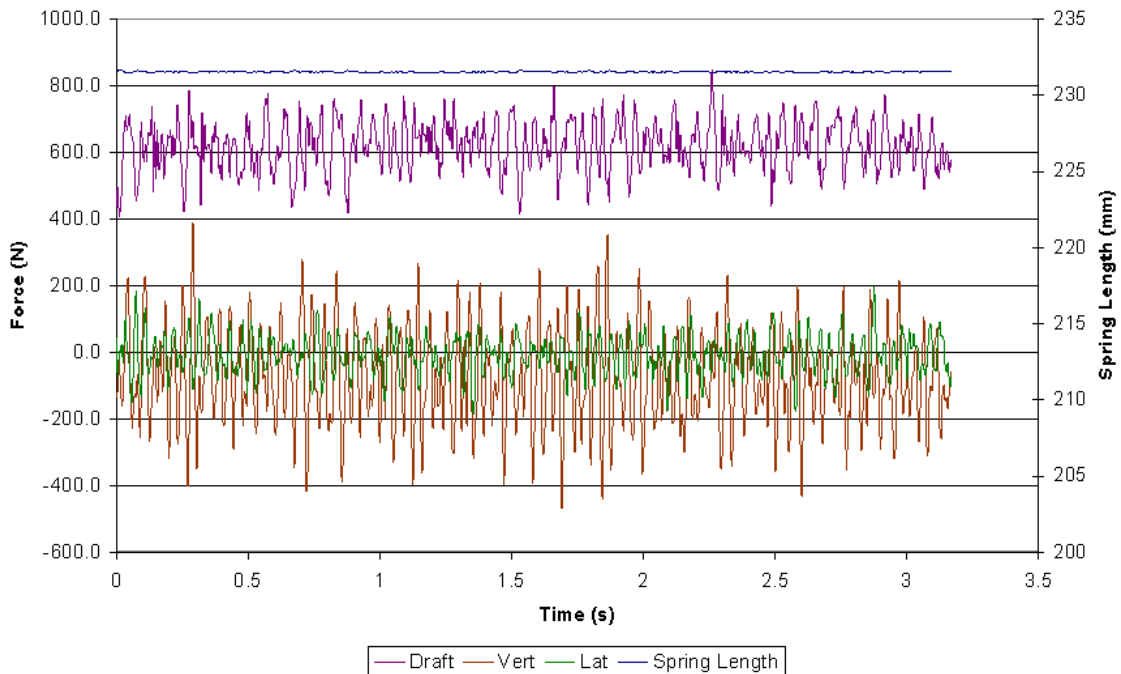


Figure A3.2: Field cultivator standard – run #2 time history results – 178 mm sweep, 76 mm depth, 2.68 m/s, high moisture (8.3% d.b.), high compaction (1,100 kPa)

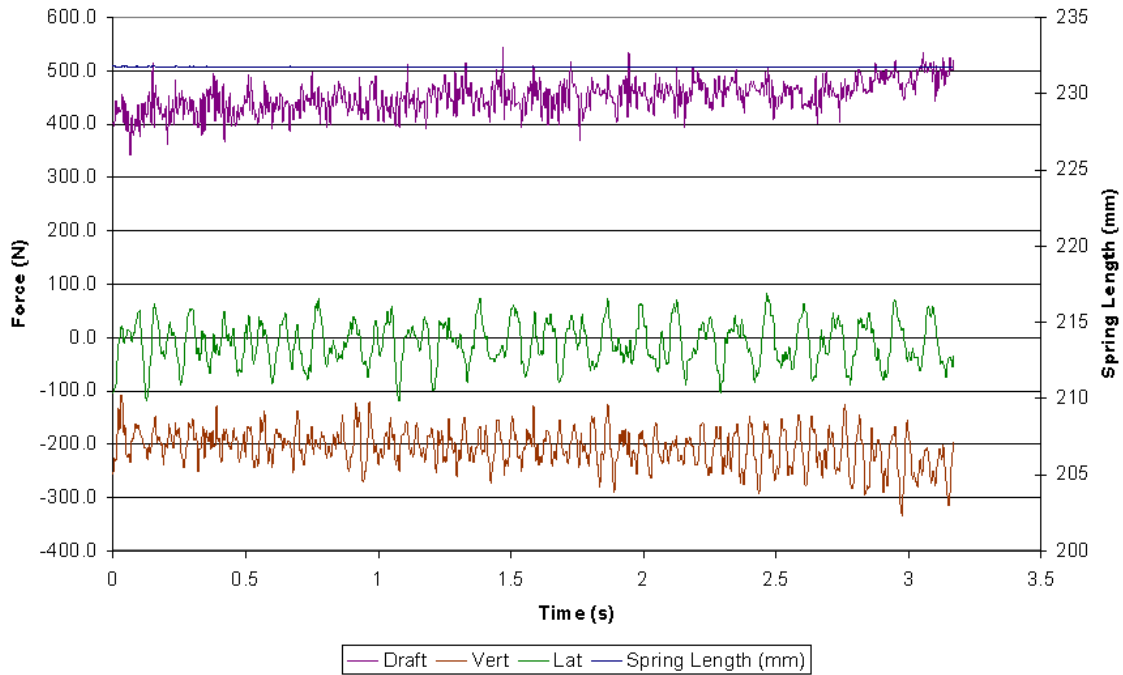


Figure A3.3: Field cultivator standard – run #3 time history results – 178 mm sweep, 152 mm depth, 2.68 m/s, high moisture (8.3% d.b.), low compaction (200 kPa)

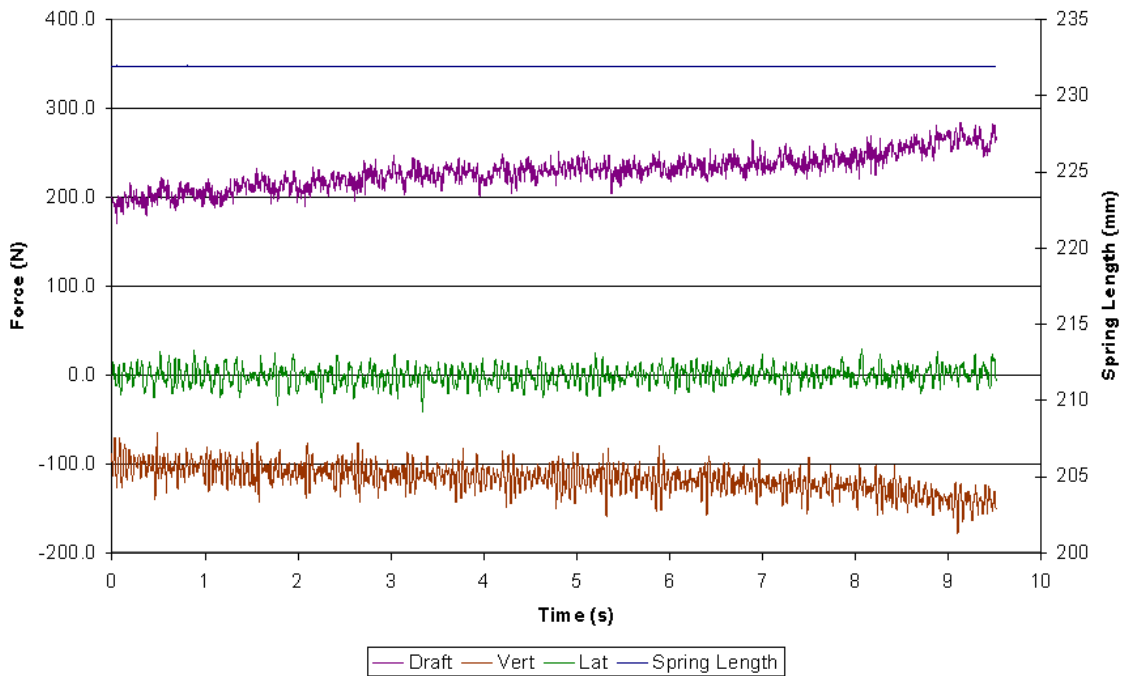


Figure A3.4: Field cultivator standard – run #4 time history results – 178 mm sweep, 152 mm depth, 0.89 m/s, high moisture (8.3% d.b.), low compaction (200 kPa)

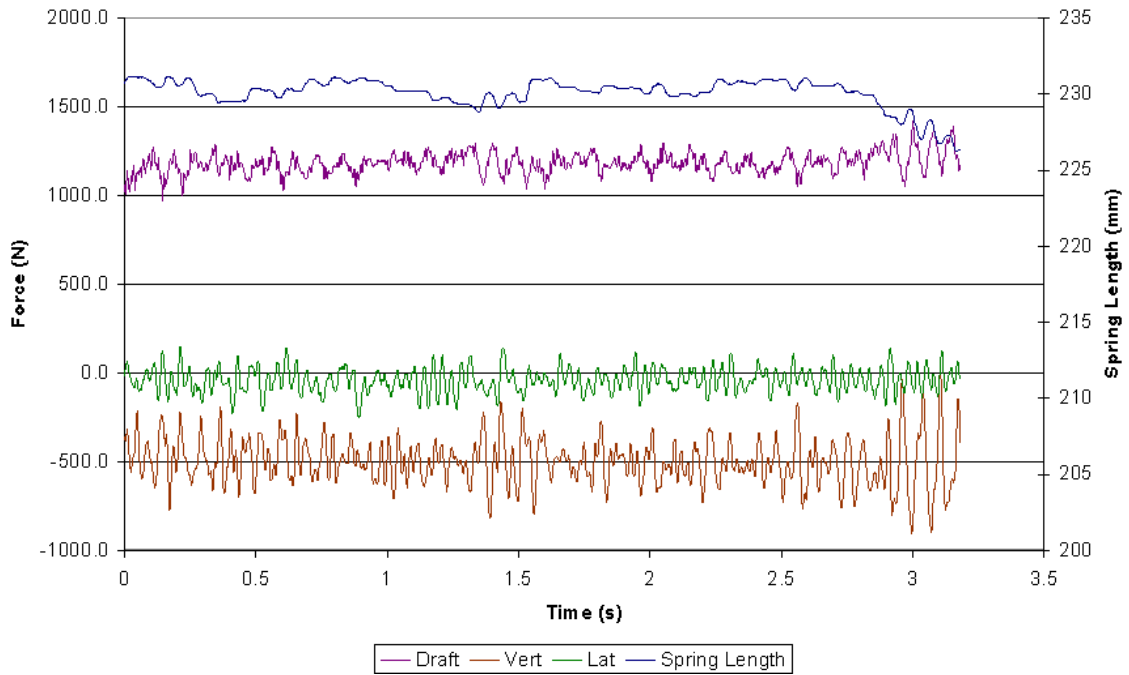


Figure A3.5: Field cultivator standard – run #5 time history results – 254 mm sweep, 152 mm depth, 2.68 m/s, high moisture (8.3% d.b.), high compaction (1,100 kPa)

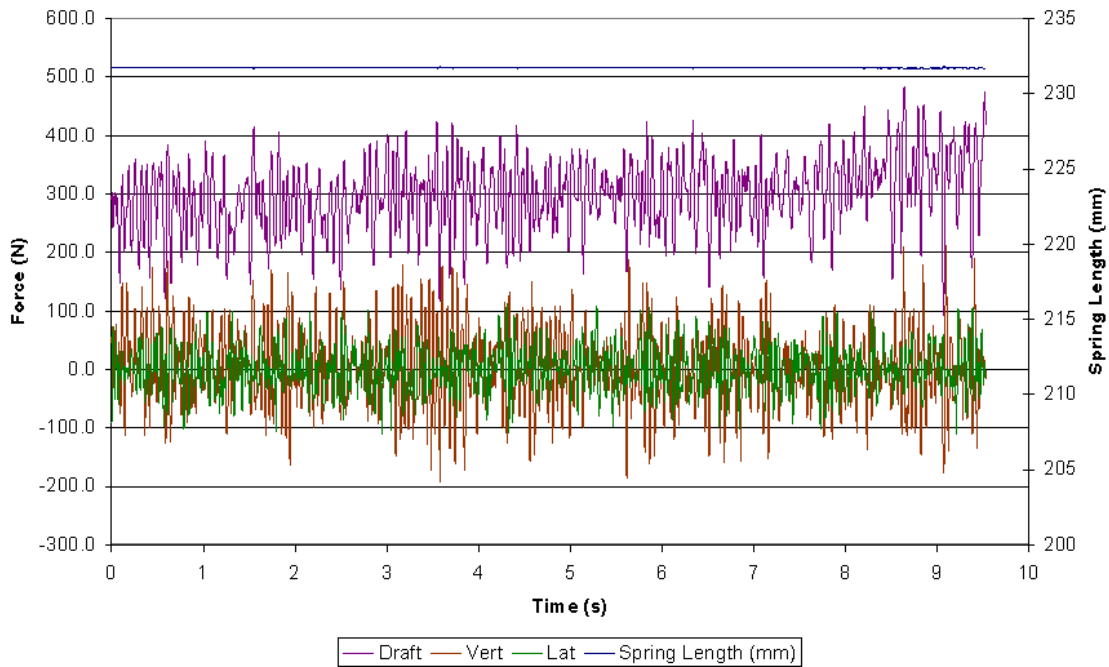


Figure A3.6: Field cultivator standard – run #6 time history results – 178 mm sweep, 76 mm depth, 0.89 m/s, high moisture (8.3% d.b.), high compaction (1,100 kPa)

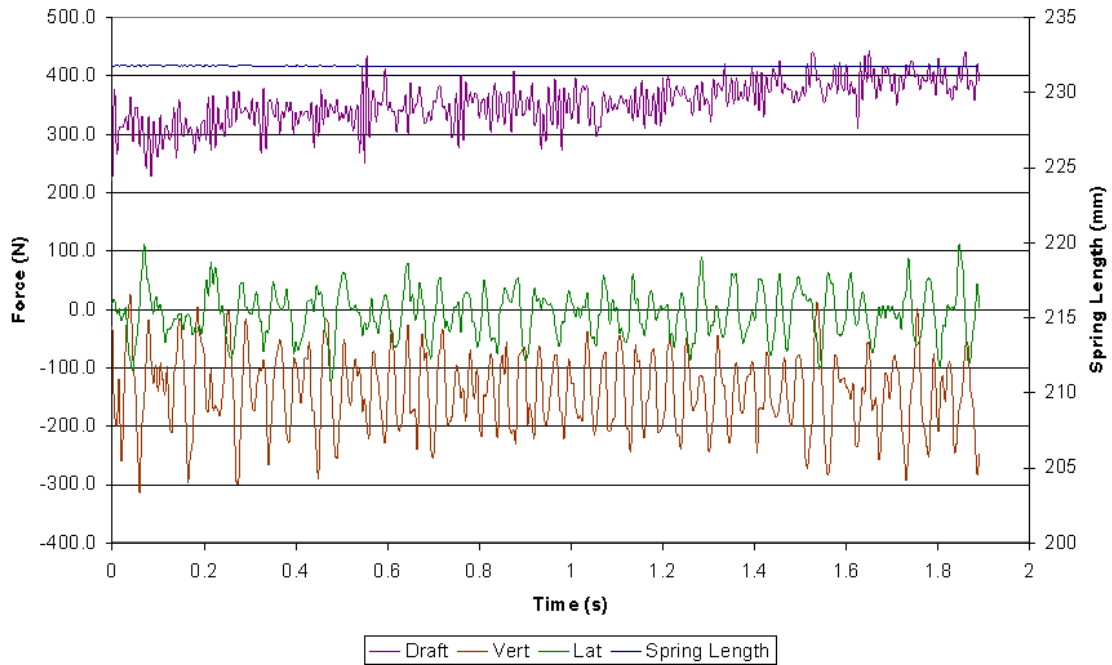


Figure A3.7: Field cultivator standard – run #7 time history results – 178 mm sweep, 76 mm depth, 4.47 m/s, high moisture (8.3% d.b.), low compaction (200 kPa)

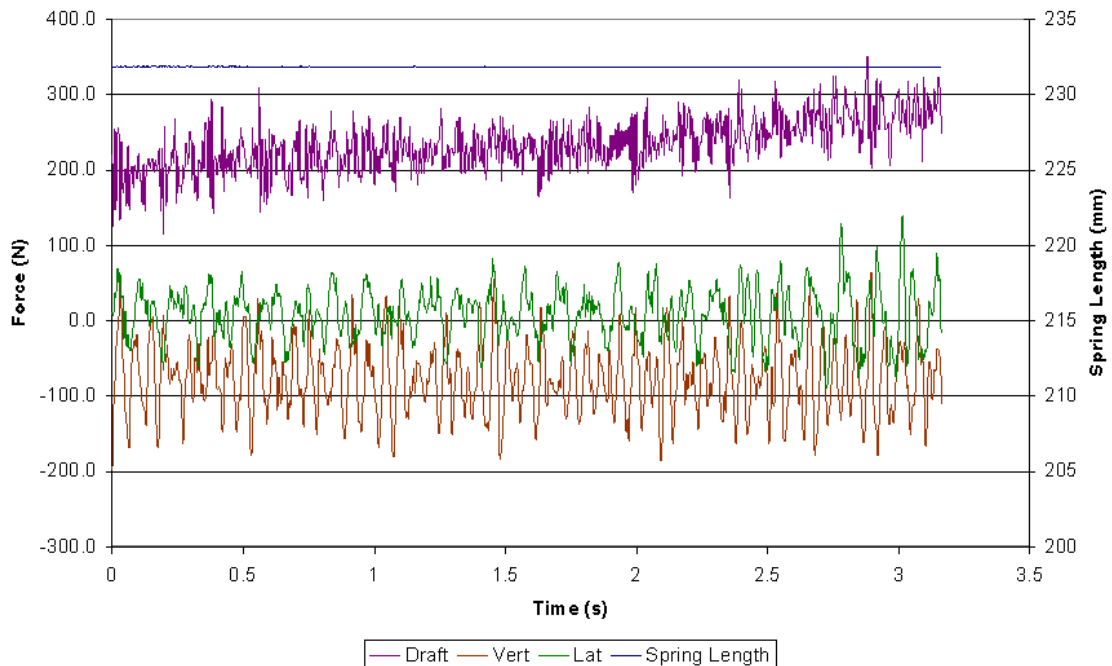


Figure A3.8: Field cultivator standard – run #8 time history results – 254 mm sweep, 76 mm depth, 2.68 m/s, high moisture (8.3% d.b.), low compaction (200 kPa)

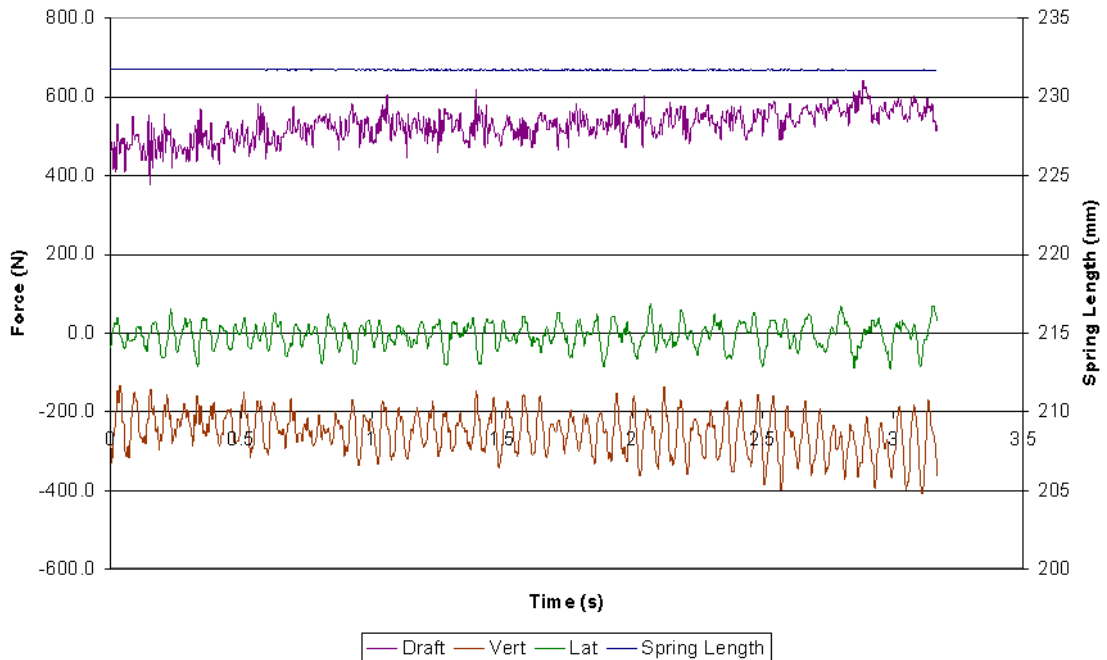


Figure A3.9: Field cultivator standard – run #9 time history results – 254 mm sweep, 152 mm depth, 2.68 m/s, high moisture (8.3% d.b.), low compaction (200 kPa)

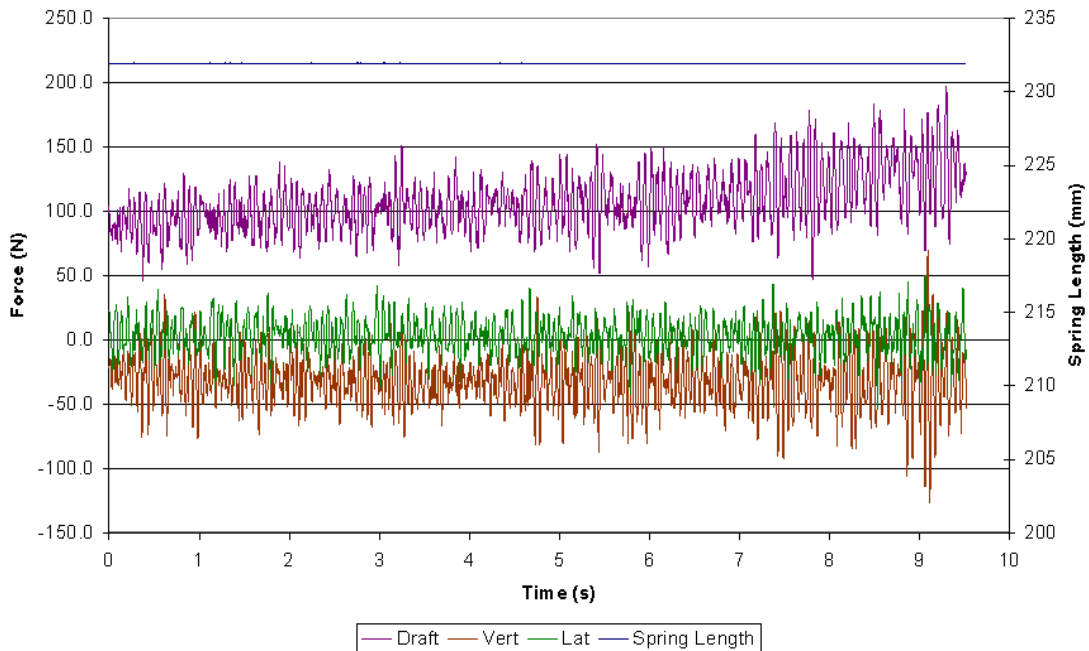


Figure A3.10: Field cultivator standard – run #10 time history results – 178 mm sweep, 76 mm depth, 0.89 m/s, high moisture (8.3% d.b.), low compaction (200 kPa)

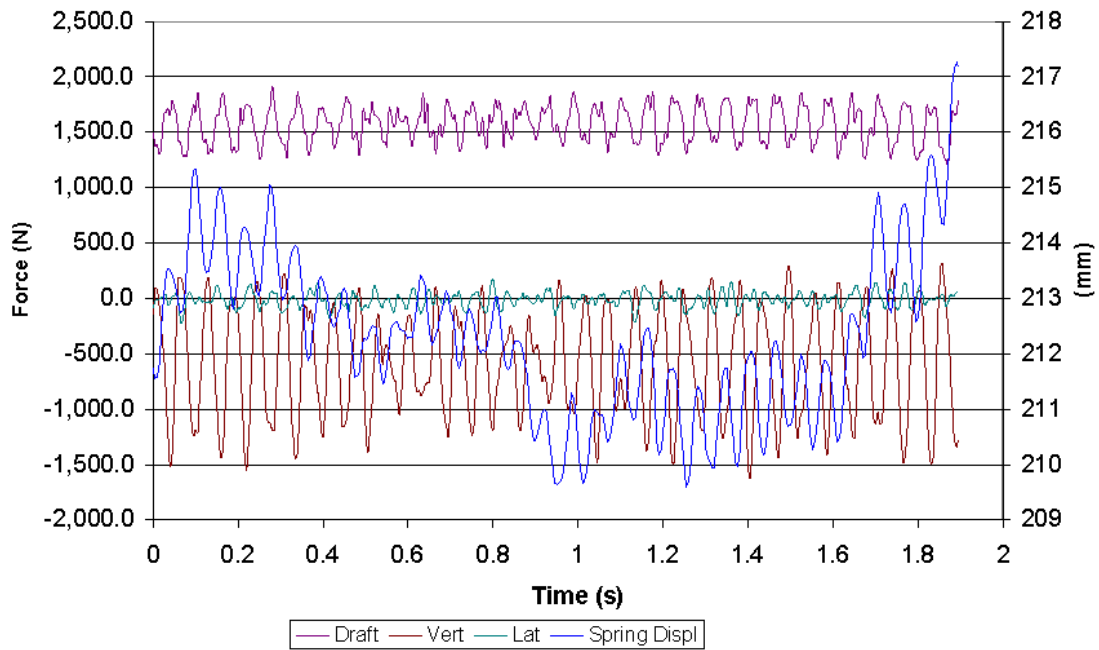


Figure A3.11: Field cultivator standard – run #11 time history results – 178 mm sweep, 152 mm depth, 4.47 m/s, high moisture (8.3% d.b.), high compaction (1,100 kPa)

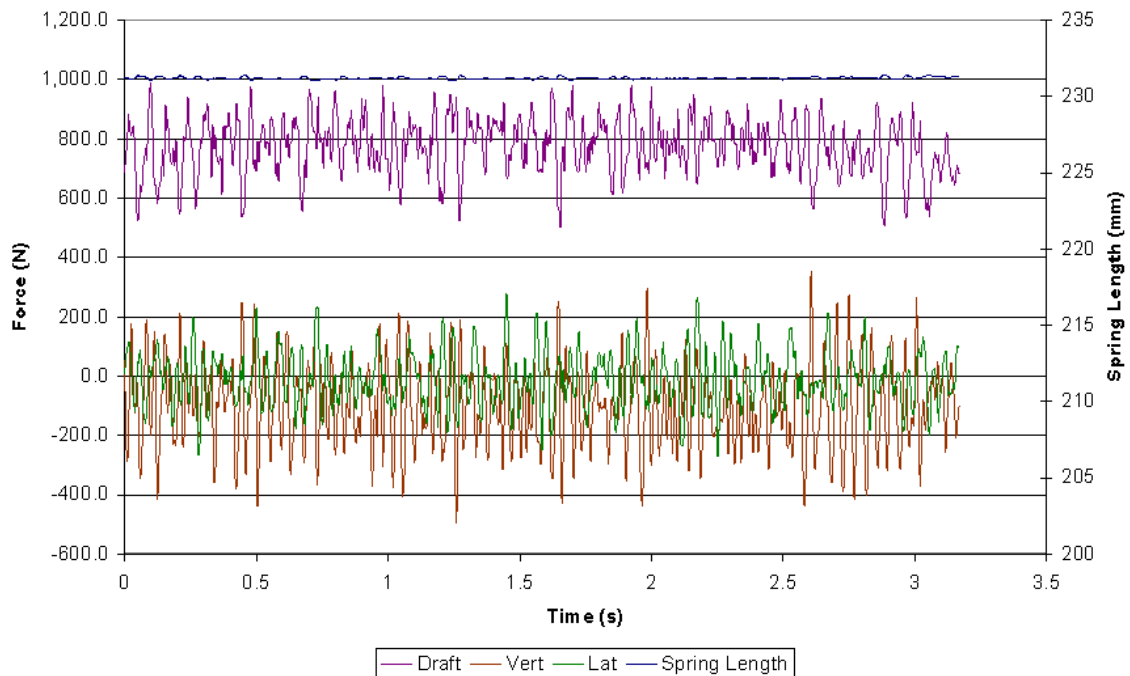


Figure A3.12: Field cultivator standard – run #12 time history results – 254 mm sweep, 76 mm depth, 2.68 m/s, high moisture (8.3% d.b.), high compaction (1,100 kPa)

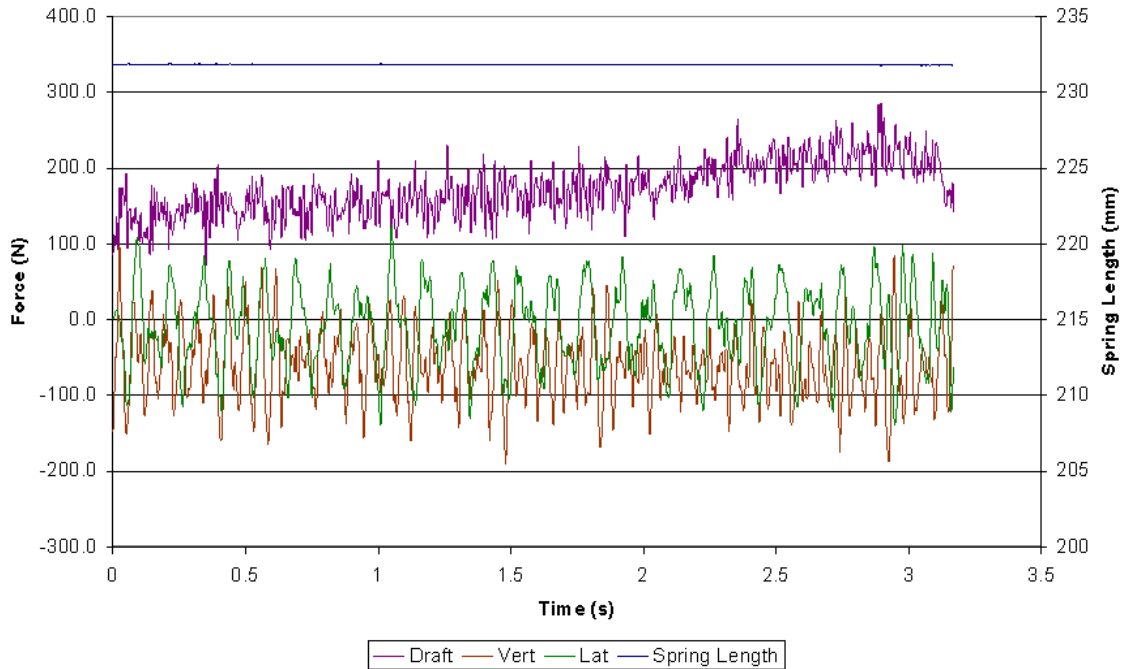


Figure A3.13: Field cultivator standard – run #13 time history results – 178 mm sweep, 76 mm depth, 2.68 m/s, high moisture (8.3% d.b.), low compaction (200 kPa)

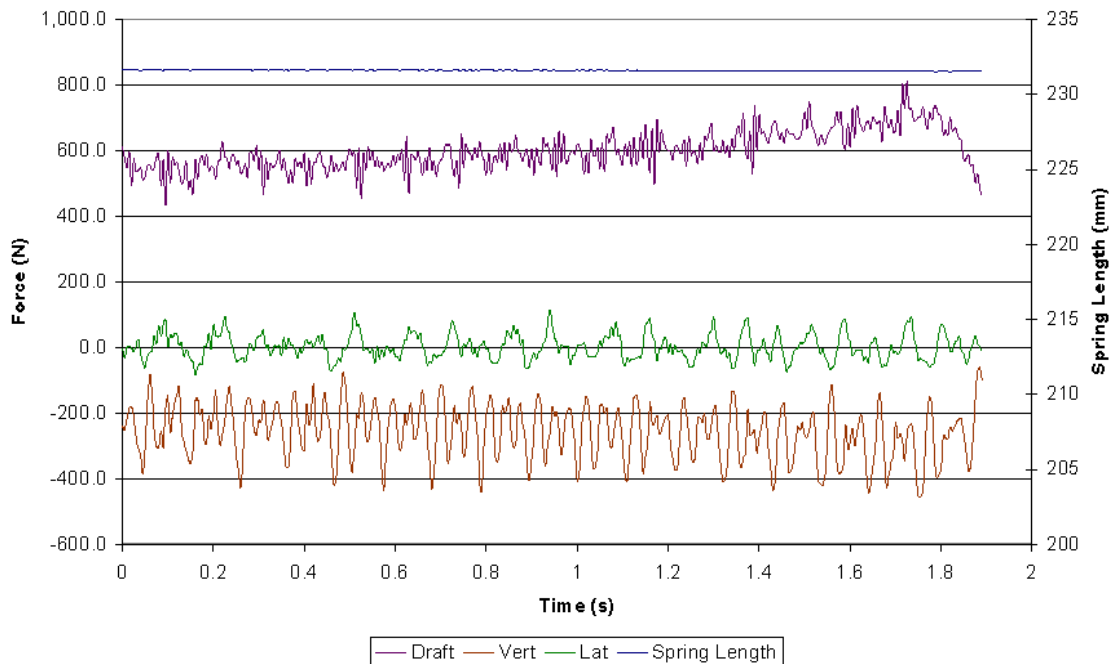


Figure A3.14: Field cultivator standard – run #14 time history results – 178 mm sweep, 152 mm depth, 4.47 m/s, high moisture (8.3% d.b.), low compaction (200 kPa)

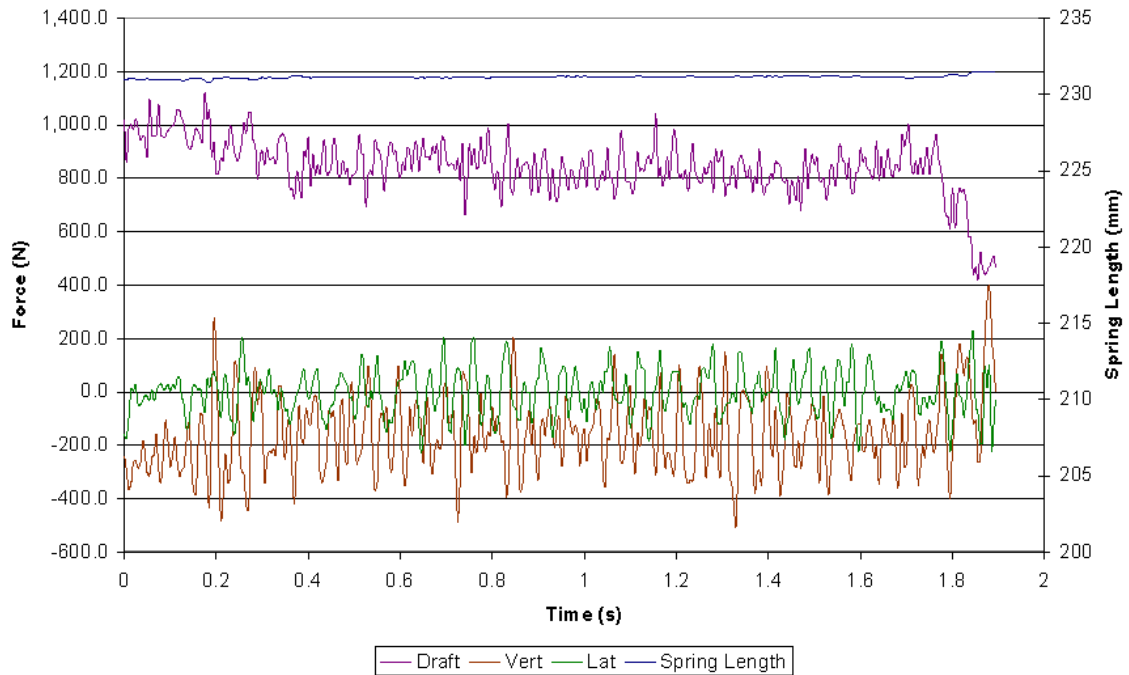


Figure A3.15: Field cultivator standard – run #15 time history results – 178 mm sweep, 76 mm depth, 4.47 m/s, high moisture (8.3% d.b.), high compaction (1,100 kPa)

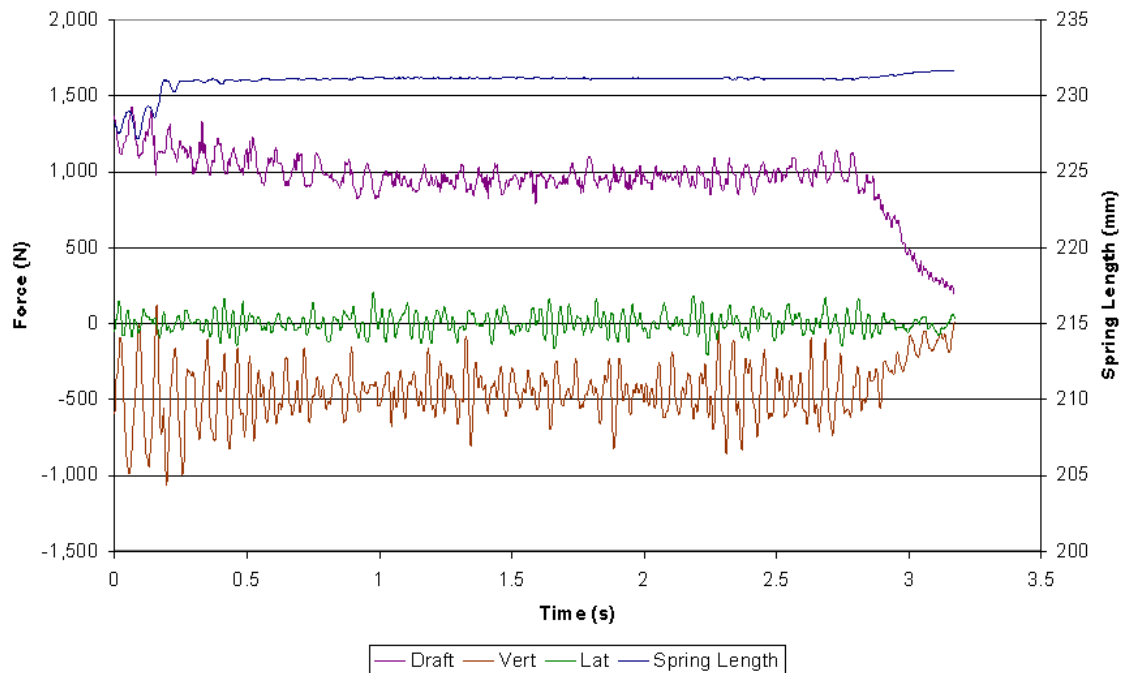


Figure A3.16: Field cultivator standard – run #16 time history results – 178 mm sweep, 152 mm depth, 2.68 m/s, high moisture (8.3% d.b.), high compaction (1,100 kPa)

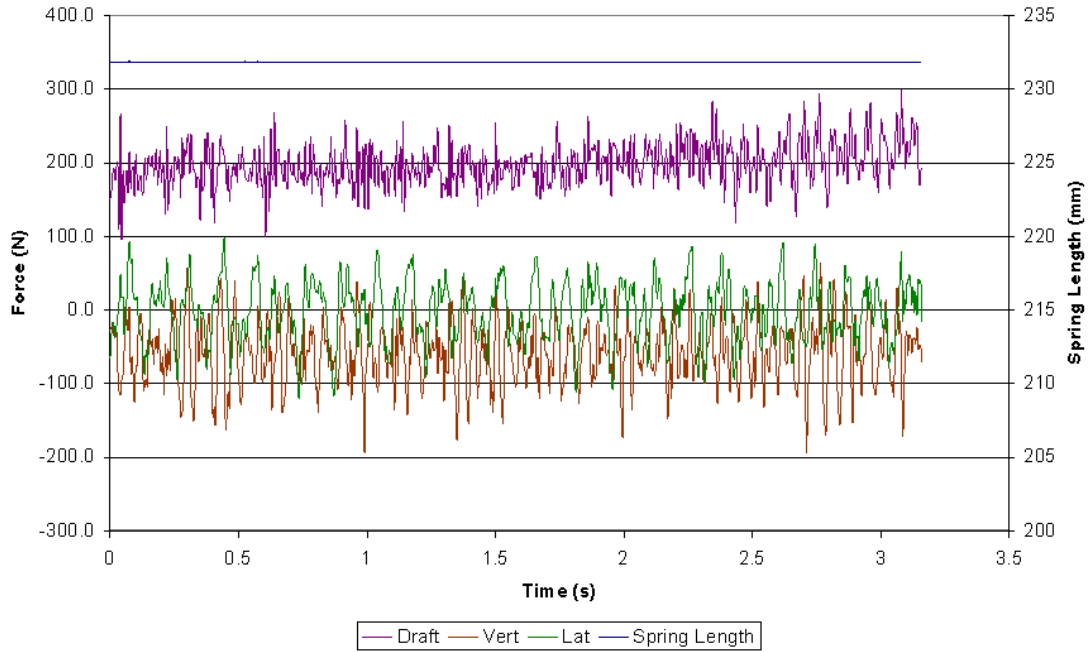


Figure A3.18: Field cultivator standard – run #18 time history results – 178 mm sweep, 76 mm depth, 2.68 m/s, high moisture (8.3% d.b.), low compaction (200 kPa)

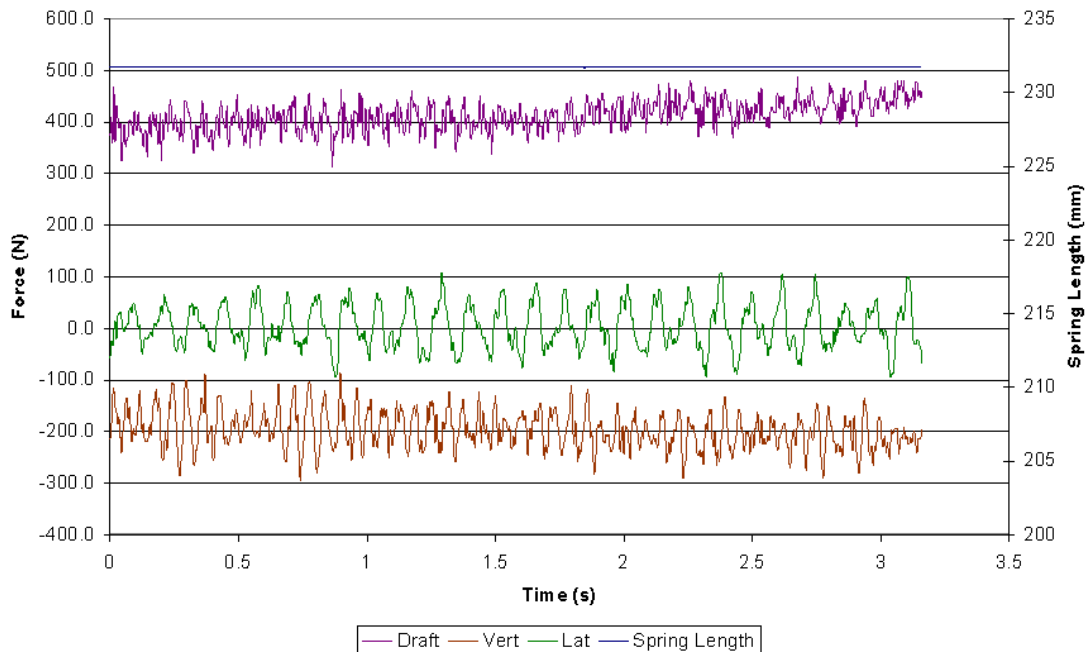


Figure A3.19: Field cultivator standard – run #19 time history results – 178 mm sweep, 152 mm depth, 2.68 m/s, high moisture (8.3% d.b.), low compaction (200 kPa)

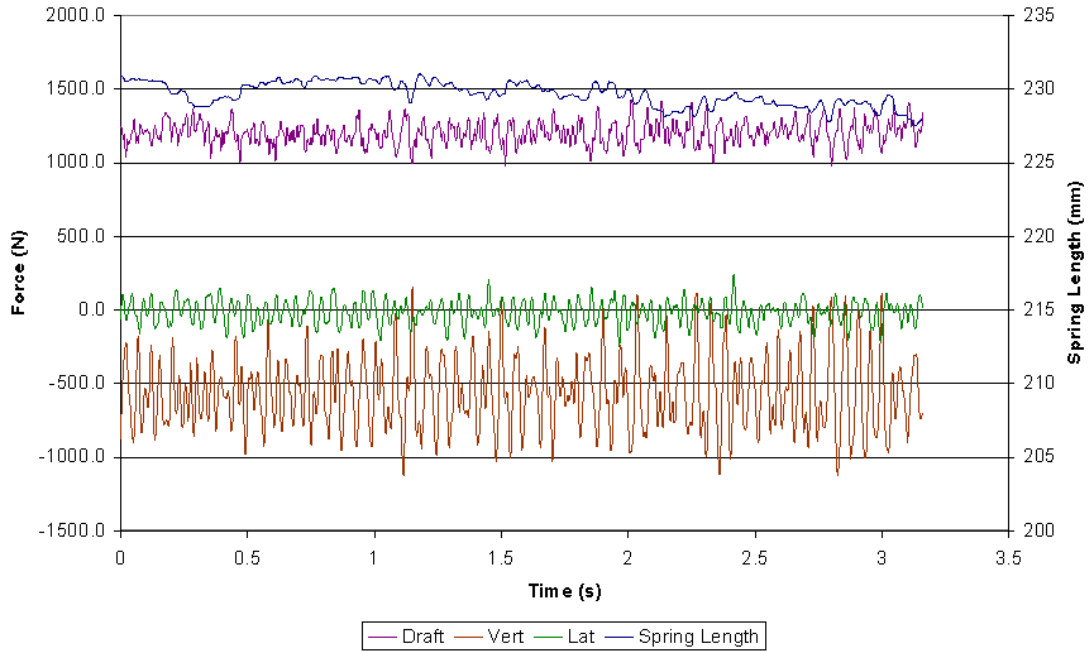


Figure A3.20: Field cultivator standard – run #20 time history results – 178 mm sweep, 152 mm depth, 2.68 m/s, high moisture (8.3% d.b.), high compaction (1,100 kPa)

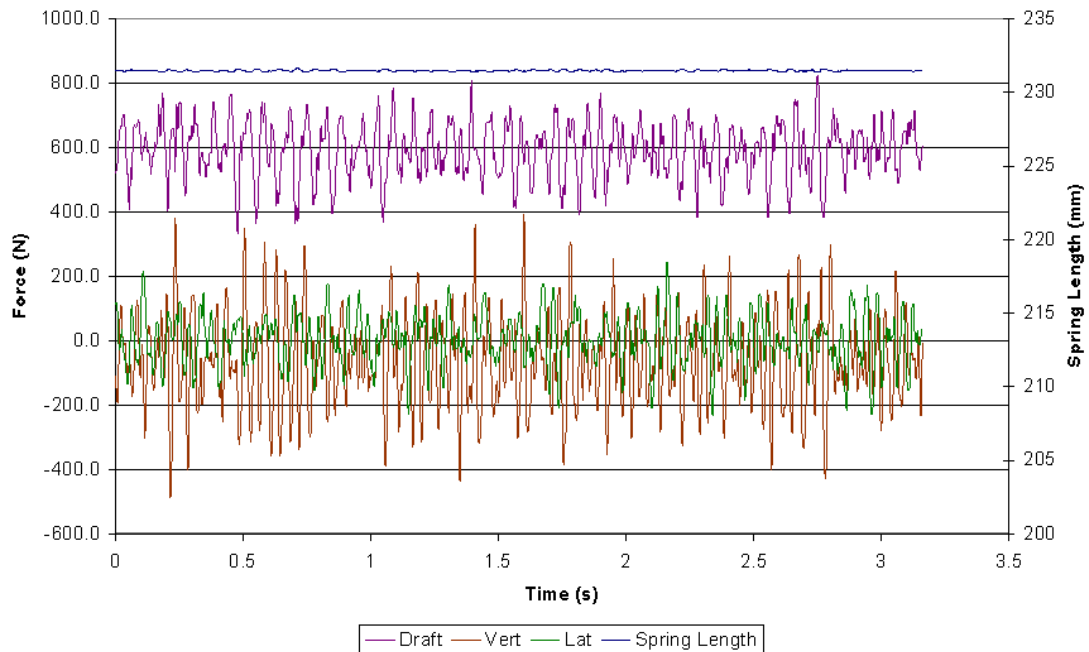


Figure A3.21: Field cultivator standard – run #21 time history results – 178 mm sweep, 76 mm depth, 2.68 m/s, high moisture (8.3% d.b.), high compaction (1,100 kPa)

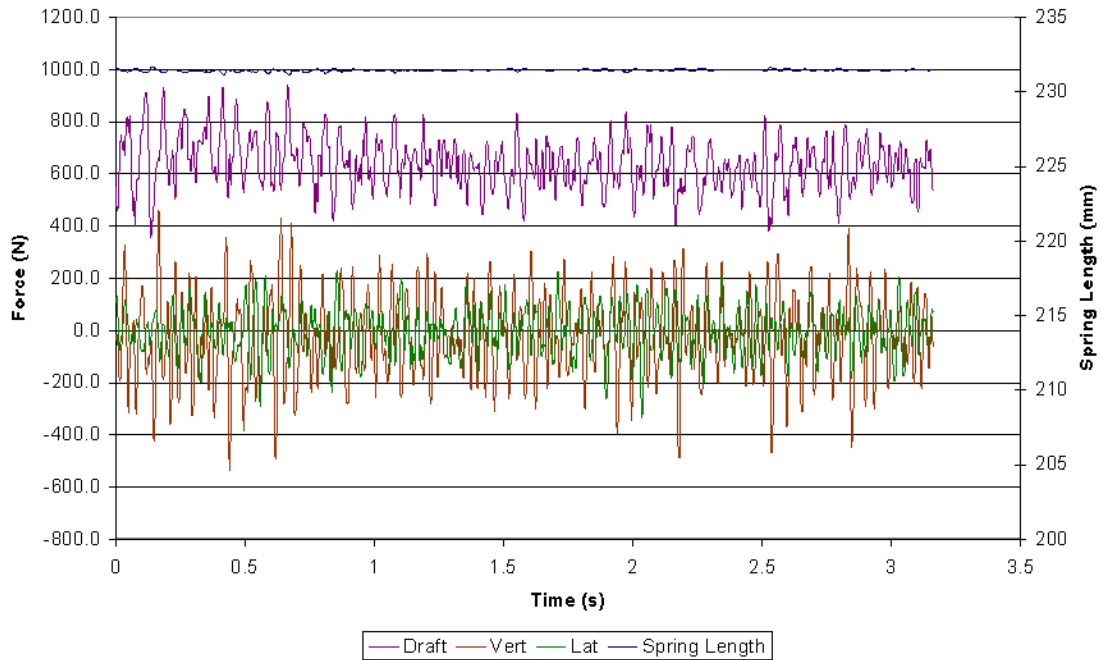


Figure A3.22: Field cultivator standard – run #22 time history results – 178 mm sweep, 76 mm depth, 2.68 m/s, high moisture (8.3% d.b.), high compaction (1,100 kPa)

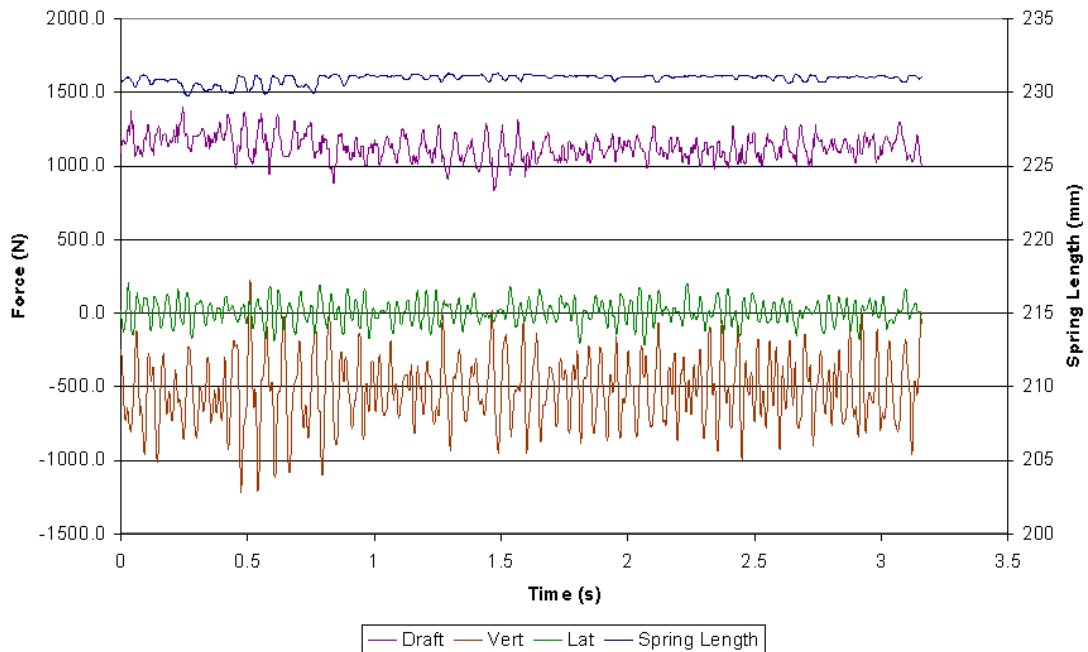


Figure A3.23: Field cultivator standard – run #23 time history results – 178 mm sweep, 152 mm depth, 2.68 m/s, high moisture (8.3% d.b.), high compaction (1,100 kPa)

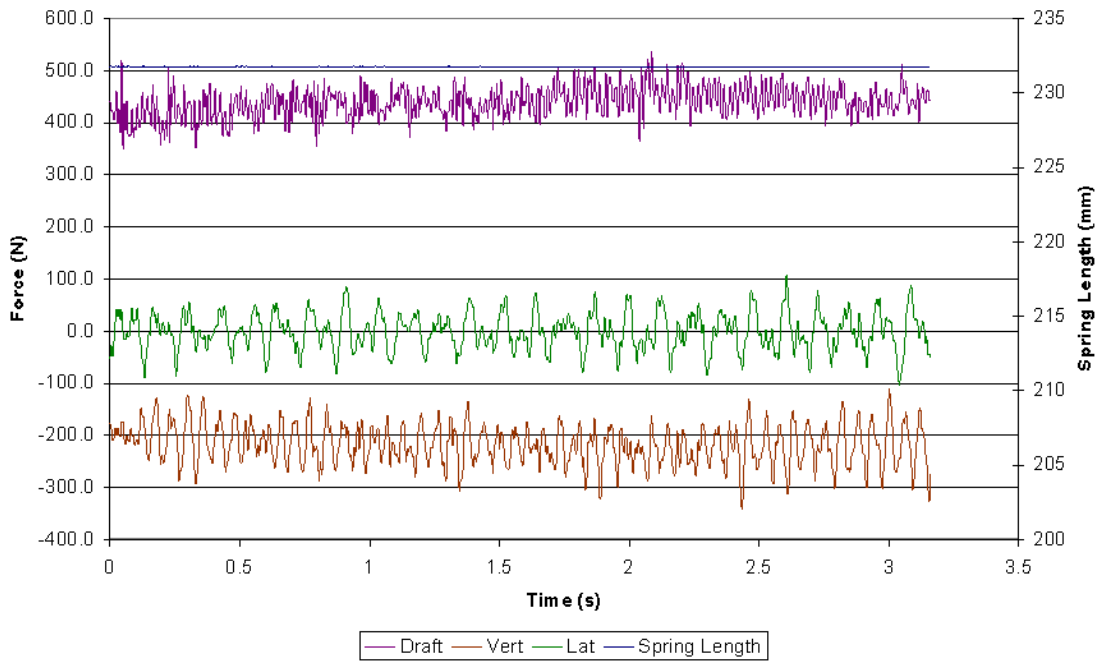


Figure A3.24: Field cultivator standard – run #24 time history results – 178 mm sweep, 152 mm depth, 2.68 m/s, high moisture (8.3% d.b.), low compaction (200 kPa)

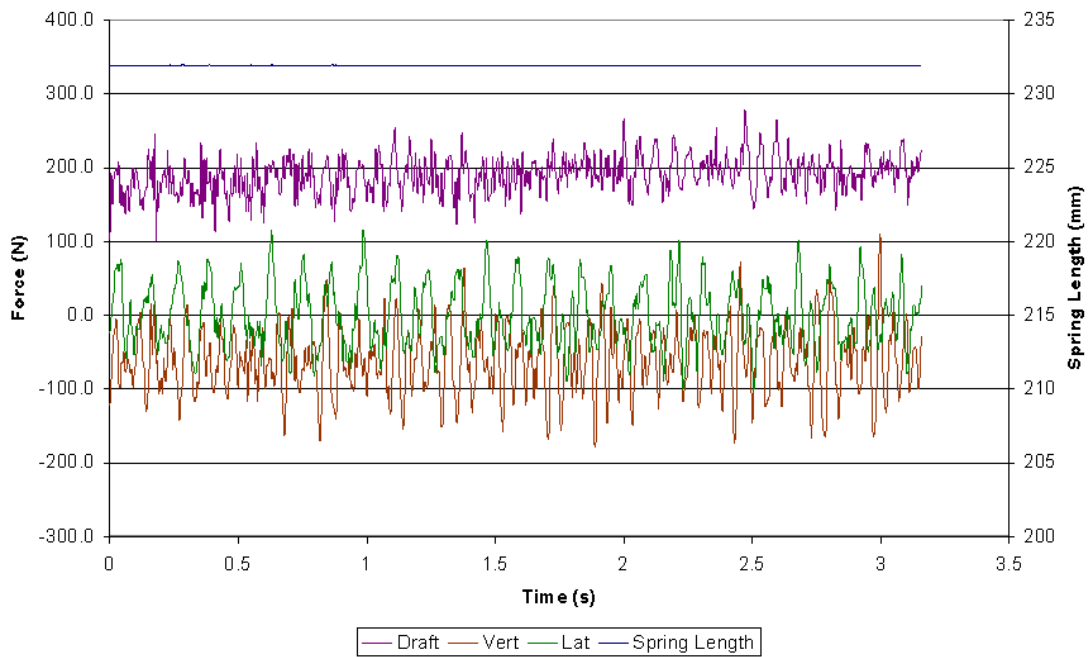


Figure A3.25: Field cultivator standard – run #25 time history results – 178 mm sweep, 76 mm depth, 2.68 m/s, high moisture (8.3% d.b.), low compaction (200 kPa)

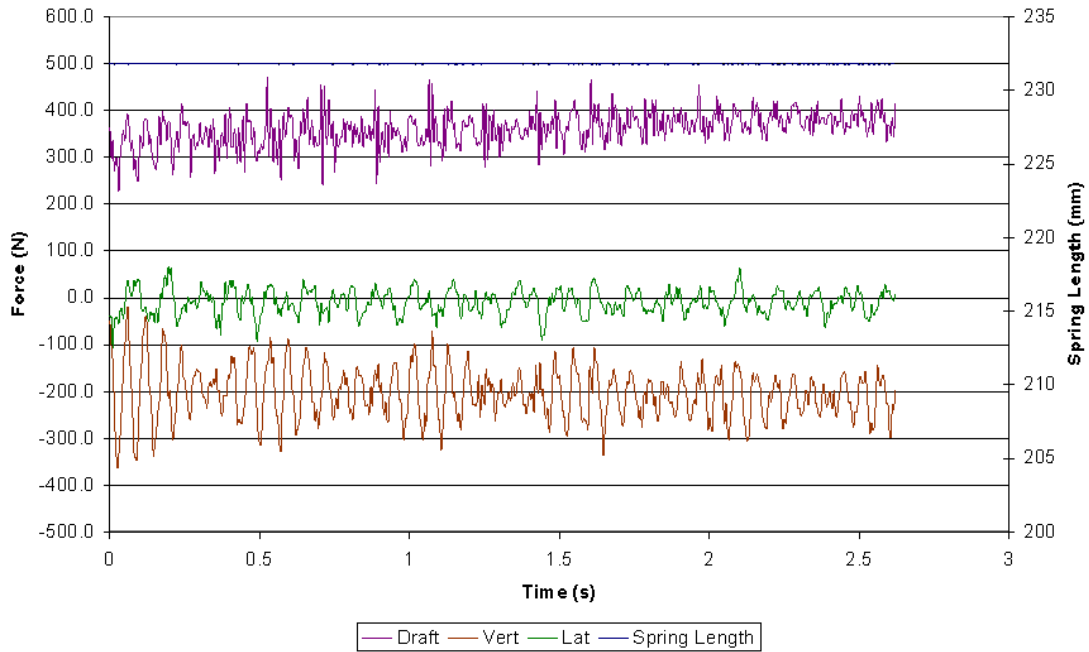


Figure A3.26: Field cultivator standard – run #26 time history results – 178 mm sweep, 76 mm depth, 2.68 m/s, low moisture (6.9% d.b.), low compaction (200 kPa)

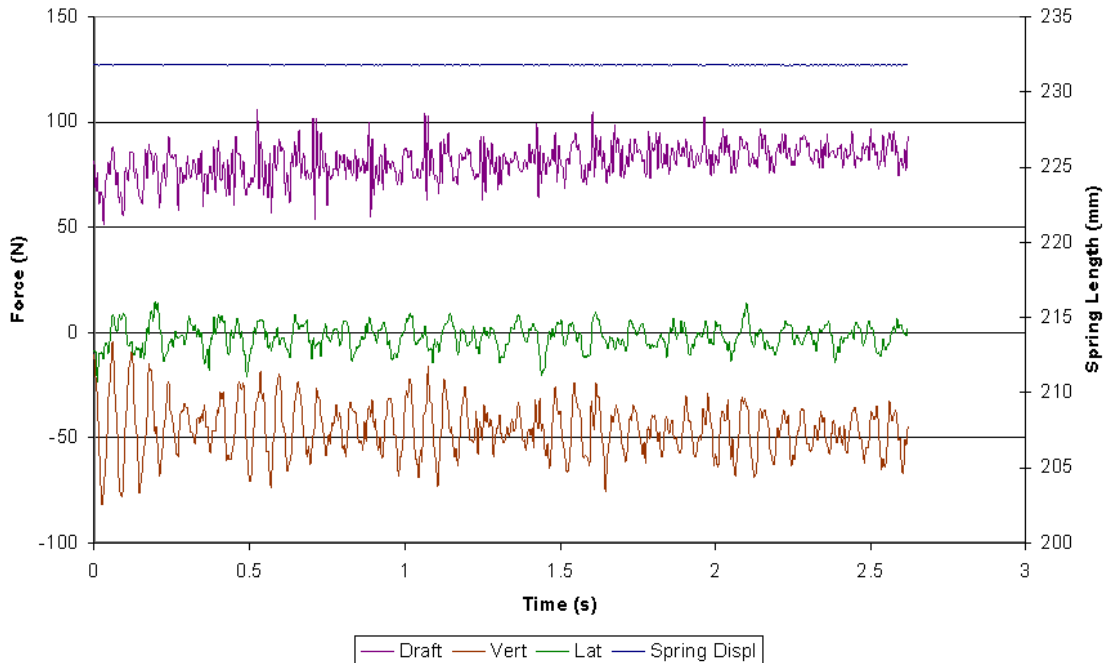


Figure A3.27: Field cultivator standard – run #27 time history results – 254 mm sweep, 152 mm depth, 2.68 m/s, low moisture (6.9% d.b.), low compaction (200 kPa)

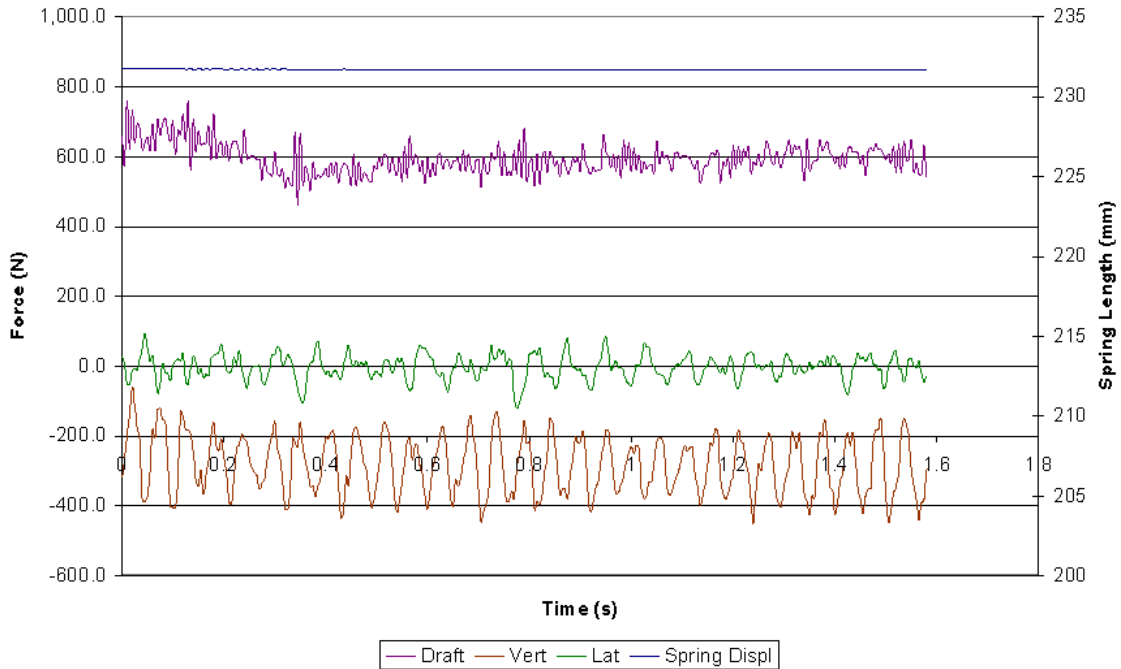


Figure A3.28: Field cultivator standard – run #28 time history results – 178 mm sweep, 152 mm depth, 4.47 m/s, low moisture (6.9% d.b.), low compaction (200 kPa)

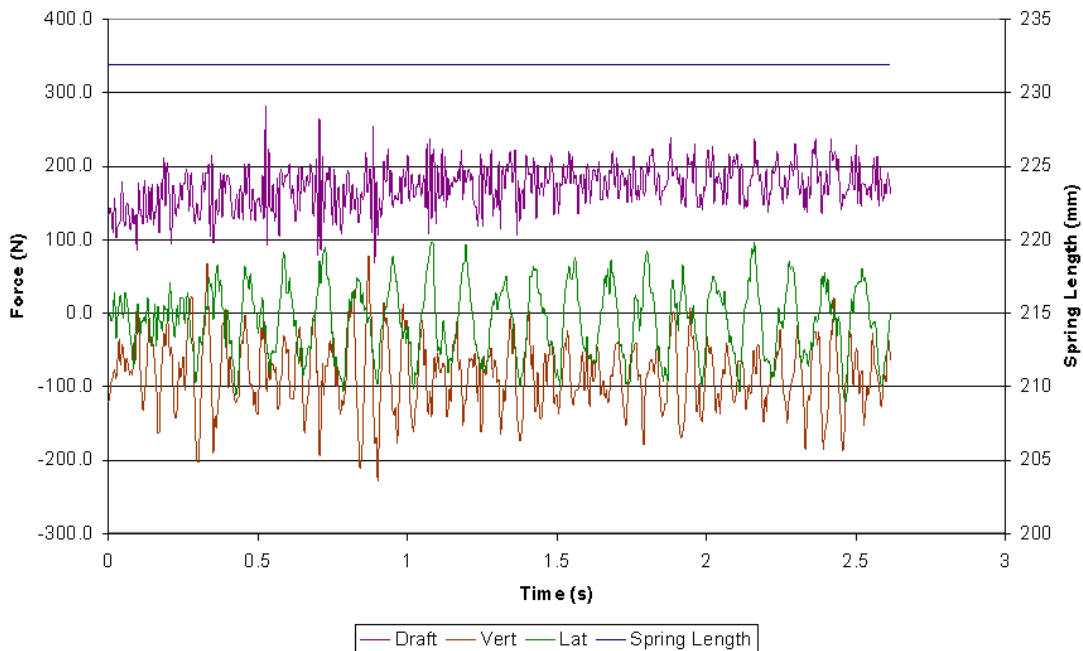


Figure A3.29: Field cultivator standard – run #29 time history results – 254 mm sweep, 76 mm depth, 2.68 m/s, low moisture (6.9% d.b.), high compaction (1,100 kPa)

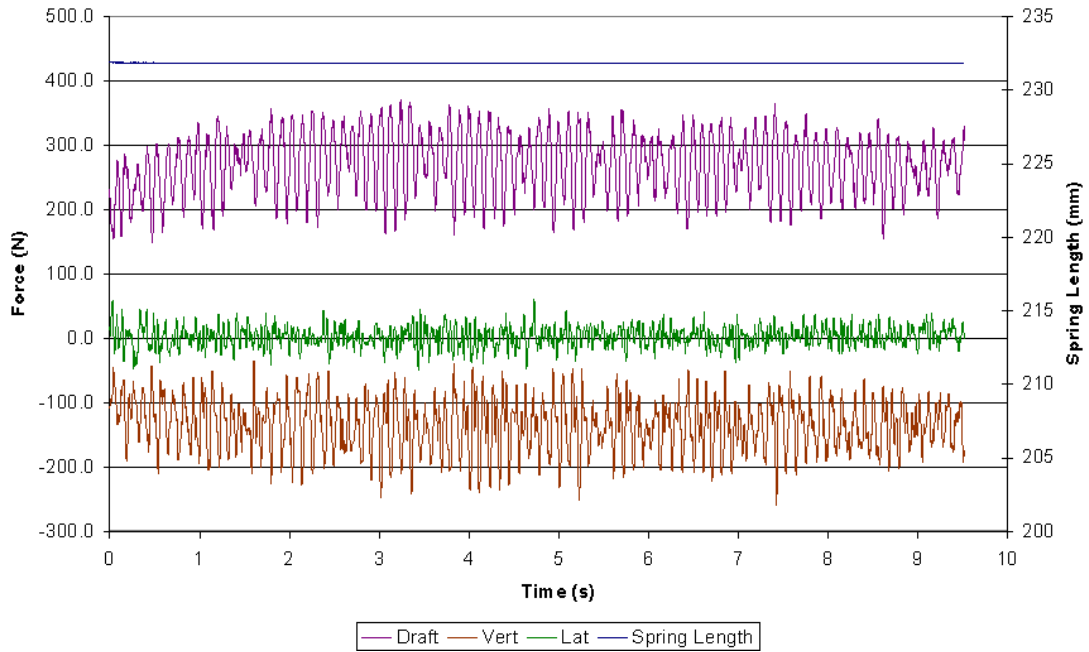


Figure A3.30: Field cultivator standard – run #30 time history results – 178 mm sweep, 152 mm depth, 0.89 m/s, low moisture (6.9% d.b.), high compaction (1,100 kPa)

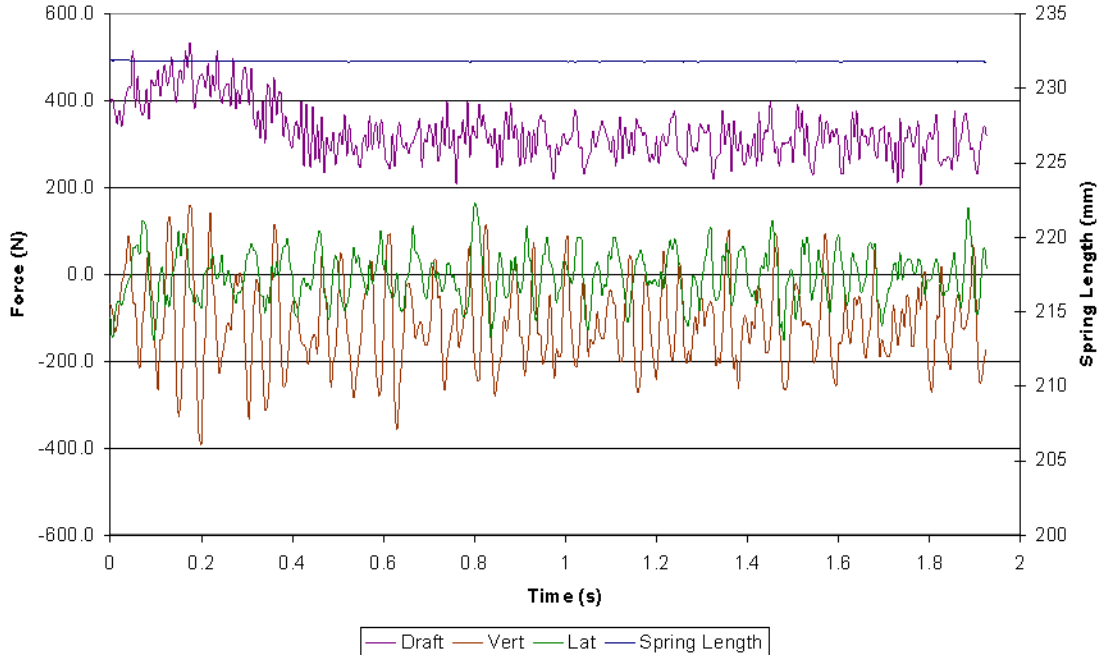


Figure A3.31: Field cultivator standard – run #31 time history results – 178 mm sweep, 76 mm depth, 4.47 m/s, low moisture (6.9% d.b.), high compaction (1,100 kPa)

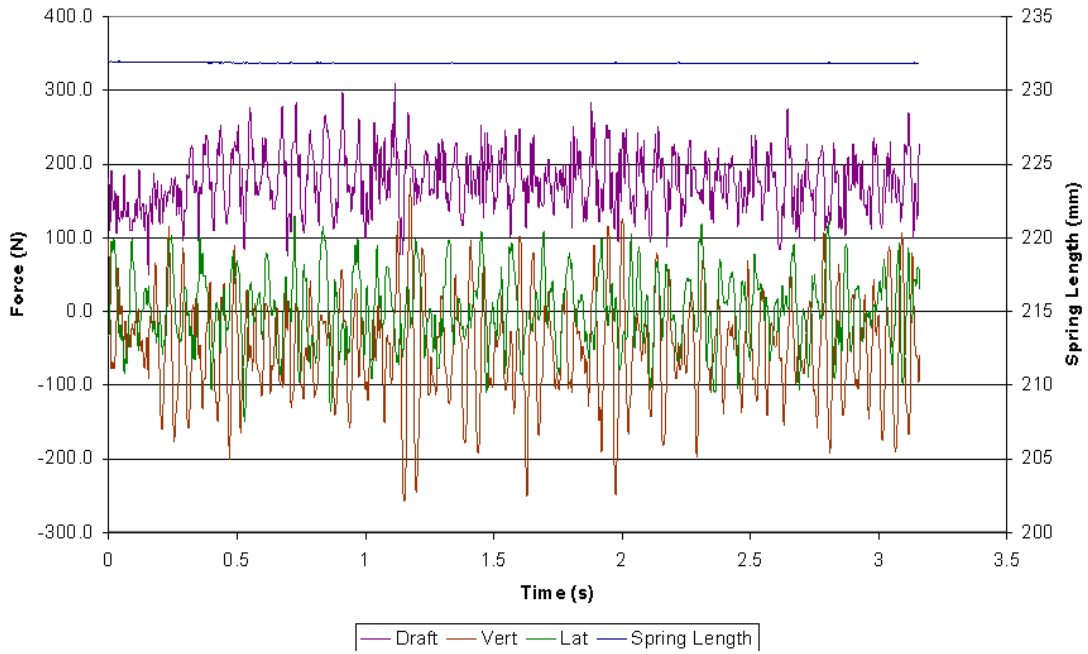


Figure A3.32: Field cultivator standard – run #32 time history results – 178 mm sweep, 76 mm depth, 2.68 m/s, low moisture (6.9% d.b.), high compaction (1,100 kPa)

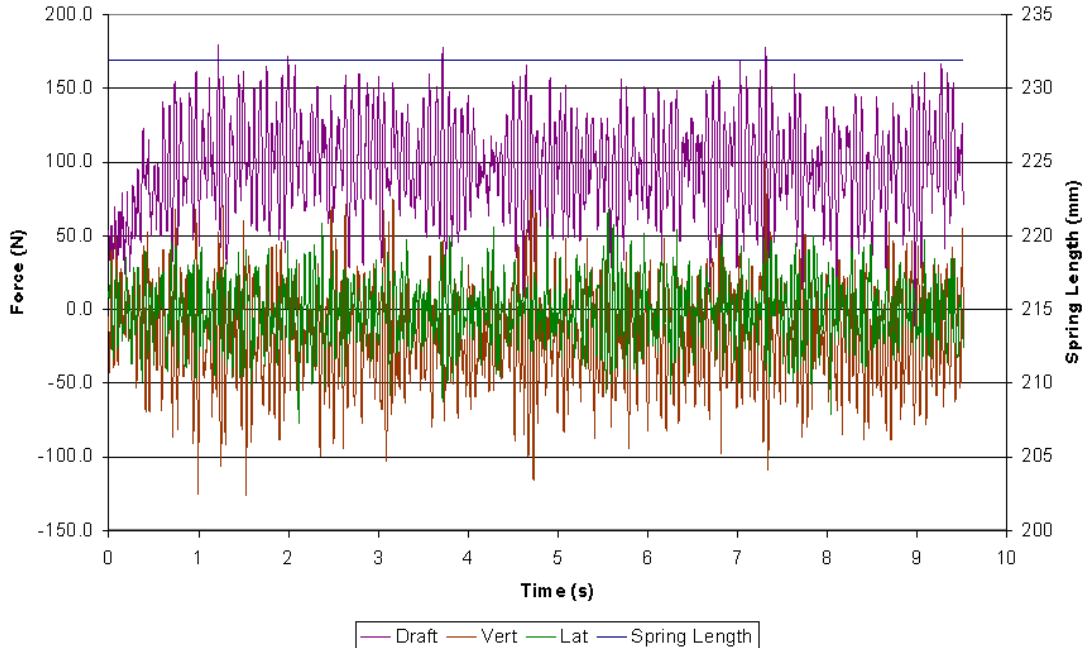


Figure A3.33: Field cultivator standard – run #33 time history results – 178 mm sweep, 76 mm depth, 0.89 m/s, low moisture (6.9% d.b.), high compaction (1,100 kPa)

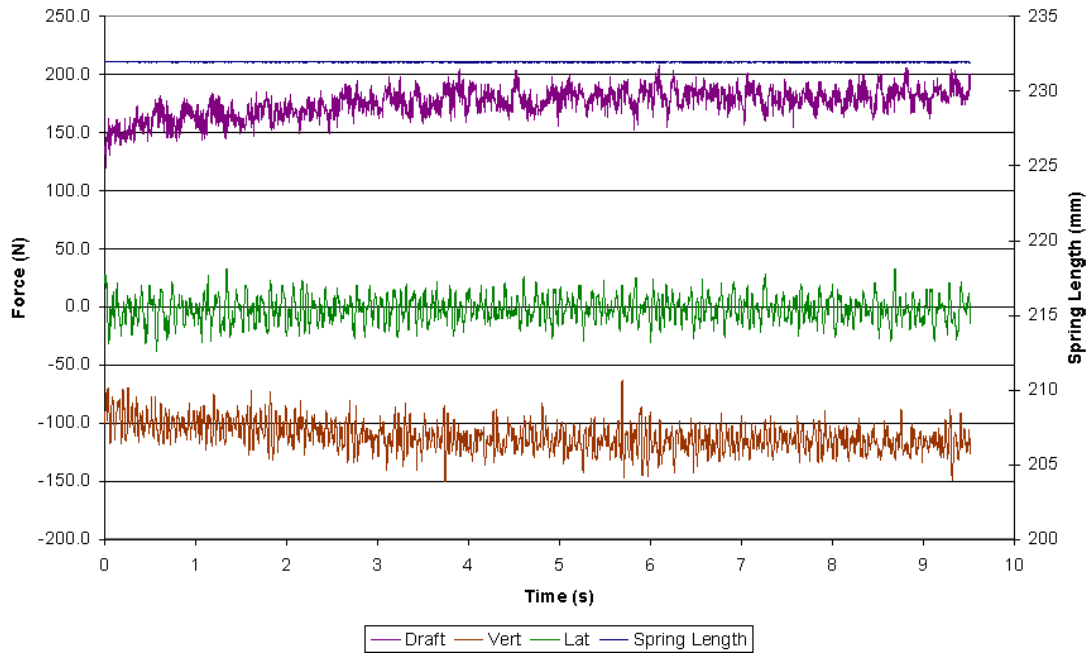


Figure A3.34: Field cultivator standard – run #34 time history results – 178 mm sweep, 152 mm depth, 0.89 m/s, low moisture (6.9% d.b.), low compaction (200 kPa)

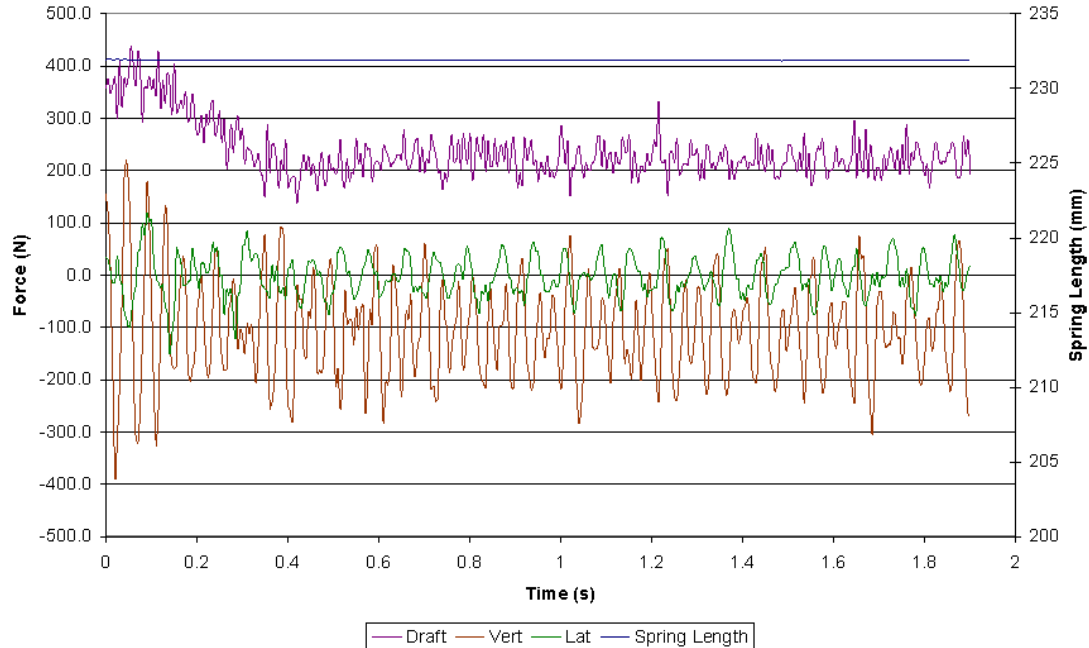


Figure A3.35: Field cultivator standard – run #35 time history results – 178 mm sweep, 76 mm depth, 4.47 m/s, low moisture (6.9% d.b.), low compaction (200 kPa)

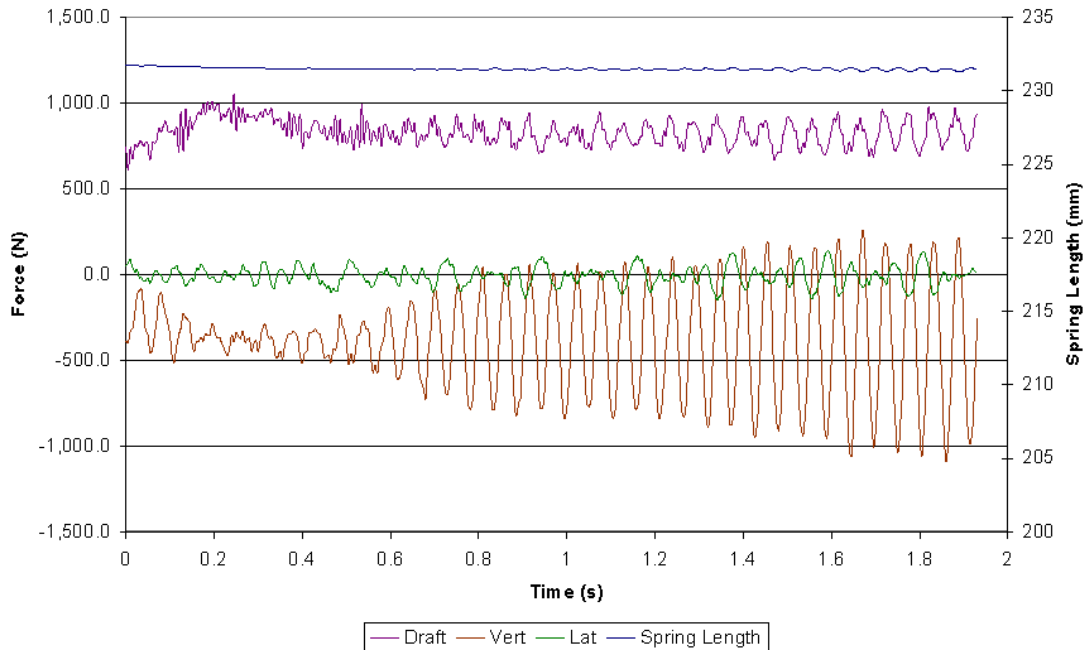


Figure A3:36: Field cultivator standard – run #36 time history results – 178 mm sweep, 152 mm depth, 4.47 m/s, low moisture (6.9% d.b.), high compaction (1,100 kPa)

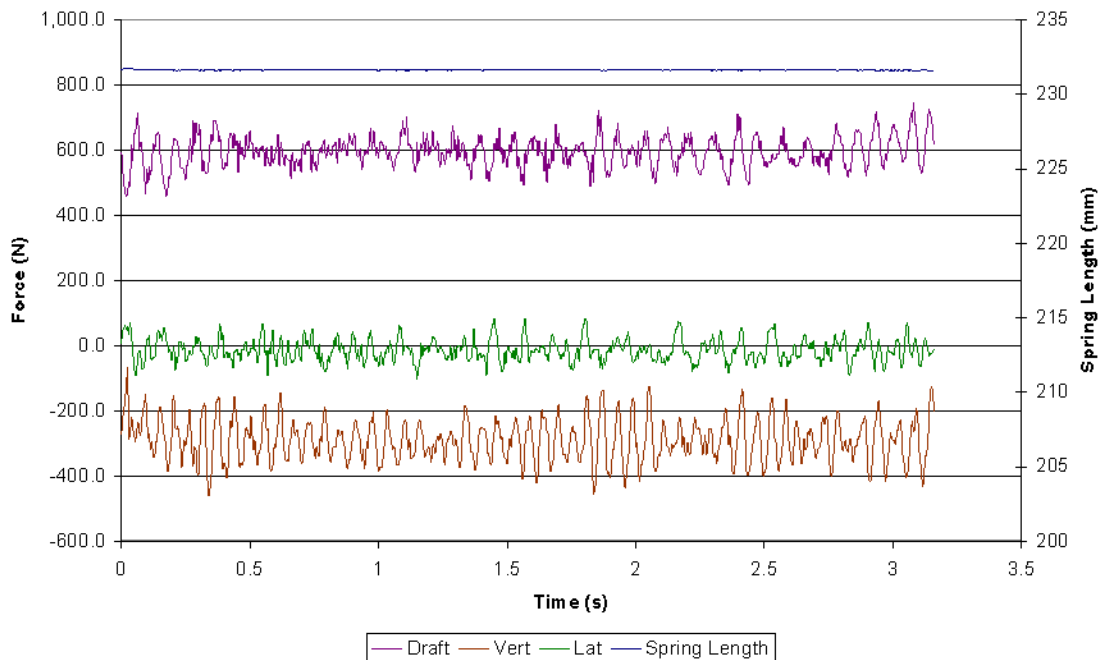


Figure A3.37 Field cultivator standard – run #37 time history results – 254 mm sweep, 152 mm depth, 2.68 m/s, low moisture (6.9% d.b.), high compaction (1,100 kPa)

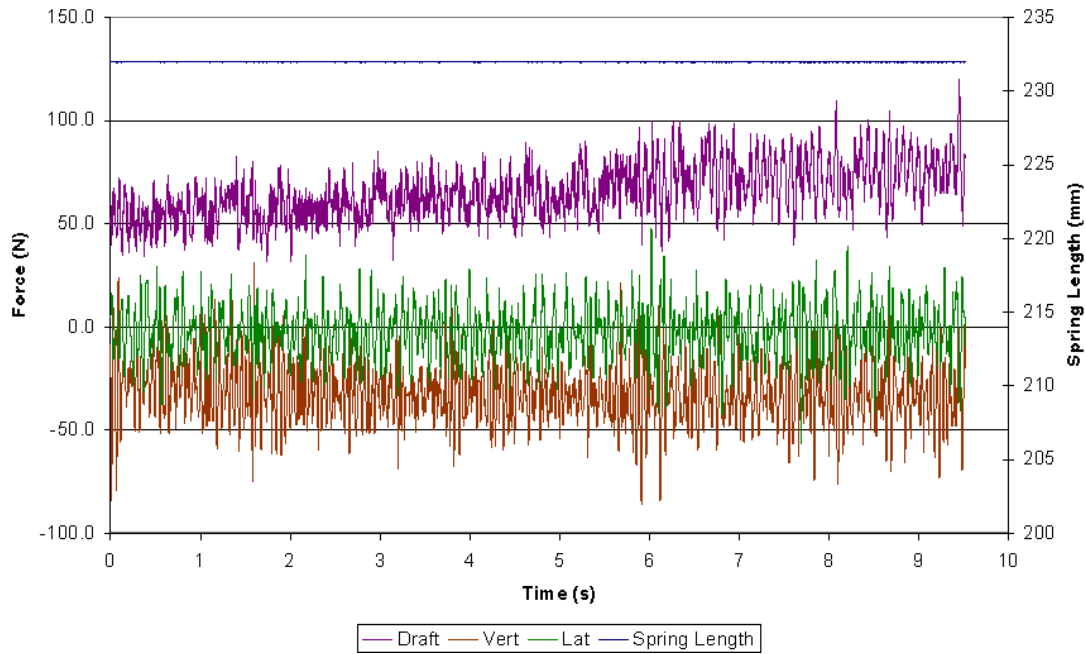


Figure A3.38: Field cultivator standard – run #38 time history results – 178 mm sweep, 76 mm depth, 0.89 m/s, low moisture (6.9% d.b.), low compaction (200 kPa)

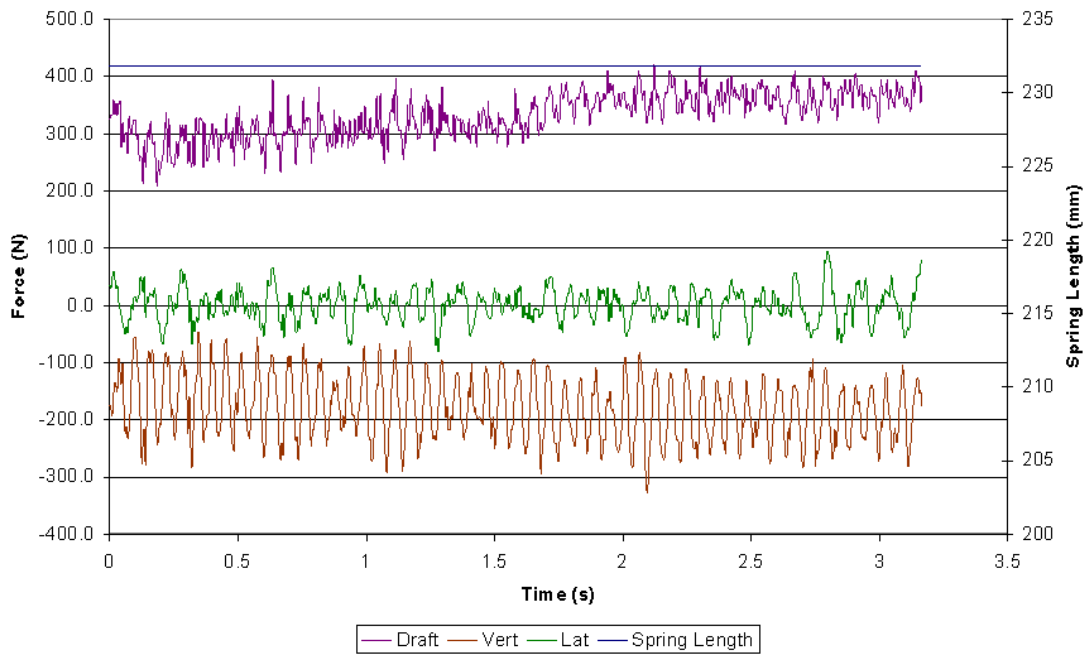


Figure A3.39: Field cultivator standard – run #39 time history results – 178 mm sweep, 152 mm depth, 2.68 m/s, low moisture (6.9% d.b.), low compaction (200 kPa)

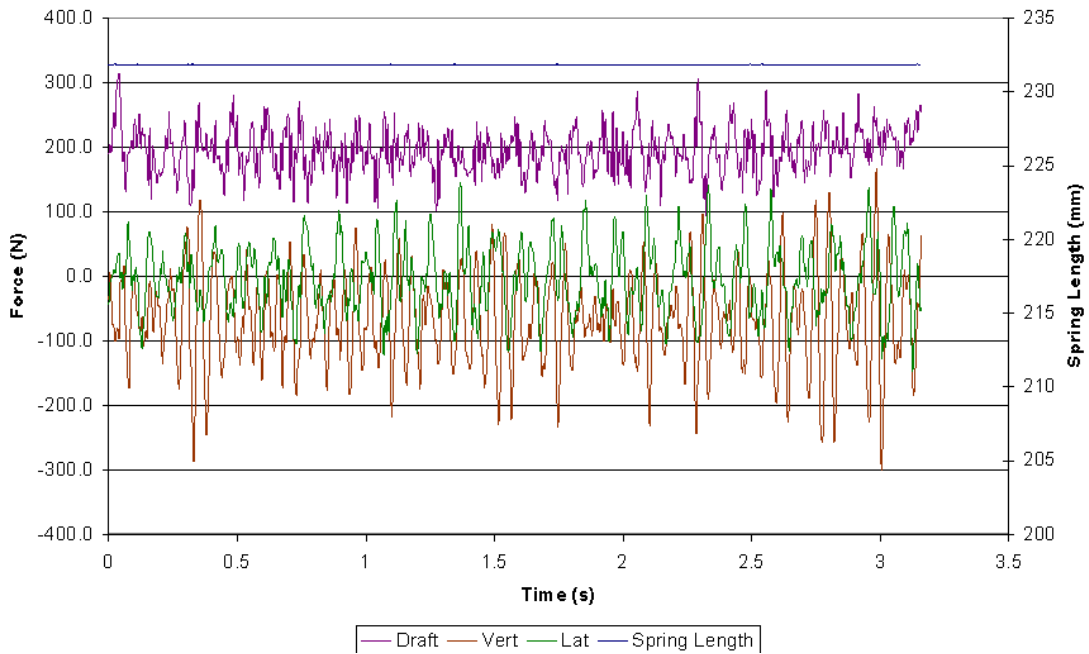


Figure A3.40: Field cultivator standard – run #40 time history results – 254 mm sweep, 76 mm depth, 2.68 m/s, low moisture (6.9% d.b.), high compaction (1,100 kPa)

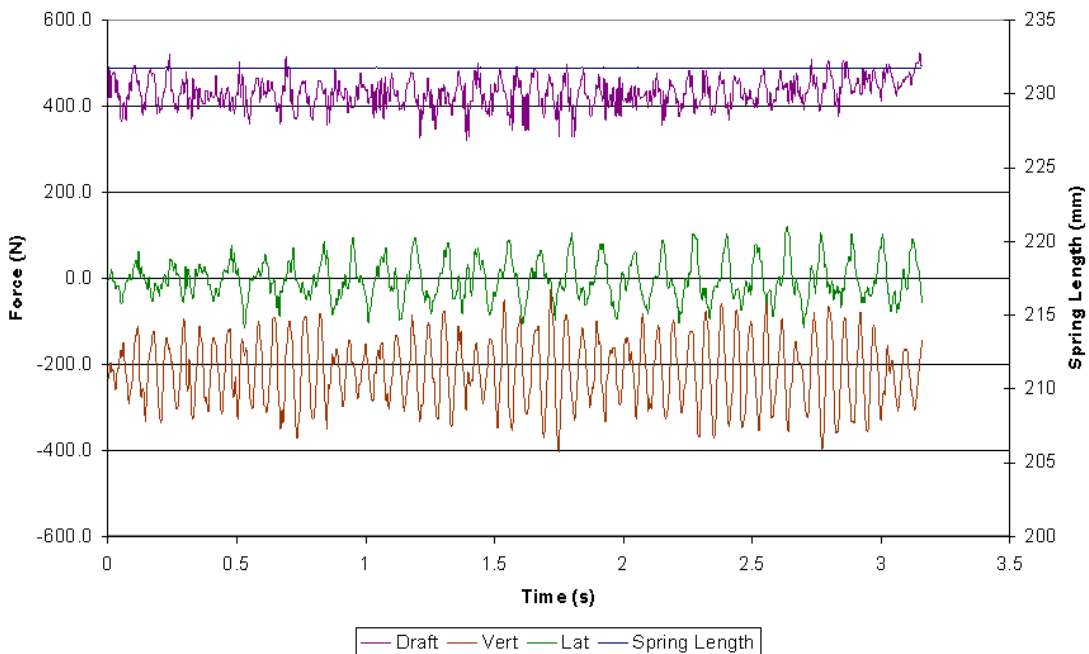


Figure A3.41: Field cultivator standard – run #41 time history results – 178 mm sweep, 152 mm depth, 2.68 m/s, low moisture (6.9% d.b.), high compaction (1,100 kPa)

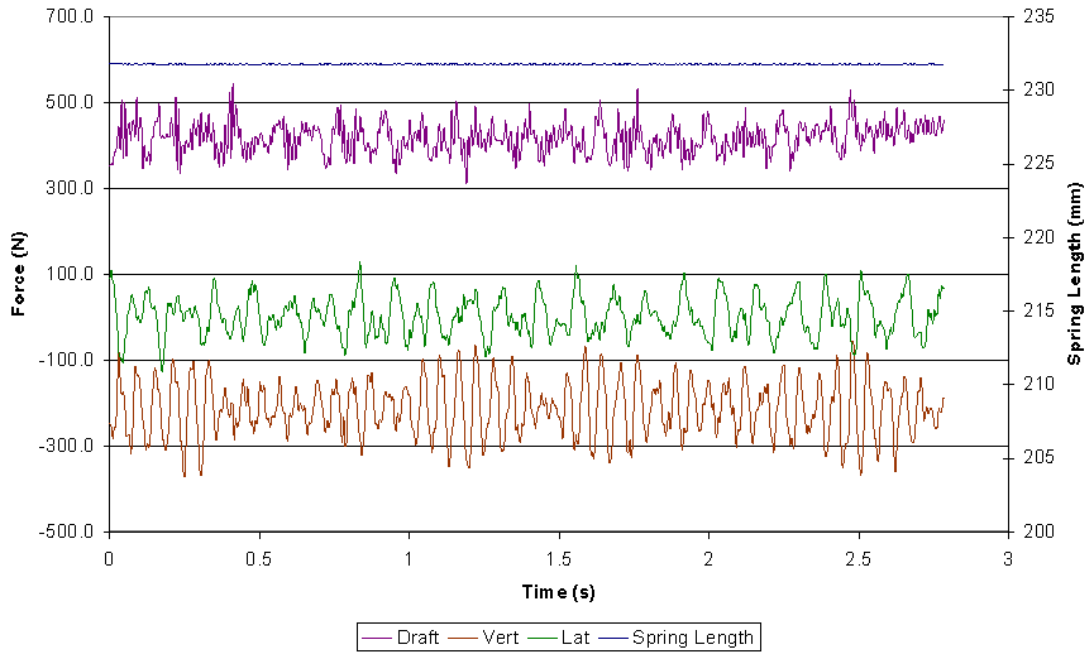


Figure A3.42: Field cultivator standard – run #42 time history results – 178 mm sweep, 152 mm depth, 2.68 m/s, low moisture (6.9% d.b.), high compaction (1,100 kPa)

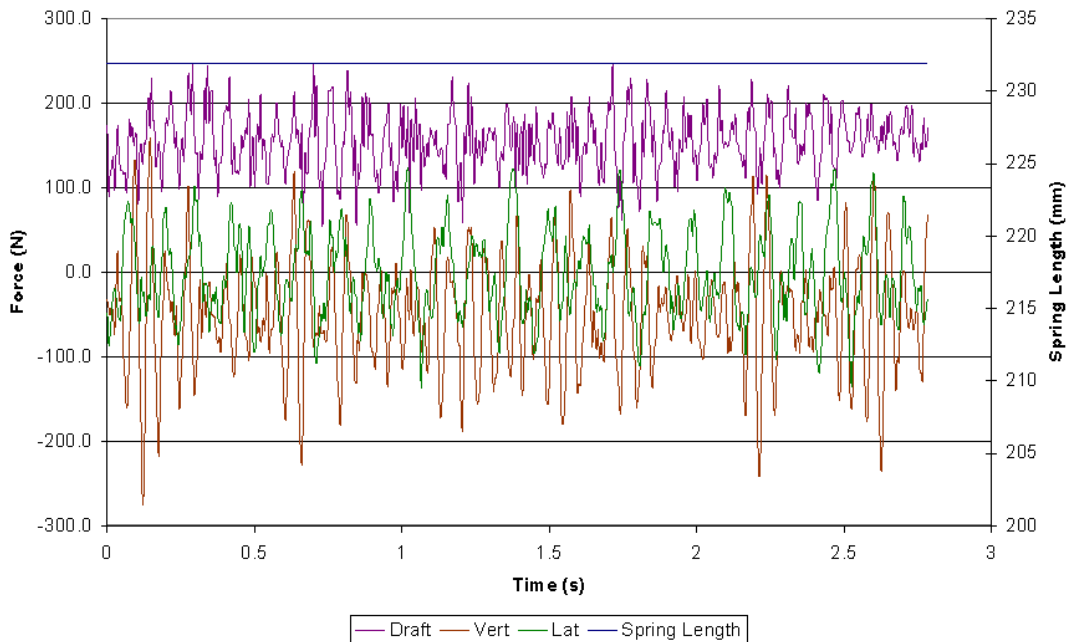


Figure A3.43: Field cultivator standard – run #43 time history results – 178 mm sweep, 76 mm depth, 2.68 m/s, low moisture (6.9% d.b.), high compaction (1,100 kPa)

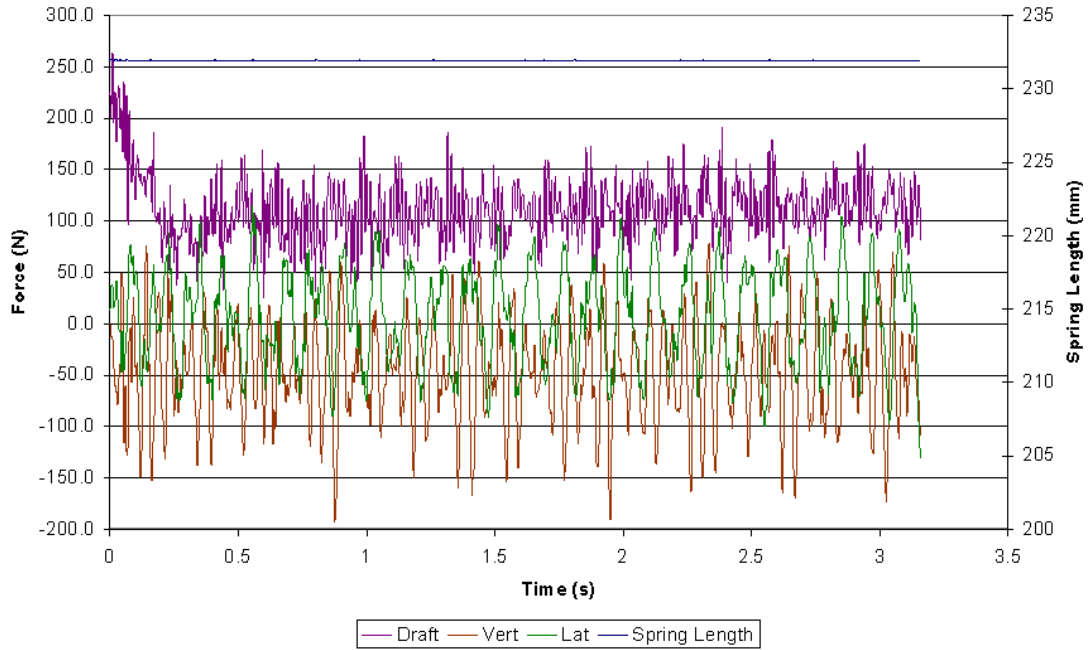


Figure A3.44: Field cultivator standard – run #44 time history results – 178 mm sweep, 76 mm depth, 2.68 m/s, low moisture (6.9% d.b.), low compaction (200 kPa)

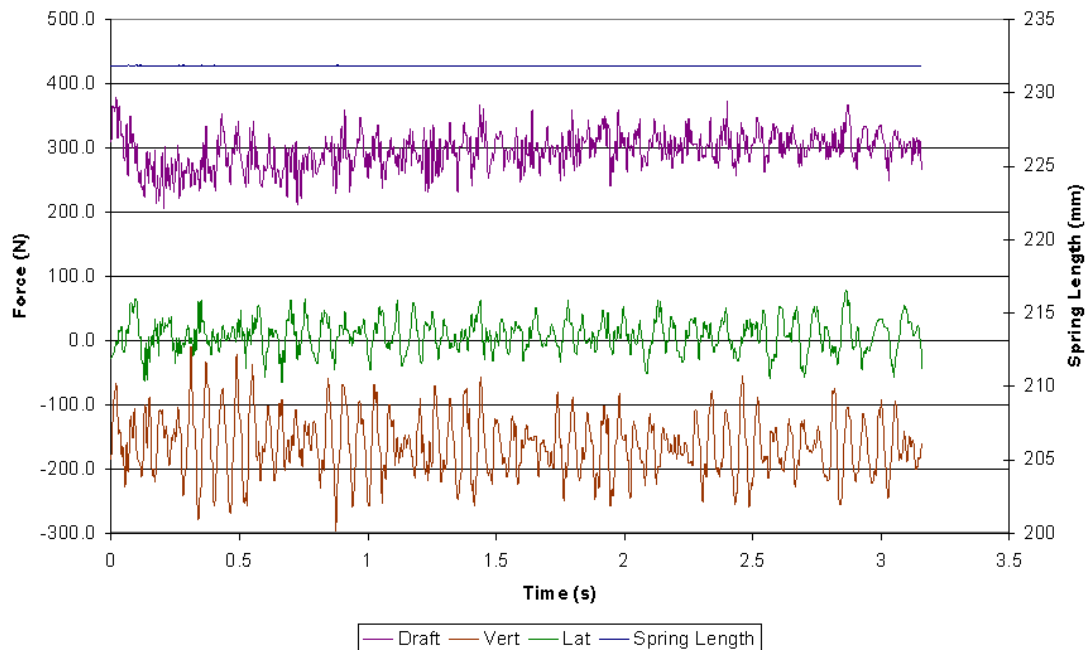


Figure A3.45: Field cultivator standard – run #45 time history results – 178 mm sweep, 152 mm depth, 2.68 m/s, low moisture (6.9% d.b.), low compaction (200 kPa)

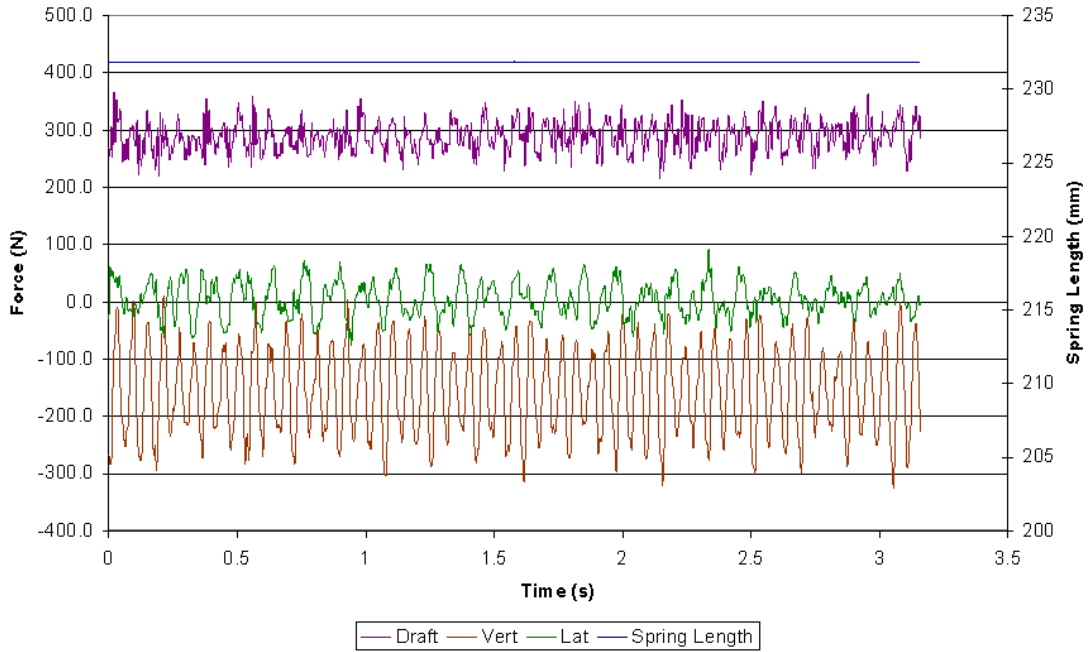


Figure A3.46: Field cultivator standard – run #46 time history results – 178 mm sweep, 152 mm depth, 2.68 m/s, low moisture (6.9% d.b.), low compaction (200 kPa)

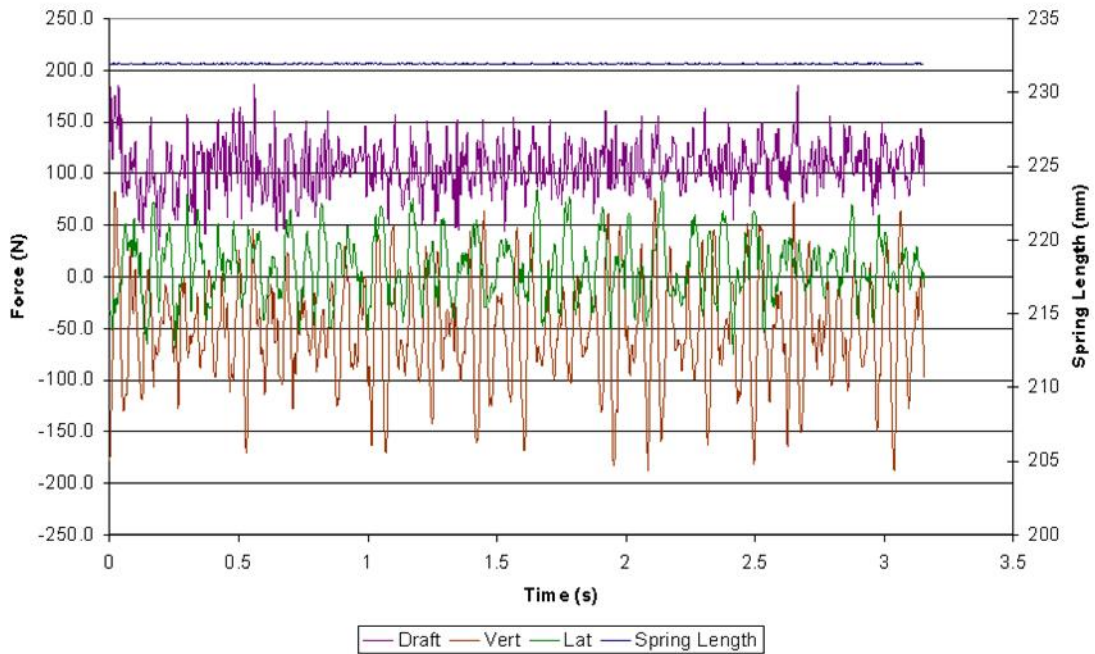


Figure A3.47: Field cultivator standard – run #47 time history results – 178 mm sweep, 76 mm depth, 2.68 m/s, low moisture (6.9% d.b.), low compaction (200 kPa)

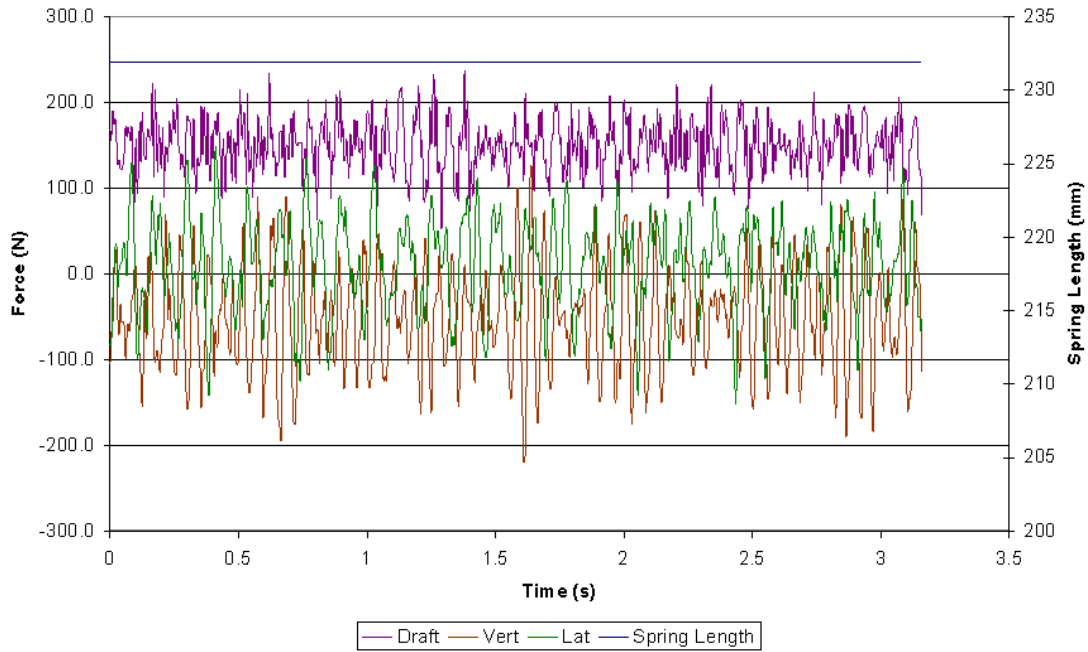


Figure A3.48: Field cultivator standard – run #48 time history results – 178 mm sweep, 76 mm depth, 2.68 m/s, low moisture (6.9% d.b.), high compaction (1,100 kPa)

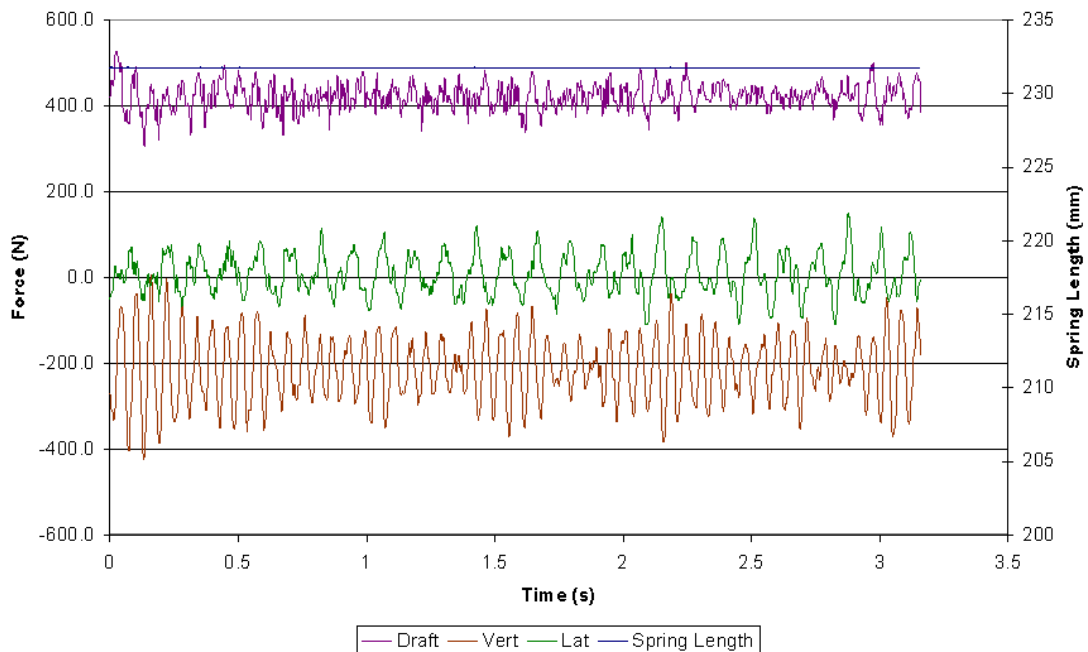


Figure A3.49: Field cultivator standard – run #49 time history results – 178 mm sweep, 152 mm depth, 2.68 m/s, low moisture (6.9% d.b.), high compaction (1,100 kPa)

Table A3.2: Field cultivator soil bin test draft load regression analysis with all variables

<i>Regression Statistics</i>								
Multiple R		0.8732						
R Square		0.7624						
Adjusted R Square		0.7277						
Standard Error		177.6771						
Observations		48						

ANOVA					
	<i>df</i>	<i>SS</i>	<i>MS</i>	<i>F</i>	<i>Significance F</i>
Regression	6	4154176.2	692362.7	21.93161	2.31126E-11
Residual	41	1294335.773	31569.17		
Total	47	5448511.973			

	<i>Coefficients</i>	<i>Standard Error</i>	<i>t Stat</i>	<i>P-value</i>	<i>Lower 95%</i>	<i>Upper 95%</i>	<i>Lower 95.0%</i>	<i>Upper 95.0%</i>
Intercept	-2,366.0310	349.6782	-6.7663	0.0000	-3,072.2205	-1,659.8416	-3,072.2205	-1,659.8416
Sweep	1.1589	0.9519	1.2174	0.2304	-0.7636	3.0813	-0.7636	3.0813
Speed	42.6384	99.3631	0.4291	0.6701	-158.0295	243.3063	-158.0295	243.3063
Speed^2	13.8699	17.9342	0.7734	0.4437	-22.3490	50.0889	-22.3490	50.0889
Depth	3.6287	0.6731	5.3909	0.0000	2.2693	4.9881	2.2693	4.9881
Compaction	0.3645	0.0570	6.3953	0.0000	0.2494	0.4796	0.2494	0.4796
Moisture	225.1805	36.6364	6.1464	0.0000	151.1918	299.1693	151.1918	299.1693

Table A3.3: Field cultivator soil bin test draft load regression analysis with Speed eliminated

<i>Regression Statistics</i>								
Multiple R		0.8726						
R Square		0.7614						
Adjusted R Squa		0.7330						
Standard Error		175.9430						
Observations		48						

ANOVA					
	<i>df</i>	<i>SS</i>	<i>MS</i>	<i>F</i>	<i>Significance F</i>
Regression	5	4148363	829672.602	26.80173602	4.58091E-12
Residual	42	1300149	30955.92768		
Total	47	5448512			

	<i>Coefficients</i>	<i>tandard Err</i>	<i>t Stat</i>	<i>P-value</i>	<i>Lower 95%</i>	<i>Upper 95%</i>	<i>Lower 95.0%</i>	<i>Upper 95.0%</i>
Intercept	-2,337.0423	339.7421	-6.8789	0.0000	-3,022.6696	-1,651.4150	-3,022.6696	-1,651.4150
Sweep	1.2839	0.8974	1.4308	0.1599	-0.5270	3.0949	-0.5270	3.0949
Speed^2	21.3214	4.4398	4.8023	0.0000	12.3616	30.2813	12.3616	30.2813
Depth	3.6287	0.6665	5.4441	0.0000	2.2836	4.9738	2.2836	4.9738
Compaction	0.3645	0.0564	6.4583	0.0000	0.2506	0.4784	0.2506	0.4784
Moisture	225.1805	36.2788	6.2069	0.0000	151.9669	298.3942	151.9669	298.3942

Table A3.4: Field cultivator soil bin test draft load regression analysis with Sweep eliminated

<i>Regression Statistics</i>	
Multiple R	0.8659
R Square	0.7497
Adjusted R Square	0.7265
Standard Error	178.0725
Observations	48

ANOVA					
	<i>df</i>	<i>SS</i>	<i>MS</i>	<i>F</i>	<i>Significance F</i>
Regression	4	4084989.664	1021247	32.20603	1.98955E-12
Residual	43	1363522.308	31709.82		
Total	47	5448511.973			

	<i>Coefficients</i>	<i>Standard Error</i>	<i>t Stat</i>	<i>P-value</i>	<i>Lower 95%</i>	<i>Upper 95%</i>	<i>Lower 95.0%</i>	<i>Upper 95.0%</i>
Intercept	-2,088.0929	295.3391	-7.0702	0.0000	-2,683.7010	-1,492.4849	-2,683.7010	-1,492.4849
Speed^2	20.7939	4.4780	4.6436	0.0000	11.7631	29.8247	11.7631	29.8247
Depth	3.6287	0.6746	5.3790	0.0000	2.2682	4.9892	2.2682	4.9892
Compaction	0.3645	0.0571	6.3811	0.0000	0.2493	0.4797	0.2493	0.4797
Moisture	225.1805	36.7179	6.1327	0.0000	151.1318	299.2293	151.1318	299.2293

Table A3.5: Field cultivator soil bin test vertical load regression analysis with all variables

<i>Regression Statistics</i>	
Multiple R	0.8116
R Square	0.6586
Adjusted R Square	0.6087
Standard Error	94.3291
Observations	48

ANOVA					
	<i>df</i>	<i>SS</i>	<i>MS</i>	<i>F</i>	<i>Significance F</i>
Regression	6	703864.5311	117310.8	13.18398	2.97121E-08
Residual	41	364817.0892	8897.978		
Total	47	1068681.62			

	<i>Coefficients</i>	<i>Standard Error</i>	<i>t Stat</i>	<i>P-value</i>	<i>Lower 95%</i>	<i>Upper 95%</i>	<i>Lower 95.0%</i>	<i>Upper 95.0%</i>
Intercept	759.9369	185.6448	4.0935	0.0002	385.0197	1,134.8541	385.0197	1,134.8541
Sweep	-0.4308	0.5054	-0.8524	0.3990	-1.4514	0.5899	-1.4514	0.5899
Speed	-24.6055	52.7520	-0.4664	0.6434	-131.1404	81.9294	-131.1404	81.9294
Speed^2	-3.5423	9.5213	-0.3720	0.7118	-22.7710	15.6864	-22.7710	15.6864
Depth	-2.5354	0.3574	-7.0949	0.0000	-3.2571	-1.8137	-3.2571	-1.8137
Compaction	-0.0937	0.0303	-3.0982	0.0035	-0.1548	-0.0326	-0.1548	-0.0326
Moisture	-53.2497	19.4503	-2.7377	0.0091	-92.5304	-13.9690	-92.5304	-13.9690

Table A3.6: Field cultivator soil bin test vertical load regression analysis with Speed² eliminated

<i>Regression Statistics</i>	
Multiple R	0.8108
R Square	0.6575
Adjusted R Square	0.6167
Standard Error	93.3565
Observations	48

ANOVA					
	<i>df</i>	<i>SS</i>	<i>MS</i>	<i>F</i>	<i>Significance F</i>
Regression	5	702632.9593	140526.6	16.12386	7.37796E-09
Residual	42	366048.6609	8715.444		
Total	47	1068681.62			

	<i>Coefficients</i>	<i>Standard Error</i>	<i>t Stat</i>	<i>P-value</i>	<i>Lower 95%</i>	<i>Upper 95%</i>	<i>Lower 95.0%</i>	<i>Upper 95.0%</i>
Intercept	770.3195	181.6428	4.2408	0.0001	403.7494	1,136.8896	403.7494	1,136.8896
Sweep	-0.3713	0.4745	-0.7825	0.4383	-1.3289	0.5863	-1.3289	0.5863
Speed	-43.6079	13.0520	-3.3411	0.0018	-69.9480	-17.2678	-69.9480	-17.2678
Depth	-2.5354	0.3537	-7.1688	0.0000	-3.2491	-1.8217	-3.2491	-1.8217
Compaction	-0.0937	0.0299	-3.1305	0.0032	-0.1542	-0.0333	-0.1542	-0.0333
Moisture	-53.2497	19.2498	-2.7662	0.0084	-92.0974	-14.4021	-92.0974	-14.4021

Table A3.7: Field cultivator soil bin test vertical load regression analysis with Sweep eliminated

<i>Regression Statistics</i>	
Multiple R	0.8078
R Square	0.6525
Adjusted R Square	0.6202
Standard Error	92.9348
Observations	48

ANOVA					
	<i>df</i>	<i>SS</i>	<i>MS</i>	<i>F</i>	<i>Significance F</i>
Regression	4	697295.8912	174324	20.18368	2.03196E-09
Residual	43	371385.729	8636.877		
Total	47	1068681.62			

	<i>Coefficients</i>	<i>Standard Error</i>	<i>t Stat</i>	<i>P-value</i>	<i>Lower 95%</i>	<i>Upper 95%</i>	<i>Lower 95.0%</i>	<i>Upper 95.0%</i>
Intercept	699.5840	156.8427	4.4604	0.0001	383.2807	1,015.8874	383.2807	1,015.8874
Speed	-43.6079	12.9931	-3.3562	0.0017	-69.8109	-17.4049	-69.8109	-17.4049
Depth	-2.5354	0.3521	-7.2014	0.0000	-3.2454	-1.8254	-3.2454	-1.8254
Compaction	-0.0937	0.0298	-3.1447	0.0030	-0.1539	-0.0336	-0.1539	-0.0336
Moisture	-53.2497	19.1628	-2.7788	0.0081	-91.8952	-14.6042	-91.8952	-14.6042

Table A3.7: Field cultivator soil bin test vertical load regression analysis as a function of draft load

<i>Regression Statistics</i>	
Multiple R	0.8719
R Square	0.7602
Adjusted R Square	0.7550
Standard Error	74.6411
Observations	48

ANOVA					
	<i>df</i>	<i>SS</i>	<i>MS</i>	<i>F</i>	<i>Significance F</i>
Regression	1	812401.7995	812401.8	145.8191	7.27526E-16
Residual	46	256279.8208	5571.3		
Total	47	1068681.62			

	<i>Coefficients</i>	<i>Standard Error</i>	<i>t Stat</i>	<i>P-value</i>	<i>Lower 95%</i>	<i>Upper 95%</i>	<i>Lower 95.0%</i>	<i>Upper 95.0%</i>
Intercept	-0.3167	17.8916	-0.0177	0.9860	-36.3307	35.6973	-36.3307	35.6973
Draft	-0.3861	0.0320	-12.0756	0.0000	-0.4505	-0.3218	-0.4505	-0.3218

Table 4.0.1: Alternative soil measurement – regression analysis output for soil shear strength

SUMMARY OUTPUT

<i>Regression Statistics</i>							
Multiple R	1						
R Square	1						
Adjusted R	65535						
Standard E	0						
Observatio	4						

ANOVA					
	<i>df</i>	<i>SS</i>	<i>MS</i>	<i>F</i>	<i>Significance F</i>
Regressor	3	40458080.44	13486027	#NUM!	#NUM!
Residual	0	0	65535		
Total	3	40458080.44			

	<i>Coefficients</i>	<i>Standard Error</i>	<i>t Stat</i>	<i>P-value</i>	<i>Lower 95%</i>	<i>Upper 95%</i>	<i>Lower 95.0%</i>	<i>Upper 95.0%</i>
Intercept	5446.522455	0	65535	#NUM!	5446.522	5446.522	5446.522	5446.522
Depth	-65.67117845	0	65535	#NUM!	-65.671	-65.671	-65.671	-65.671
Draft	19.16934706	0	65535	#NUM!	19.169	19.169	19.169	19.169
Slope	-17.69028426	0	65535	#NUM!	-17.690	-17.690	-17.690	-17.690

Table 4.0.2: Alternative soil measurement – regression analysis output for soil viscosity

SUMMARY OUTPUT

<i>Regression Statistics</i>							
Multiple R	1						
R Square	1						
Adjusted R	65535						
Standard E	0						
Observatio	4						

ANOVA					
	<i>df</i>	<i>SS</i>	<i>MS</i>	<i>F</i>	<i>Significance F</i>
Regressor	3	13721.07677	4573.692	#NUM!	#NUM!
Residual	0	0	65535		
Total	3	13721.07677			

	<i>Coefficients</i>	<i>Standard Error</i>	<i>t Stat</i>	<i>P-value</i>	<i>Lower 95%</i>	<i>Upper 95%</i>	<i>Lower 95.0%</i>	<i>Upper 95.0%</i>
Intercept	162.5745836	0	65535	#NUM!	162.575	162.575	162.575	162.575
Depth	-1.209389712	0	65535	#NUM!	-1.209	-1.209	-1.209	-1.209
Draft	0.353019569	0	65535	#NUM!	0.353	0.353	0.353	0.353
Slope	-0.32578139	0	65535	#NUM!	-0.326	-0.326	-0.326	-0.326

BIBLIOGRAPHY

- Abo-Elnor M, Hamilton R, Boyle JT. 3d dynamic analysis of soil-tool interaction using the finite element method. *J of Terramechanics* 2003; 40: 51-62.
- Abo-Elnor M, Hamilton R, Boyle JT. Simulation of soil-blade interaction for sandy soil using advanced 3d element analysis. *Soil & Tillage Research* 2004; 75: 61-73.
- ANSYS, Inc. ANSYS CFX Release 11.0 User Manual. ANSYS Europe LTD. 2007.
- Asaf Z, Rubinstein D, Shmulevich I. Determination of discrete element model parameters required for soil tillage. *Soil & Tillage Research* 2007; 92: 227-242.
- ASTM D 2573-01. Standard test method for field vane shear test in cohesive soil. 2001.
- Bathe KJ. Finite element procedures. Englewood Cliffs, New Jersey: Prentice Hall. 1996.
- Chandrupatla TR, Belegundu AD. Introduction to finite elements in engineering. Upper Saddle River, New Jersey: Prentice Hall. 1991.
- Davidson JB, Chase LW. Farm machinery and farm motors. New York: Orange Judd Company; 1908.
- Desbiolles JMA, Godwin RJ, Kilgour J, Blackmore BS. A novel approach to the prediction of tillage tool draught using a standard tine. *J Agric Eng Res* 1997; 66: 295-309.
- Desbiolles JMA, Godwin RJ, Kilgour J, Blackmore BS. Prediction of tillage implement draught using cone penetrometer data. *J Agric Eng Res* 1999; 73, 65-76.
- Fielke JM. Interactions of the cutting edge of tillage implements with soil. *J of Agric Eng Res* 1996; 63: 61-72.
- Fielke JM. Finite element modeling of the interaction of the cutting edge of tillage implements with soil. *J of Agric Eng Res* 1999; 74: 91-101.
- Glancey JL, Upadhyaya SK, Chancellor WJ, Rumsey JW. An instrumented chisel for the study of soil-tillage dynamics. *Soil & Tillage Research* 1989; 14: 1-24.
- Jayasuriya HPW, Salokhe VM. A review of soil-tine models for a range of soil conditions. *J of Agric Eng Res* 2001; 79: 1-13.
- Karmakar S, Kushwaha RL. CFD simulation of soil forces on a flat tillage tool. ASAE 2005 Annual Intl Meeting. Paper 051160.
- Karmakar S, Kushwaha RL. Soil viscosity and yield stress measurement using a motorized rheometer. ASABE 2006a Annual Intl Meeting. Paper 061094.
- Karmakar S, Kushwaha RL. Dynamic modeling of soil-tool interaction: an overview from a fluid flow perspective. *J Terramechanics* 2006b; 43: 411-425
- Karmakar S, Kushwaha RL. Development and laboratory evaluation of a rheometer for soil visco-plastic parameters. *J Terramechanics* 2007; 44: 197-204.
- Karmakar S, Sharma J, Kushwaha RL. Critical state elasto-plastic constitutive models for soil failure in tillage – a review. *Canadian Biosystems Engineering* 2004; 46:2.19-2.23.
- Keedwell MJ. Rheology and soil mechanics. Essex, England: Elsevier Applied Science Publishers LTD. 1984.
- Kepner, RA, Bainer Roy, Barger EL. Principles of farm machinery. Second edn. Westport, Connecticut: The AVI Publishing Company, Inc. 1972.
- Koolen AJ, Kuipers H. Agricultural soil mechanics. New York: Springer-Verlag. 1983.

- Lipscomb GG, Denn MM. Flow of bingham fluids in complex geometries. *J Non-Newtonian Fluid Mech* 1984; 14: 337-346.
- Mouazen AM, Nemeny M. Tillage tool design by the finite element method: part 1. finite element modeling of soil plastic behavior. *J Agric Eng Res* 1999a; 72: 37-51.
- Mouazen AM, Nemeny M. Tillage tool design by the finite element method: part 2. experimental validation of the finite element results with soil bin test. *J Agric Eng Res* 1999b; 72: 53-58.
- Mouazen AM, Nemeny M. Finite element analysis of subsoiler cutting in non-homogeneous sandy loam soil. *Soil & Tillage Research* 1999c; 51: 1-15.
- Mouazen AM, Ramon H. A numerical-statistical hybrid modeling scheme for evaluation of draught requirements of a subsoiler cutting a sandy loam soil, as affected by moisture content, bulk density and depth. *Soil & Tillage Research* 2002; 63: 155-165.
- Palmer J, Grasbey CA. Evaluation of load cycles generated on a fixed tine working in soil. *J Agric Eng Res* 1990; 45: 295-311.
- PLAXIS Version 8 material Models Manual
- Rajaram G, Gee-Clough D. Force-distance behavior of tine implements. *J Agric Eng Res* 1988; 41: 81-98.
- Renon N, Montmitonnet P, Laborde P. Numerical formulation for solving soil/tool interaction problem involving large deformation. *Eng Comp: Intl J for Comp-Aided Eng and Software* 2005; 22: 87-109.
- Robertson JA, Crowe CT. *Engineering fluid mechanics*. Fourth edn. Boston: Houghton Mifflin Company. 1990.
- Rosa UA, Wulfsohn D. Constitutive model for high speed tillage using narrow tools. *J of Terramechanics* 1999; 36: 221-234.
- Shen J, Kushwaha RL. Quick finite element analysis of soil tool interactions. *Comp and Electr in Agric* 1993; 9: 289-299.
- Shen J, Kushwaha RL. *Soil-machines interactions: a finite element perspective*. New York: Marcel Dekker, Inc. 1998.
- Stafford JV. An application of critical state soil mechanics: the performance of rigid tines. *J. of Eng Res* 1981; 26: 387-401.
- Swick WC, Perumpral JV. A model for predicting soil-tool interaction. *J of Terramechanics* 1988; 25: 43-56.
- Tannehill JC, Anderson DA, Pletcher RH. *Computational fluid mechanics and heat transfer*. Second edn. Philadelphia: Taylor & Francis. 1997.
- Thomas JJ. *Farm implements and farm machinery and the principles of their construction and use*. New York: Orane Judd and Company. 1869.
- Upadhyaya SK, Ma TX, Chancellor WJ, Zhao YM. Dynamics of soil-tool interaction. *Soil & Tool Research* 1987; 9: 187-206.
- Wheeler PN, Godwin RJ. Soil dynamics of single and multiple tines at speeds up to 20 km/h. *J Agric Eng Res* 1996; 63: 243-250.
- Willatt ST, Willis AH. Soil compaction in front of simple tillage tools. *J Agric Eng Res* 1965; 10: 109-113.
- Zhixiong L, Yaohua W, Junzheng P. Mechanical properties of soils under explosive loading. *J Agric Eng Res* 2001; 80: 217-222.